UNIVERSITY OF CALIFORNIA, SAN DIEGO

Development of Fluorescent Methods for the Detection of Amyloidosis in Neurodegeneration

A dissertation submitted in partial satisfaction of the requirements for the degree Doctor of Philosophy

in

Chemistry

by

Kevin Jay Cao

Committee in charge:

Professor Jerry Yang, Chair
Professor Emmanuel Theodorakis, Co-Chair
Professor Thomas Hermann
Professor Judy Kim
Professor Christina Sigurdson

2016

This Dissertation of Kevin Jay Cao is approved, and it is acceptable in quality and form for publication on microfilm and electronically:

_____

_____

_____

_____

Co-Chair

_____

Chair

University of California, San Diego

2016

DEDICATION

To 外公 & 外婆.

EPIGRAPH

"*Great things are done by a series of small things brought together.*"

-Vincent van Gogh

TABLE OF CONTENTS

LIST OF FIGURES

LIST OF TABLES

LIST OF ABBREVIATIONS

Aβ	β-amyloid
AD	Alzheimer's Disease
AMD	Age-related macular degeneration
ANCA	Amino-naphthalene cyanoacrylate
CJD	Creutzfeldt-Jakob's Disease
CR	Congo-Red
CSF	Cerebrospinal fluid
CTE	Chronic traumatic encephalopathy
CWD	Chronic wasting disease
DCM	Dichloromethane
DMF	Dimethyl formamide
EtOAc	Ethyl acetate
GCL	Granule cell layer
GPI	Glycosylphospotidylinositol
IAPP	Islet amyloid polypeptide
INL	Inner nuclear layer
IPL	Inner plexiform layer
IR	Infrared
MeOH	Methanol
MS	Mass spectroscopy
NIRF	Near-infrared fluorescence

NFT	Neurofibrillary tangles
NMR	Nuclear magnetic resonance
OLM	Ooshika-Lippert-Mataga
ONL	Outer nuclear layer
OPL	Outer plexiform layer
PD	Parkinson's Disease
PE	Pre-eclampsia
PET	Positron emission tomography
PrP	Prion protein
RML	Rocky Mountain Laboratory
SEVI	Semen-derived enhancer of viral infection
THF	Tetrahydrofuran
TIRF	Total internal reflectance fluorescence
ThT	Thioflavin-T

ACKNOWLEDGEMENTS

Graduate school has been an amazing learning experience for me. I am a reserved person, but I will say that I am definitely going to miss this place, so I would like to take this space to thank the people that have been there for me, both professionally and personally, over these past five years.

To my mom and my dad, thank you for your unconditional support and never ending questions of if I'm a "real doctor". Jason and Julia, thanks for making home enjoyable and for keeping me grounded, I am lucky to have you two in my life. To my friends Jarrod and Pete, thank you guys for well over a decade of friendship.

To the Yang lab, thank you guys for struggling with me over five years, and for sharing all the successes and disappointments together. To Christina, thank you for your initial guidance in navigating this wild ride. Yuchen, thank you for being a great source of advice over the years. Tim and Leibniz, thank you guys for all those tennis breaks and late nights purifying material. Kate, baby gurl thanks for the fun conversations about chemistry. Jamie, thanks for using big words that I don't understand, and for the completely unnecessary, but appreciated, heart-to-hearts.

To Jessica, you've been there since day one, even if you still don't believe that I was really present that first summer when it was just you, Cliff, and me. Thank you for your constant friendship, the coffee and lunch breaks, and for putting up with me for five years. Dan, thanks for being a great guy to talk sports and video games with and for keeping it real in lab. I forever hope the Blackhawks never win the cup again. K2, thanks for being a good friend to share teaching philosophies, and board games,

with. Young-Hun, thank you for making lab enjoyable and for your cosmic ability to outdrink everyone. Geoffray, thank you for the great discussions about sports, culture, and life in general. Sylvia, thank you for being a great undergrad to work with and for making fun of my Chinese. To the new Yang members, Tak and John, thank you two for being fun guys to hang out with; keep on persevering, it is definitely worth it.

To my collaborators, thank you for putting up with my constant badgering for data. Jordi, thank you for your heroic efforts in modeling the ANCA systems in all those solvent environments, and thank you for the tour of Barcelona. Kristy, thank you for being both an amazing friend and a great colleague to work with. Patricia Gaffney and Patricia Aguilar, thank you two for your expertise of tissue histology and animal studies, and for making sure I didn't do something dumb to give myself prions.

To my friends around the department, I am truly grateful for your friendships. My Pacific Beach buddies Cliff and Jacquelin, thanks for the fun nights at Cass St. Bar & Grill and Shore Club. I hope you two enjoy Los Angeles and all the amazing food, sports, and traffic that come with it. Lisa and Alex, thanks for the 6th floor hangouts and for being great people to enjoy North Park with; I'm stoked to see you two back in the San Francisco. Sarah, I wish I could stay and kick it with you for a while longer, but this is my stop off the struggle bus. Thank you for being one of my best friends, and for all the adventures around San Diego. I hope to see you fly off into space; otherwise the Bay works, too. Brandon, Charles, DJ, Colin, Swagat and Frankie, thank you guys for the brews, and poker nights and for taking all my money. Ed and Vivi, thanks for being great company to hang and have coffee with outside of lab. To those I inevitably forgot, thank you for all the good times.

To my college friends John, Saul, Mike, Garlen, and Phirun, thank you guys for struggling through undergrad and post-grad life with me. As much as I enjoy living by myself, I have to say that the League of Ordinary Gentlemen will be missed.

Lastly, I would like to thank my committee for their guidance and presence during my graduate school career. To Prof. Hermann and Prof. Kim, thank you for your support of both my academic and educational pursuits. To Prof. Sigurdson and Prof. Theodorakis, thank you for all the discussions about our respective projects, and for allowing me to sit and work in your labs. I really valued having the opportunity to collaborate with such a diverse group of students and post-docs. Finally to Jerry, thank you for your direction and counsel over the past half-decade. And thank you for your confidence in me and for the freedom you allowed me to have in my pursuit of science.

Chapter 2 is a partial reprint of the material as it appears in "Aminonaphthalene 2-Cyanoacrylates (ANCA) Probes Fluorescently Discriminate between Amyloid-β and Prion Plaques in Brain". Cao, Kevin; Farahi, Mona; Dakanali, Marianna; Chang, Willy M.; Sigurdson, Christina J.; Theodorakis, Emmanuel A.; Yang, Jerry. (2012) *Journal of the American Chemical Society*, 134 (42), 17338-17341. I am the primary author on this publication.

Chapter 3 is based on material currently being prepared for submission for publication "Rational Design of Amyloid-Discriminating Fluorophores". Cao, Kevin J.; Elbel, Kristyna M.; Cirera, Jordi; Sigurdson, Christina J.; Paesani, Francesco;

Theodorakis, Emmanuel A.; Yang, Jerry; *In preparation.* I am the primary author on this publication.

Chapter 4 is a partial reprint of the material as it appears in "Real-time Monitoring of Alzheimer's-related amyloid via Probe Enhancement-Fluorescence Correlation Spectroscopy". Guan, Yinghua; Cao, Kevin J.; Cantlon, Adam; Elbel, Kristyna; Theodorakis, Emmanuel A.; Walsh, Dominic, Yang, Jerry, Shah, Jagesh V. (2015) *ACS Chemical Neuroscience*, 6 (9), 1503-1508. I am co-author on this publication. Chapter 4 is also based on material currently being prepared for submission for publication "A Fluorescent Method to Monitor Amyloidosis in the Retina". Cao, Kevin J.; Aguilar-Calvo, Patricia; Liu, Jun; Sigurdson, Christina J.; Yang, Jerry. *In preparation.* I am the primary author on this publication.

Chapter 5 is a partial reprint of the material as it appears in "Real-time Monitoring of Alzheimer's-related amyloid via Probe Enhancement-Fluorescence Correlation Spectroscopy". Guan, Yinghua; Cao, Kevin J.; Cantlon, Adam; Elbel, Kristyna; Theodorakis, Emmanuel A.; Walsh, Dominic, Yang, Jerry, Shah, Jagesh V. (2015) *ACS Chemical Neuroscience*, 6 (9), 1503-1508. I am co-author on this publication. Chapter 5 is also based on material currently being prepared for submission for publication "Amyloid-binding Fluorescence Diagnostic Assay for Pre-eclampsia". Do, Jamie P.; Cao, Kevin J.; Laurent, Louise; Parast, Mana; Yang, Jerry. *In preparation.* I am co-author on this publication.

VITA

University of California, San Diego

2016 Doctor of Philosophy in Chemistry

2011 Bachelors of Science in Biochemistry/Chemistry

2011 Bachelors of Science in Physiology & Neuroscience

PUBLICATIONS

Cao, K.J., Elbel, K.M., Cirera, J., Sigurdson, C.J., Paesani, F., Theodorakis, E.A., Yang, J. (2016) Rational Design of Amyloid-Discriminating Fluorophores. *In preparation.*

Cao, K.J., Calvo-Aguilar, P., Liu, J., Sigurdson, C.J., Yang, J. (2016) Development of a Fluorescent Platform for Retinal Imaging of Amyloidosis. *In preparation*.

Do, J.P., **Cao, K.J.**, Laurent, L., Parast, M., Yang, J. (2016) Amyloid-Binding Fluorescence Diagnostic Assay for Pre-Eclampsia. *In preparation*.

Guan, Y., **Cao, K.J.**, Cantlon, A., Elbel, K., Theodorakis, E.A., Walsh, D., Yang, J., Shah, J.V. (2015) Real-time Monitoring of Alzheimer's-related amyloid via Probe Enhancement-Fluorescence Correlation Spectroscopy. *ACS Chemical Neuroscience,* 6 (9), 1503-1508

Cao, K., Farahi, M., Dakanali, M., Chang, W.M., Sigurdson, C.J., Theodorakis, E.A., Yang, J. (2012). Aminonaphthalene 2-Cyanoacrylates (ANCA) Probes Fluorescently Discriminate between Amyloid-β and Prion Plaques in Brain. *Journal of the American Chemical Society*, 134 (42), 17338-17341

PRESENTATIONS

Cao, K.J., Elbel., K.M, Fu, L., Sigurdson, C.J., Theodorakis, E.A., Yang, J.
Rational Design of Environment Sensitive Fluorophores for Detection of Aggregated Amyloid Protein Biomarkers in Neurological Diseases. Poster presentation at *AD/PD 2015*, Nice, France; March, 2015

Cao, K., Elbel K., Sigurdson, C.J., Theodorakis, E.A., Yang, J.
A Fluorescence Approach to Discrimination of Aggregated Amyloid Proteins. Poster presentation at *Fluorescent Biomolecules and Their Building Blocks: Design and Applications (FB^3)*, La Jolla, CA; August, 2014

Cao, K., Elbel K., Sigurdson, C.J., Theodorakis, E.A., Yang, J.
A Fluorescence Approach to Discrimination of Aggregated Amyloid Proteins. Poster presentation at the Annual Meeting of the *Biophysical Society*, San Francisco, CA; February, 2014

Flores-Garcia, L., Ray, J., **Cao, K.**, Xie, W., Sanchez, I., Alcaraz, W.A., Baponi, E., Hou, A., Gage, F.H., Hamilton, B.A.
Zinc finger protein 423 integrates signaling pathways by the niche and targets hedgehog signaling gene expression during adult neurogenesis. Poster presentation at the Annual Meeting of the *Society for Neuroscience*, San Diego, CA; November, 2013

ABSTRACT OF THE DISSERTATION

Development of Fluorescent Methods for the Detection of Amyloidosis in Neurodegeneration

by

Kevin Jay Cao

Doctor of Philosophy in Chemistry

University of California, San Diego 2016

Professor Jerry Yang, Chair

At the molecular level, neurodegeneration is characterized by the appearance of aggregates of misfolded proteins known as amyloids. These assemblies are often associated with neurotoxicity and are classically the defining feature of neurodegenerative diseases such as Alzheimer's Disease (AD). The appearance of these aggregates in the brain often preludes the clinical symptoms of neurodegeneration, and thus are valuable targets for the early diagnoses of the diseases.

This thesis documents the development of amino-naphthalene cyanoacrylate (ANCA) fluorophores and their use towards detecting these amyloid aggregates.

Chapters 2 and 3 describe the rational design and synthesis of the ANCA family and their colorimetric sensitivity to different amyloid species. This unique capability was found to originate from their environmentally sensitive molecular structure, which was utilized to characterize amyloids based on their fluorescence emission lambda max.

Chapter 4 describes the development of an *in vivo* imaging methodology to detect amyloidosis in the retina of AD and prion mice using the fluorescence of an ANCA derivative, ARCAM-1. This preliminary study on retinal imaging supports the use of the eye as a window to peer into the central nervous system.

Finally, Chapter 5 presents the utility of ARCAM-1 as a sensor for the detection of the smaller, transient oligomeric amyloid species by use of fluorescence correlation spectroscopy (FCS), and as a sensor for amyloidosis in the urine of pregnant women with pre-eclampsia (PE).

Chapter 1

Introduction: The Detection of Amyloidosis

1.1 Amyloids & Disease

A common motif found in systemic and neurologic degenerative diseases is the accumulation of misfolded protein assemblies known as amyloids. Under normal circumstances, proteins adopt precise folding conformations, known as native states, due to intramolecular interactions between the amino acid residues.[1,2] Disease states can shift the balance from these native states to misfolded states, where the secondary structures of the proteins tend to adopt β-sheet arrangements. Amyloidosis results from the self-assembly of misfolded proteins rich in these β-sheets into oligomers and higher order aggregates known as protofibrils, fibrils, and ultimately as insoluble proteinaceous tissue deposits.[3–5]

Structural elucidation of amyloids has been limited by the difficulties in the crystallization of the assemblies. Much of the known information has originated from

optical interference experiments such as circular dichroism (CD) or x-ray diffraction, and nuclear magnetic resonance (NMR) studies.[6–9] Between these types of experiments, the defining characteristics of amyloids have been attributed as a predominantly cross β-sheet arrangement, where intramolecular hydrogen bonding generates monomer units of either parallel or anti-parallel β-sheets, which then stack upon each other to form the oligomeric and fibrillar assemblies. Parallel to fibrillar axes are the side-chain grooves, which line the length of the aggregates and vary in hydrostatic nature between amyloids, depending on the protein sequence.[10]

Historically, the formation of insoluble amyloid aggregates has long been considered the pathological hallmark of neurodegenerative diseases such as Alzheimer's Disease (AD).[11] For example, in AD the improper production of β-amyloid (Aβ) leads to the accumulation of soluble toxic oligomeric species as well as the classical insoluble macroscopic senile plaques. Over the past twenty years, work using small molecules and antibodies has revealed many additional amyloidogenic proteins associated with different neurologic and non-neurologic diseases. These include α-synuclein in Parkinson's Disease (PD), the prion proteins found in Creudzfeldt-Jakob's Disease (CJD) and related spongiform encephalopathies, islet amyloid polypeptide (IAPP, also known as amylin) in Type II Diabetes Mellitus, and semen-derived enhancer of viral injection (SEVI) in HIV, among others (Figure 1.1).[11–13]

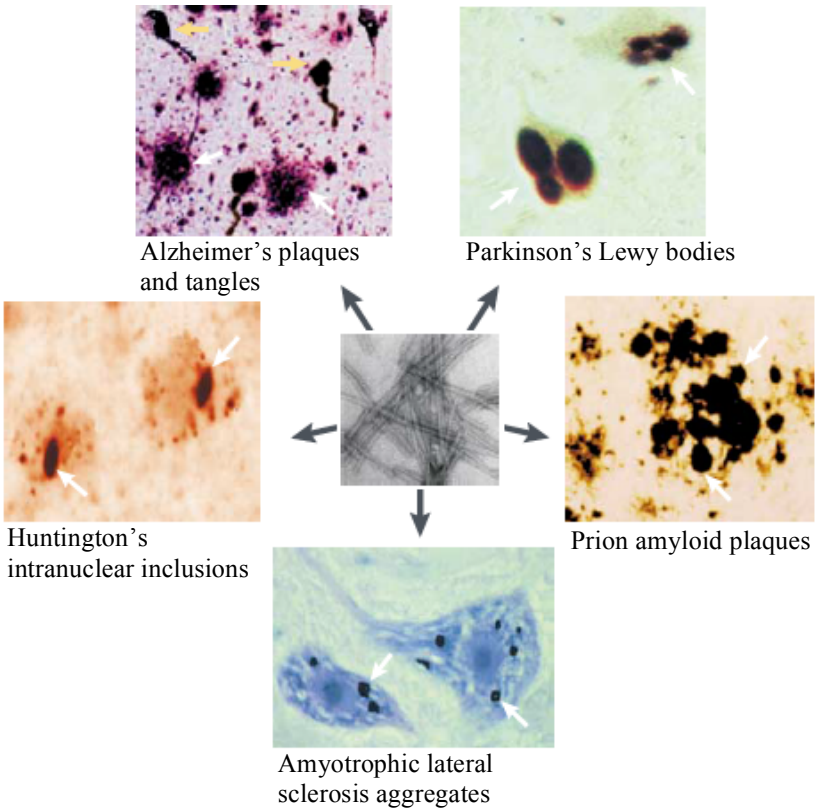

Figure 1.1 Amyloidosis is seen in many neurodegenerative diseases and is typically visualized with amyloid-specific dyes or by immunohistochemical methods. Adapted with permission from Nature Publishing Group. Nature Reviews Neuroscience, *Unfolding the role of protein misfolding in neurodegenerative diseases*, 4, 49-60. Figure 1, copyright 2003.

1.2 Small Molecule Detection of Amyloids

Coinciding with the discovery of amyloidogenic proteins has been the development of innovative dyes tailored to the detection of amyloid assemblies (Figure 1.2). These types of compounds all exhibit non-selective, but specific, detection of amyloid aggregates in tissue, show comparable binding affinities, and possess photophysical properties that have revealed biological information complementing that gained from the classical amyloid-binding compounds Congo Red (CR) and Thioflavin-T (ThT).

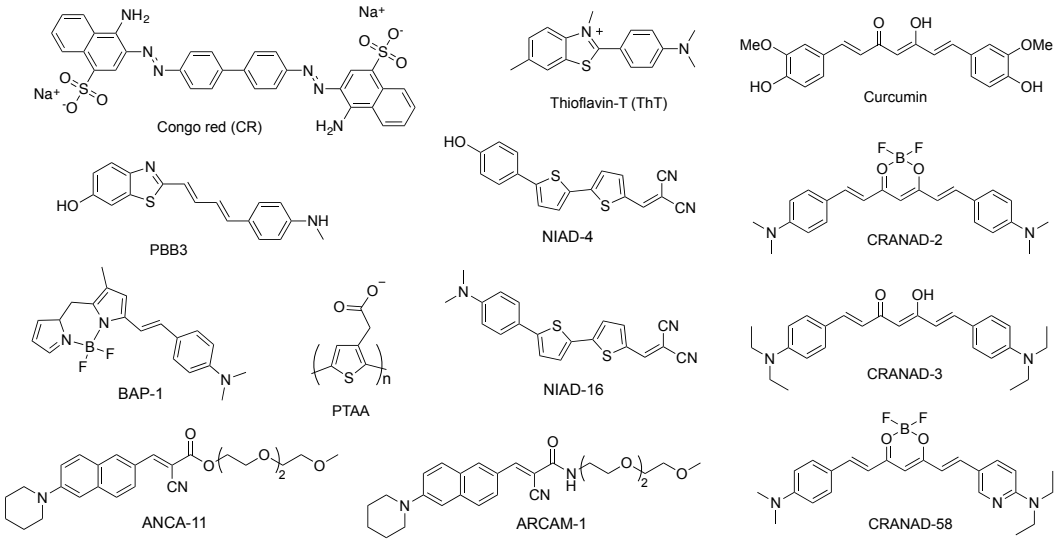

Figure 1.2 A representative survey of recently reported amyloid-binding fluorophores, along with the conventional Congo Red (CR) and Thioflavin-T (ThT) dyes.

In the past two decades, many of these amyloid-binding fluorophores have been used as frameworks to incorporate features suitable for biomedical uses. In particular, the early 2000's saw the introduction of radiolabels to the scaffolds in order to generate radiolabeled positron emission tomography (PET) tracers for following and diagnosing neurological diseases. ThT was one of the first scaffolds to undergo derivatization, leading to the compound Pittsburgh Compound B (PiB) and one of the first clinical trials of diagnosing AD in living patients (Figure 1.3).[14,15]

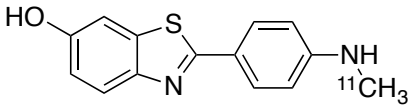

Pittsburgh compound B (PiB)

Figure 1.3 Pittsburgh compound B (PiB) is a radioligand derivative of Thioflavin-T (ThT) used for positron emission tomography for diagnosing Alzheimer's Disease.

Though the development of PET ligands for AD and other neurodegenerative diseases has been thoroughly evaluated in recent years and has found success in the clinical setting, the inherent disadvantage of the short half life of the radiolabels, high cost-of-use, and lack of a standardized definition of a positive scan across different PET centers (and for different PET agents) has encouraged a continued effort in finding alternative diagnostic methods using amyloid-binding small molecules.[15–17]

While PET imaging continues to serve as a primary tool for measuring amyloid accumulation in clinical trials, new methods for safely measuring amyloid levels *in vivo* or in readily available biofluids (e.g., CSF, blood, or urine) that overcome the current challenges with PET could help with widespread integration of amyloid burden measurements into the general population.

1.2.1 Traditional Fluorophore Scaffold Designs

Congo-Red (CR) was first discovered to bind to the pancreatic islets in patients with diabetes, where it was able to enhance the native birefringence of amyloid plaques.[18] The enhancement of birefringence occurred along the long axis of the fibrils. By computational modeling, CR was shown to bind perpendicularly to grooves along the amyloid surface formed by polar residues of the stacked β-sheets, parallel to the fibril axis. As a result, CR becomes organized along the fibrillar axis with individual dipole moments lying in an ordered array, resulting in the anisotropic effects seen with polarized light (Figure 1.4).[19–22] Additionally, it was found that binding induces a stabilization of the torsional rotation between the two diazo moieties, resulting in a red-shift of absorption from 490 to 540 nm and a subsequent

enhancement of fluorescence intensity.[10,20] Due to this duality of birefringence and fluorescence, CR has predominantly seen use as a histopathological dye to confirm the presence of AD in post-mortem brain tissue.

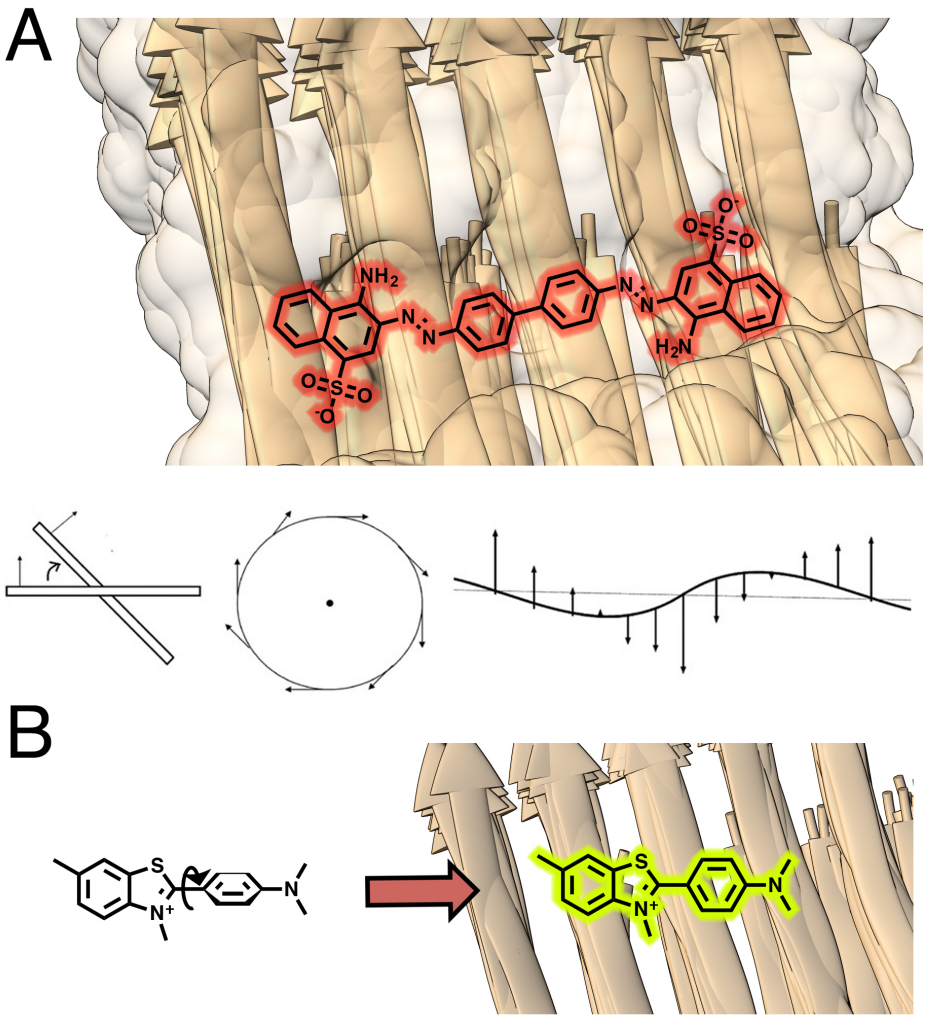

Figure 1.4 Amyloid-binding properties of Congo-Red and Thioflavin-T. A) CR binds in an ordered fashion into side chain grooves formed parallel to the fibril axis (top cartoon). The birefringent property of CR is thought to arise from the anisotropic arrangement of CR molecules along the fibril axis, forcing the dipole moments to be arranged unidirectional (bottom). B) ThT shows turn-on fluorescence once bound to amyloid, resulting from the inhibition of the benzothiazole-aniline bond rotation. Adapted with permission from Elsevier. Biophysical Journal, *Binding of Congo Red to Amyloid Protofibrils of the Alzheimer Aβ(9–40) Peptide Probed by Molecular Dynamics Simulations*, 103, 550-557. Figure 6, copyright 2012.

The binding of ThT to amyloid also induces an enhancement of fluorescence by restriction of torsional rotation along the benzothiazole-aniline bond. ThT consists of a push-pull molecular rotor motif, in which fluorescence is achieved through a donor-acceptor electronic network via an n - π^* transition.[10,23] This transition is hypothesized to be permitted upon binding of the molecule to a set of grooves formed from β-sheets, analogous to the binding mode of CR (Figure 1.4).[10,21] Additional work by Singh and colleagues have suggested that ThT forms micelles that may act as the primary amyloid-binding partner at concentrations greater than 10 μM.[24] Regardless, as a result of binding to amyloids, ThT emission at 480 nm is typically seen to greatly increase in a dose-dependent manner as the concentration of amyloid increases.

The molecular rotor structure of Thioflavin-T and related benzothiazoles has shown high-contrast labeling for amyloids in tissue sections, and in cell-free environments as protein aggregation markers. ThT in particular shows ubiquitous binding for several amyloidogenic proteins, ranging from cerebral amyloids such as β-amyloid and α-synuclein to systemic amyloids such as insulin and prions.[25–27] However, recent work by Higuchi and coworkers revealed that tailoring both the length of the aromatic π-network and the lipophilicity of benzothiazole molecular rotors allowed them to tune the selectivity of their phenyl/pyridinyl-butadienyl-benzothiazoles/benzothiazolium (PBB) compounds between β-amyloid senile plaques and hyper-phosphorylated neurofibrillary tangles (NFTs) composed of the amyloidogenic tau protein, which are co-deposited in AD.[28] By increasing the lipophilicity, the selectivity for binding of the probes shifted from NFTs to β-amyloid senile plaques (Figure 1.5).

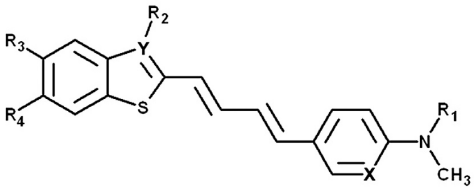

Compound	R_1	R_2	R_3	R_4	X	Y	ClogP
PBB1	CH_3	-	H	H	C(H)	N	5.44
PBB2	H	-	H	OH	C(H)	N	3.57
PBB3	H	-	H	OH	N	N	3.30
PBB4	H	-	OH	OH	C(H)	N	2.97
PBB5	CH_3	CH_3CH_2	H	H	C(H)	N^+	2.32

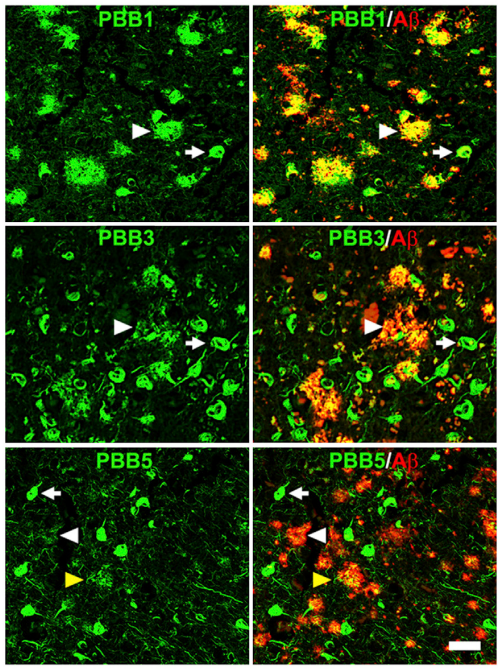

Figure 1.5 Design of selective fluorophores for β-amyloid and tau aggregates based on the benzothiazole motif. Increasing the lipophilicity of the compounds showed selective staining of senile plaques, whereas decreasing lipophilicity caused a selection of neurofibrillary tangles. Adapted with permission from Elsevier. Neuron, *Imaging of Tau Pathology in a Tauopathy Mouse Model and in Alzheimer Patients Compared to Normal Controls*, 79, 1094-1108. Figure 1, copyright 2013.

Furthermore, by increasing the length of the π-network between 13.2 and 18.5Å, they were able to selectively bind tau aggregates associated with AD and Pick's disease, a non-AD form of dementia.[28,29] Taken together, these results reveal both a length-dependence and a lipophilicity parameter for design of tau or β-amyloid specific probes. These benzothiazole probes were compatible with two-photon microscopy, enabling access to new imaging modalities for study of amyloids in tissue that overcome the limitations of using ThT such as poor tissue penetration for fluorescence emission, and phototoxicity.[30]

Concomitant with work on tuning the benzothiazole core, incorporation of the *N*-methyl aniline moiety of ThT has also found success in developing amyloid-binders. The Akkaya and Ono groups have developed a series of molecules based on the boron-dipyrromethene (BODIPY) fluorophore family with nanomolar affinities to amyloid aggregates in AD and prion diseases.[31–33] In particular, they developed BAP-1 as a styryl-conjugated BODIPY dye incorporating an *N*-methyl aniline handle with near-IR fluorescence emission. Like the observations from Higuchi, they also found that increasing the lipophilicity increased binding affinities for amyloid aggregates, albeit the use of lipophilic probes in brain tissue was found to have nonspecific binding and high background.[34]

1.2.2 Recent Amyloid-Binding Fluorophores

Recently fluorophore designs have strayed from the use of non-benzothiazole constructs for amyloid detection. Like ThT, these compounds also rely on the binding-induced fluorescence enhancement, and typically are thought to also target the side chain grooves of the amyloid.[35,36] However, these compounds have also shown to have unique biocompatibilities and additional imaging modalities.

Conjugated oligothiophenes have found uses in electronics as electron-rich organoelectric materials. Due to their flexible scaffold, they also serve as strong environmental sensors, similar in application to push-pull molecular rotors, and have recently been found to bind amyloid aggregates with low nanomolar affinities.[36,37] The dithiophene molecular rotor NIAD-4 developed by Swager and colleagues retains the strong binding-induced fluorescence enhancement seen in ThT without its inherent

quenching effects.[38,39] In particular, NIAD-4 was found to have a binding affinity of 10 nanomolar, approximately 50 times stronger than that of ThT. They also revealed that NIAD-4 and other members of this family of fluorophores were able to bind selectively to β-sheet aggregates over α-helical aggregates, reducing nonspecific background signal for both histology and *in vitro* studies.[38]

Additional work by Swager and coworkers has shown that the fluorescence lifetime of the NIAD fluorophores depended on the type of aggregate being bound. Using their NIAD-16 derivative, they showed that vasculature amyloid generated a shorter fluorescence lifetime than plaque amyloid, allowing them to discriminate between amyloid deposition patterns.[40]

The Nilsson group has shown that larger oligo(polythiophene) compounds can bind multiple types of protein aggregates in tissue samples, with polythiophene acetic acid (PTAA) exhibiting the capability to bind both NFTs and senile plaques with distinct fluorescence emission profiles for each aggregate. Their discriminatory capability has been hypothesized to originate from conformational interactions with the unique tertiary and quaternary conformations adopted by amyloid aggregates.[37] Nonetheless, the capability to discriminate aggregate types has prompted much research in the area for molecules that can act both as detection agents as well as diagnostic tools to selectively identify diseases.[41]

Curcumin is a naturally fluorescent diarylheptanoid found in turmeric, and has been shown to bind amyloid aggregates with low nanomolar affinity.[42] *In vivo* and *in vitro* studies have also suggested that the compound has anti-aggregation properties when interacting with amyloids.[43–45] Similar to ThT and CR, molecular docking

simulations have suggested a binding mode where the molecule lies parallel with the long axis of the fibril; although here binding occurs along grooves formed by both polar and non-polar residues.[46] Its fluorescent properties fall in between those of ThT and CR, where binding induces a sharp enhancement of fluorescence emission at approximately 530 nm.[47]

Koronyo-Hamaoui and coworkers found that curcumin could label β-amyloid plaques in the brain and in the retina of 10 month-old transgenic AD mice, carrying the APP_{SWE} and $PSEN1_{\Delta 9}$ early onset-AD genes, upon intravenous administration over several days. Closer inspection of human AD patient retinal tissue also exhibited the presence of plaques, detected by immunofluorescence as well as curcumin binding.[48] Due to the oral biocompatibility and the fluorescence window near that of fluorescein, curcumin has been a popular candidate, alongside NIAD-4, as an *in vivo* diagnostic tool for monitoring AD in rodent models.[44]

Recent derivatization of the curcumin scaffold by Moore and coworkers has resulted in the CRANAD family of fluorophores.[49–51] By introducing an electron-deficient difluoroboron into the 1,3-diketone moiety of curcumin, they achieved a red-shift in the fluorescence emission window from the 530 nm to the near-infrared, between 650-900 nm. Additionally, they replaced the phenyl rings of curcumin with pyridyl groups to introduce hydrogen bonding to amyloid fibrils. The resulting CRANAD-2 and CRANAD-3 molecules, have thus been shown to be both stronger binders with affinities in the low nanomolar, as well as strong candidates for near-infrared fluorescence (NIRF) microscopy.[34,49,50]

1.3 Applications of Amyloid-Binding Fluorophores

1.3.1 *In Vitro* and Cell-Free Detection of Oligomers and Fibrils

Thioflavin-T is extensively used for *in vitro* aggregation studies.[22,52–54] In 2011 Nishida and coworkers reported the development of the real-time quaking induced conversion (RT-QuIC) assay for rapid detection of prion particles in cerebrospinal fluid (CSF) using a ThT read-out.[55,56] By seeding recombinant prion proteins with patient CSF samples containing trace amounts of PrP^{Sc}, the stable proteinase-resistant conformation or prion aggregates, aggregation could be rapidly monitored via ThT fluorescence rather than the conventional western-blot detection analyses in standard QuIC assays (Figure 1.6A). This facile approach to detection or prion aggregates has allowed the RT-QuIC assay to become adopted into the National Prion Disease Pathology Surveillance Center at Case Western University, a CLIA lab, as a tool for screening CSF for prion infection. Extensive standardization of the lag-phase for seeding by Shi and coworkers resulted in a calibration curve for the assay, now named qRT-QuIC, allowing for trace amounts of PrP^{Sc} to be quantified down to the 10^{-15} to 10^{-16} gram range in CSF samples.[27]

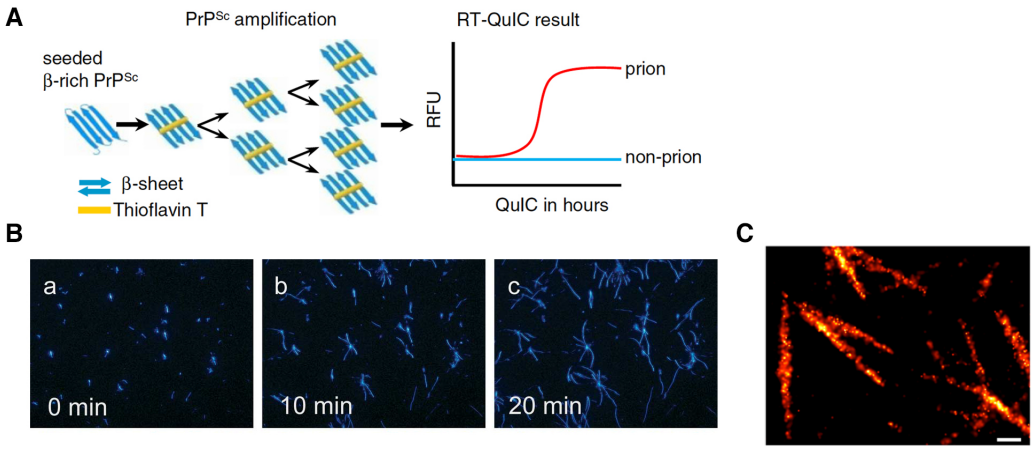

Figure 1.6 Spectroscopic and microscopic applications of amyloid-binding fluorophores. A) RT-QuIC assay has shown the ability to detect trace amounts of PrP^{Sc} in CSF samples, utilizing a seeding assay and ThT as the real-time readout for aggregation of prions. B) Total internal reflection fluorescence microscopy (TIRFM) with ThT used to monitor, in real-time, the formation of amyloid-β (1-40) fibrils on glass slides. C) Single-molecule binding-activation localization microscopy (BALM) super-resolution imaging of cell-free alpha-synuclein amyloid fibrils labeled with the oligothiophene p-FTAA. Scale bar in D) = 200 microns. Figure A adapted under the terms of the Creative Commons Attribution License, Acta Neuropathologica Communications.[27] Figure B adapted with permission from Elsevier. Journal of Molecular Biology.[57] Figure C adapted with permission from the American Chemical Society. ACS Chemical Neuroscience.[58]

Additionally, it was found that amyloid-binding fluorophores could be used to visualize aggregate fibrils at resolutions below the diffraction limit. ThT was recently found to be compatible with total internal reflection fluorescence microscopy (TIRFM) to monitor in real time the formation of β-amyloid (1-40) fibrils) (Figure 1.6B).[57] Using this technique, the Goto group was able to directly show the first-order kinetics of Aβ (1-40) fibril formation with a calculated rate constant of 0.045 s^{-1}. Similarly, the oligo(polythiophenes) were found to have binding-activated fluorescence suitable for super-resolution imaging (Figure 1.6C).[58] Recent work by the Wood and Klenerman groups has shown the capability of ThT to act as an identifier

for general β-sheet character in oligomeric species, circumventing the specificity of antibodies. Whereas ThT is known for its ability to bind protofibrils and fibrils, their single aggregate visualization by enhancement (SAVE) method was able to visualize 25-mer oligomeric Aβ, tau, and alpha-synuclein aggregates *in vitro*, as well as show a higher synuclein oligomer concentration in the CSF of PD patients compared to healthy controls.[59]

Taken together, these techniques have provided efficient methods to directly monitor and visualize amyloid aggregation dynamics that compliment the traditionally used atomic force microscopy (AFM) and transmission electron microscopy (TEM) techniques for single molecule analysis.

1.3.2 *In Vivo* Near-Infrared Fluorescence Imaging

Several amyloid-binding fluorophores have been developed into radioligands for PET imaging. These molecules have all seen success as diagnostic agents for detecting amyloid aggregates in AD, PD, chronic traumatic encephalopathy (CTE), and other neurodegenerative diseases. However, due to the costs associated with preparing PET tracers in the clinic as well as the short half-life of their radiolabels, there has been a strong interest in developing near-infrared amyloid-binding fluorophores.[28,60–62]

Near-infrared fluorescence (NIRF) has seen success in animal models as a rapid and efficient alternative for *in vivo* and deep tissue imaging. The use of fluorescence provides higher spatial resolution imaging that found in PET, and the shift of emission into the near-infrared region reduces both tissue scattering and tissue

autofluorescence. In contrast to PET development, which involves addition of the radioligand to a distal part of the molecule, the fluorogenic core of the molecule has to be modified in order to achieve a fluorescence emission window in the near-IR. Nonetheless, near-IR molecules such as the NIAD, CRANAD, and BAP families have been developed in which the near-infrared emission window of the compounds allows *in vivo* tissue imaging of amyloidosis.

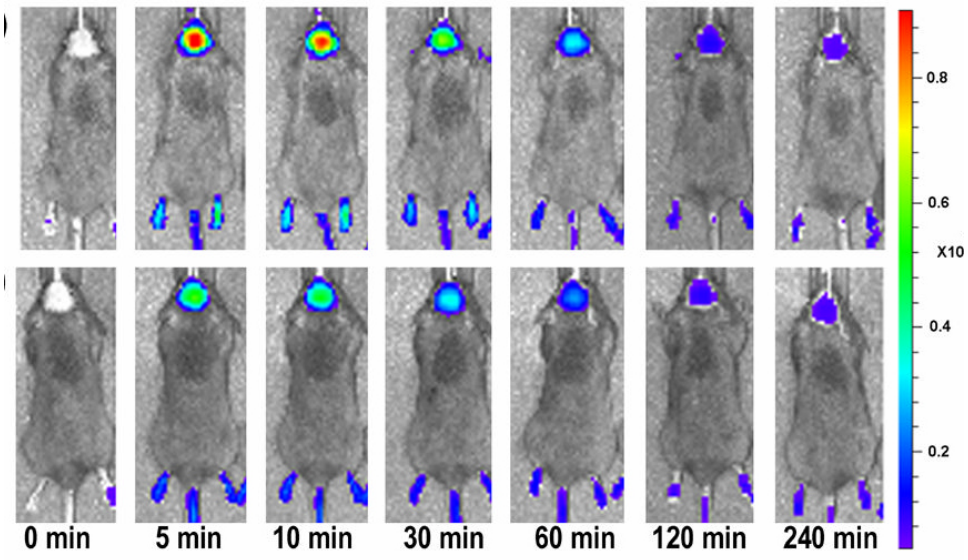

Figure 1.7 CRANAD-58 showed an increased NIRF signal in a 4-month old APP/PS1 mouse (top) compared to a wild-type age-matched control (bottom), suggesting the ability of the fluorophore to detect pre-fibrillar aggregates for early detection of AD. Adapted with permission from the American Chemical Society. Journal of the American Chemical Society. *Design and Synthesis of Curcumin Analogues for in Vivo Fluorescence Imaging and Inhibiting Copper-Induced Cross-Linking of Amyloid Beta Species in Alzheimer's Disease*, 135 (44), 16397–16409. Figure 6, copyright 2013.

The CRANAD family of fluorophores developed by Moore and coworkers has seen success in detecting plaque burden in aged Tg2576 mouse models. Additionally, their CRANAD-3 and CRANAD-58 fluorophores showed a higher signal in younger

4-month old Tg2576 and APP/PS1 mouse models, suggesting the presence of early-stage, non-fibrillar, aggregates bound with their compound and therefore a potential use as an early diagnostic (Figure 1.7).[49,51,63] Similarly, the Ono group found that their BAP-1, BODIPY-based, fluorophore also was capable of penetrating past the blood-brain barrier and labeling deposits in Tg2576 mice models.[32]

Though NIR fluorophores show robust labeling of amyloid plaques in rodents, when applied to humans, the average fluorescence penetration depth of 1 to 2 mm would be incapable of imaging subcortical regions in humans.[64,65] The rapid drop-off of signal intensity is largely due to scattering and absorption in tissue, which has been regiospecifically circumvented in fatty tissue using trans-fluorescence tomography (TFM) techniques, with depth penetration in the centimeters.[66] However, translation of NIRF techniques into the central nervous system is still encumbered by the depth of the brain regions of interest.

1.3.3 Retinal Imaging with Curcumin

A growing body of evidence has revealed that amyloid deposition also occurs in the eyes of patients with AD, with some studies supporting that the presence and abundance of ocular amyloid deposits that mirror the concentration of amyloid accumulation in the brain. Such an apparent correlation between brain and eye amyloid deposition may not be so surprising since the retina consists of several neuronal layers originating from the same ectoderm germ layer as the brain, which could provide a optical window into the central nervous system.[67]

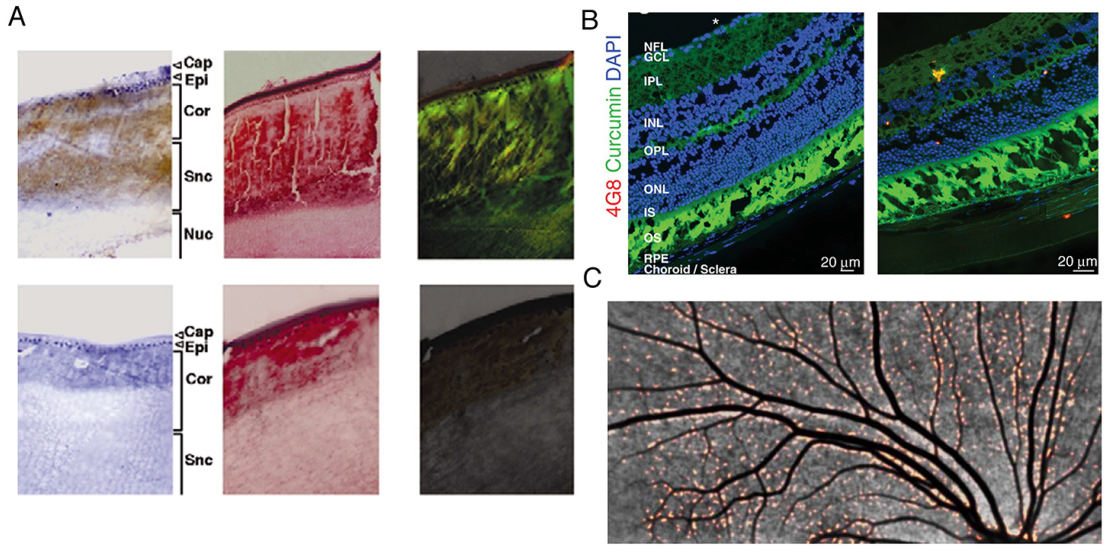

Figure 1.8 Detection of ocular amyloidosis using small fluorophores. A) Congo-Red was shown to detect birefringent amyloidogenic deposits in the lens of an 80-year old AD patient (top row) whereas no birefringence was seen with an age-matched healthy patient (bottom row). B) Intravenous administration of curcumin (yellow fluorescent objects) was shown to label small lipid-associated β-amyloid deposits in aged APP/PS1 mice (right image) whereas no deposits were seen in a wild-type control (left image). C) The retina of a Down's syndrome (DS) patient after oral administration of curcumin twice-daily for two days showed significant plaque labeling, particularly near the vasculature in a retinal fundus fluorescence image. Figures A & B adapted with permission from Elsevier. The Lancet,[68] Neuroimage.[48] Figure C adapted under the terms of the Creative Commons Attribution License, Frontiers in Behavioral Neuroscience.[69]

Although ocular amyloidosis is a typically found as a primary disease (i.e., it arises spontaneously and not due to a pre-existing condition), Goldstein and coworkers showed that the regiospecific appearance of β-amyloid (1-42) deposits in the lens could lead to AD-related cataracts (Figure 1.8A).[68] Using lifetime fluorescence microscopy, Hartung and coworkers have translated lens-based detection into a viable tool for screening for AD with sensitivity and specificity comparable to the FDA-approved PET agent, Florbetapir.[70]

The initial work by Koronyo-Hamaoui and coworkers in 2011 suggested the possibility of using the retina as an imaging platform for diagnosing AD. Intravenous administration of curcumin at 7.5 mg/kg over 5 days led to the labeling of deposits in the retina of transgenic $APP_{SWE}/PS1_{\Delta 9}$ mice, which were found in ganglia cell layer (GCL), the inner and outer plexiform layers (IPL, OPL), and sclera, consistent with previous reports (Figure 1.8B). When they stained human retinal tissue from AD patients with curcumin, they also observed small lipid-associated deposits ranging from 1-10 microns in diameter. Interestingly, the degree of plaque load in the retina showed a positive qualitative correlation with the severity of clinical diagnoses.

More recently, β-amyloid deposits have been found in the retina of patient with Down's[69] and in AD patients[71], further supporting a high correlation of amyloid deposition in the brain and eye (Figure 1.8C). Additionally, it has been found that age-related macular degeneration (AMD) was found to contain trace amounts of β-amyloid in its hallmark drusen deposits.[72] Furthermore, the amyloid-related prion diseases and diabetes show distant pathology in retinal tissue.[73–75] The optical accessibility of the eye, therefore, provides several new opportunity for assessing amyloid deposition associated with multiple amyloid-associated diseases in living patients using fluorescence-based imaging modalities.

1.3.4 Investigations of Amyloids in Biofluids Using CR and ThT

Outside of the central nervous system, ThT and CR have found utility in the detection of amyloids in biofluids such as urine. Buhimschi and coworkers, for instance, have reported the presence of congophilic species in the urine of pregnant

women exhibiting symptoms for pre-eclamspia (PE), a placental disorder that increases the risk of complications for both mother and child.[76] They showed that CR absorption and fluorescence emission of ThT were capable of discriminating patients with PE versus healthy patients by spectroscopic analysis of urine samples containing these probes (Figure 1.9A).

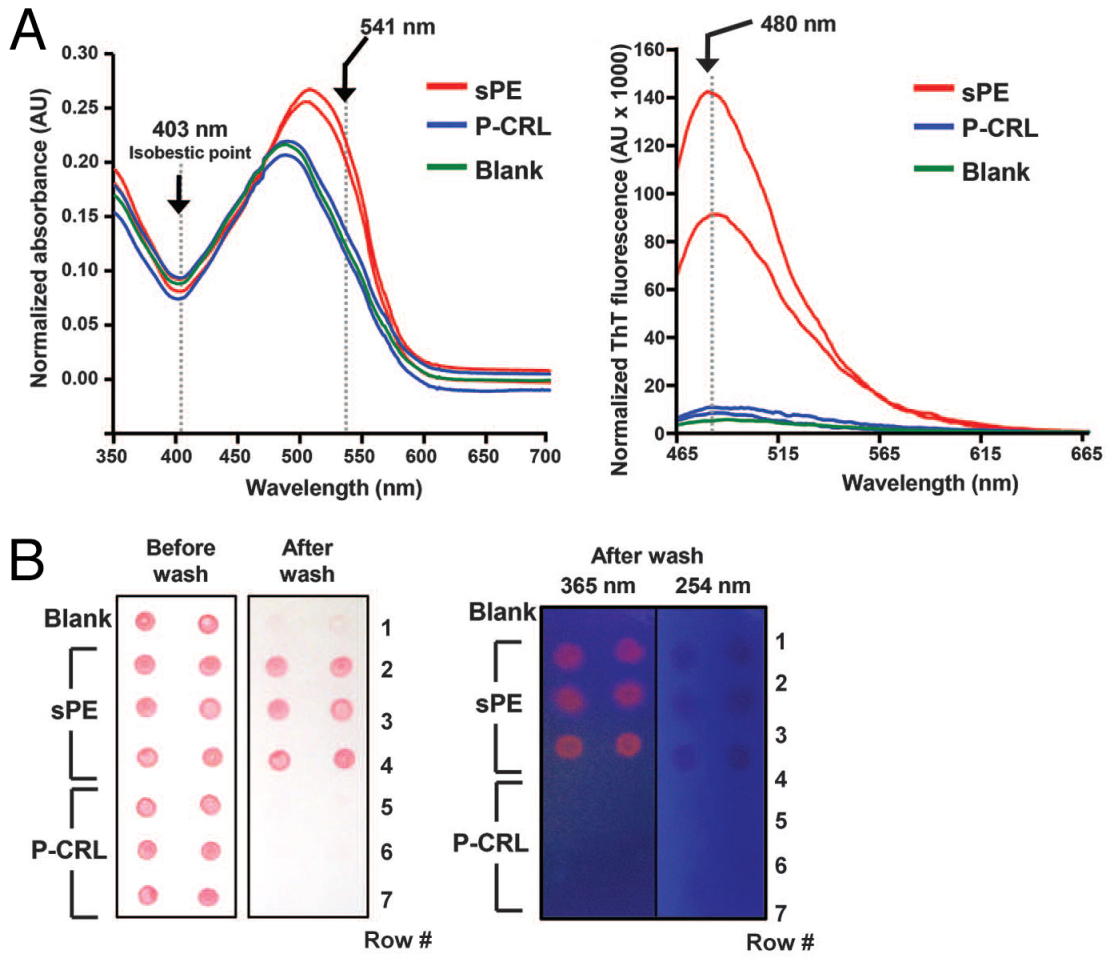

Figure 1.9 CR and ThT were able to bind amyloidogenic species in the urine of pre-eclampsic women. A) Spectroscopic analysis of CR absorption and ThT emission showed characteristic shifts and enhancement. B) CR-treated urine samples retained the CR fluorescence after washing with methanol. Adapted with permission from the American Association for the Advancement of Science. Science Translational Medicine. *Protein misfolding, congophilia, oligomerization, and defective amyloid processing in preeclampsia*, 6 (245), 245ra92. Figure 2, copyright 2014.

CR was particularly unique in that it could stain and identify PE patients from urine samples spotted on nitrocellulose, similar in application to a pregnancy test (Figure 1.9B). While additional work is necessary to confirm the abundance, composition, and origin of protein aggregates, these results support the possibility to aid in the diagnosis of PE by spectroscopic detection of possible amyloid species present in urine samples from PE patients.

Additionally, the saliva of AD patients was recently found to contain elevated levels of hyperphosphorylated tau, though there have conflicting reports regarding the presence of β-amyloid.[77,78] Furthermore, in 2014, it was shown that the urine of patients suffering from variant Creutzfeldt Jakob's Disease (vCJD) contained trace amounts of the infectious PrP^{Sc} protein, at concentrations of 10^{-16} grams per milliliter of urine.[79] Taken together, the prevalence of these protein species in non-cerebral regions of the body may hold additional avenues for non-invasive detection and diagnosis of amyloid-based disease states.

1.4 Future outlook

As more amyloid-binding compounds are generated and as more amyloidogenic proteins are discovered, the use of fluorescence will become a valuable tool in the development of more rapid and efficient methods to detect disease. A chemical approach towards modifying compounds with amyloid affinity may ultimately lead to disease-specific fluorescence detection methods, which is particularly valuable due to the overlapping nature of many amyloid-based diseases.[13]

As an introduction, I have shown here several scaffolds with amyloid-specific recognition, each of which has been utilized in unique ways to identify, characterize, and visualize amyloid aggregates. In light of these scaffolds and their applications, I worked with a family of environmentally sensitive fluorophores known as the amino-naphthalene cyanoacrylates (ANCA) and developed methodologies for their design and their applications towards detecting amyloids in select environments.

1.5 Thesis Research Goals

I joined the Yang lab coming from a neurogenetics lab. Though I had an educational background in physical chemistry, I wanted to pursue research in the physical organic realm and ultimately the projects I pursued were the perfect blend of both physical organic chemistry and neuroscience.

My initial research focused on the elucidation of the mechanism by which a class of environmentally sensitive fluorophores, developed by the Yang and Theodorakis labs, could emit different colors depending on the amyloid aggregate being bound. This project originated from an observation by Christina Sigurdson during initial staining experiments with the fluorophores, where she saw different green emission upon staining AD plaques and yellow emission from prion plaques. In Chapter 2 I discuss the analytical and histological methods we took towards proposing the mechanism of action.

I built upon the results of Chapter 2 in the second and third years of my graduate career by focusing on the rational design of fluorophores that could further discern between amyloid species by their emission wavelengths. This project was an

intensive collaboration between four research groups where I performed synthesis, histology, and microscopy towards determining the efficiency of our design hypothesis. We also undertook computational modeling towards this end and were able to ultimately determine a set of guidelines that could be used in the design of future amyloid-binding fluorophores based on this family of compounds. Chapter 3 summarizes these efforts.

Chapter 4 summarizes the main project during the last two years in the Yang lab, where I worked on the translation of our amyloid-binding fluorophores to an in vivo setting by using retinal fluorescent imaging. The main experiments in this project involved the derivatization of the optimal fluorophore from the work in Chapters 2 and 3 into more a bioavailable compound known as ARCAM-1, the administration of the compound into transgenic mice expressing AD and prion pathology and the resulting imaging and post-mortem analyses. Ultimately we sought to address the recent proposals that the eye could serve as a non-invasive window into the central nervous system.

Additional work with the ARCAM-1 fluorophore used in Chapter 4 is presented in Chapter 5 where we collaborated with the Shah lab at Harvard in using the compound as a tool for fluorescence correlation spectroscopy (FCS). This tool is an optical microscopy technique where we essentially monitored the fluorescent signal from the diffusion thermodynamics of amyloid aggregates. This allowed us to determine a general idea of the detection limit for the size of aggregates capable of being bound with our fluorophores. Finally, the second half of Chapter 5 describes an ongoing clinical project where we are monitoring the progression of pre-eclamspia

using ARCAM-1. In collaboration with a clinical team at the UCSD Hillcrest Medical Center, we measured the fluorescence enhancement of ARCAM-1 of blinded urine samples from pregnant women, with the goal of being able to accurately detect amyloidogenic species that were previously found in pre-eclampsic urine samples.

Chapter 2

Fluorescence Discrimination of β-Amyloid and Prion Aggregates

2.1 Introduction

Amyloid plaque accumulation in the brain is the hallmark of many neurodegenerative disorders, including Alzheimer's (AD) and Creutzfeldt-Jakob Disease (CJD).[4,80,81] Approaches to clinically diagnose and monitor the progression of these diseases include targeting of amyloid deposits with small molecule imaging agents. Along these lines, an amyloid-labeling probe for use in positron emission tomography (PET) has gained recently FDA approval as a diagnostic agent for Alzheimer's disease.[16,82,83] While PET imaging represents a great first step toward the diagnosis of neurodegenerative diseases, this technique is limited by the binary nature of the radioactive signal that does not allow for discrimination between amyloids associated with different, but closely related, diseases. Alternative techniques that can discern between different types of amyloids may offer important information

necessary to develop effective treatment strategies that are tailored to specific diseases.

Fluorescence-based imaging of amyloids has emerged as a potentially lower cost, more accessible, and non-radioactive alternative method to PET for imaging plaque deposits. In principle, fluorescence-based probes offer an advantage over their radioactive counterparts since their fluorescence profiles could be used to distinguish different amyloids in tissue without loss of signal. Given these advantages, recent work has been aimed in the development of fluorophores suitable for the *in vivo* imaging of various neurodegenerative diseases.[50,63,84]

2.1.1 Alzheimer's Disease

First documented by Alois Alzheimer in 1901, AD is a common form of progressive dementia resulting from a wide range of environmental and genetic factors.[5] The early signs are the slow, mild decline in memory and cognition. As the staging of the disease progresses, changes in personality accompany severe memory loss. While the exact pathophysiology of the disease is not clear, there is strong correlation between the accumulation of aggregated β-amyloid peptides and the appearance of the cognitive symptoms. Briefly, improper cleavage by a set of secretases of the integral membrane protein amyloid precursor protein (APP) leads to the formation of various cleavage fragments, ranging from 38 to 43 amino acids in length.[85–87] The 40 and 42 amino acid fragments are known as Aβ(1-40) and Aβ(1-42)

are found as the primary components of total Aβ and in plaque Aβ, respectively, and are known for their tendency of aggregation into fibrils and plaque assemblies.[88,89]

The role of amyloid aggregation in AD was initially thought to be due to tissue atrophy surrounding the insoluble senile plaques, though recent work suggests that the primary toxic agents are the oligomeric species which can interact and penetrate into neurons, disrupting cell-signaling and communication (Figure 2.1).[90]

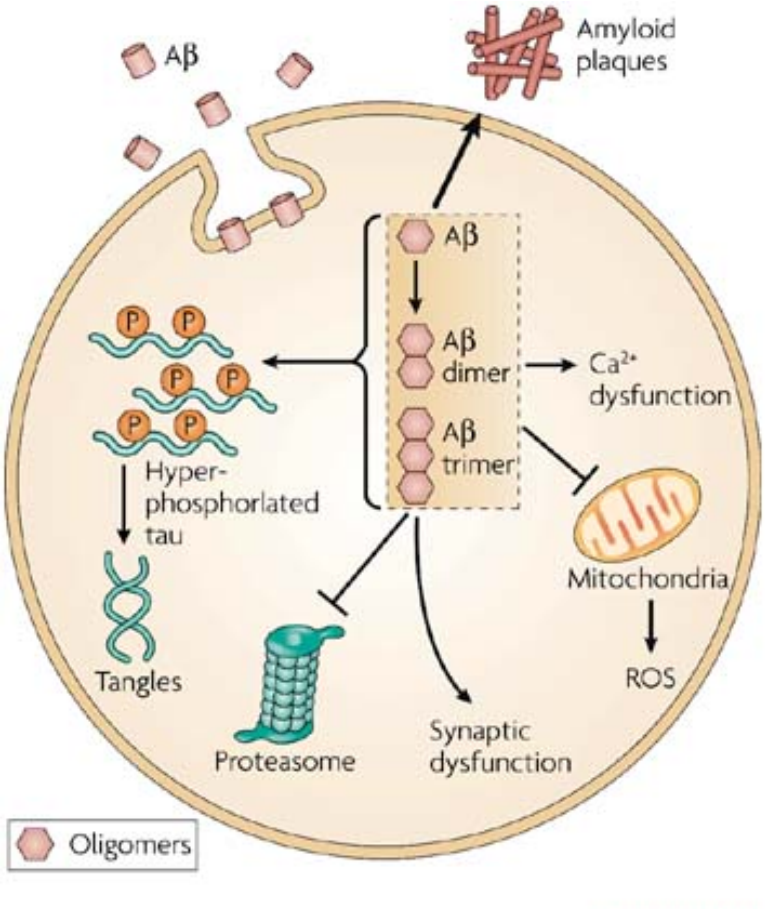

Figure 2.1 The role of Aβ in neurotoxicity. ROS = reactive oxygen species. Adapted with permission from Nature Publishing Group. Nature Reviews Neuroscience, *Intracellular amyloid-β in Alzheimer's Disease*, 8, 499-509. Figure 3, copyright 2007

Regardless of the mechanism, AD has been projected to affect approximately 13.8 million Americans by 2050, exponentially increasing from the current 5.4 million sufferers as the Baby Boomer generation ages. Financially, the costs of AD in the United States is currently estimated around 236 billion dollars for total expenses associated with care and hospice, with a 2050 cost projection of 1 trillion dollars.[91] This large socioeconomic burden emphasizes the need for the development of treatments and preventative care. Concomitant with this need comes the need to develop detection methods to help screen for and diagnose the disease before the severe symptoms develop.

2.1.2 Prion Diseases

Stanley Prusiner coined the term prion in 1982 for proteins with viral-like transmissibility.[92,93] The prion particle is typically found as a 14-28 unit oligomer composed of ubiquitous prion protein (PrP), encoded by the *Prnp* gene and which exists in several isoforms, the most common being the non-infectious, protease-sensitive PrP^{C} conformation.[94–96] Though the natural function of the PrP is unknown, the protein is typically membrane bound through a glycosylphosphitidylinositol (GPI) anchor on the cell surface.[97–99] The PrP^{C} isoform can be transformed into the infectious, protease-resistant amyloidogenic PrP^{Sc} conformation by means of genetic and environmental factors. The presence of PrP^{Sc} is thought to catalyze the rapid conversion of native PrP^{C} into the infectious form by a seeding mechanism whereby the dynamic equilibrium between the protease sensitive and resistant forms shifts towards the resistant conformation upon the appearance of a prion seed (Figure 2.2).[100]

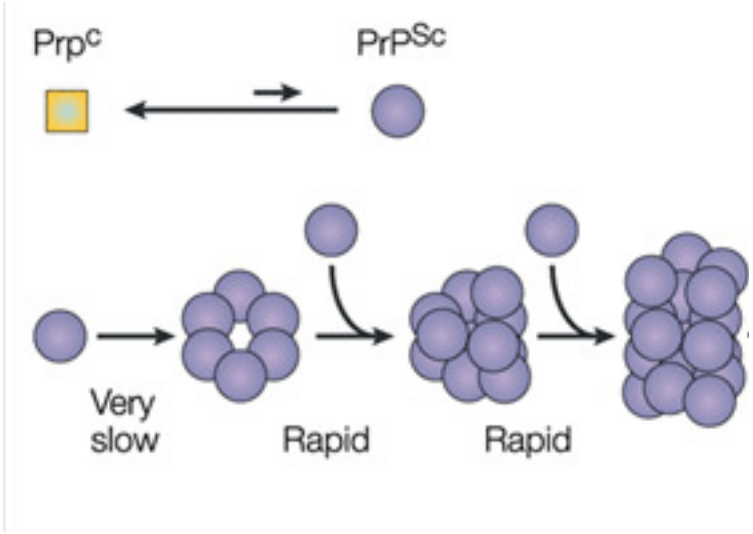

Figure 2.2 The seeding mechanism of prion pathology. The dynamic equilibrium between PrP^{C} and PrP^{Sc} shifts towards the latter once a prion seed is introduced. Adapted with permission from Nature Publishing Group. Nature Reviews Microbiology, *The state of the prion*, 2, 861-871. Figure 2, copyright 2004

The appearance of the PrP^{Sc} isoform typically precludes the neurodegeneration found in the transmissible spongiform encephalopathies (TSEs), also known as proteinopathies. TSEs are present in a wide range of species with unique strain identities that depend on the PrP sequence and the subsequent folding conformation (Table 2.1).[96,101]

Table 2.1 A selection of well-documented prion diseases

Species	Prion disease
Human	Creutzfeldt-Jakob Disease (CJD); variant, spontaneous
Human	Gerstmann-Straussler-Scheinker Syndrome (GSSS)
Human	Fatal familial insomnia
Human	Kuru
Bovine	Bovine spongiform encephalopathy (BSE), “Mad cow disease”
Deer/Elk	Chronic wasting disease (CWD)
Sheep	Scrapie (Sc)
Feline	Feline spongiform encephalopathy

These diseases, in contrast to AD, often are rapid in their progression and can be systemic in nature rather than solely neuronal, but also exhibit similar plaque deposition. While identifying a treatment or cure for these diseases has proven to be inherently difficult due to their protein-based mode of transmission, much work has gone into developing detection technology to detect their presence to avoid spreading their infectivity. For example, in the case of bovine spongiform encephalopathy (BSE or "Mad cow disease"), the spread of BSE and subsequent rise in variant Creutzfeldt-Jakob's Disease (vCJD) in the United Kingdom epidemic seen in the late 1990's showcased the need for better screening methods.[55,102,103]

2.2 Environmentally Sensitive Fluorophores

The Yang and Theodorakis labs previously reported that aminonaphthalene cyanoacrylate (ANCA) probes (Figure 2.3) could label Aβ plaques in human neuronal tissues from AD patients.[104] Tissues stained with these probes showed strong overlap of fluorescence with a mouse monoclonal anti-human Aβ IgG, indicating that these probes could mark the location of Aβ deposits with good specificity compared to surrounding background tissue (Figure 2.4)

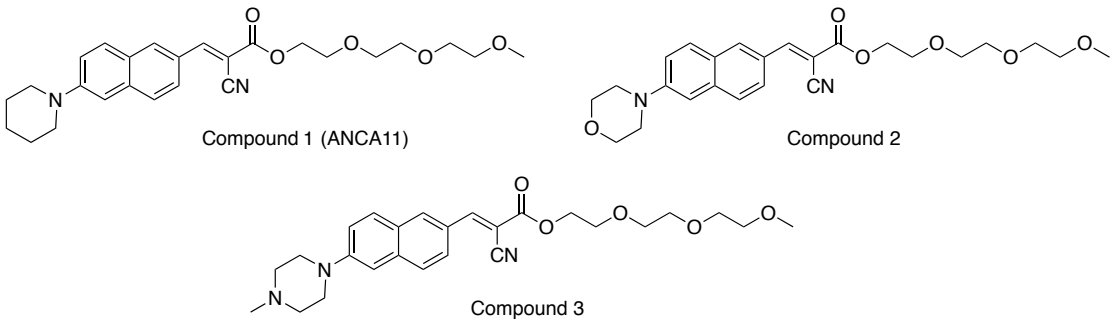

Figure 2.3 ANCA compounds 1-3. Compound 1 is also referred to as ANCA11

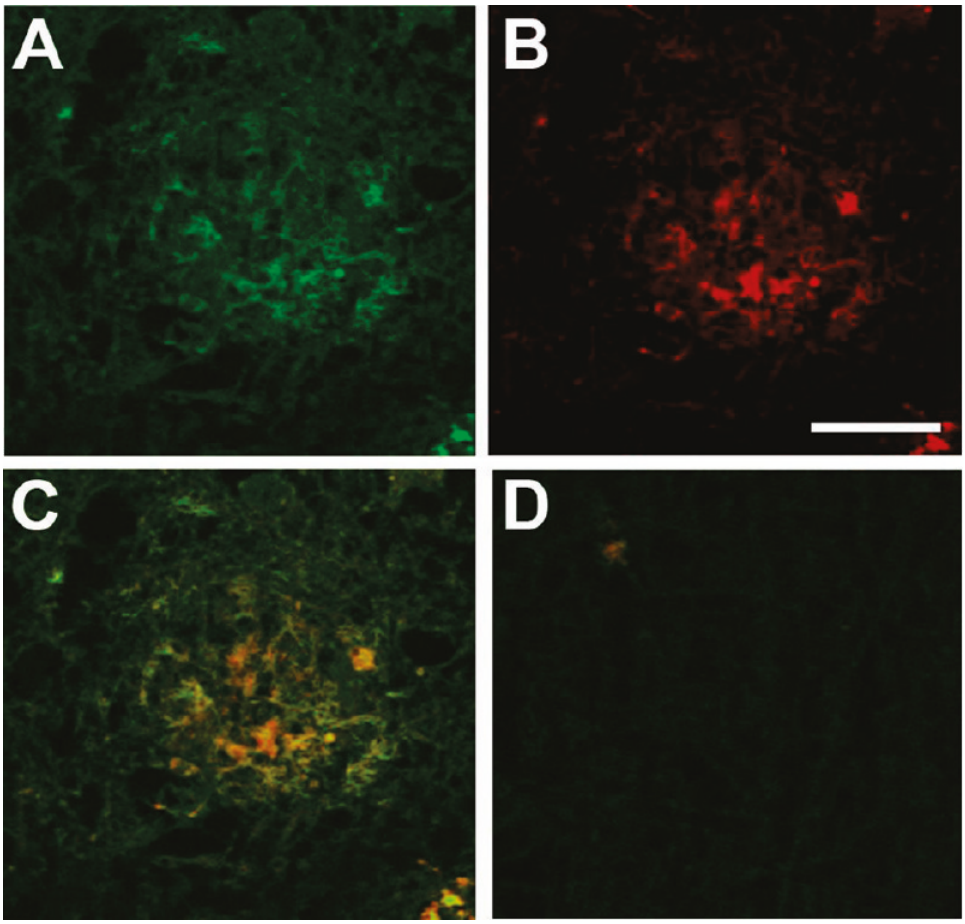

Figure 2.4 Fluorescence micrograph of human AD tissue expressing Aβ plaques costained with ANCA11 (compound 1, green) and an Aβ antibody (red). Colocalization regions are shown as yellow in panel C. Adapted with permission from the American Chemical Society. ACS Chemical Neuroscience. *ANCA: A Family of Fluorescent Probes that Bind and Stain Amyloid Plaques in Human Tissue*, 2(5), 249-255. Figure 5, copyright 2011.

2.3 Results and Discussion

The origin of fluorescence of the ANCA probes was attributed to a photon-induced dipole mechanism, where the electron rich amine functionality, attached to the naphthalene moiety, donates electron density to the electron deficient cyano ester through the π-system of the ANCA scaffold.[35,104–106] The excitation of these compounds is enhanced upon restriction of the rotation around the single bonds

between the donor amine and acceptor cyano ester groups. The ANCA probes, therefore, exhibit a large enhancement in fluorescence properties upon binding to amyloid substrates compared to the weaker fluorescence of the free compounds when in solution (Figure 2.5).

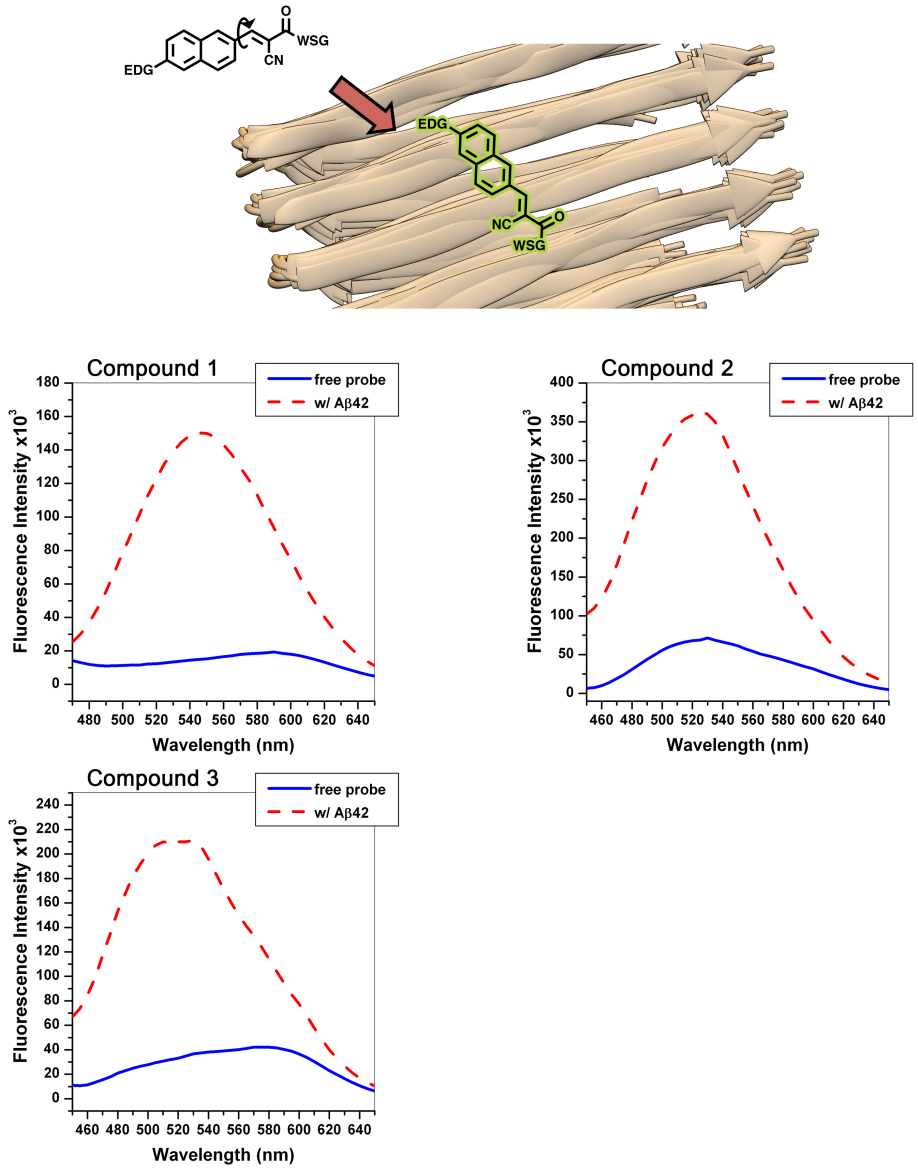

Figure 2.5 Fluorescence emission spectra of ANCA probes 1-3 in PBS buffer in the presence or absence of aggregated Aβ peptide. Probe 1 was excited at λ_{max} = 410 nm. Probes 2 and 3 were excited at λ_{max} = 400 nm. EDG = Electron donating group, WSG = water solubilizing group.

To explore the ability of the ANCA probes to fluorescently label amyloid deposits from proteins other than Aβ in tissue, I compared fluorescence micrograph images of plaques derived from Aβ and PrP^{Sc} stained with compound **1** in neuronal tissue from mouse models for AD and chronic wasting disease (CWD) (Figure 2.6).[107,108] Importantly, compound **1** exhibited a strong capability to label amyloid plaques in both tissue types and displayed a visually observable difference in color of emission of the stained plaques. Probes **2** and **3** exhibit similar properties, albeit without the obvious visual differences in color by the naked eye.

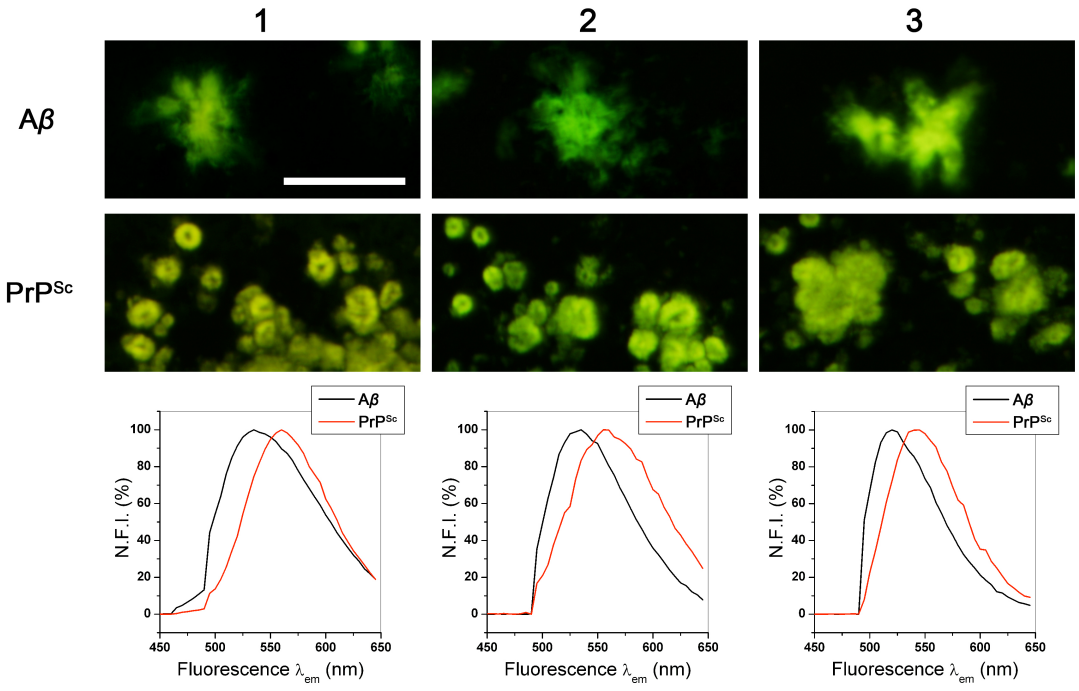

Figure 2.6 Brightfield true color images of compounds **1**, **2**, and **3** bound to plaque deposits in brain tissue sections from mice. Scale bar = 100 μm. Aβ plaque deposits shown were located in the hippocampus; PrP^{Sc} deposits were located in the corpus callosum. Fluorescence emission maximas of Aβ and PrP^{Sc} stained plaques for compound **1** were measured at 535 ± 3 nm and 554 ± 2 nm, respectively. For compound **2**, Aβ and PrP^{Sc} stained plaques had emission maximas at 525 ± 4 nm and 541 ± 4 nm, respectively. For compound **3**, Aβ and PrP^{Sc} stained plaques had emission maximas at 515 ± 4 nm and 538 ± 3 nm, respectively.

Table 2.2 Binding affinities and emission profiles for ANCA compounds 1-3 bound to Aβ and PrP^{Sc} plaques.

Compound	**K_d for Aβ fibrils (μM)**	**Aβ plaque emission (nm)**	**PrP^{Sc} plaque emission (nm)**
1 (ANCA11)	1.4 ± 0.2	535 ± 3	554 ± 2
2	13.8 ± 3.1	525 ± 4	541 ± 4
3	4.6 ± 0.2	515 ± 4	538 ± 3

Table 2.2 shows that the ANCA probes, when bound to amyloid deposits, exhibit a difference in maximal emission wavelength (λ_{max}) of ~20 nm, depending on the type of amyloid protein present in the plaque. Surprisingly, the variability in the observed λ_{max} between plaques in either tissue type was quite narrow (± 2-3 nm, average λ_{max} determined from inspection of ≥ 25 plaques in each tissue sample). Moreover, inspection of prion plaques stained with compound **1** from different parts of the brain (e.g., hippocampus, hypothalamus, cortex) of the same mouse, or from plaques stained with compound **1** from the corpus callosum of different mice, all exhibited essentially the same a λ_{max} for fluorescence emission (within the same associated error of ± 2 nm).

In contrast, I did not observe such fluorescence discrimination when we stained the amyloid plaques with Congo-Red (Figure 2.7). Aβ plaques showed a λ_{max} at 593 ± 3 nm and prion aggregates showed a λ_{max} 594 ± 8 nm. This observation was consistent with the structure of CR, where it does not have a molecular rotor motif, and therefore does not exhibit the environment sensitivity by stabilization of the excited state.

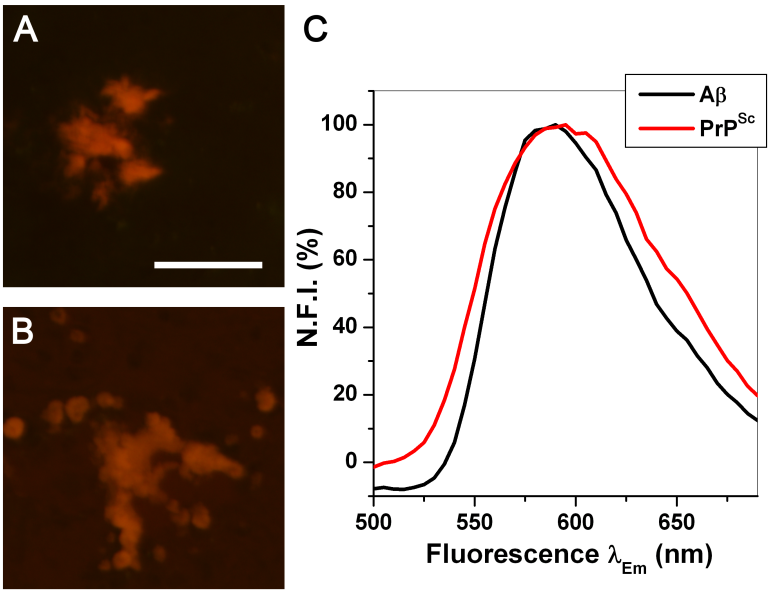

Figure 2.7 Aβ and PrP^{Sc} deposits in brain tissue sections stained with Congo red. Scale bar = 100 μm. A) Image of Congo red staining in transgenic mice with deposits of Aβ. B) Real-color image of Congo red staining in prion-infected mice. C) Fluorescence emission spectra of stained plaques. The maximum fluorescence was measured at 593 ± 3 nm for Aβ deposits, and at 594 ± 8 nm for PrPSc deposits.

Previous solution studies show that the small differences in the polar environment of proteins and lipids can affect the Stokes shift of bound fluorophores.[109,110] If the time dependence of fluorescence polarization of probes **1-3** can be neglected—that is, if we assume that any reorientation of molecules on the amyloid peptides in the binding pocket is fast compared to the lifetime of the excited state of the probes—the dependence of the polar environment on the frequency of the absorbance and fluorescence emission spectra of **1-3** can be approximated by the Ooshika-Lippert-Mataga (OLM) equation:[111,112]

$$\Delta\tilde{\nu} = \frac{2(\mu_e - \mu_g)^2}{ha^3}\left[\left(\frac{\varepsilon - 1}{2\varepsilon + 1}\right) - \left(\frac{n^2 - 1}{2n^2 + 1}\right)\right]$$

Equation 2.1 The Ooshika-Lippert-Mataga (OLM) equation

where $\Delta\tilde{\nu}$ is the average frequency of the Stokes shift between the absorption and emission, μ_e and μ_g are the dipole moments of the molecules in the excited state and ground state respectively, h is Plank's constant, a is the approximate radius of the molecules assuming a spherical cavity with a rigid dipole at the center, ε_0 is the static relative permittivity (i.e., dielectric constant) of the dielectric continuum surrounding the molecules, and n is the refractive index of the surrounding medium.

Since the frequency of absorption for molecules **1-3** remained relatively constant when measured in different solvents of various polarities, I found an approximately linear relationship between the Stokes shifts of **1-3** and their observed λ_{max} for fluorescence emission (Figure 2.8).

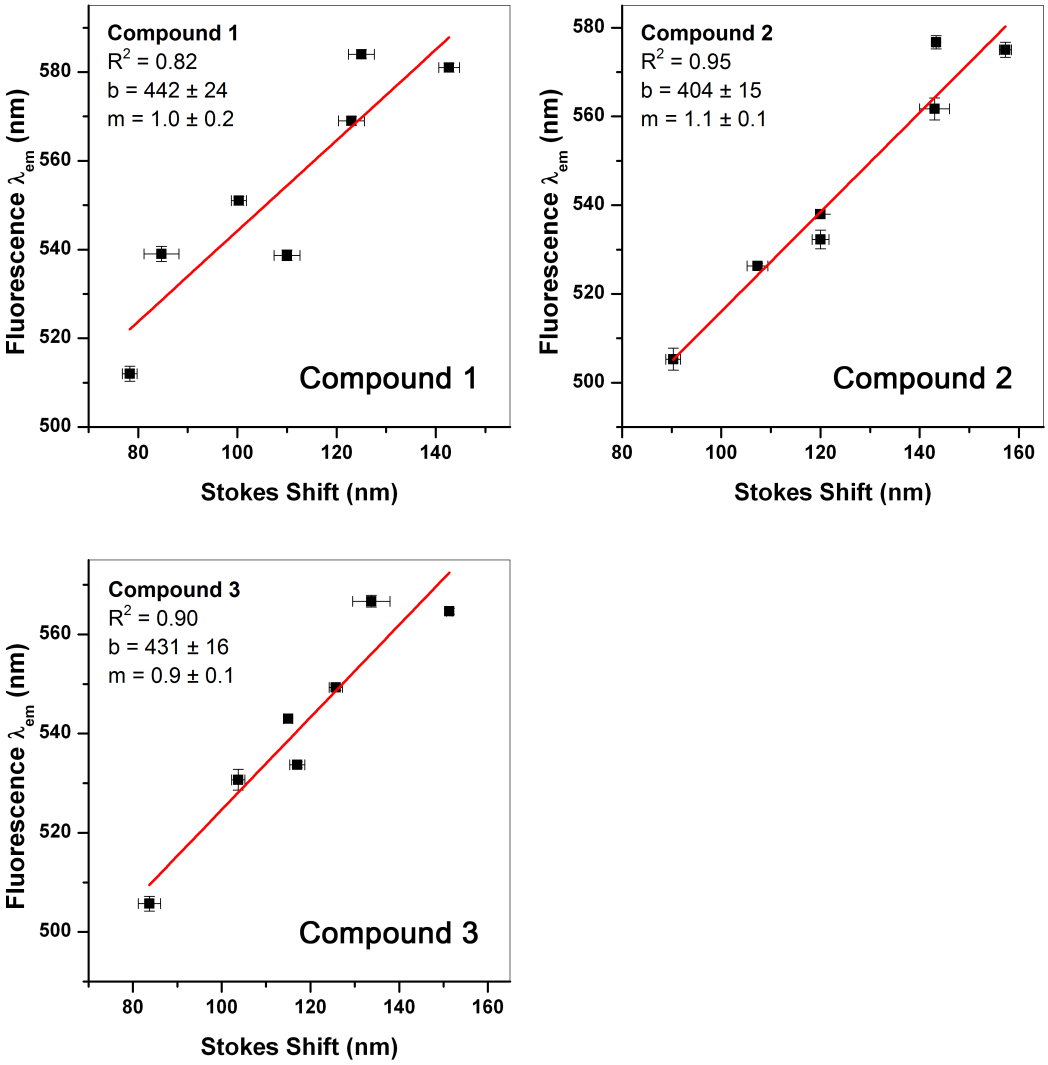

Figure 2.8 Plots of the fluorescence emission λ_{max} versus Stokes shift for compounds **1-3** measured in different organic solvents. Each compound was dissolved in solvent to a final concentration of 1.5 μM. Error bars represent the standard deviation from at least two independent runs. Plots were fit with the linear function: $Y = m \cdot X + b$. The linear fits are shown in red, and the values for slope and intercept obtained from these fits are given within each graph.

This linear correlation made it possible to use only the λ_{max} of emission to analyze the effect of the polar environment within the binding pockets of the amyloids

on the fluorescence properties of compounds **1-3**. Equation 1 could, therefore, be simplified to[109]

$$\frac{1}{\lambda_{\max}(\text{Emission})} = C_1\left[\left(\frac{\varepsilon - 1}{2\varepsilon + 1}\right) - \left(\frac{n^2 - 1}{2n^2 + 1}\right)\right] + C_2$$

Equation 2.2 Reduced OLM equation for measuring the polarity of amyloid binding pockets.

where C_1 and C_2 are constants that reflect the inherent molecular size and polarizability, and the Frank-Condon property (relatively no change in the absorption of the fluorophores), respectively, of the ANCA probes. Equation 2.2 was used to fit the solvatochromic trends of compounds **1-3**.

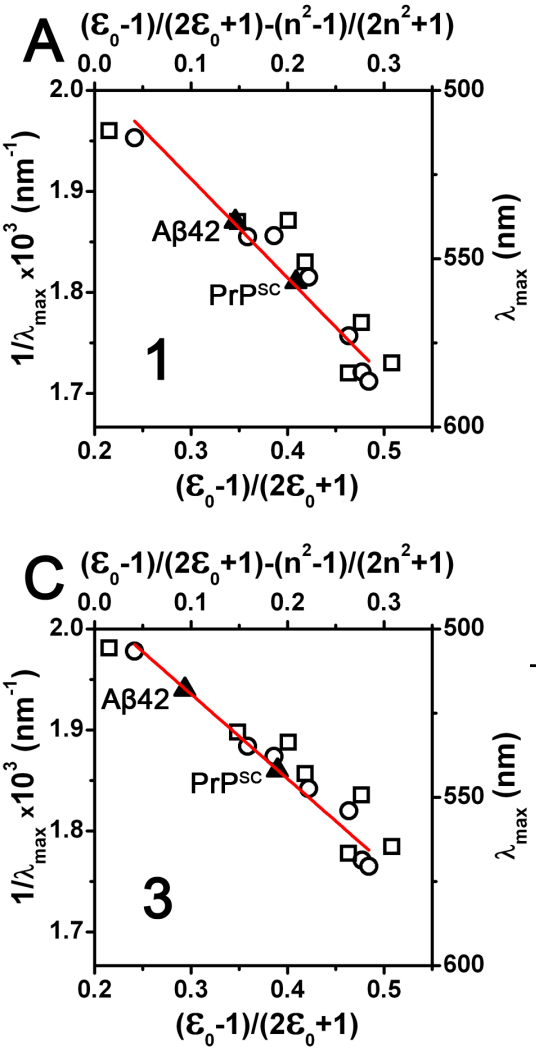

D Estimated Static Relative Permittivity

Cmpd	Aβ(1-42)	PrP^{Sc}
1	4.4 ± 0.3	7.8 ± 0.7
2	4.1 ± 0.4	6.6 ± 0.8
3	3.1 ± 0.3	6.3 ± 0.7

Figure 2.9 Dependence of fluorescence emission of probes **1-3** on the polarity of different organic solvents. (A-C) Graphs of the relationship between $1/\lambda_{max}$ for emission of **1-3** as functions of solvent static relative permittivity (ε_0), with (open squares, □) or without (open circles, ○) the contribution of refractive index (n). For each graph, the linear fits of the data according to eq. 2 are shown in red, excluding the contribution from n. (D) Estimated ε_0 for the binding pockets of Aβ42 and PrP^{Sc} deposits extrapolated from the observed λ_{max} for emission of probes **1-3** in tissue samples.

Figure 2.9A-C (open circles, ○) plots the dependence of $1/\lambda_{max}$ for fluorescence emission of **1-3** in solvents of various polarities (Figure 2.10) as a function of the static relative permittivity (ε_0) and refractive index (n) of each solvent

according to equation 2.2. The observed linear behavior shown in Figures 2.9A-C suggest that the OLM equation (equation 2.1) describes fairly well the dependence of the observed fluorescence of compounds **1-3** on the polarity of the surrounding environment. These results suggest that the origin of the observed fluorescence discrimination between the two different types of amyloid deposits using probes **1-3** could indeed be explained by small differences in the polar environment within the binding pockets of the amyloid proteins.

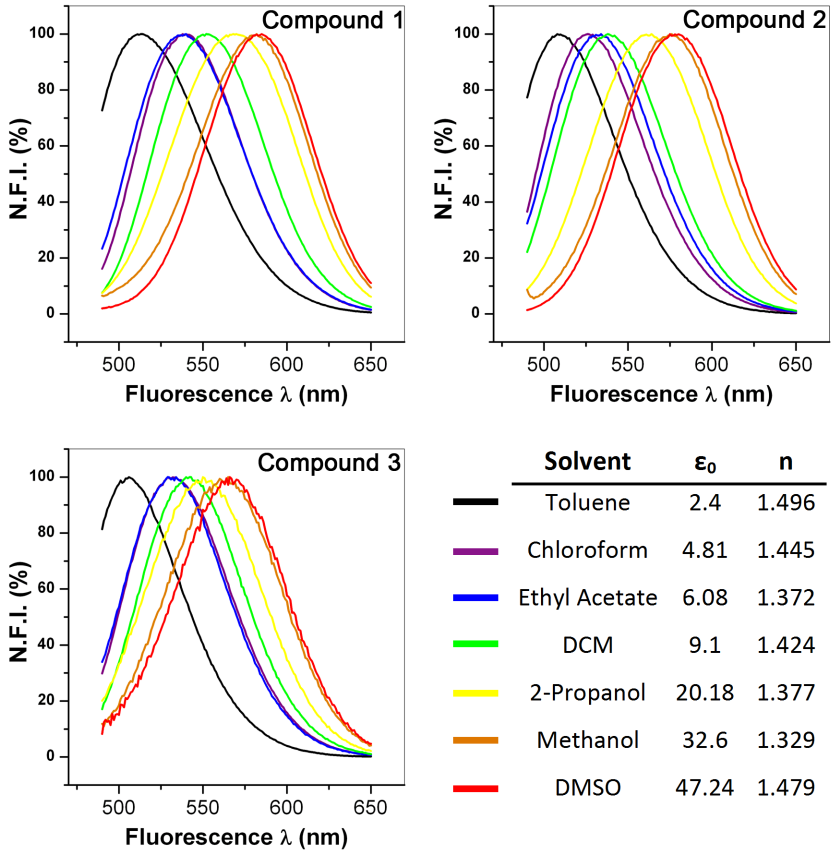

Figure 2.10 Solvent studies on fluorescence emission of compounds **1-3**. The values for λ_{max} obtained from these experiments and the published values for relative static permittivity and refractive indices of these solvents were used to generate the Lippert-Mataga plots. N.F.I. = normalized fluorescence intensity.

In order to gain some additional insight into the nature of the polar environment within the binding pockets of the amyloid tissues, I re-plotted the dependence of $1/\lambda_{max}$ for fluorescence emission of **1-3** in different solvents as a function of ε_0 only, while omitting the refractive index of the solvent (Figure 2A-C, open squares, □). I found that the linear fit of $1/\lambda_{max}$ versus $(\varepsilon_0-1)/(2\varepsilon_0+1)$ was consistently better compared to when the refractive index was included as in equation 2.2 (Figure 2.11).

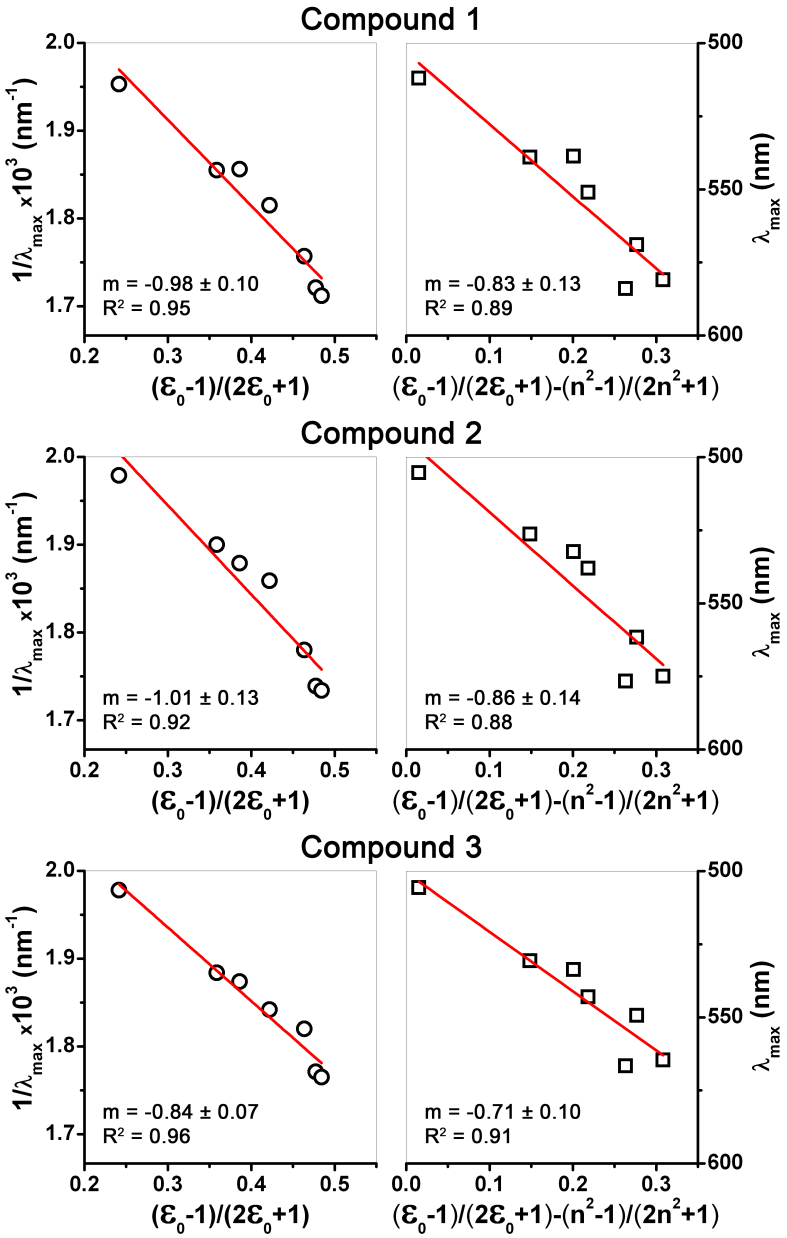

Figure 2.11 Plots of the solvatochromic relationship of $1/\lambda_{max}$ for the emission of probes **1-3** versus either the static relative permittivity (ε_0) of the solvent alone (open circles, ○) or versus the static relative permittivity and the refractive index (n) of the solvent (open squares, □). Data were fit to the linear equation $y = m \cdot X + b$ with the best-fit line shown in red. The slopes (m) are in units of $x10^{-3}$ nm^{-1}.

This linear correlation between $1/\lambda_{max}$ versus $(\varepsilon_0-1)/(2\varepsilon_0+1)$ suggests that the static relative permittivity (ε_0) dominated the dependence of the polar environment on

the λ_{max} for fluorescence emission of **1-3**. This simple relationship between λ_{max} and ε_0 then made it possible to estimate the static relative permittivity of the binding pockets of the two different amyloids in tissue by the observed emission maxima of plaques stained with compounds **1-3**.

Figure 2.9D summarizes the estimated values for ε_0 of the binding pockets for molecules **1-3** in plaques comprised of Aβ or PrP^{Sc} proteins. The estimated ε_0 values for the two amyloid proteins were in fairly good agreement (given the approximations made in equations 2.1 and 2.2), regardless of which ANCA probe was used for measurement. The data reveals that both amyloid binding pockets are relatively hydrophobic as expected, but that the permittivity within the binding pocket of prion plaques is roughly two-fold greater than the permittivity within the binding pocket of Aβ plaques. To provide a reference point for calibration, these results suggest that the binding pocket of Aβ plaques provides a polar environment roughly similar to diethyl ether, whereas the binding pocket of the prion plaques provides a polar environment roughly similar to tetrahydrofuran.

Although small differences in the polar environment within the binding pockets of the amyloids can reasonably account for the observed fluorescence discrimination of the amyloids with probes **1-3**, I tested another plausible explanation for this observation. We considered the possibility that acid-based interactions between the amyloid protein and the probes could affect the electron donor capability of the amine group of these probes, thus affecting their observed emission profiles. To investigate this possibility, I examined the excitation and emission profiles of **1-3** as a function of pH in free aqueous solution (Figure 2.12).

Figure 2.12 A,C shows that probes **1** and **2** exhibit a sharp 100-125 nm change in excitation maxima at a pH of ~4.2 and ~1.7, respectively. These changes presumably reflect the protonation of the nitrogen donor of the piperidine in **1** or morpholine in **2**, and provide an estimate of the pKa's of the protonated forms of these groups. A much smaller change in excitation λ_{max} (~10 nm) was observed for 3 at a pH of ~6.9, which presumably reflects the pKa of the protonated N-methyl tertiary amine. More importantly, the emission profiles of **1-3** (Figure 2.12 B, D, and F) in acidic (pH 3.8) versus neutral (pH 7.8) solutions indicate that only probe **1** should exhibit a strong (~125 nm) difference in emission λ_{max} when bound to amyloid plaques, if the origin of fluorescence discrimination of amyloids is due to an acid-base interaction. Since I observe a difference (~20 nm) in emission λ_{max} between Aβ versus prion plaques stained with all 3 probes **1-3**, it is unlikely that the origin of fluorescence discrimination is due to acid-base interactions between the probes and the proteins within the binding pocket of the amyloid deposits.

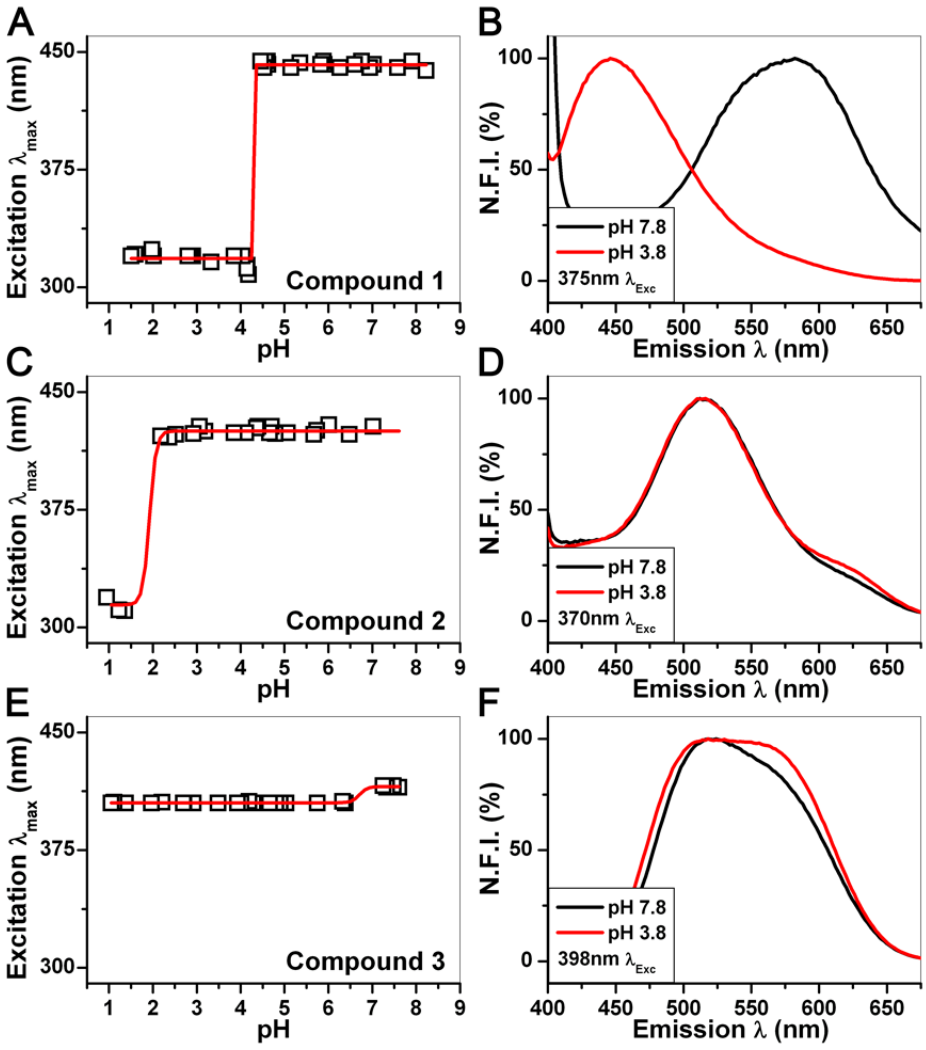

Figure 2.12 Plots of absorption (A, C, E) and emission (B, D, F) λ_{max} versus pH of probes **1-3**. For fluorescence emission spectra, I chose an excitation λ_{max} that was maximized at both pH 3.8 and 7.8.

2.4 Conclusions

In conclusion, I analyzed a set of fluorescent amyloid-binding probes that could report a different color of fluorescence emission when bound to different types of amyloid deposits in tissue samples. The origin of this fluorescence discrimination was attributed to the sensitivity of these probes to the local polar environment within

the binding pocket of an amyloid plaque. Subtle changes to the structure (i.e., electron donor moiety) in these ANCA probes make it possible to tune the spectral window of fluorescence discrimination. I found that compound **1**, ANCA11, had both the best visual and spectroscopic properties upon binding different amyloid aggregates, had a pK_a in a biologically compatible range, and had the strongest binding affinity.

The strong correlation between fluorescence emission of the probes and polarity of the environment afforded estimates of the static relative permittivity of the binding pocket in the amyloid plaques. Analysis of amyloid deposits in tissue revealed that the prion deposits exposed a significantly more polar environment to the probes than the Aβ deposits. This previously unreported, fundamental difference between these two types of amyloids in tissue make it possible to distinguish them in tissue by simple inspection of the fluorescence emission of molecules that target them.

2.5 Materials and Methods

All reagents were purchased at highest commercial quality and used without further purification except where noted. Air- and moisture-sensitive liquids and solutions were transferred via syringe or stainless steel cannula. Organic solutions were concentrated by rotary evaporation below 40 °C at approximately 20 mmHg. All non-aqueous reactions were carried out under anhydrous conditions. Yields refer to chromatographically and spectroscopically (^{1}H NMR, ^{13}C NMR) homogeneous materials, unless otherwise stated. Reactions were monitored by thin-layer chromatography (TLC) carried out on 0.25 mm Dynamic Adsorbents, Inc. silica gel plates (60F-254) and visualized under UV light and/or developed by dipping in

solutions of 10% ethanolic phosphomolybdic acid (PMA) and applying heat. Dynamic Adsorbents, Inc. silica gel (60, particle size 0.040-0.063 mm) was used for flash chromatography. NMR spectra were recorded on the Varian Mercury 400, 300 and/or Unity 500 MHz instruments and calibrated using the residual non-deuterated solvent as an internal reference. The following abbreviations were used to explain the multiplicities: s = singlet, d = doublet, t = triplet, q = quartet, m = multiplet, b = broad. High resolution mass spectra (HRMS) were recorded on a VG 7070 HS mass spectrometer under electron spray ionization (ESI) or electron impact (EI) conditions.

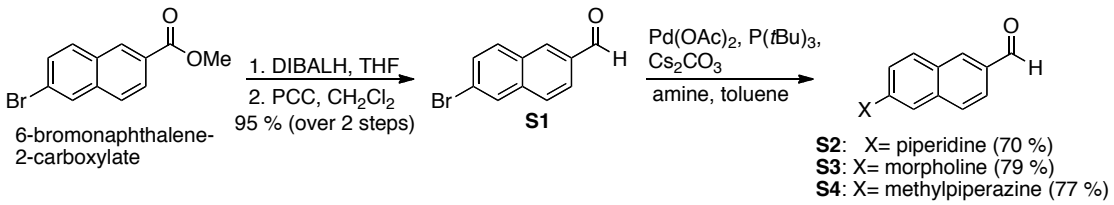

6-bromo-2-naphtaldehyde (S1)

To a solution of DIBAL-H (1.0 M in heptane, 34 mL, 34 mmol) at 0 °C under argon, a solution of 6-bromonaphthalene-2-carboxylate (3.0 g, 11 mmol) in anhydrous THF was added dropwise. The reaction mixture was allowed to warm up to room temperature and left stirring overnight. Upon completion, MeOH was added, followed by a saturated sodium potassium tartrate solution and ethyl acetate (EtOAc). After the two phases were separated, the organic phase was washed with saturated solution of ammonium chloride and brine, dried over $MgSO_4$ and concentrated under reduced pressure to yield 6-bromo-2-(hydroxymethyl)naphthalene.

R_f = 0.33 (EtOAc:Hexanes 3:7); ^{1}H NMR (400 MHz, CDCl3): d 7.99 (bs, 1H), 7.77 (bs, 1H), 7.74 (d, J= 8.5 Hz, 1H), 7.69 (d, J= 8.7 Hz, 1H), 7.55 (dd, J= 1.7, 8.7 Hz, 1H), 7.49 (dd, J= 1.7, 8.5 Hz, 1H), 4.84 (bs, 2H); ^{13}C NMR (100 MHz, $CDCl_3$) d 138.8, 133.9, 131.7, 129.7, 129.5, 129.5, 127.4, 126.1, 125.2, 119.8, 65.2.

To a suspension of pyridinium chlorochromate (2.4 g, 11 mmol) in anhydrous CH_2Cl_2 (60 mL) was added a solution of the above alcohol in anhydrous CH_2Cl_2, and the reaction was heated under reflux for 5 hours. Upon completion, it was cooled to room temperature and poured into diethyl ether. The solution was then filtered through a pad of silica and concentrated under reduced pressure to yield S1 (2.4 g, 95%). **S1**: white solid.

R_f = 0.67 (EtOAc:Hexanes 3:7); ^{1}H NMR (400 MHz, CDCl3) d 10.15 (s, 1H), 8.31 (bs, 1H), 8.08 (bs, 1H), 7.98 (dd, J= 1.5, 8.5 Hz, 1H), 7.86 (m, 2H), 7.67 (dd, J= 1.5, 8.5 Hz, 1H); ^{13}C NMR (100 MHz, CDCl3) d 191.8, 137.3, 134.3, 134.1, 131.0, 131.0, 130.6, 130.2, 128.2, 124.0, 123.6

General procedure for the synthesis of 6-amino-substituted naphthaldehydes (S2-S4)

In dry and degassed toluene (0.8 mL), were added $Pd(OAc)_2$ (0.022 mmol) and $P(tBu)_3$ (0.078 mmol) After stirring for 20 min, **S1** (0.207 mmol), the appropriate amine (0.249 mmol) and Cs_2CO_3 (0.280 mmol) were added and the reaction left stirring for three days under reflux. After three days, the reaction was cooled at room

temperature, diluted with CH_2Cl_2, filtered, concentrated under reduced pressure and purified via silica gel flash chromatography (hexanes/EtOAc 0-10%).

6-(piperidin-1-yl)naphthalene-2-carbaldehyde (S2). 70% yield, yellow solid; R_f = 0.61 (EtOAc:Hexanes 3:7); ^{1}H NMR (400 MHz, $CDCl_3$) d 10.03 (s, 1H), 8.15 (s, 1H), 7.83 (m, 2H), 7.68 (d, J= 8.6 Hz, 1H) 7.32 (dd, J= 2.4, 9.1 Hz, 1H), 7.08 (d, J= 2.4 Hz, 1H), 3.38 (m, 4H), 1.78-1.63 (m, 6H); ^{13}C NMR (100 MHz, $CDCl_3$) d 191.9, 151.9, 138.5, 134.4, 131.3, 130.4, 127.2, 126.3, 123.4, 119.5, 108.8, 49.6, 25.5, 24.3; HRMS Calc for $C_{16}H_{18}NO$ $(M+H)^+$ 240.1383 found 240.1381.

6-morpholinonaphthalene-2-carbaldehyde (S3). 79% yield, yellow solid; R_f = 0.56 (EtOAc:Hexanes 3:7); ^{1}H NMR (400 MHz, $CDCl_3$) d 10.06 (s, 1H), 8.20 (s, 1H), 7.88 (m, 2H), 7.73 (d, J= 8.4 Hz, 1H), 7.32 (m, 1H), 7.11 (d, J= 1.2 Hz, 1H), 3.92 (m, 4H), 3.36 (m, 4H); ^{13}C NMR (100 MHz, $CDCl_3$) d 191.9, 151.3, 138.1, 134.2, 131.8, 130.6, 127.5, 127.0, 123.6, 118.7, 109.0, 66.7, 48.5; HRMS Calc for $C_{15}H_{15}NO_2Na$ $(M+Na)^+$ 264.0995 found 264.0996.

6-(4-methylpiperazin-1-yl)naphthalene-2-carbaldehyde (S4). 77% yield, yellow solid; R_f = 0.36 (EtOAc:Hexanes 3:7); ^{1}H NMR (300 MHz, $CDCl_3$) d 10.00 (s, 1H), 8.13 (s, 1H), 7.80 (m, 2H), 7.66 (d, J= 8.6 Hz, 1H), 7.28 (dd, J= 2.1, 9.2 Hz, 1H), 7.06 (d, J= 2.1 Hz, 1H), 3.36 (m, 4H), 2.57 (m, 4H), 2.33 (s, 3H); ^{13}C NMR (100 MHz, $CDCl_3$) d 191.5, 151.0, 138.0, 134.0, 131.3, 130.2, 127.1, 126.4, 123.1, 118.7, 108.7, 54.5, 47.8, 45.7; HRMS Calc for $C_{16}H_{19}N_2O$ $(M+H)^+$ 255.1492 found 255.1491.

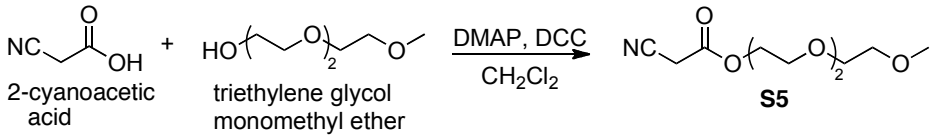

2-(2-(2-methoxyethoxy)ethoxy)ethyl-2-cyanoacetate (S5). To a solution of 2-cyanoacetic acid (230 mg, 2.72 mmol), triethylene glycol monomethyl ether (0.4 mL, 2.27 mmol) in CH_2Cl_2 (2.5 mL) and DMAP (2 mg, 0.013 mmol) was added dropwise at 0 °C. Finally, DCC (560 mg, 2.72 mmol) was added and the reaction mixture was stirred at 0 °C for 6 hours. The reaction was diluted with CH_2Cl_2 and the formed DCU was filtered off. The filtrate was dried over $MgSO_4$ and concentrated under reduced pressure. The residue was purified by silica gel flash chromatography to yield **S5** (450 mg, 86% yield). **S5**: colorless liquid; R_f = 0.45 (100% ether)

^{1}H NMR (400 MHz, $CDCl_3$) δ 4.29 (m, 2H), 3.67, (m, 2H), 3.59 (m, 6H), 3.50 (m, 2H), 3.49 (s, 2H), 3.32 (s, 3H); ^{13}C NMR (100 MHz, $CDCl_3$) δ 163.0, 113.0, 71.7, 70.4, 70.3, 68.3, 65.5, 58.8, 24.5; HRMS: calcd. for $C_{10}H_{17}NO_5$: $(M+H)^+$ 232.1185, found 232.1199.

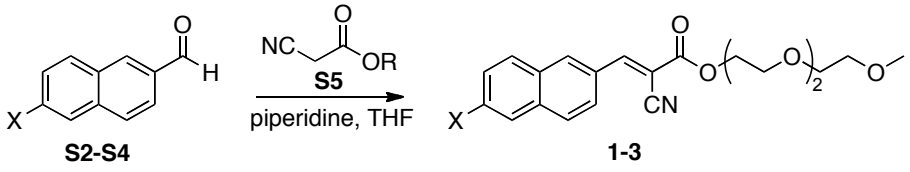

General procedure for the synthesis of fluorescent probes (1-3)

To a round bottom flask containing a solution of aldehyde (0.21 mmol) and the appropriate 2-cyanoacetate (0.23 mmol) in THF (0.8 mL), piperidine (0.02 mmol) was added and the mixture left stirring at 50 °C. The reaction was monitored by TLC and was completed within 21 hours. The crude mixture was concentrated under reduced pressure and the product was purified via flash column chromatography (10-30% EtOAc in hexanes).

(E)-2-(2-(2-methoxyethoxy)ethoxy)ethyl-2-cyano-3-(2-(piperidin-1-yl)napthalen-6-yl) acrylate (compound 1, ANCA11). 90% yield; red liquid.

R_f = 0.44 (EtOAc:Hexanes 1:1); ^{1}H NMR (400 MHz, $CDCl_3$) d 8.31 (s, 1H), 8.22 (bs, 1H), 8.10 (d, J= 8.8 Hz, 1H), 7.76 (d, J= 9.2 Hz, 1H), 7.65 (d, J= 8.8 Hz, 1H), 7.30 (dd, J= 2.1, 9.2 Hz, 1H), 7.05 (d, J= 2.1 Hz, 1H), 4.47 (m, 2H), 3.83 (m, 2H), 3.74-3.66 (m, 6H), 3.56 (m, 2H), 3.42-3.38 (m, 4H), 3.37 (s, 3H), 1.74 (m, 6H); ^{13}C NMR (100 MHz, $CDCl_3$) d 163.3, 155.4, 151.9, 137.7, 134.7, 130.6, 127.2, 126.4, 125.9, 125.6, 119.2, 116.4, 108.3, 71.8, 70.7, 70.5, 70.5, 68.7, 65.3, 58.9, 49.3, 25.4, 24.3; HRMS Calc for $C_{26}H_{32}N_2O_5Na$ $(M+Na)^+$ 475.2203 found 475.2197.

(E)-2-(2-(2-methoxyethoxy)ethoxy)ethyl-2-cyano-3-(2-morpholinonapthalen-6-yl) acrylate (compound 2). 83% yield; red liquid.

R_f = 0.76 (2% MeOH in CH_2Cl_2); ^{1}H NMR (300 MHz, $CDCl_3$) d 8.31 (s, 1H), 8.24 (s, 1H), 8.11 (dd, J= 1.9, 8.8 Hz, 1H), 7.80 (d, J= 9.1 Hz, 1H), 7.69 (d, J= 8.8 Hz, 1H), 7.28 (m, 1H), 7.06 (d, J= 1.9 Hz, 1H), 4.47 (m, 2H), 3.90 (m, 4H), 3.83 (m, 2H), 3.70 (m, 6H), 3.55 (m, 2H), 3.35 (m, 7H); ^{13}C NMR (100 MHz, $CDCl_3$) d 163.0, 155.2, 151.3, 137.2, 134.4, 130.6, 127.4, 127.0, 126.1, 126.0, 118.5, 116.1, 108.5, 99.4, 71.8,

70.7, 70.5, 70.4, 68.6, 66.5, 65.3, 58.9, 48.2; HRMS Calc for $C_{25}H_{30}N_2O_6Na$ $(M+Na)^+$ 477.1996 found 477.1995.

(E)-2-(2-(2-methoxyethoxy)ethoxy)ethyl-2-cyano-3-(2-(4-methylpiperazin-1-yl) napthalen-6-yl)acrylate (compound 3). 85% yield; red liquid.

R_f = 0.71 (2% MeOH in CH_2Cl_2); ^1H NMR (400 MHz, $CDCl_3$) d 8.31 (s, 1H), 8.23 (s, 1H), 8.10 (d, J= 8.6 Hz, 1H), 7.78 (d, J= 9.1 Hz, 1H), 7.67 (d, J= 8.6 Hz, 1H), 7.29 (d, J= 9.1 Hz, 1H), 7.06 (s, 1H), 4.46 (m, 2H), 3.83 (m, 2H), 3.73 (m, 2H), 3.67 (m, 4H), 3.55 (m, 2H) 3.42 (bs, 4H), 3.36 (s, 3H), 2.61 (bs, 4H), 2.37 (s, 3H); ^{13}C NMR (100 MHz, $CDCl_3$) d 163.2, 155.4, 151.4, 137.5, 134.5, 130.6, 127.4, 126.9, 126.1, 126.1, 119.0, 116.2, 108.7, 99.3, 71.9, 70.8, 70.6, 70.5, 68.8, 65.4, 59.0, 54.8, 48.0, 46.1; HRMS Calc for $C_{26}H_{34}N_3O_5$ $(M+H)^+$ 468.2493 found 468.2494.

Staining of brain tissue sections

Male and female transgenic mice overexpressing wild type mouse PrP (Tga20) were inoculated with the mouse-adapted prion strain mCWD and were euthanized upon developing terminal signs of prion disease. Transgenic mice (19959) harboring the Aβ plaques express the mutant human amyloid precursor protein 695 APP_{SweInd}, which bears both the Swedish (K670N/M671L) and the Indiana (V717F) mutations, under the control of the Syrian hamster prion protein promoter. Mice were euthanized between 9 - 13 months of age.

Frozen brain sections from transgenic mice producing Aβ and PrP^{Sc} protein were dried for 1 hr, hydrated with 100%, 95%, and 70% ethanol for 5 min each, and then rinsed with deionized water. Sections were then buffered with phosphate-buffered

saline (1X PBS) for 30 min. Compounds **1**, **2**, and **3** were diluted 1:50 in 1X PBS (from stock solutions of 3mM) to a final concentration of 60 μM, added to brain sections, incubated for 30 min at room temperature, washed three times with 1X PBS, and coverslipped using DAKO fluorescent mounting media.

Fluorescence microscopy

Brain tissue samples were excited with a 488 nm laser on an Olympus FluoView FV1000 spectral deconvolution confocal microscope. The emission spectra of compounds **1**, **2**, and **3** bound to Aβ, PrP^{Sc}, and background were collected in 1 nm increments from 450-650 nm. A minimum of 10 measurements was collected for each compound bound to plaque and non-plaque regions as a background control. The wavelength corresponding to the maximum relative fluorescence intensity was taken as the emission λ_{max}.

Spectroscopic studies of the ANCA probes versus pH

Each probe was dissolved in 95:5 deionized water:DMSO solution to a final concentration of 200 μM upon titration with 10 mM or 1 M HCl with aliquots removed in approximately pH=0.5 increments starting from basic pH. Aliquots were evaluated on a SpectraMAX 190 absorbance microplate reader (Molecular Devices) in 1 nm increments from 250-550 nm. Fluorescence emission spectra for each aliquot were obtained using a PTI spectrofluorimeter in 1 nm increments from 400-650 nm. Each probe was excited with a wavelength corresponding to the spectral window in which both base probe and protonated probe showed good absorption. Maximum intensity wavelengths were plotted against pH and fit to a Boltzmann sigmoidal curve to estimate the pKa.

Fluorescence studies with aggregated Aβ peptides

Aggregated Aβ peptide was prepared by dissolving Aβ42 in PBS pH 7.4 to a final concentration of 100 μM. This solution was magnetically stirred at 1200 rpm for 3 days at room temperature. Aliquots of 15 mL of the pre-aggregated Aβ42 solution was added to 285 mL of the probe (5% DMSO in nanopure water) to attain a final concentration of 5 mM Aβ42 and 4 mM of the probe. The solution was transferred to a 300 mL cuvette and the fluorescence was measured at 22.5 °C.

Determination of K_d binding constants

As previously reported, in order to estimate the binding constant (K_d) for the probe-Aβ complexes from the fluorescence studies, we made the following assumptions:

1. All probes are completely in solution and free of any significant competing binding process such as self-aggregation.
2. The concentration of unbound probes can be approximated as close to the total concentration of the probes.
3. The binding sites in the aggregated Aβ peptides are not completely occupied at the concentration of Aβ binding probes used for the fluorescence studies (i.e., the experiments are carried out under non-saturated binding conditions).

Pre-aggregated Aβ42 (5 mM final concentration) was mixed with various concentrations of probes (10, 5, 2.5, 1.25 mM) in 5% DMSO in nanopure water and their K_d's were determined by fitting data to a one-site specific binding algorithm: $Y = B_{max}*X/(K_d+X)$, where X is the concentration of the probe, Y is specific binding

fluorescence intensity, and B_{max} corresponds to the apparent maximal observable fluorescence upon binding of probes to aggregated Aβ42 peptide.

Brightfield color imaging

Brain tissue sections were imaged under an Olympus MVX10 Macroview equipped with a MWB2 (Japan) long-pass filter. Each sample was illuminated with epifluorescence and imaged with an exposure time of 0.2 sec. Congo red samples were imaged with an exposure time of 0.1 sec.

Staining of frozen brain sections with Congo red

Frozen brain sections from transgenic mice with Aβ and PrP^{Sc} plaques were dried for 1 hr, hydrated with 100%, 95%, and 70% ethanol for 5 min each, and then rinsed with deionized water. Sections were then buffered with a working solution of sodium chloride in 1X PBS for 20 min. A 2% solution of Congo red was prepared in 1X PBS, added to brain sections, incubated for 1 hr at room temperature, washed with deionized water, and coverslipped using DAKO fluorescent mounting media.

Solvent studies of probes

Each probe was dissolved in freshly distilled anhydrous dimethylsufloxide (DMSO), methanol (MeOH), 2-propanol (iPrOH), dichloromethane (DCM), ethyl acetate, chloroform, and toluene to a final concentration of 1.5 μM. Excitation and fluorescence emission spectra of each solution were obtained on a PTI spectrofluorimeter in 1 nm increments from 350-520 nm and 400-650 nm, respectively. The wavelength corresponding to the maximum intensity was taken as λ_{max}.

2.6 Additional Figures

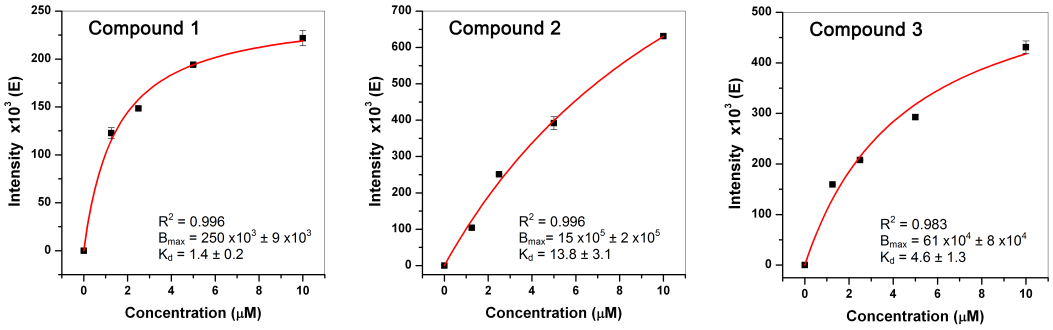

Figure 2.13 Plots of the fluorescence intensity versus concentration of probes **1-3** in the presence of aggregated Aβ peptide. The K_d was determined by fitting the data to a one-site specific binding algorithm: $Y = B_{max}*X/(K_d+X)$, where X is the concentration of the probe, Y is specific binding fluorescence intensity, and B_{max} corresponds to the apparent maximal observable fluorescence upon binding of probes to aggregated Aβ42 peptide.

Acknowledgements

Chapter 2 is a partial reprint of the material as it appears in "Aminonaphthalene 2-Cyanoacrylates (ANCA) Probes Fluorescently Discriminate between Amyloid-β and Prion Plaques in Brain". Cao, Kevin; Farahi, Mona; Dakanali, Marianna; Chang, Willy M.; Sigurdson, Christina J.; Theodorakis, Emmanuel A.; Yang, Jerry. (2012) *Journal of the American Chemical Society*, 134 (42), 17338-17341. I am the primary author on this publication.

Chapter 3

The Rational Design of Amyloid-Discriminating Fluorophores

3.1 Introduction

It was previously shown that environment sensitive amino-naphthalene cyanoacrylate (ANCA) molecular rotors were able to bind and fluorescently discriminate amyloid aggregates in tissue.[113] In general, the excitation of these molecules generates a charge-separated dipole where local solvent interactions can modulate the excited state energy (Figure 3.1). Members of the molecular rotor family are known to undergo twisted-intramolecular charge transfer (TICT) states whereby excited states can adopt non-planar arrangements, forcing complete charge separation, which upon solvation with polar solvents reduces the potential energy and redshifts the emission.[114]

In the presence of amyloid aggregates, the binding onto the protein oblates both non-radiative de-excitation from the excited state as well as TICT state formation and in doing so causes a large increase in the fluorescence signal and quantum yield. By using this type of molecular rotor scaffold in our ANCA compounds, we were previously able to detect differences in the local protein binding pocket environments surrounding the molecules.

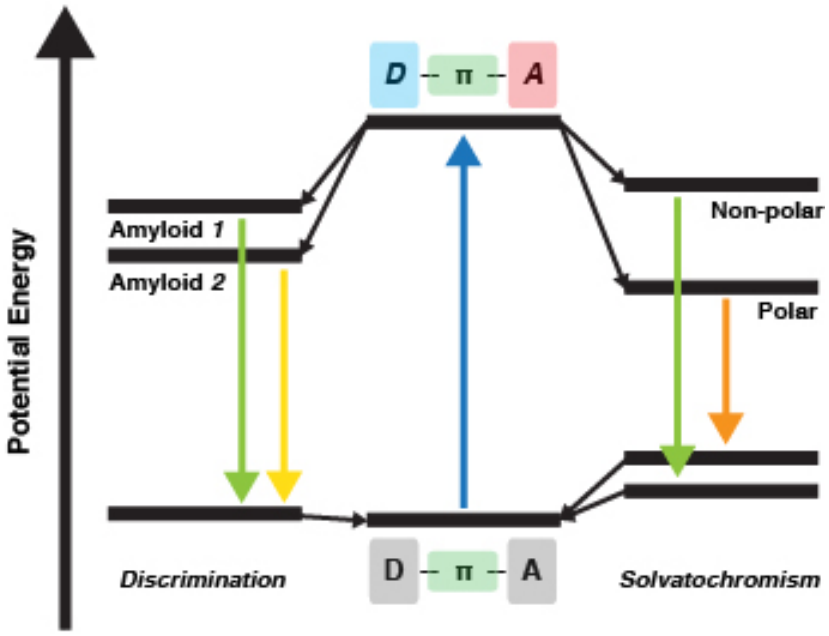

Figure 3.1 General photophysics of ANCA fluorophores. In pure solvent (left side), solvatochromism results from the stabilization of the excited state dipole by solvent molecules. In amyloid-aggregates (right side), the local binding pocket permittivity achieves a similar effect. D = donor moiety, A = acceptor moiety.

In an amyloid, the side-chain groups along each type of aggregate create a unique binding pocket that generates an amyloid-specific fluorescence emission wavelength when bound with the fluorophore.[20,115,116] I sought to use these fluorescence signatures to characterize the binding pockets of amyloid species with the goal of generating a library of fluorescence-based "fingerprints" that could ultimately

be used as diagnostic criteria for amyloid-based neurodegenerative diseases. Here I present the rational design of a series of these fluorophores based on the ANCA motif and their applications in the detection and fluorescence characterization of select amyloids.

3.2 Results & Discussion

3.2.1 Design of Second Generation ANCA Fluorophores

Molecule design was developed from the Ooshika-Lippert-Mataga (OLM) equation (Equation 3.1), which, briefly, is a quantitative relationship of the observed Stokes Shift $\Delta\tilde{\nu}$ of a fluorogenic species to the local environment permittivity, described by the dielectric constant, ε, and the refractive index, n.

$$\Delta\tilde{\nu} = \frac{2(\mu_e - \mu_g)^2}{hca^3}\left[\left(\frac{\varepsilon - 1}{2\varepsilon + 1}\right) - \left(\frac{n^2 - 1}{2n^2 + 1}\right)\right]$$

Equation 3.1 The OLM equation describes the solvatochromic behavior of point dipoles in a polar environment.

This equation is commonly used to describe the solvatochromic behavior of donor-acceptor fluorophores, and is governed by a molecular term defined by the ground and excited state dipoles, μ_g and μ_e, as well as the Onsager solvation cavity radius, a, taken up by the fluorophore in the solvation field. Closer inspection of Equation 3.1 reveals that the molecular term can be adjusted to tune the solvatochromic character by changing the dipole and Onsager radius parameters.

In collaboration with Kristy Elbel from the Theodorakis lab, we began with the previously published ANCA11, compound **1**, as the parent scaffold. We designed four

new molecules where the Onsager radius and dipole moments were tuned by both modulating the length and the polarizability. We first shortened the Onsager radius by reducing the naphthalene core of compound **1** (ANCA11) to benzene, resulting in compound **4** (aminobenzyl cyanoacrylate, ABCA) (Figure 3.2).

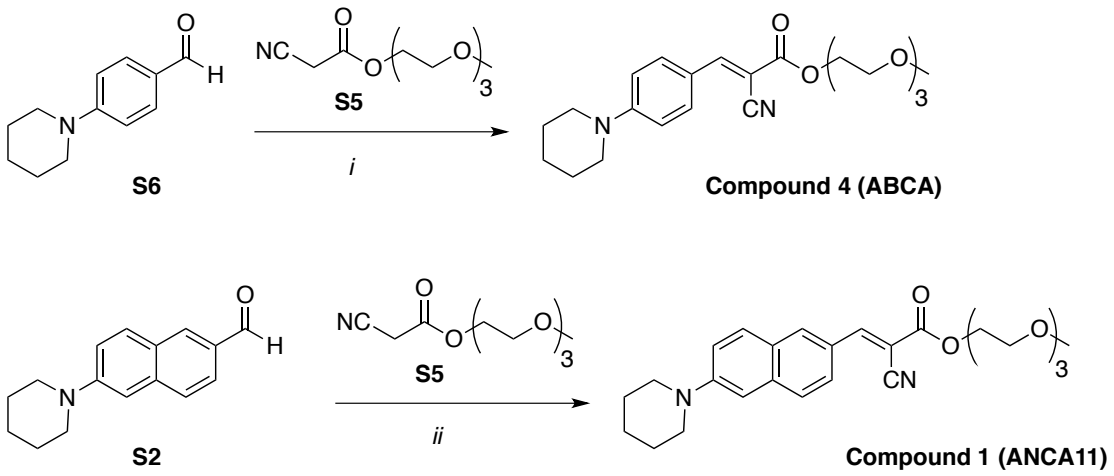

Figure 3.2 Synthesis of compound **4** and previously published compound **1**. Conditions: *i*. DBU, THF, 60°C. *ii.* piperidine, THF, 60°C.

Next the Onsager radius was increased by introducing an electron rich heterocycle into the π-network. We decided to introduce an aromatic heterocycle over an additional benzene ring in order to avoid decreasing the solubility of the final fluorophores in aqueous media (Figure 3.3). Insertion of an *N*-methyl pyrrole (compound **5**, ANCA-p), a furan (compound **6**, ANCA-f), and a thiophene (compound **7**, ANCA-t) allowed us to also adjust the polarizability by affecting the charge-transfer absorption without altering the piperidine donor, which I had previously found to regulate the pK_a.

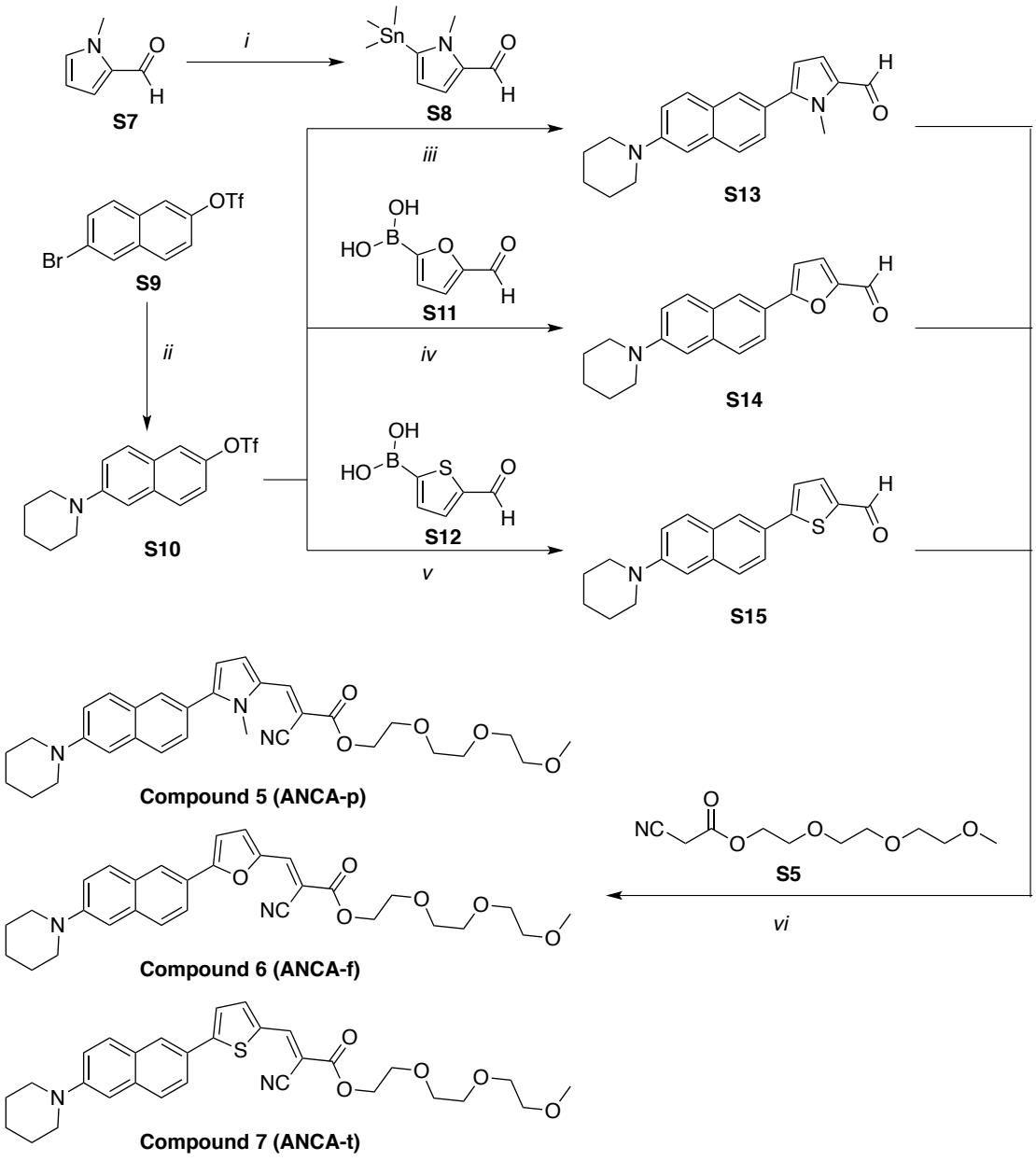

Figure 3.3 Synthesis of compounds **5** – **7**. Conditions: *i.*nBuLi, TMEDA, Me_3SnCl *ii.* $Pd(OAc)_2$, $P(tBu)_3$, NaOtBu, piperidine, toluene, 110°C. *iii*. $PdCl_2(PPh_3)_2$. *iv*. $Pd(PPh_3)_4$, K_2CO_3. *v*. $Pd(PPh_3)_4$, K_2CO_3. *vi.* DBU, THF, r.t. 5 minutes.

With respect to Equation 3.1, we predicted that the thiophene conjugate, compound **7,** would have the strongest solvatochromic properties with the relatively low electron density of the *p*-orbitals in the heterocyclic ring driving the donor

electrons into the π-network, increasing the change in dipole moment, in contrast to the more electron rich pyrrole and furan rings.[117,118]

3.2.2 Solvatochromic behavior of ANCA probes

The photophysical properties of the ANCA fluorophores were characterized using the Lippert-Mataga solvatochromic plots, where the Stokes shift was plotted as a function of the local environment permittivity, or orientation polarizability, Δf. This term accounts for both the low frequency (nuclear) and high frequency (electronic) polarization of solvent molecules around the solute dipole, given as[111,119,120]

$$\Delta f = \left(\frac{\varepsilon - 1}{2\varepsilon + 1}\right) - \left(\frac{n^2 - 1}{2n^2 + 1}\right)$$

Equation 3.2 The orientation polarizability term accounts for the nuclear and electronic rearrangement of solvent dipoles around a point solute dipole.

where ε is the dielectric constant (previously described as the relative permittivity), and n^2 is the square of the refractive index, also known as the optical dielectric constant. The slopes of the Lippert-Mataga plots thus correspond to the molecular term of Equation 3.1, which we defined as a measure of the solvatochromic behavior, or environment sensitivity.

Solvatochromic assays were performed in a collection of aprotic solvents, where we measured the Stokes shift for each compound in toluene, diethyl ether (Et_2O), anisole, tetrahydrofuran (THF), dichloromethane (DCM), acetone, and acetonitrile (ACN) (Figure 3.4). I did not see correlation between the absorption bands and the local permittivity, indicating that the sensitivity originated solely from solvent

stabilization of the emissive S_1 excited state; i.e. that absorption was not affected by solvent.

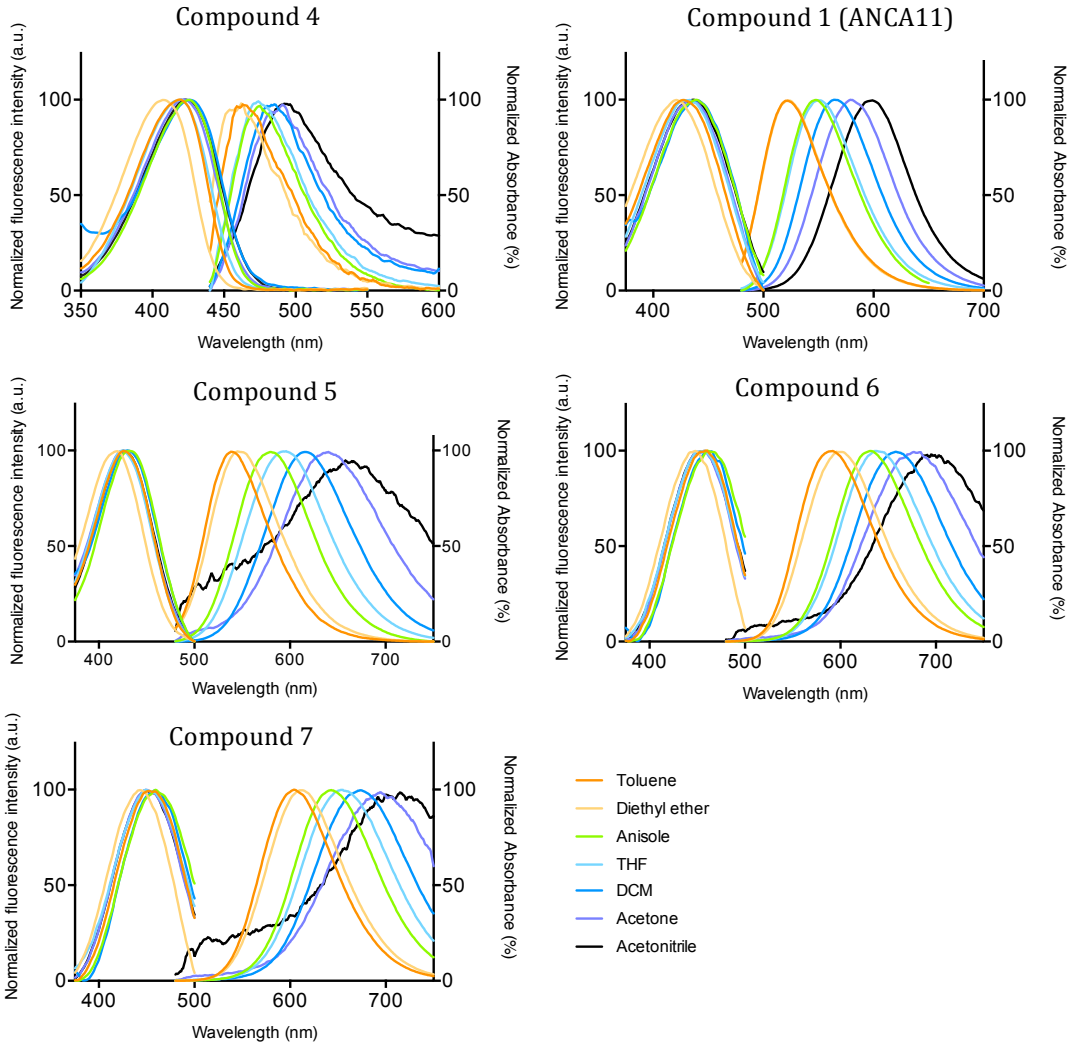

Figure 3.4 Solvatochromism of the ANCA compounds **4**, **1**, **5** - **7**.

Furthermore, the experimental Lippert-Mataga plots showed a linear correlation of the observed Stokes Shift to Δf, implying that the environment sensitivities were largely a result of the local relative permittivity and not strongly influenced by additional solvent parameters such as chlorination or aromaticity (Figure 3.5).

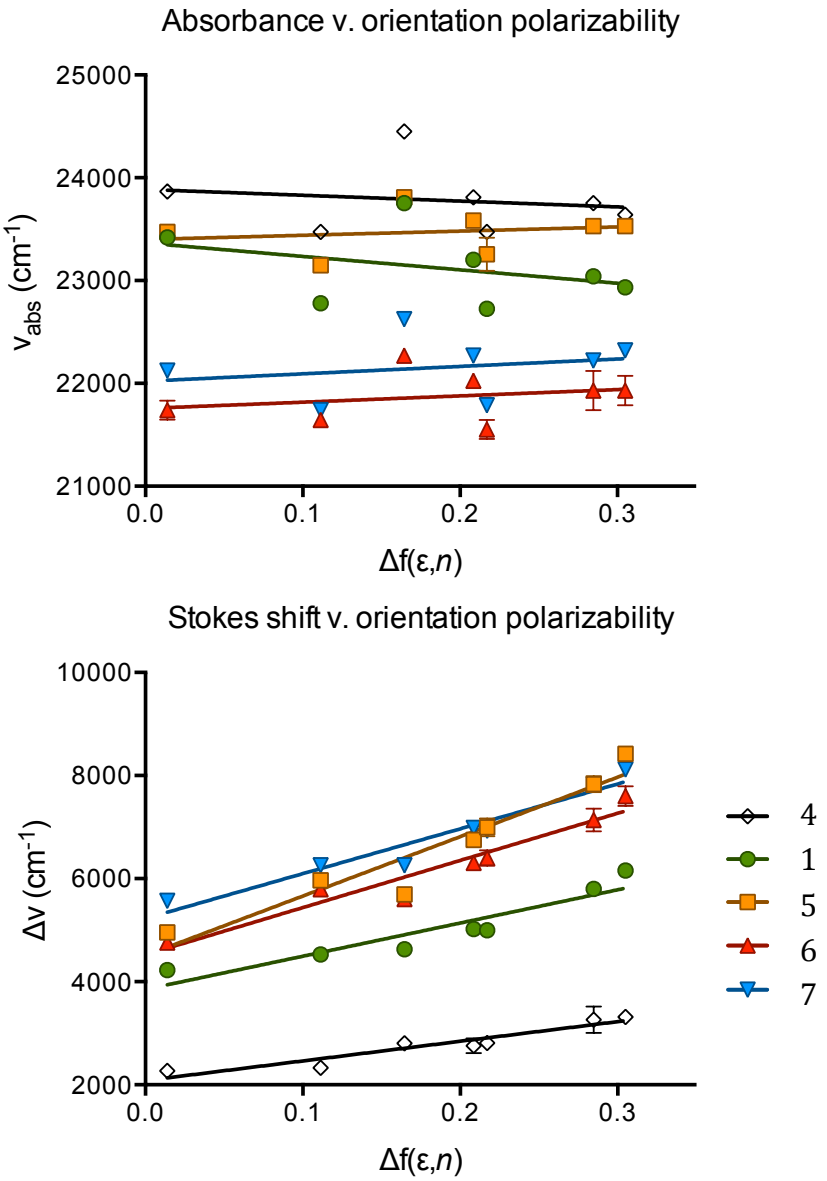

Figure 3.5 Lippert-Mataga solvatochromism plots of compounds **1**, **5** - **7**. Top: plots of absorbance as a function of the orientation polarizability show no correlation, in compliance with the Franck-Condon principle. Bottom: Lippert plots of the Stokes Shift as a function of the orientation polarizability.

As the length of the π-network was increased from benzene to naphthalene to the naphthalene-heterocycle conjugate, the solvatochromic behavior was found to increase in response (Table 3.1). Compound **4** (ABCA) was found to have an environment sensitivity of 3814 ± 556.7 cm^{-1}, followed by the original parent

compound **1** (ANCA11) with 6443 ± 1122 cm^{-1}, and finally the three heteroaromatic conjugates with an average trend of 9795 ± 740 cm^{-1}. These slopes were statistically distinct (P = 0.02) and the trend was attributed to the increased distance between the partial charges in the excited state, resulting in a larger change in dipole moment as the length of the fluorophore was increased.

Table 3.1 Solvatochromic trends of ANCA compounds **4**, **1**, **5** - **7** for absorption and the Stokes shift as a function of the local environment permittivity Δf. The correlation values are the regression values for a linear trend line fit to the Lippert-Mataga plots.

	Absorbance		Stokes Shift	
Compound	Lippert-Mataga slope (cm^{-1})	Correlation	Lippert-Mataga slope (cm^{-1})	Correlation
4	-565.1 ± 1454	0.029	3814 ± 556.7	0.904
1	-1306 ± 1519	0.129	6443 ± 1122	0.868
5	407 ± 949	0.036	11535 ± 1627	0.910
6	612.2 ± 1055	0.063	9152 ± 1101	0.933
7	720.2 ± 1336	0.055	8699 ± 1032	0.934

In comparing the three heteroaromatic conjugates, I discovered that the *N*-methyl pyrrole conjugate (compound **5**, ANCA-p) had the greatest solvatochromic behavior in comparison to the furan (compound **6**) and thiophene conjugate (compound **7**). Although the trend is not significant (P = 0.15), we observed a 123 nm range of Stokes shifts over the same solvents for the *N*-methyl pyrrole, indicating a greater range of sensitivity compared to the furan (a range of 113 nm) and thiophene (104 nm) (Figure 3.6).

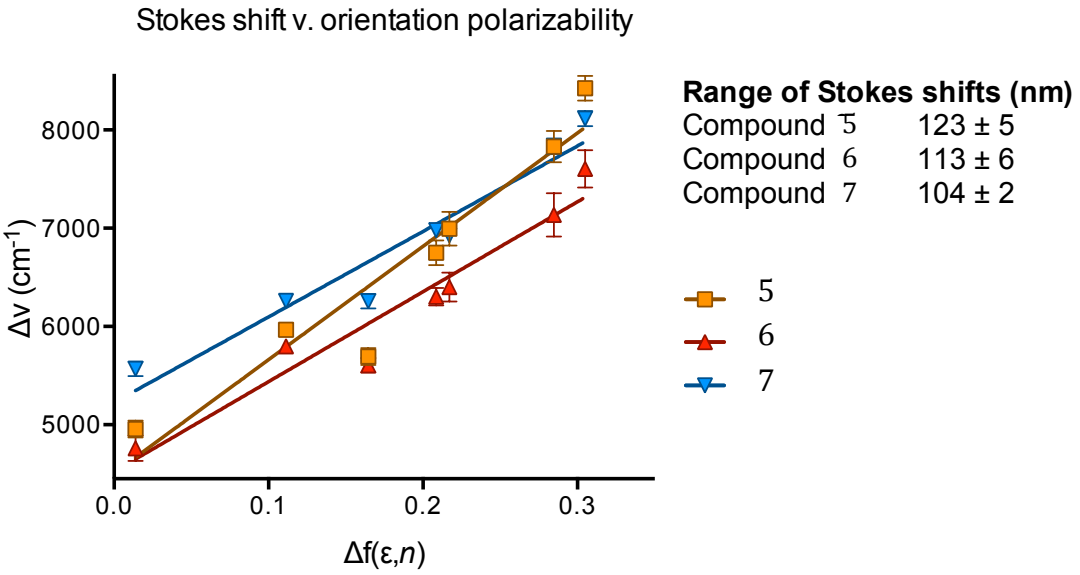

Figure 3.6 Lippert plots of the Stokes shift as a function of the solvent orientation polarizability. The range of Stokes shifts measures the difference between the largest and smallest measured Stokes shifts (i.e. the Stokes shift in DMSO versus the Stokes shift in toluene).

In order to explain this enhanced sensitivity, Jordi Cirera from the Paesani lab performed DFT solvation modeling experiments of compounds **5**, **6**, and **7** in vacuum, toluene, anisole, acetone, acetonitrile (ACN), and dimethyl sulfoxide (DMSO) (Table 3.2). In particular, he performed modeling on truncated analogs of the conjugates where the water solubilizing triethylene glycol monomethyl ether tail was removed.

Table 3.2 Dihedral angle between the naphthalene and heterocycle in the ground and excited states for compounds **5** - **7**.

Compound	Compound 5 Dihedral angle Ground state	Compound 5 Dihedral angle Excited State	Compound 6 Dihedral angle Ground state	Compound 6 Dihedral angle Excited state	Compound 7 Dihedral angle Ground state	Compound 7 Dihedral angle Excited state
Vacuum	-48.71	-27.16	-3.74	-0.03	-27.92	-0.03
Toluene	-48.09		0.33	0.18	-26.56	-0.14
Anisole	-47.18		0.16	0.51	-26.55	-0.55
Acetone	-46.82	-21.62	3.49	0.62	-24.93	-20.30
Acetonitrile	-46.85		1.59	-0.08	-25.05	-16.73
Dimethyl sulfoxide	-46.79	-21.37	-2.21	-1.04	-24.70	-16.88

When we monitored the dihedral angle between the heterocycles and the naphthalene ring as a function of solvent dielectric, the solvation models suggested that the enhanced sensitivity to the environment originated from the out-of-plane arrangement of the *N*-methyl pyrrole ring relative to the naphthalene in the excited state, resulting in a more pronounced charge-separation and therefore stronger interactions with the surrounding solvent environment (Figure 3.7). In this state the donor and acceptor charges are readily stabilized by polar solvent molecules, resulting in a lower energy emissive S_1 state.[114] In contrast, nonpolar solvents do not solvate the charges as well, resulting a higher energy emissive S_1 state.

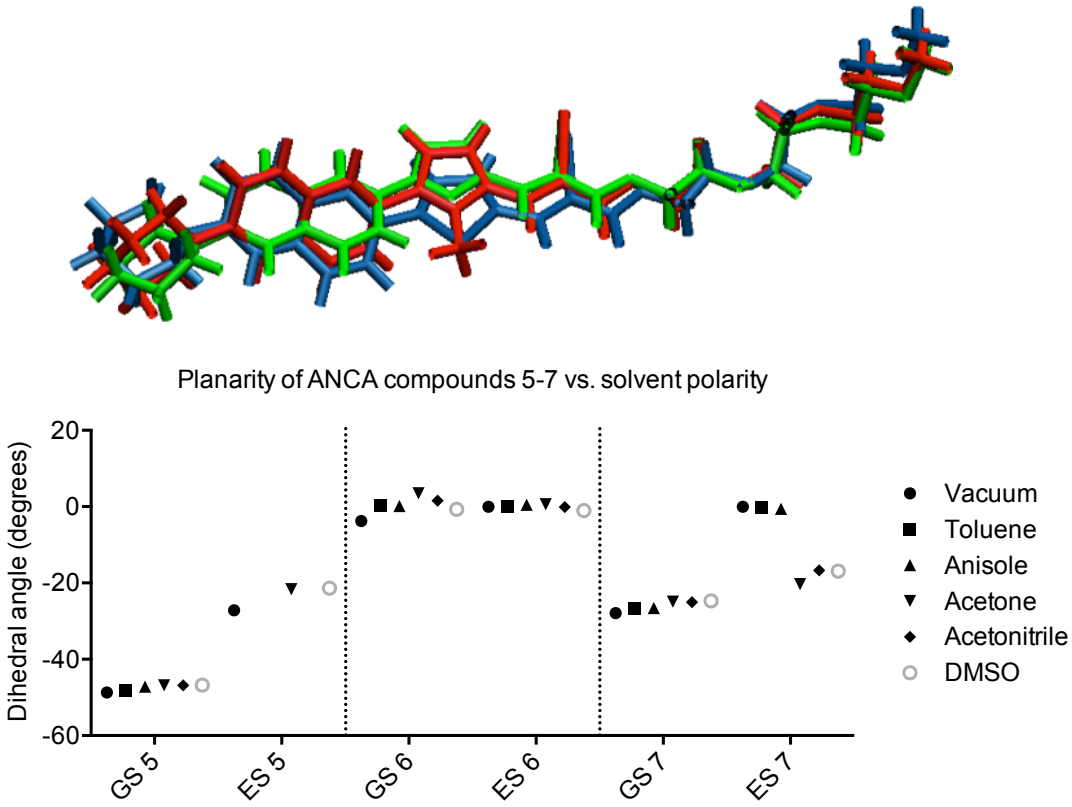

Figure 3.7 Top: Overlay of ground state ANCA compounds **5** (red), **6** (green), and **7** (blue) in vacuum. Bottom: Dihedral angles between the naphthalene and heterocycle were plotted as a function of solvent polarity. GS = ground state, ES = excited state.

As Figure 3.7 shows compound **5** adopted a planar conformation in the ground and excited states, so solvation becomes the sole factor affecting environment sensitivity. Compound **6** was seen to adopt a planar arrangement in vacuum and non-polar solvents, but returned to a twisted conformation in polar solvents, suggesting a TICT state formation that would be more readily stabilized by polar solvents than a planar state. For compound **5**, the torsional angles of approximately -20° for the excited states resemble TICT states, which would have lower excited state energies in more polar solvents with red-shifted emission values, and much higher energies in

non-polar solvents. This was consistent with the experimental sensitivities shown in Figure 3.6 (Table 3.3).

Table 3.3 Absorption and emission wavelengths for compounds **5** - **7** in aprotic solvents.

	Absorption wavelenght (nm)			Emission wavelength (nm)		
Solvent	Compound 5	Compound 6	Compound 7	Compound 5	Compound 6	Compound 7
Toluene	426 ± 1	460 ± 2	452 ± 1	540 ± 2	589 ± 3	604 ± 2
Et_2O	420 ± 1	449 ± 1	442 ± 1	552 ± 2	600 ± 2	611 ± 2
Anisole	432 ± 1	462 ± 1	460 ± 1	582 ± 1	631 ± 1	646 ± 2
THF	424 ± 1	454 ± 1	449 ± 1	594 ± 4	636 ± 3	654 ± 2
DCM	430 ± 3	464 ± 2	459 ± 1	615 ± 2	660 ± 5	673 ± 1
Acetone	425 ± 1	456 ± 4	450 ± 1	637 ± 6	676 ± 5	695 ± 3
Acetonitrile	425 ± 1	456 ± 3	448 ± 1	662 ± 5	698 ± 6	705 ± 3

While this torsional strain for the dihedral angle between the heterocycle and naphthalene seemed to affect the solvatochromic behavior, the absolute emission wavelengths were still longest for compound **7** (ANCA-t). Because the observed Stokes shift is directly proportional to the dipole moments, we also calculated the dipole moments of compounds **5** - **7**. The absorption spectra were not solvatochromic, so when correlating dipole moment to observed Stokes shift, we only used emission wavelengths. Consistent with experimental fluorescence emission data where compound **7** had the longest emission of the three per solvent, we were happy to see that the theoretical model held **7** to have the largest change in dipole per solvent as well (Figure 3.8).

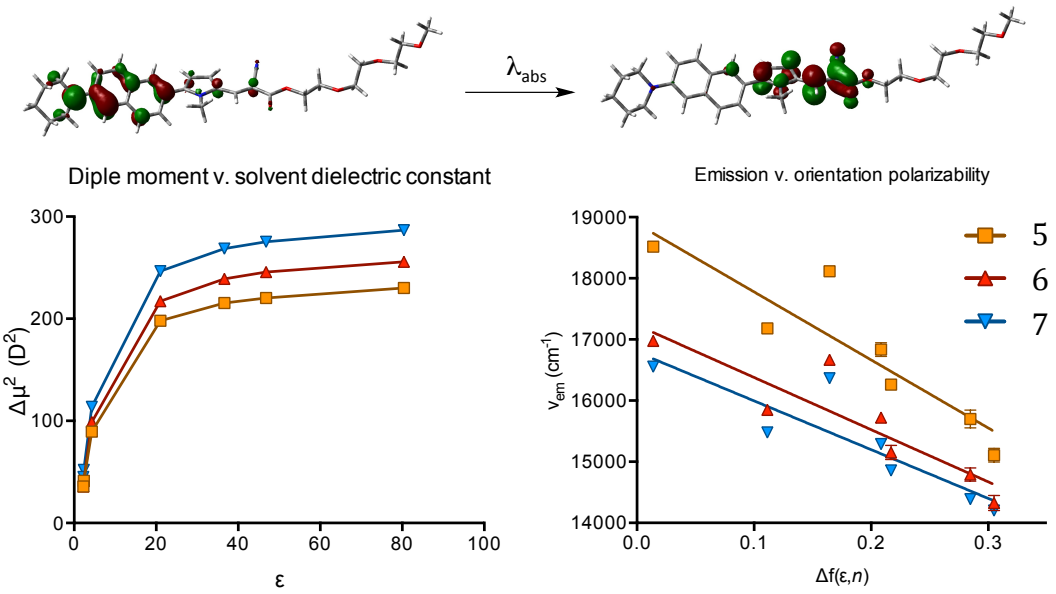

Figure 3.8 Comparison of computational and experimental solvatochromic behavior with respect to dipole strength. Top: *Ab initio* solvation DFT calculations were performed to measure the dipole characters of each compound in aprotic solvents (Compound **5** in vacuum shown). Left: DFT calculations of the change in dipole moments show that compound **7** had the largest change in dipole as a function of the solvent dielectric constant. Right: Experimental solvatochromic assays show compound **7** having the longest emission wavelength in each polar solvent.

Since the slope of the Lippert-Mataga plots is also inversely proportional to the size of the compounds, I looked at the Onsager cavity radius as a secondary cause for the enhanced environment sensitivity. DFT calculations were performed on model systems without the triethylene glycol monomethyl ether water solubilizing group; we determined the radius of compound **5** to be 8.59Å, compared to 9.01Å for compound **6** and 9.23Å for compound **7**. We rationalized that as the length of the fluorophore increased, the solvation cavity expands resulting in an increased reaction field surrounding the molecule. This results in a larger degree of solvation, resulting in a lowering of the excited state energies in nonpolar and polar solvents and consequently a redshift in emission. With compound **5** (ANCA-p) having the smallest radius of the

trio, it would be less solvated than compounds **6** and **7**, which correlates with the shorter emission wavelengths seen (Table 3.3).

3.2.3 ANCA fluorophores detect *ex vivo* amyloid plaques

With compound **5** (ANCA-p) determined to be the most environment sensitive in homogenous environments, we next tested the applicability in a heterogenous biological setting by staining amyloid aggregates in frozen brain tissues. 5 micron midbrain tissue slices from transgenic (Tg) Alzheimer's disease mice (19959 PRNP-APP_{swe}Ind) and Tg prion mice (Tga20, expression 10 times the regular amount of PrP^{C}) afflicted with chronic wasting disease (mCWD) were stained with 60 μM of each compound in 1X PBS (Figure 3.9).

As previously seen, true-color microscopy of the resulting stained tissues showed that each compound exhibited a protein aggregate-dependent fluorescence emission profile. β-amyloid (Aβ) aggregates in the hippocampus of AD mice showed a blue-shifted emission for each compound compared to the prion aggregates in the corpus callosum of the prion mice. I next measured the emission spectra of the stained aggregates and found that there were discrete differences in emission wavelengths depending on the aggregate (Figure 3.9). Prions were consistently found to have binding pockets with more hydrophilic character than those in Aβ, leading to a more redshifted emission. Of the five compounds, compound **5** (ANCA-p) showed the greatest difference in emission, with a maxima difference of 41 ± 9 nm between Aβ and prion aggregates. This was consistent with the enhanced sensitivity for compound **5** found in the Lippert-Mataga plots for pure solvents.

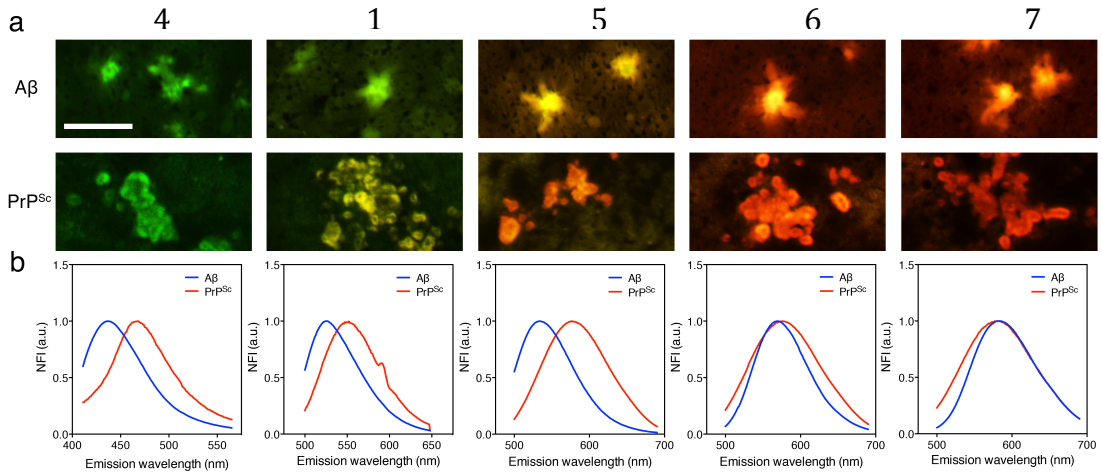

Figure 3.9. *Ex vivo* tissue histology of amyloid aggregates in a Tg Alzheimer's Disease mice model and a Tg prion model. A. Real-color micrographs of AD hippocampus and prion corpus callosum stained with compounds **4**, **1**, **5** – **7**. B. Emission spectra of amyloid deposits measured with a 488 nm excitation. Scale bar = 50 microns.

For histology quantification, we reduced the Lippert-Mataga equation to suit imaging biological systems with the assumption that the solvatochromic nature of the fluorophores was weighted more by the excited state dipole moments than the ground state (i.e. that solvent reorganization around the molecule was more pronounced for the excited state, so the energy of the ground state destabilization was relatively minimal compared to the energy of the stabilization of the excited state). This allowed us to use the fluorescence emission bands as the sole reporter for protein binding pocket polarity. In calculating the binding pocket polarities, we also omitted the refractive index, used as the optical dielectric constant in the Lippert-Mataga equation. Because the refractive index is the high-frequency response of solvent dipoles in response to a transient solute dipole, it only affects the absorption band due to the Frank-Condon principle.[121] Therefore we could remove it in the permittivity field, since we would only measure the emission band as the reporter of binding pocket

permittivity. The truncation of the Lippert-Mataga equation results in Equation 3.3, where we describe the relationship of emission wavelength to the local dielectric constant.

$$\tilde{\nu}_{\mathrm{em}} = \frac{2(\mu_e - \mu_g)^2}{hca^3}\left(\frac{\varepsilon - 1}{2\varepsilon + 1}\right) + C$$

Equation 3.3 Truncated Lippert-Mataga equation used to quantify the binding pocket permittivities of amyloid aggregates.

We next extrapolated the binding pocket permittivities of each compound for the two aggregate types using the standard regression lines of the Lippert plots graphed using Equation 3.3 (Figure 3.10). We discovered that compound **1** and compound **5** had similar binding pocket permittivities, suggesting that they may bind the same type of side chain grooves. The compound **4** was found to have a highly non-polar binding pocket on β-amyloid, with a permittivity of 1.17 ± 0.07, and a relatively more polar binding pocket on prions, at 3.45 ± 0.34. Interestingly, the furan (ANCA-f) and thiophene (ANCA-t) conjugates had low-polarity binding pockets in both amyloid-beta and prion aggregates, with relative permittivity differences of 0.16 and 0.07 in their discriminating capabilities, respectively. In contrast compounds **4**, **1**, and **5** had differences of relative permittivity of 2.28, 2.44, and 1.90, respectively.

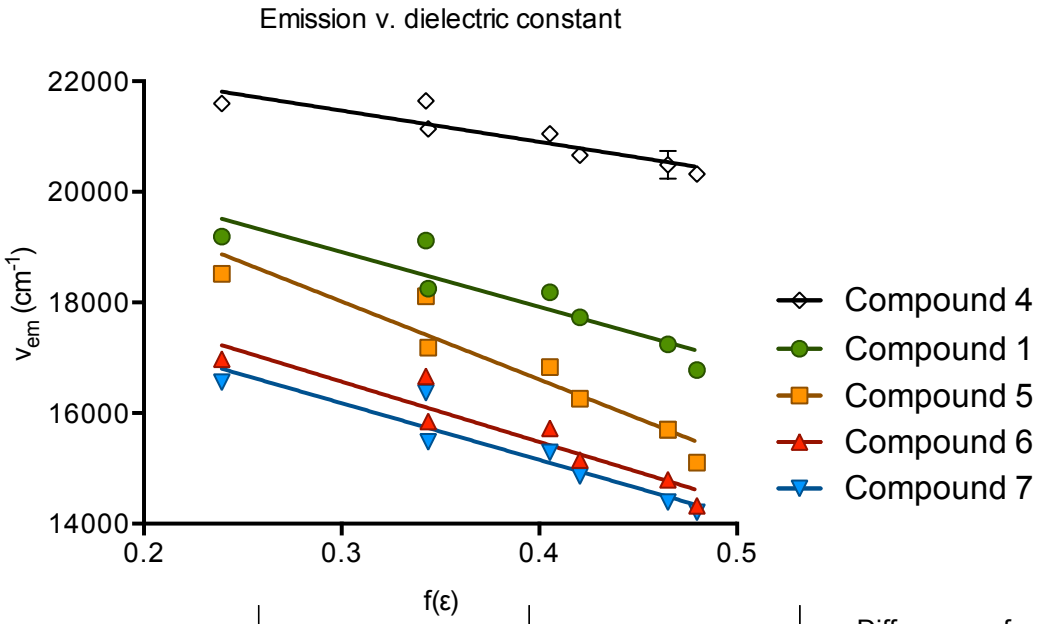

Compound	Amyloid-β	Prion	Difference of permittivities
4	1.17 ± 0.07	3.45 ± 0.34	2.28
1	3.02 ± 0.12	5.45 ± 0.47	2.44
5	2.56 ± 0.28	4.46 ± 0.21	1.90
6	2.09 ± 0.15	2.25 ± 0.08	0.16
7	2.04 ± 0.10	1.97 ± 0.09	0.07

Figure 3.10 Extrapolation of binding-pocket permittivities from standard regression lines of compounds **4**, **1**, **5** - **7**. Top: Plots of the emission wavelength as a function of low frequency solvent polarizability. Bottom: Emission maxima of compounds **4**, **1**, **5** - **7** stained to AD and prion plaques were extrapolated from the regression lines.

Taken together, these results suggest that there is an optimal length for discriminating amyloid aggregates, based upon their binding pocket recognition. Consistent with the solvatochromism assays in pure solvents, the longer compounds **6** and **7** exhibit a decrease in the environment sensitivity whereas compounds with

shorter solvation cavity radii (compound **1**) or torsional strain (compound **5**) exhibit a larger capacity to discriminate between small differences in the environment permittivity. As the molecular length increases, the compounds prefer non-polar regions on both types of aggregates, whereas shorter compounds are able to find more polar pockets.

Finally, due to the indirect assumptions made regarding the solvent-solute interactions, we neglected additional intermolecular solvent effects such as hydrogen bonding or additional orthogonal dipole interactions. While this simplification follows most readily in pure solvents, we cannot exclude the possibility that the amyloid-sensitivity seen with compounds **4, 1,** and **5** stem from non-polarizability effects such as protonation or hydrogen-bonding from protic and polar residues in the local binding pocket.[122,123] In particular, the peptide sequence exposed to the surface in an amyloid fibril is rich in lysines and aspartic acid residues, prompting the possibility that the charge-transfer excited state of the compounds is stabilized by these charges.

3.2.4 Fluorescent fingerprinting amyloids

The use of one fluorophore to characterize and discriminate between amyloid aggregates suffers from the drawback of spectral overlap between amyloids of similar binding pocket permittivity (Figure 3.11).

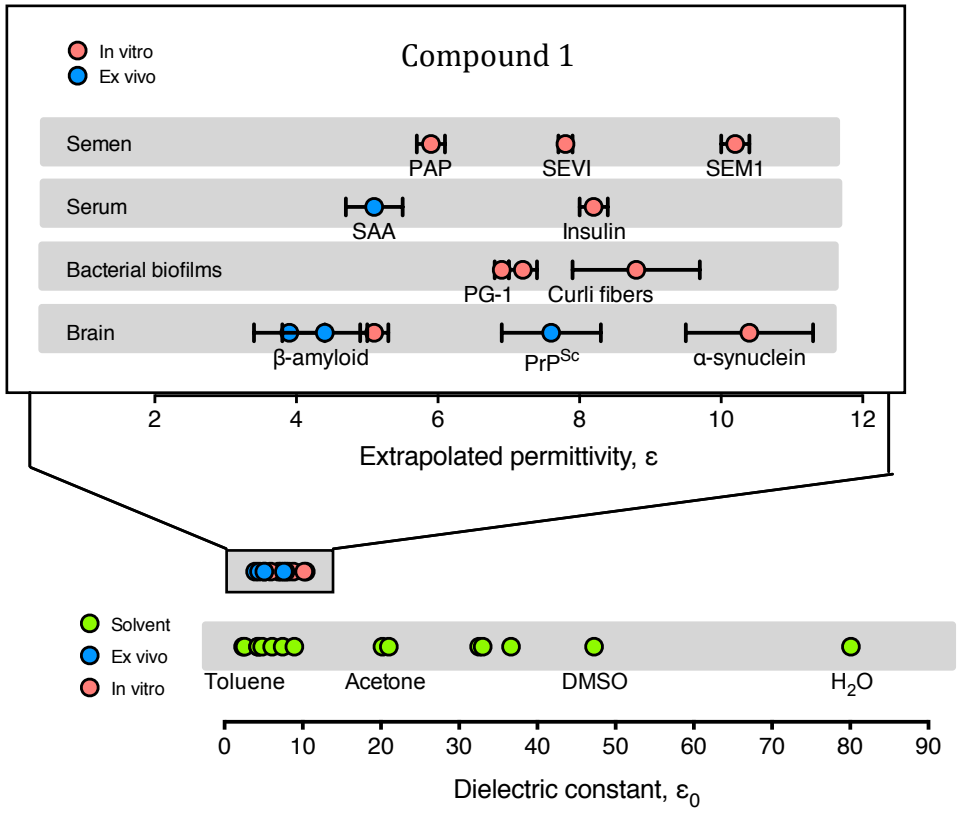

Figure 3.11 Compound **1** (ANCA11) is able to discriminate various amyloids. The overall range of extrapolated binding pocket permittivities is narrow within the overall range of solvent dielectrics.

In order to circumvent this potential issue, I began assaying the ability of compounds **4, 1, 5 - 7** to bind aggregated Aβ(1-42) *in vitro* as a set of control experiments. Since a one-dimensional approach towards labeling aggregates results in all the amyloids lying within a narrow relative permittivity window, expansion to a two- or three-dimension permittivity field would allow us to be able to tease out minute differences in binding pocket permittivity.

As expected, compounds **1, 5 - 7** showed an enhancement of fluorescence upon binding Aβ(1-42) fibrils (Figure 3.12). Compound **4** interestingly had a very weak

fluorescence signal enhancement, likely due to a weak-binding affinity towards the fibrils with a K_d of 19.4 ± 10.3 μM (Figure 3.13).

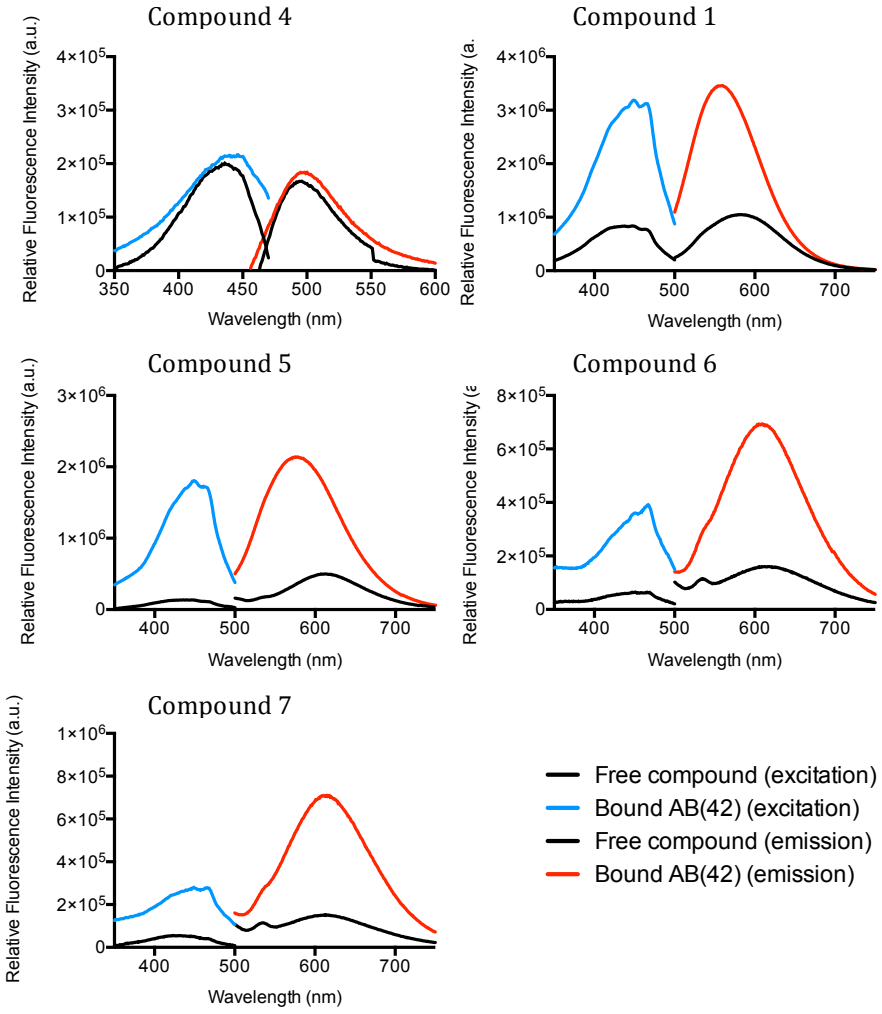

Figure 3.12 Excitation (blue) and emission (red) spectra of the binding of compounds **4**, **1**, and **5** - **7** to aggregated Aβ(1-42) fibrils in solution.

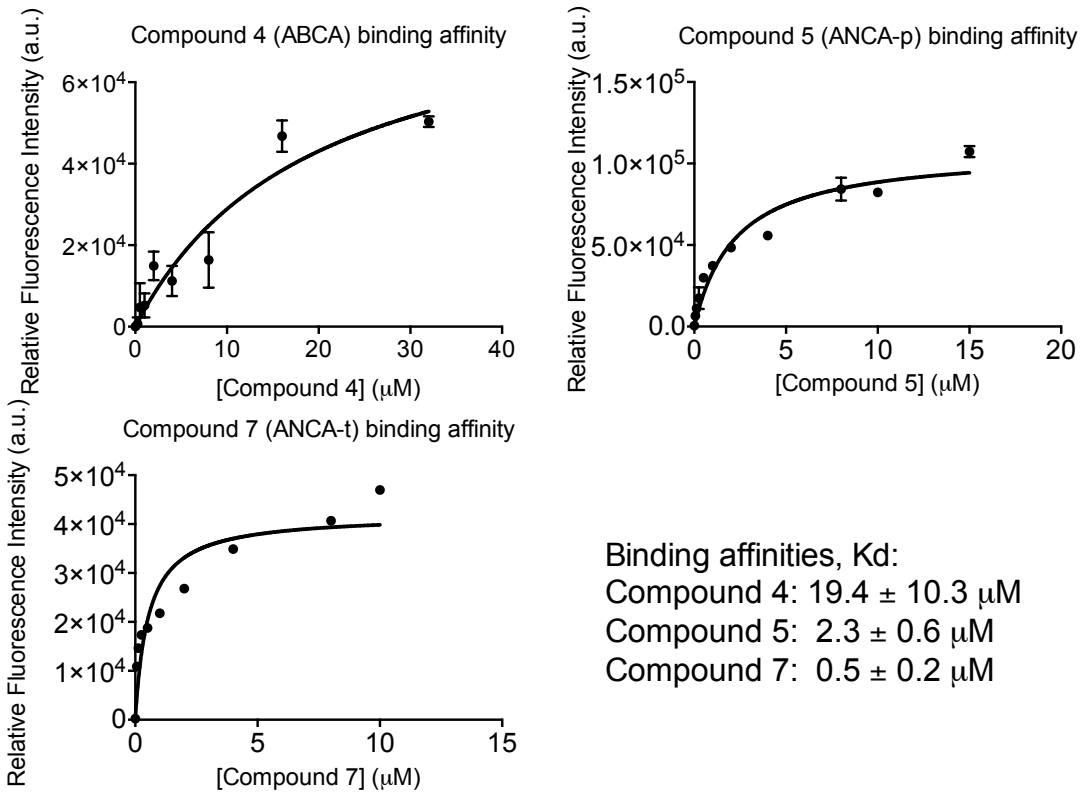

Figure 3.13 Binding constants, K_d, for compounds **4**, **5**, and **7** in the presence of aggregated Aβ(1-42) fibrils.

Comparison of the raw fluorescence intensities, and their relative fold increase of fluorescence enhancement upon binding, show that compounds **1** and **5** have the largest fluorescence yield upon binding amyloid aggregates, with a 2.4 and 3.6 fold increase of intensity over unbound probe, respectively. Interestingly, while the heterocyclic conjugates all show >3 fold increase of fluorescence enhancement upon binding, they are all less bright than parent compound **1** (Figure 3.14). As a result, compound **1** with the inherently higher fluorescence would be better suited for translational approaches towards detecting amyloid over background tissue *in vivo*..

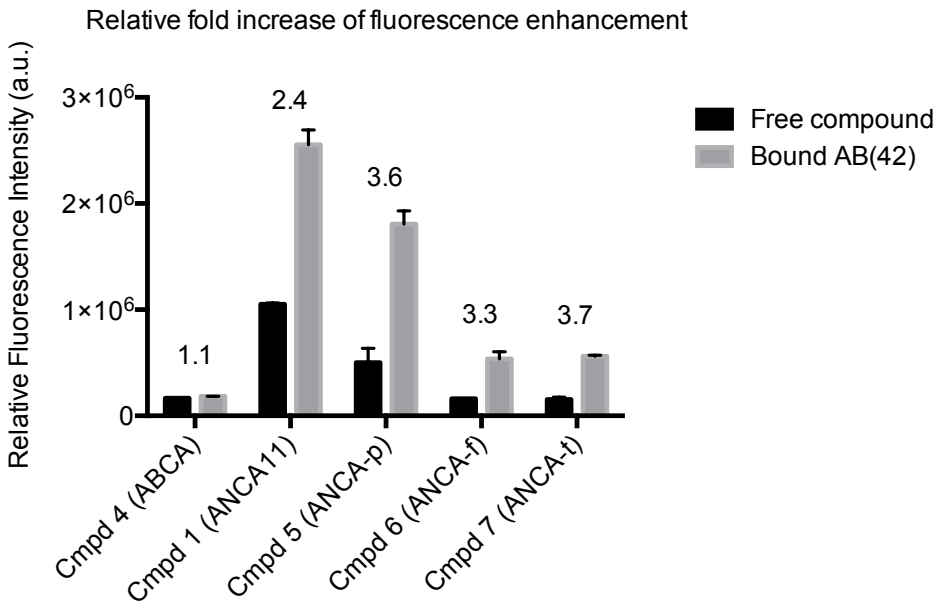

Figure 3.14 Fluorescence enhancement and yield of compounds **4**, **1**, **5** - **7** when bound to Aβ(1-42) fibrils in solution. Values above bars indicate the fold increase over free probe.

In order to resolve amyloids that are close in binding pocket permittivity, I generated a three-dimensional correlation plot where the fluorescence emission maxima of Aβ in tissue deposits, PrP^{Sc} in tissue deposits, cell-free insulin, and cell-free α-synuclein fibrils bound to compound **1** were plotted against their respective emission values when bound to compounds **4** and **7** (Figure 3.15). Compound **4** was chosen because it had fluorescence emission, albeit weak, in the 500 nm range, relatively far removed from the emission of compound **1**. Compound **7** was chosen as the third metric because it had the most red-shifted fluorescence emission values.

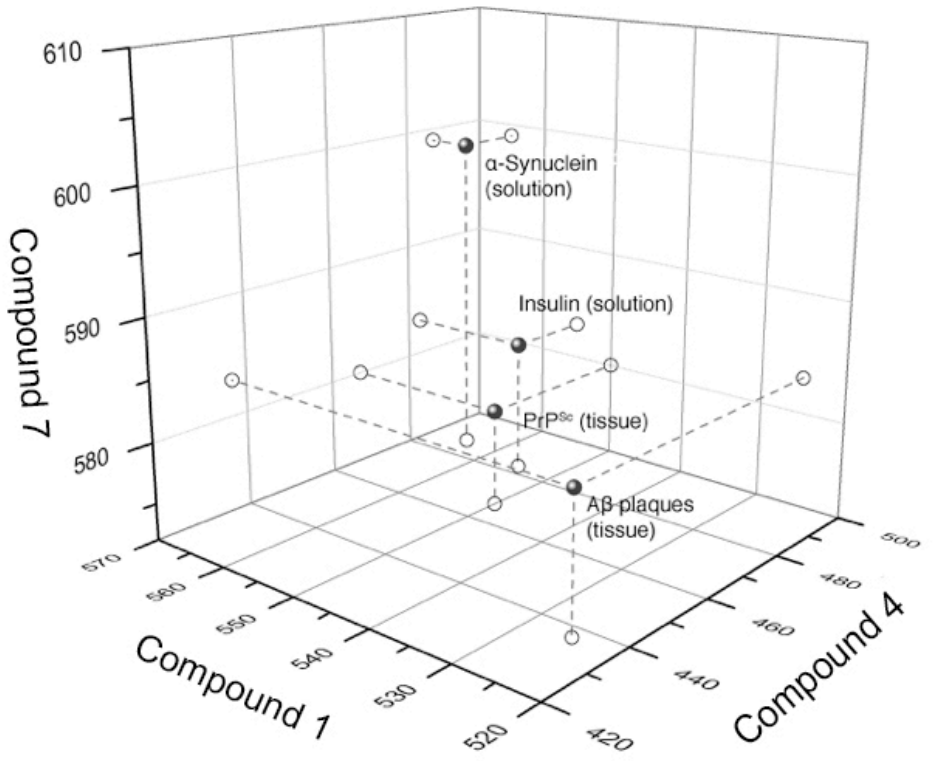

Figure 3.15 3-dimensional fingerprinting of amyloid aggregates bound with ANCA compounds **4**, **1**, and **7**.

As Figure 3.15 suggests, population of this three-dimensional space with additional amyloids would provide insight into the binding pocket permittivities of the different amyloid species. I have begun initial work into mapping these emission (or permittivity) values to their respective peptide sequences, with the aim of correlating the protein identity based on emission to disease states using this three-dimensional space.

3.3 Conclusions

I ultimately discovered that our parent compound **1** maintained the best quantitative discrimination capabilities, with the short compound **4** and the naphthalene-pyrrole conjugate, compound **5**, having comparable properties. In amyloid fibril binding experiments, compound **1** exhibited the highest relative fluorescence intensity with an approximately 2.5 fold increase in fluorescence enhancement. However, due to the emission wavelengths of compound **1** in the 500-550nm range, compound **5** would be best suited for biological and histological applications as it falls closer to the biologically silent region of the visible spectrum.

Computational modeling, along with experimental solvatochromism data suggest that the torsional strain of compound **5** due to the *N*-methyl group of the pyrrole causes it to achieve a TICT-like charge separated excited state, which becomes more sensitive to the environment, over the more planar excited states of compound **6** and **7**. Finally, the compounds showed low micromolar to nanomolar binding affinities towards amyloid aggregates, which I utilized to generate a three-dimensional correlation plot to further discriminate amyloid aggregates by their fluorescence emission values.

3.4 Appendix: Additional Experiments

3.4.1 Application of ANCA fluorophores in histopathology

The primary experiments conducted for Chapter 3 involved the design and preliminary evaluation of the compounds with the well-known amyloid-forming proteins, β-amyloid, prions, α-synuclein, and insulin. However, recent work around the world has uncovered many new amyloidogenic proteins in a wide range of species.[12,124–126] In collaboration with Patricia Gaffney and Peter Kolbaka from the Sigurdson lab, I stained a wide range of amyloidogenic tissue from human and various animal sources. We aimed this exploratory research towards determining the applicability of the compounds for use as general histological stains in the clinical setting.

I first wanted to examine the translatability of the compounds into a clinical setting. Compounds **1** and **7** were chosen as staining candidates due their fluorescence emission profiles being suitable for traditional microscopy filter sets (green and red, respectively). Adjacent transgenic AD mice cortical and hippocampal tissue and frontal cortex tissue from a human AD patient (Figure 3.16) were stained with compounds **1** and **7**. Consistent with mice plaque deposits, the human deposits were found to have similar fluorescence emission profiles, with compound **1** having a maximum emission of 526 ± 6 nm, and compound **7** having a maximum emission at 579 ± 6 nm over an average of 6 plaques samples.

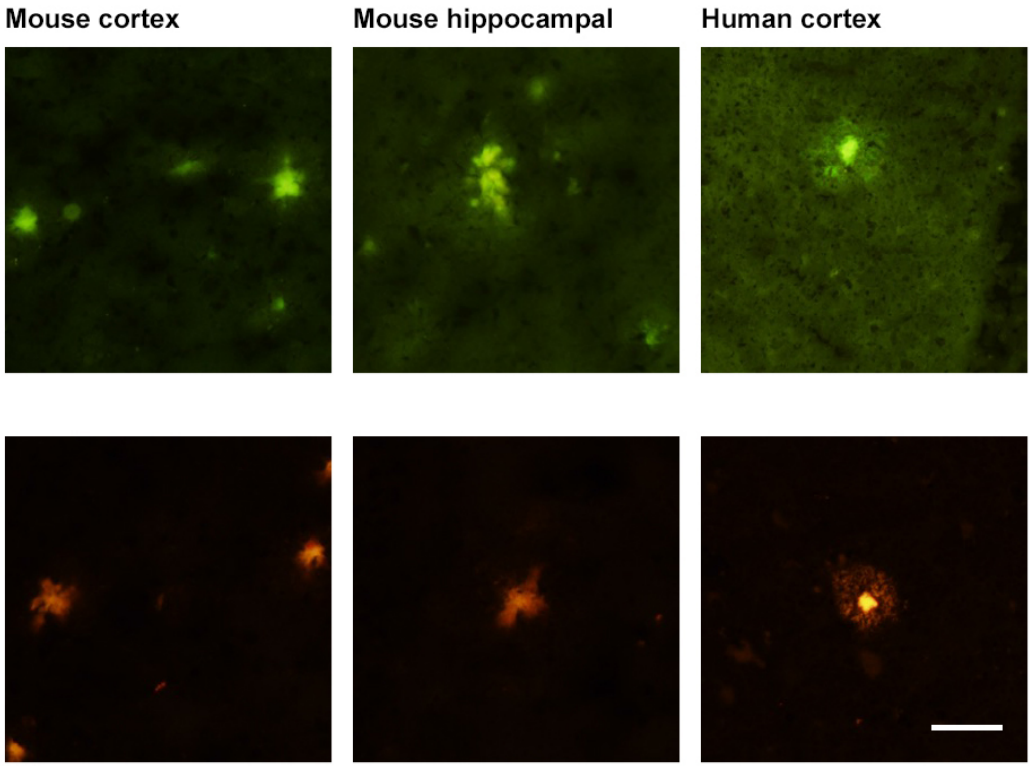

Figure 3.16 Mouse and human neuronal tissue stained with compounds **1** and **7**. Scale = 50 microns.

Additionally, we imaged the amyloidosis present in a case of hepatic amyloidosis from a duck as a model system for systemic amyloidosis detection (Figure 3.17). Here we discovered that while the fluorescence signal from compound **1** matched that of human and mouse β-amyloid (538 ± 3 nm), the compound **7** signal (603 ± 2 nm) was approximately 20 nm more red-shifted than when bound to β-amyloid. Taken together these initial results suggested again the use of a set of fluorophores to appropriately distinguish amyloid species that show similar binding pocket fluorescence emission wavelengths.

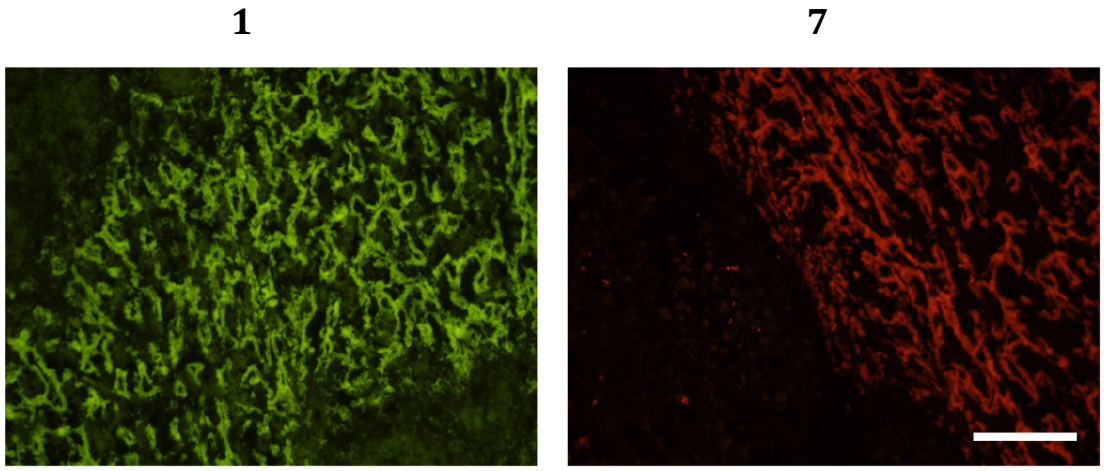

Figure 3.17 Hepatic amyloidosis of a duck model stained with compounds **1** and **7**. Scale bars = 100 microns

3.5 Materials and Methods

General Techniques

Unless indicated, all commercially available reagents and anhydrous solvents were purchased at the highest commercial quality and were used as received without further purification. All non-aqueous reactions were carried out under argon atmosphere using dry glassware that had been flame-dried under a stream of argon unless otherwise noted. Anhydrous tetrahydrofuran (THF) and dichloromethane (CH_2Cl_2) were obtained by passing commercially available pre-dried, oxygen-free formulations through activated alumina columns. Flash column chromatography was performed on silica gel (Merck Kieselgel 60, 230-400 mesh) using Hexanes-EtOAc or EtOAc-MeOH or toluene-acetone or diethyl ether mixtures of increasing polarity. The progress of all the reactions was monitored by thin-layer chromatography (TLC) using glass plates precoated with silica gel-60 F254 to a thickness of 0.5 mm (Merck), and compounds were visualized by irradiation with UV light and/or by treatment with a solution of CAM stain or potassium permanganate ($KMnO_4$) in water stain followed by heating. ^{13}C NMR and ^{1}H NMR spectra were recorded on either 400 MHz or 500 MHz Varian instrument or 500 MHz JEOL instrument. $CDCl_3$ was treated with anhydrous K_2CO_3, chemical shifts (δ) are quoted in parts per million (ppm) referenced to the appropriate residual solvent peak reference ($CDCl_3$), with the abbreviations s, br s, d, t, q, m, td, dt and qd denoting singlet, broad singlet, doublet, triplet, quartet, multiplet, quartet of doublets, triplet of doublets, doublet of triplets and quartet of doublets respectively. J = coupling constants given in Hertz (Hz). High-resolution Mass spectra (HRMS) were recorded on a trisector WG AutoSpecQ spectrometer.

Intermediate 2 was prepared as reported in Chapter 2.

(E)-2-(2-(2-methoxyethoxy)ethoxy)ethyl 2-cyano-3-(4-(piperidin-1-yl)phenyl) acrylate (Compound 4, ABCA)

Commercially available 4-piperidinyl benzaldehyde (S6) (0.05 g, 0.255 mmol) was dissolved in THF (2.0 mL) under nitrogen. 2(2-(2-methoxyethoxy)ethoxy)ethyl-2-cyanoacrylate (S5) (0.216 mmol) and 1,8-Diazabicyclo[5.4.0]undec-7-ene (DBU) (0.02 mmol) were then added and the mixture left stirring at 30 C. The reaction was monitored by TLC and was completed in 6 hrs. The crude solution was concentrated under reduced pressure and the product purified with flash chromatography (1:1 Hexanes/ethyl acetate) to give an orange solid (90%). R_f =0.70 (1:1 Hexanes/Ethyl acetate);

^{1}H NMR (500 MHz, $CDCl_3$) δ 8.06 (s, 1H), 7.91-7.93 (d, J = 9.0 Hz, 2H), 6.84-6.86 (d, J = 9.5 Hz, 2H), 4.41-4.43 (m, 2H), 3.80-3.82 (m, 2H), 3.72-3.74 (m, 2H), 3.67-3.69 (m, 4H), 3.54-3.56 (m, 2H), 3.45-3.46 (m, 4H), 3.37 (s, 3H), 1.67-1.68 (m, 6H); ^{13}C NMR (125 MHz, $CDCl_3$) δ 164.3, 154.6, 154.2, 134.4, 120.2, 117.4, 113.4, 94.4, 72.1, 71.0, 70.8, 70.7, 69.1, 65.2, 59.2, 48.3, 25.5, 24.5; HRMS calcd. for $C_{14}H_{22}O_6SNa$ $[M+Na]^+$ 341.1029, found 341.1030 by ESI.

6-(piperidin-1-yl)naphthalen-2-yl trifluoromethanesulfonate (S10)

To a microwave vial containing degassed toluene (6.7 mL), commercially available 6-bromonaphthalen-2-yl trifluoromethanesulfonate (S9) (0.25 g, 0.704 mmol), $Pd(OAc)_2$ (0.008 g, 0.0352 mmol), and NaOtBu (0.088 g, 0.915 mmol) was added and allowed to stir for 5 minutes under argon at room temperature followed by addition of $P(t\text{-}Bu)_3$

(0.0704 mmol) via syringe and continued stirring for an additional 30 minutes. Piperidine (0.845 mmol) dissolved in toluene (0.845 mL) was added dropwise via syringe and the vial was sealed and heated to 110 C for 12 hours. The reaction was then allowed to cool to room temperature and diluted with CH_2Cl_2 (5 mL), filtered through a pad of celite, and concentrated. The crude material was then adsorbed on to silica and chromatographed (0-20% EtOAc/hexanes) to give S10as a white solid (0.152 mg, 60%). R_f = 0.59 (10 % EtOAc/hexanes)

^{1}H NMR (400 MHz, $CDCl_3$) δ 7.69-7.72 (d, J = 12.0 Hz, 2H), 7.59 (m, 1H), 7.35-7.38 (dd, J = 8.0 Hz, 4.0 Hz, 1H), 7.25-7.27 (m, 1H), 7.11 (bs, 1H), 3.29 (m, 4H), 1.73-1.79 110 (m, 4H), 1.62-1.67 (m, 2H); ^{13}C NMR (100 MHz, $CDCl_3$) δ 151.0, 145.2, 134.1, 128.7, 127.6, 121.5, 120.5, 119.8, 118.9, 117.4, 109.7, 50.6, 25.8, 24.4; HRMS calcd. For $C_{16}H_{17}F_3NO_3S$ $[M + H]^+$ 360.0876, found 360.0876 by ESI.

5-(6-(piperidin-1-yl)naphthalen-2-yl)thiophene-2-carbaldehyde (S15)

To a solution of 6-(piperidin-1-yl)naphthalen-2-yl trifluoromethanesulfonate S10(0.01 g, 0.028 mmol) and (5-formylthiophen-2-yl)boronic acid (S12) (0.042 mmol) in a mixture of THF (0.06 mL) and water (0.025 mL) was added K_2CO_3 (0.0476 mmol) and $Pd(PPh_3)_4$ (0.0042 mmol). The solution was then degassed with argon and microwaved at 50 C for 1 hour. The reaction was then filtered through cotton and concentrated. The crude mixture was adsorbed on to silica and chromatographed (0-10% EtOAc/hexanes) to give S15 (5.9 mg, 66%) as a yellow powder. R_f = 0.44 (20 % EtOAc/hexanes)

^{1}H NMR (500 MHz, $CDCl_3$) δ 9.89 (s, 1H), 8.01 (s, 1H), 7.73-7.76 (m, 2H), 7.66-7.70 (m, 2H), 7.46 (d, J = 5.0 Hz, 1H), 7.32 (d, J = 10.0 Hz, 1H), 7.09 (bs, 1H), 3.31-3.33

(m, 4H), 1.76 (m, 4H), 1.65-1.67 (m, 2H); ^{13}C NMR (125 MHz, $CDCl_3$) δ 182.8, 155.4, 150.9, 141.7, 137.8, 135.3, 129.3, 127.8, 127.6, 127.5, 125.4, 124.4, 123.5, 120.6, 109.6, 50.4, 29.8, 25.8, 24.4; HRMS calcd. for $C_{20}H_{19}NOS$ $[M+H]^+$ 322.1260, found 322.1257 by ESI.

5-(6-(piperidin-1-yl)naphthalen-2-yl)furan-2-carbaldehyde (S14)

6-(piperidin-1-yl)naphthalen-2-yl trifluoromethanesulfonate (S10) (50.0 mg, 0.139 mmol), (5-formylfuran-2-yl)boronic acid (S11) (44.0 mg, 0.209 mmol), K_2CO_3 (33.0 mg, 0.236 mmol), and $Pd(PPh_3)_4$ (24.0 mg, 0.0209 mmol) was dissolved in a mixture of THF (0.3 mL) and water (0.13 mL) in a microwave vial equipped with a stir bar and capped with a septa. The reaction mixture was degassed with argon, sealed, and microwaved for 1 hour at 50 C. The reaction mixture was then dried with anhydrous Na_2SO_4, condensed in vacuo and purified by silica flash chromatography (0-10% EtOAc/hexanes) to give S14 38.4nmg, 91%) as a yellow solid. R_f = 0.25 (20 % EtOAc/hexanes)

^{1}H NMR (400 MHz, $CDCl_3$) δ 9.63 (s, 1H), 8.21 (s, 1H), 7.67-7.76 (m, 3H), 7.26-7.34 (m, 2H), 7.08 (d, J = 2.0 Hz, 1H), 6.85 (d, J = 3.6 Hz, 1H), 3.31 (m, 4H), 1.64-1.77 (m, 6H); ^{13}C NMR (100 MHz, $CDCl_3$) δ 177.0, 160.5, 151.8, 151.0, 135.5, 129.5, 127.6, 127.4, 123.0, 120.4, 109.6, 107.2, 50.4, 25.8, 24.5; HRMS calcd. for $C_{20}H_{20}NO_2$ $[M+H]^+$ 306.1489, found 306.1491 by ESI.

1-methyl-5-(trimethylstannyl)-1H-pyrrole-2-carbaldehyde (S8)

To a solution of N-methyl piperazine (S7) (0.535 g, 5.038 mmol) and TMEDA (1.17 g, 10.076 mmol) in hexanes (10 mL) was added n-BuLi (3.4 mL, 5.038 mmol) at -40 C and allowed to stir for 30 minutes. Then 1-methylpyrrole carbaldehyde (0.5g, 4.58

mmol) was added dropwise at -40 C and reaction continued to stir for an additional 45 minutes. A second portion of n-BuLi (6.3 mL, 10.076 mmol) was added dropwise at -40 C and the reaction was allowed to stir for 1 hour. Trimethyltin chloride solution (1.0M, 10.076 mmol) was added dropwise and the reaction was allowed to come to room temperature and stir overnight. The reaction was then quenched with water, extracted with diethyl ether (3 x 10 mL), dried with anhydrous $MgSO_4$, and concentrated in vacuo to give S8 (442 mg, 35%) as a clear, pale yellow oil which was used without further purification. R_f = 0.71 (20 % EtOAc/hexanes)

^{1}H NMR (500 MHz, $CDCl_3$) δ 9.53 (s, 1H), 6.93 (d, J = 4.0 Hz, 1H), 6.29 (d, J = 4.0 Hz, 1H), 3.99 (s, 3H), 0.38 (s, 9H); ^{13}C NMR (125 MHz, $CDCl_3$) δ 178.5, 148.1, 135.5, 124.4, 119.1, 37.5, 18.8; HRMS calcd. For $C_9H_{16}NOSn$ $[M+H]^+$ 274.0250, found 274.0247 by ESI.

1-methyl-5-(6-(piperidin-1-yl)naphthalen-2-yl)-1H-pyrrole-2-carbaldehyde (S13)

To a solution of S8 (0.05 g, 0.184 mmol) and S10 (0.0794 g, 0.221 mmol) in degassed DMF (0.2 mL) under argon was added $PdCl_2(PPh_3)_2$ (0.0092 mmol) and the reaction was heated to 60 C and allowed to stir for 30 minutes. The reaction was then cooled to room temperature and diluted with water (0.2 mL) and diethyl ether (0.2 mL) and filtered through a pad of celite. The reaction mixture was the extracted with diethyl ether (3 x 1 mL) and combined organic layers were washed with brine (1 x 2 mL), dried with anhydrous $MgSO_4$, and concentrated. The residue was adsorbed on to silica and purified by flash column chromatography (0-5% EtOAc/hexanes) to give S13 (42 mg, 72%) as a light yellow powder. R_f = 0.46 (20 % EtOAc/hexanes)

^{1}H NMR (400 MHz, $CDCl_3$) δ 9.58 (s, 1H), 7.73-7.75 (m, 3H), 7.41-7.43 (dd, J = 8.4

Hz, 2.0 Hz, 1H), 7.32- 7.35 (dd, J = 9.2 Hz, 2.4 Hz, 1H), 7.14 (d, J = 2.0 Hz, 1H), 7.00 (d, J = 4.4 Hz, 1H), 3.99 (s, 3H), 3.29-3.32 (m, 4H), 1.74-1.80 (m, 4H), 1.64-1.66 (m, 2H); ^{13}C NMR (100 MHz, $CDCl_3$) δ 179.5, 150.8, 145.1, 134.6, 133.0, 129.0, 128.3, 127.7, 127.0, 126.9, 125.4, 124.8, 120.7, 110.9, 109.8, 50.7, 34.7, 25.9, 24.5; HRMS calcd. for $C_{21}H_{23}N_2O$ $[M+H]^+$ 319.1805, found 319.1809 by ESI.

(E)-2-(2-(2-methoxyethoxy)ethoxy)ethyl-2-cyano-3-(5-(6-(piperidin-1-yl)naphthalen-2-yl)thiophen-2-yl)acrylate (Compound 7, ANCA-t)

Compound S15 (0.05 g, 0.156 mmol) and S5 (0.125 mmol) were dissolved in THF (0.62 mL) under an argon atmosphere. DBU (0.0078 mmol) was added and the reaction was allowed to stir at room temperature for 5 minutes during which the reaction developed a dark red color. The reaction was then concentrated, adsorbed on to silica, and chromatographed (0-5% acetone/toluene) to give Compound 7, ANCA-t (48.0 mg, 71%) as a red viscous oil. R_f = 0.38 (70 % EtOAc/hexanes)

^{1}H NMR (500 MHz, $CDCl_3$) δ 8.31 (s, 1H), 8.05 (bs, 1H), 7.75 (d, J = 5.0 Hz, 2H), 7.69 (bs, 2H), 7.47 (d, J = 5.0 Hz), 7.33 (bs, 1H), 7.08 (bs, 1H), 4.45-4.47 (m, 2H), 3.82 (m, 2H), 3.72-3.74 (m, 2H), 3.67-3.69 (m, 4H), 3.56 (m, 2H), 3.38 (s, 3H), 3.33 (m, 4H), 1.65-1.76 (m, 6H); ^{13}C NMR (125 MHz, $CDCl_3$) δ 174.1, 163.1, 156.1, 150.8, 146.9, 139.9, 134.2, 129.3, 127.7, 127.5, 127.0, 125.6, 124.2, 123.7, 120.4, 116.2, 109.6, 96.7, 77.1, 72.0, 70.9, 70.7, 70.6, 68.9, 65.4, 59.1, 50.3, 29.8, 25.7, 24.4; HRMS calcd. For $C_{30}H_{34}N_2O_5SNa$ $[M+Na]^+$ 557.2081, found 557.2079 by ESI

(E)-2-(2-(2-methoxyethoxy)ethoxy)ethyl 2-cyano-3-(5-(6-(piperidin-1-yl)naphthalen-2-yl)furan-2-yl)acrylate (Compound 6, ANCA-f)

S14 (0.017 g, 0.0557 mmol) and S5 (0.0121g, 0.0524 mmol) were dissolved in THF

(0.25 mL) under argon atmosphere. DBU (0.000557 mmol) was added via syringe and the reaction was allowed to stir at room temperature for 5 minutes. The reaction was then concentrated, adsorbed on to silica, and purified via flash chromatography (10-90% EtOAc/hexanes) to give Compound 6, ANCA-f (23.3 mg, 86%) as a red viscous oil. R_f = 0.3 (60 % EtOAc/hexanes)

^{1}H NMR (400 MHz, $CDCl_3$) δ 8.24 (s, 1H), 7.97 (s, 1H), 7.93 (m, 2H), 7.69-7.71 (m, 1H), 7.33 (m, 2H), 7.10 (bs, 1H), 6.94 (d, J = 4.0 Hz, 1H), 4.46 (m, 2H), 3.82-3.84 (m, 2H), 3.73-3.76 (m, 2H), 3.66-3.69 (m, 4H), 3.55-3.58 (m, 2H), 3.38 (s, 3H), 3.32-3.35 (m, 4H), 1.77 (m, 4H), 1.65 (m, 2H); ^{13}C NMR (100 MHz, $CDCl_3$) δ 163.5, 161.2, 151.0, 147.7, 138.2, 135.6, 129.9, 127.6, 125.9, 125.2, 123.0, 120.2, 116.3, 109.6, 108.9, 72.1, 71.0, 70.8, 70.7, 69.0, 65.5, 59.2, 59.2, 50.4, 29.8, 25.7, 24.4; HRMS calcd. for $C_{30}H_{34}N_2O_6Na$ $[M+Na]^+$ 541.2309, found 541.2310 by ESI.

(E)-2-(2-(2-methoxyethoxy)ethoxy)ethyl 2-cyano-3-(1-methyl-5-(6-(piperidin-1-yl)naphthalen-2-yl)-1H-pyrrol-2-yl)acrylate (Compound 5, ANCA-p)

To a solution of S13 (0.02 g, 0.063 mmol) and S5 (0.0116 g, 0.05 mmol) in THF (0.25 mL) under argon was added DBU (0.001 mmol) and the reaction was allowed to stir at room temperature for 10 minutes. The reaction was then concentrated in vacuo, adsorbed on to silica, and purified by flash chromatography (5-80% EtOAc/hexanes) to give Compound 5, ANCA-p (24.5 mg, 92%) as an orange viscous oil. R_f = 0.38 (80 % EtOAc/hexanes)

^{1}H NMR (500 MHz, $CDCl_3$) δ 8.16 (s, 1H), 7.87 (d, J = 4.0 Hz, 1H), 7.72-7.74 (m, 3H), 7.38-7.40 (dd, J = 8.5 Hz, 1.5 Hz, 1H), 7.33-7.35 (dd, J = 9.0 Hz, 2.0 Hz, 1H), 7.13 (bs, 1H), 6.55 (d, J = 4.5 Hz, 1H), 4.42-4.44 (m, 2H), 3.81-3.83 (m, 2H), 3.78 (s,

3H), 3.73-3.75 (m, 2H), 3.66-3.70 (m, 4H), 3.38 (s, 3H), 3.30-3.33 (m, 4H), 1.74-1.78 (m, 4H), 1.64-1.65 (m, 2H); ^{13}C NMR (125 MHz, $CDCl_3$) δ 164.7, 151.0, 145.2, 139.7, 134.7, 129.0, 128.4, 127.6, 127.2, 126.8, 125.2, 120.7, 120.6, 117.7, 114.0, 109.6, 91.1, 72.1, 71.0, 70.8, 70.7, 69.0, 65.2, 59.2, 50.6, 32.2, 29.8, 25.8, 24.4; HRMS calcd. for $C_{31}H_{37}N_3O_5Na$ $[M+Na]^+$ 554.2625, found 554.2626 by ESI

Brain tissue samples

Male and female transgenic mice overexpressing wild type mouse PrP (Tga20) were inoculated with the mouse-adapted prion strain mCWD and were euthanized upon developing terminal signs of prion disease. Transgenic mice (19959) harboring the Aβ plaques express the mutant human amyloid precursor protein 695 APP_{SweInd}, which bears both the Swedish (K670N/M671L) and the Indiana (V717F) mutations, under the control of the Syrian hamster prion protein promoter. Mice were euthanized between 9 - 13 months of age and their brains extracted into optical cutting temperature (OCT) fixation media. Frozen brain sections were cut from these frozen blocks.

5 micron frozen human brain samples (case ID 5573) from AD patients were generously provided by Peter Kobalka from the Sigurdson lab. Frozen duck liver samples were generously provided by Patricia Gaffney from the Sigurdson lab.

Staining frozen brain samples

Frozen tissue sections were dried for 1 hr, hydrated with 100%, 95%, and 70% ethanol for 5 min each, and then rinsed with deionized water. Sections were then buffered with phosphate-buffered saline (1X PBS) for 30 min. Compounds **4,1 5-7**

were diluted 1:50 in 1X PBS (from stock solutions of 3mM) to a final concentration of 60 μM, added to brain sections, incubated for 30 min at room temperature, washed three times with 1X PBS, and coverslipped using DAKO fluorescent mounting media.

Fluorescence microscopy

Brain tissue samples were excited with a 488 nm laser on an Olympus FluoView FV1000 spectral deconvolution confocal microscope with 5% power under 10x magnification. The emission spectra of compounds 1-5 bound to Aβ, PrP^{Sc}, and background were collected in 1 nm increments from 450-650 nm. A minimum of 10 measurements was collected for each compound bound to plaque and non-plaque regions as a background control. The wavelength corresponding to the maximum relative fluorescence intensity was taken as the emission λ_{max}.

Brightfield color imaging

Brain tissue sections were imaged under an Olympus MVX10 Macroview equipped with a MWB2 (Japan) long-pass filter and a 2x MVX (PF) Plan Apochromat lens with a 0.5 numerical aperture. Each sample was illuminated with epifluorescence and imaged with an exposure time of 0.2-0.8 sec, depending on sample.

Preparation of Aβ(1-42), α-synuclein, and insulin fibrils

Aggregated Aβ peptide was prepared by dissolving Aβ42 in 1xPBS pH 7.4 to a final concentration of 100 μM. This solution was magnetically stirred at 1200 rpm for 3 days at room temperature. Aggregation state was verified by Thioflavin-T activity.

Insulin fibrils were prepared in pH 1.6 1xPBS at 200 μM for 8 days with constant stir at 1200 rpm at 65 C, upon which the aggregates were transferred to a SnakeSkin pleated dialysis chamber with a 3500 molecular weight cutoff (Thermo

#68035). Dialysis was performed using pH 7.4 1xPBS for 48 hours, upon which the solution was transferred to a 37 C incubator at let aggregate without stir for 24 hours.

α-synuclein fibrils were prepared by dissolving α-synuclein monomers to a final concentration of 100 μM in pH 7.4 1xPBS and let sit without stir for 7 days at 37 C.

Fluorescence studies with aggregated amyloid fibrils

15 μL of the aggregated amyloid solution was added to 285 μL of the probe (5% DMSO in nanopure water) to attain a final concentration of 5 μM Aβ42 and 4 μM of the probe. The solution was transferred to a 300 μL cuvette and the fluorescence was measured at 22.5 °C. Excitation wavelength depended on the probe; compound 4 was excited at 420 nm, compounds 1,5-7 were excited at 450 nm.

Determination of K_d binding constants to Aβ42

As previously reported, in order to estimate the binding constant (K_d) for the probe-Aβ complexes from the fluorescence studies, we made the following assumptions:

1. All probes are completely in solution and free of any significant competing binding process such as self-aggregation.
2. The concentration of unbound probes can be approximated as close to the total concentration of the probes.
3. The binding sites in the aggregated Aβ peptides are not completely occupied at the concentration of Aβ binding probes used for the fluorescence studies (i.e., the experiments are carried out under non-saturated binding conditions).

Pre-aggregated Aβ(1-42) (5 μM final concentration) was mixed with various concentrations of probes 4, 1, 5-7 in 5% DMSO in nanopure water and their K_d's were determined by fitting data to a one-site specific binding algorithm: $Y = B_{max}*X/(K_d+X)$, where X is the concentration of the probe, Y is specific binding fluorescence intensity, and B_{max} corresponds to the apparent maximal observable fluorescence upon binding of probes to aggregated Aβ42 peptide.

Solvent studies of probes

Each probe was dissolved in freshly distilled anhydrous acetonitrile (ACN), acetone, dichloromethane (DCM), tetrahydrofuran (THF), diethyl ether (Et_2O), anisole, and toluene to a final concentration of 1.5 μM. Excitation and fluorescence emission spectra of each solution were obtained on a PTI spectrofluorimeter in 1 nm increments from 350-520 nm and 400-650 nm, respectively. The wavelength corresponding to the maximum intensity was taken as λ_{max}. For absorption studies, compound solutions in dry solvents were prepared at 5 μM, Absorption spectra were obtained from a NanoDrop using a clear quartz cuvette.

3.6 Additional Figures & Tables

Table 3.4 Solvent parameters and the absorption and emission maxima for compounds **4** and **1** in select solvents.

			Absorption wavelenght (nm)		Emission wavelength (nm)	
Solvent	Dieletric constant	Refractive Index	Compound 4	Compound 1	Compound 4	Compound 1
Toluene	2.379	1.4941	419 ± 1	427 ± 1	463 ± 2	521 ± 2
Et_2O	4.266	1.3526	409 ± 1	421 ± 1	462 ± 1	523 ± 1
Anisole	4.30	1.5174	426 ± 1	439 ± 1	473 ± 1	548 ± 1
THF	7.42	1.4050	420 ± 1	431 ± 1	475 ± 3	550 ± 2
DCM	8.93	1.4242	426 ± 1	440 ± 1	484 ± 3	564 ± 2
Acetone	21.01	1.3588	421 ± 1	434 ± 1	488 ± 6	580 ± 1
Acetonitrile	36.64	1.3442	423 ± 1	436 ± 1	492 ± 3	596 ± 3

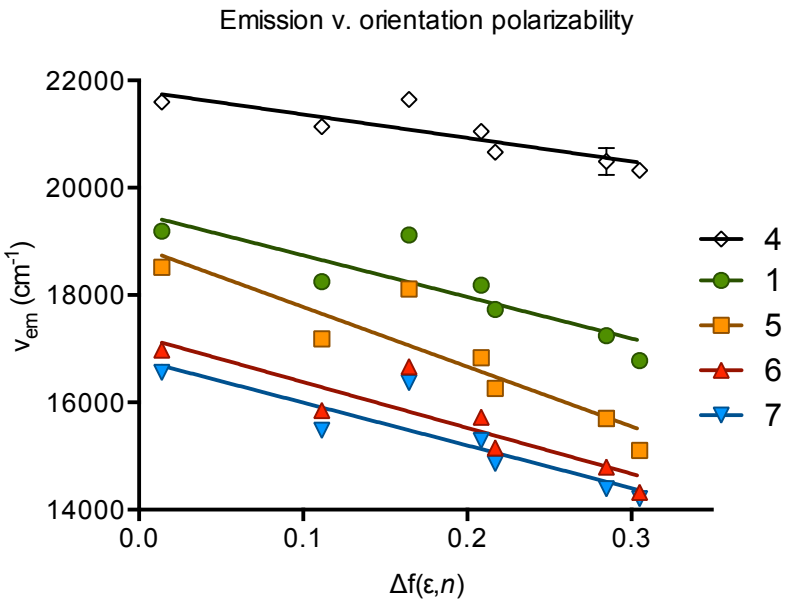

Figure 3.18 Emission wavenumbers for compounds **4**, **1**, **5** - **7** as a function of the orientation polarizability.

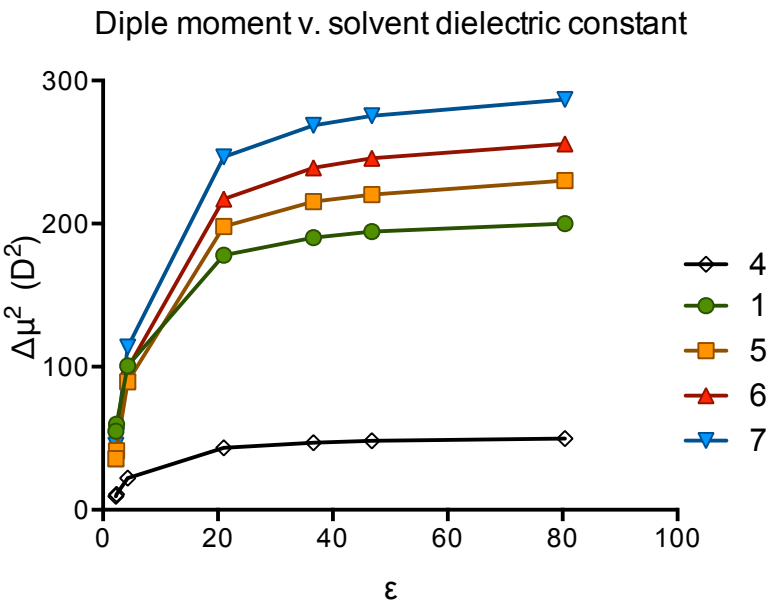

Figure 3.19 Dipole moments from *ab initio* calculations of compounds **4**, **1**, **5** - **7** in vacuum, anisole, acetone, acetonitrile, DMSO, and water

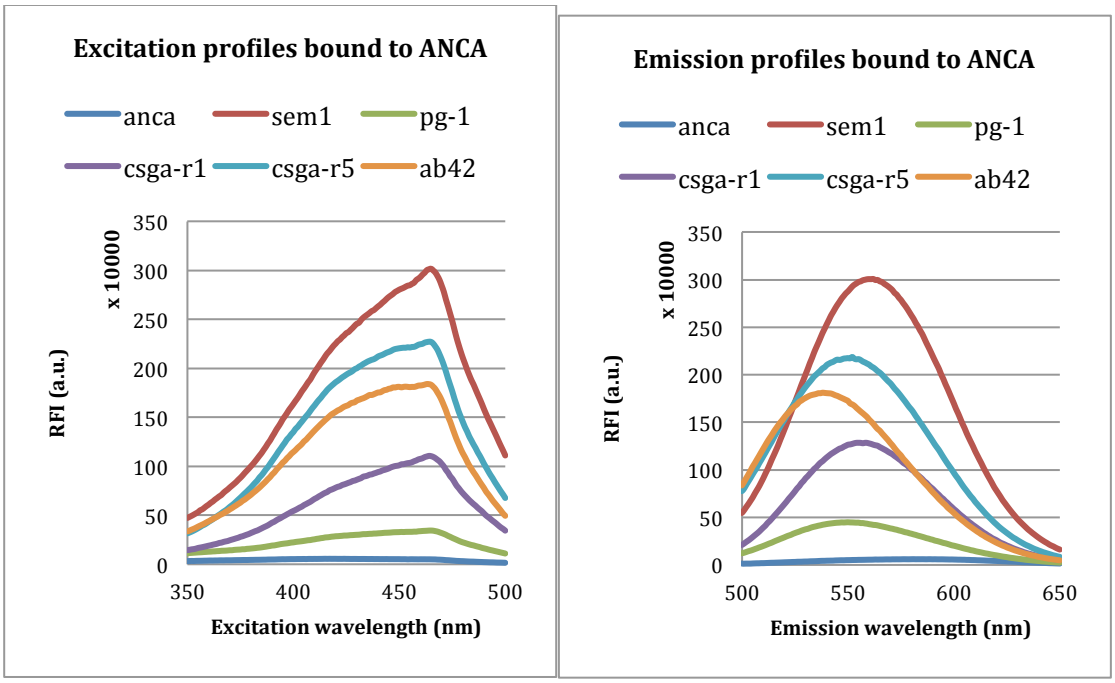

Figure 3.20 Emission spectra of various amyloids bound with ANCA11 collected at 450nm excitation, excitation spectra collected at 550nm emission

Table 3.5 Summary of amyloid aggregates bound to ANCA11 and their corresponding dielectric constants based on emission wavelength only (not stokes shift)

	Emission (nm)	**Excitation (nm)**	**Stokes shift (nm)**	**Binding pocket permittivity using only emission wavelength**
ANCA11	583	419	165	-
SEM1	561	465	97	10.2
PG-1	550	464	85	6.9
CsgA-R1	557	464	93	8.8
CsgA-R5	551	464	87	7.2
Aβ(1-42)	538	463	75	5.1
PAP	544	462	81	5.9
Insulin	555	463	92	8.2
SEVI	554	461	93	7.8

Acknowledgements

Chapter 3 is based on material currently being prepared for submission for publication “Rational Design of Amyloid-Discriminating Fluorophores”. Cao, Kevin J.; Elbel, Kristyna M.; Cirera, Jordi; Sigurdson, Christina J.; Paesani, Francesco; Theodorakis, Emmanuel A.; Yang, Jerry; *In preparation.* I am the primary author on this publication.

Chapter 4

Detection of Amyloidosis in the Retina

4.1 Introduction

The accumulation of amyloid aggregates is a hallmark of many neurodegenerative diseases. In Alzheimer's Disease (AD), the gradual production of improperly cleaved β-amyloid leads to extracellular deposits termed senile plaques.[4,11,86] Prion diseases, in contrast, show a rich variety of morphological features in tissue but in general also exhibit large amorphous deposits with Congophilia (CR) birefringence and Thioflavin-T (ThT) fluorescence activity.[127] In the clinical setting, the diagnosis of these neurodegenerative diseases has predominately relied on the use of neuropsychological evaluations based on behavioral cues and memory tests.[128,129] Absolute verification of the diseases comes from post-mortem histology of the afflicted tissue regions, where clinicians rely on the identification of the

aforementioned aggregates using antibodies and small amyloid-binding molecules such as CR and ThT.

4.1.1 Amyloidosis and the retina

Studies of the eyes of AD and prion patients have suggested the possible presence of accumulated amyloid and prion protein aggregates in the retinal cell layers.[48,67,72] The hypothesis of neurodegeneration in the retina originates from the common origin of the central nervous system and retina. During development, the ectoderm germ layer matures into the neural plate, which then folds into the neural tube containing the neuroepithelium.[130] These architectures ultimately differentiate into the central nervous system and retina (Figure 4.1)

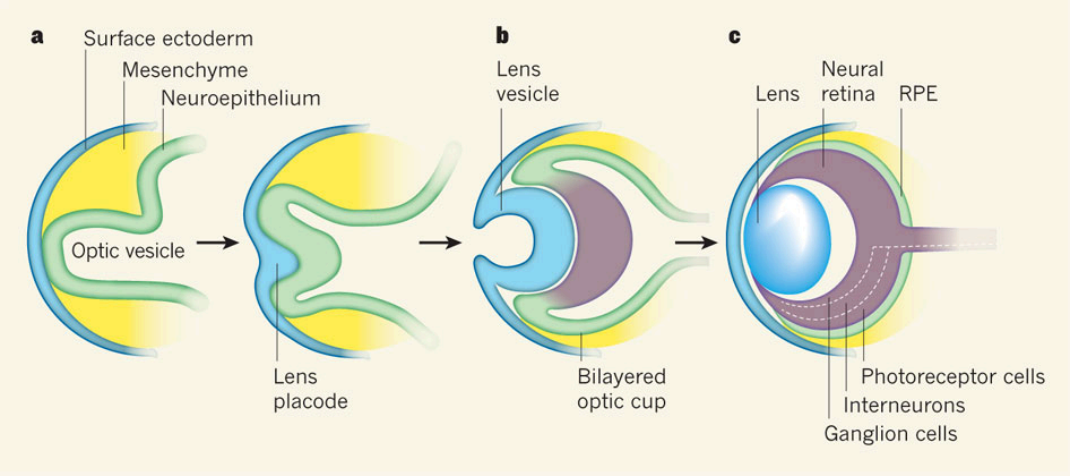

Figure 4.1 The development of the retina. The neuroepithelium originates from the same ectoderm germ layer as the central nervous system. Adapted with permission from Nature Publishing Group, Nature. *Regenerative medicine: DIY eye*, 472, 42-43. Figure 1, copyright 2011.

The mature retina consists of seven unique cell layers, each with a particular function in establishing vision (Figure 4.2).[131] As in the central nervous system, the

retinal layers are highly networked with one another and undergo complex cross-talk between adjacent neurons in the same layer in order to generate the ability to see contrast and other visual phenomenon.

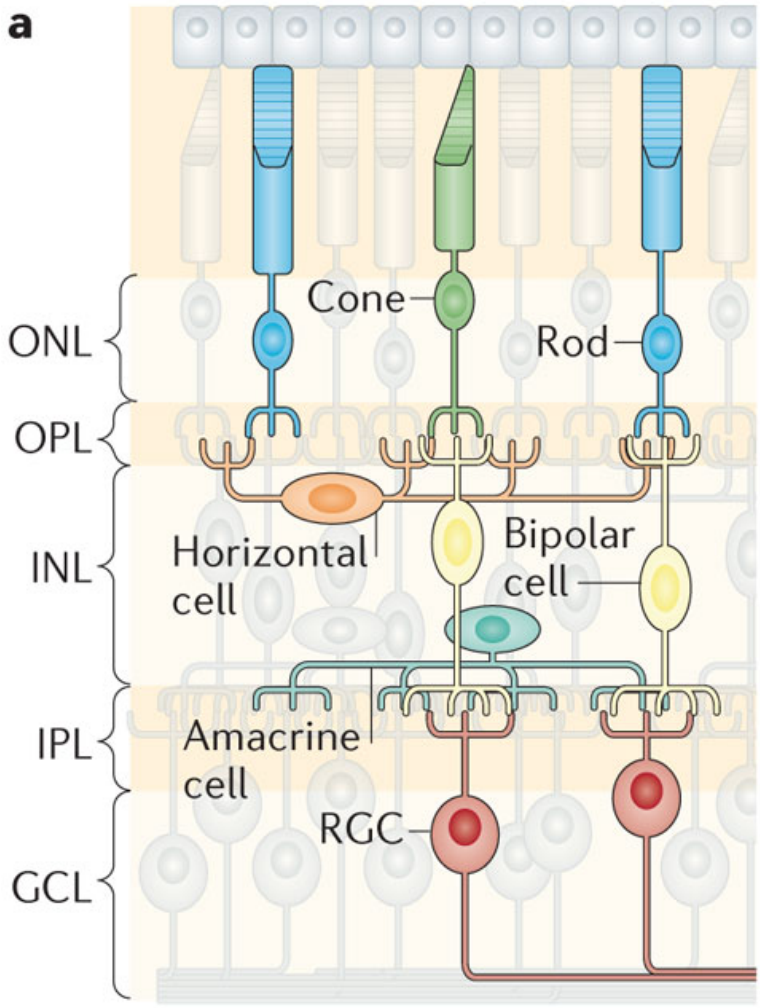

Figure 4.2 Retinal layers of the mammalian eye. ONL = outer nuclear layer, OPL = outer plexiform layer, INL = inner nuclear layer, IPL = inner plexiform layer, GCL = granule cell layer, RGC = retinal ganglia cell. Adaption with permission from Nature Publishing Group, Nature Reviews Neuroscience. *Intrinsically different retinal progenitor cells produce specific types of progeny*, 15, 615-627. Figure 1, copyright 2014.

In recent years, there have been conflicting reports of the appearance of β-amyloid aggregates in these layers, with the supporting evidence suggesting that

deposition occurs typically in the outer and inner plexiform (synaptic) layers. However, a lack of consistency in the approach to the histology between the groups has resulted in an unclear set of conclusions.[132,133] In particular, a 2011 study led by Koronyo-Hamaoui showed the presence of amyloid deposits in retinal flat-mounted frozen tissue of AD patients upon staining with curcumin or antibodies. This antibody staining suggested the presence of β-amyloid aggregates; other groups using formalin-fixed retinal cross-sections, however, were unable to detect amyloidosis by histological and biochemical means.[48,132]

In contrast, cells in the retinal pigment epithelium (RPE) layer behind the retina have been shown to produce the amyloid precursor protein (APP) as well as the β-amyloid cleavage products. In age-related macular degeneration (AMD), a common pathological manifestation indicative of the disease is the formation of drusen deposits in the RPE. Recent work by the Ohno-Matsui and Johnson labs has shown that drusen contains Aβ aggregates, though the mechanism and conformation characteristics remain unclear.[134,135]

In prion diseases such as Creutzfeldt-Jakob Disease (CJD), it was recently reported the appearance of protease resistant PrP^{Sc} in the plexiform layers of the retina of a sporadic CJD (sCJD) by Western blot and immunohistochemistry analyses.[136] Additionally, in variant CJD (vCJD), PrP^{Sc} was detected in the retina at approximately 25% of the concentration found in the brain.[73,137] Scrapies-infected tg7 mice also exhibited deposition of prion aggregates in both the plexiform and nuclear layers.[138] Interestingly, curcumin was also shown to bind prion plaques from brain samples of patients with vCJD.[127]

Compound **1** (ANCA11) was recently reported to be useful as a fluorescent diagnostic tracer for the detection of β-amyloid aggregates in the lens of living AD patients.[70,139] Cognoptix, Inc. licensed ANCA11 and the related family of compounds from UCSD in 2011 and developed an ophthalmologic technique based on fluorescence lifetime imaging microscopy (FLIM), where β-amyloid aggregates in the lens of the eye could be identified by their increased fluorescence lifetimes compared to unbound background fluorescence by approximately 0.85 nanoseconds (Figure 4.3). As with the fluorescence emission discrimination described in Chapters 2 and 3, this property arises from the stabilization of the excited state by the local protein environment when ANCA11 is bound to an amyloid deposit.

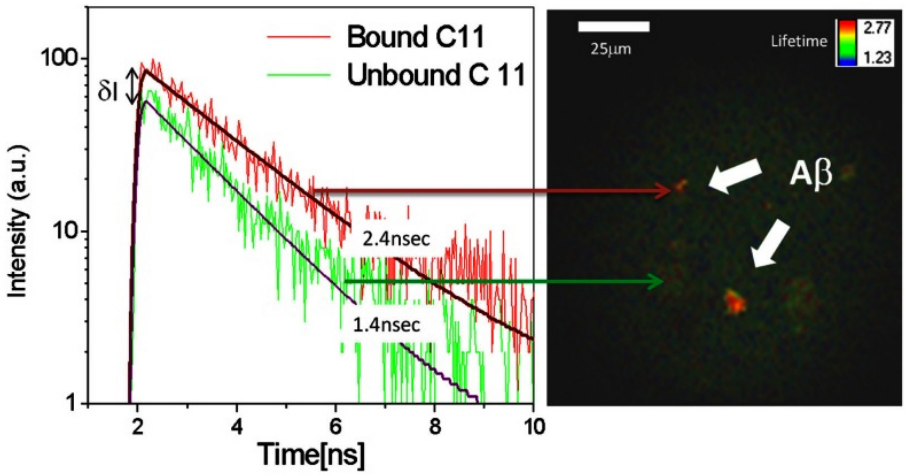

Figure 4.3 Fluorescence lifetime imaging of β-amyloid deposits with compound **1** shows distinct fluorescence lifetime signatures within a 0.85 nanosecond threshold when the probe is free or bound to aggregates. Adapted under the terms of the Creative Commons Attribution License, Frontiers in Neurology. *Alzheimer's disease diagnosis by detecting exogenous fluorescent signal of ligand bound to beta amyloid in the lens of human eye: an exploratory study*, 4 (62), 1-9. Figure 3, copyright 2013.

In comparison to the PET tracers F^{18}-Florbetapir and C^{11}-Pittsburgh compound B (C^{11}-PiB), which have general sensitivities and specificities of 92% and 100%, and 93.5% and 56.2%, respectively, fluorescence lifetime imaging of the lens was able to achieve a diagnostic sensitivity of 85% and a specificity of 95%. The group led by Hartung and coworkers has advanced this technique through clinical trials (currently in phase III) and is currently the farthest along towards clinical application among all ophthalmic approaches for AD diagnostics.[15,70,83]

Here, I present the development and use of a biocompatible derivative of ANCA11 (**1**) to detect amyloid and prion deposits in the eyes of living transgenic AD and prion mice models, respectively. The development of this method provided a rapid, non-invasive approach to visualizing the deposition patterns of these two disease states, allowing us to potentially follow and quantify the progression of neurodegenerative disease such as AD or CJD.

4.2 Results & Discussion

4.2.1 Staining prion aggregates using compound 1 (ANCA11)

Recent reports of Aβ in the retina of AD patients and in transgenic (Tg) mice indicated the appearance of discrete 20-50 micron puncta capable of being labeled with both amyloid-binding fluorophores and antibodies. However, with prion diseases, the variability of the deposition patterns for aggregates has been shown to, in some cases, lack traditional amyloid binding activity. In order to assess the ability of ANCA fluorophores to detect an unknown type of amyloid deposition pattern in the retina, I

performed preliminary staining experiments using compound **1 (**ANCA11) on various prion tissues from Tga20 mice, which overexpress native cell-surface PrP^C, inoculated with mouse brain homogenates infected with chronic wasting disease from elk brain (mCWD) (Figure 4.4).

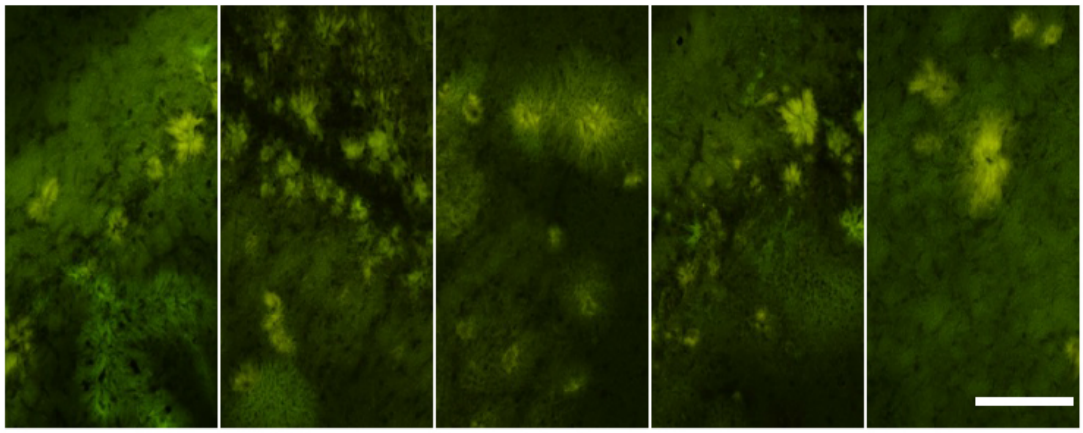

Figure 4.4 Transgenic prion mouse brain tissues stained with compound **1** show a wide range of detectable prion aggregate morphologies (yellow). Scale bar = 50 microns

Fluorescence microscopy allowed me to characterize the spectral emission of these aggregates, which were found to emit with a consistent 553 ± 3 nm, consistent with the globular aggregates seen in the original set of studies in Chapters 2 and 3.

4.2.2 Derivatization of ANCA11

Compound **1** and other cyanoacrylate members of this family are suitable for *ex vivo* histology and rapid bulk fluorescence measurements in cell-free solutions. However, in a biological environment these compounds would be readily susceptible to hydrolysis and various enzymatic processes. We aimed to ultimately translate the histopathology results into a living system. We rationalized that the most susceptible

moiety of the compound **1** structure to biological interference would be the cyanoacrylate. Because ester would likely be readily cleaved or hydrolyzed upon administration *in vivo*, we aimed to increase the biostability by substituting the ester with an amide. I utilized the modular nature of the synthesis for compound **1** and was able to readily substitute the cyanoacrylate for a cyanoacrylamide, resulting in ARCAM-1 (Figure 4.5).

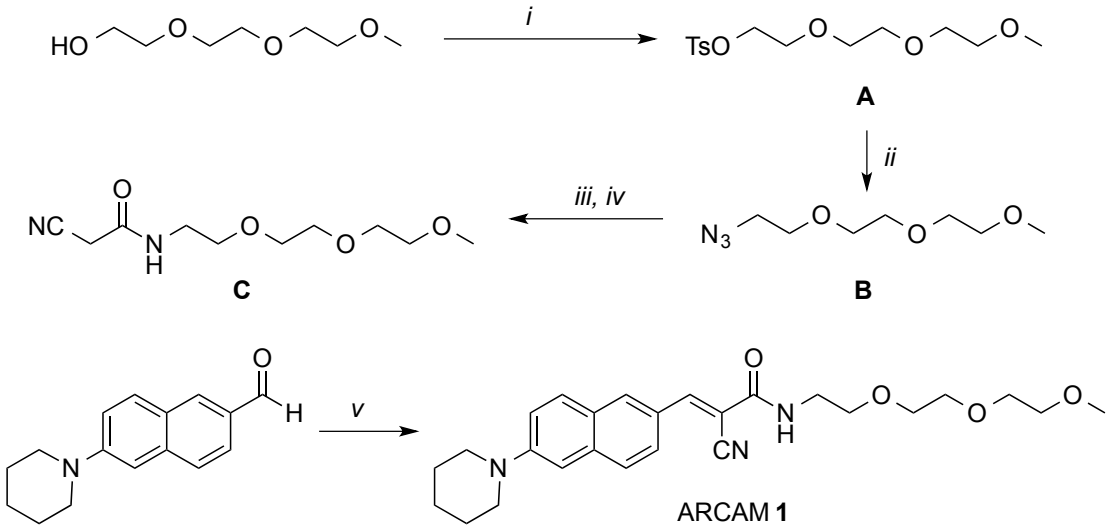

Figure 4.5 Synthesis of ARCAM-1. *i*. p-TsCl, pyridine, DCM. *ii*. NaN_3, DMF. *iii*. PPh_3, Et_2O, H_2O. *iv*. Cyanoacetic acid, EDC, HOBt, DCM. *v*. C, piperidine (cat), THF

In vitro binding assays to Aβ(1-42) fibrils in solution were performed in order to assess the binding efficacy of the derivative. As expected, binding ARCAM-1 to Aβ(1-42) fibrils showed identical photophysical properties to ANCA11 (compound **1**), which allowed it to be compatible with typical fluorescein or GFP filter sets for microscopy (Figure 4.6). I observed an 8-fold enhancement of fluorescence upon binding, comparable with the previously reported ANCA-fluorophores in Chapters 2

and 3. Additionally, ARCAM-1 was found to have a binding constant of 870 ± 280 nM at physiological pH (Figure 4.7).

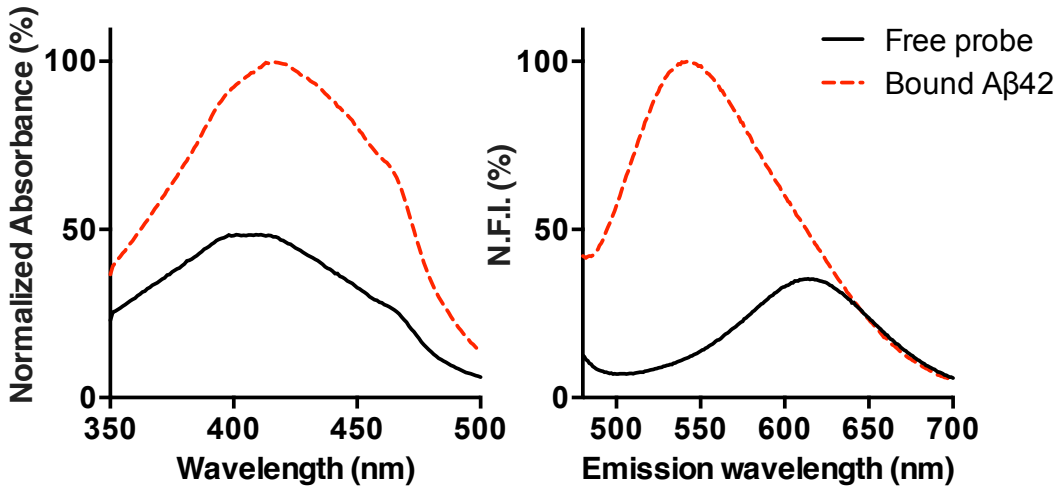

Figure 4.6 ARCAM-1 excitation and emission properties in the presence (red) or absence (black) of aggregated Aβ(1-42).

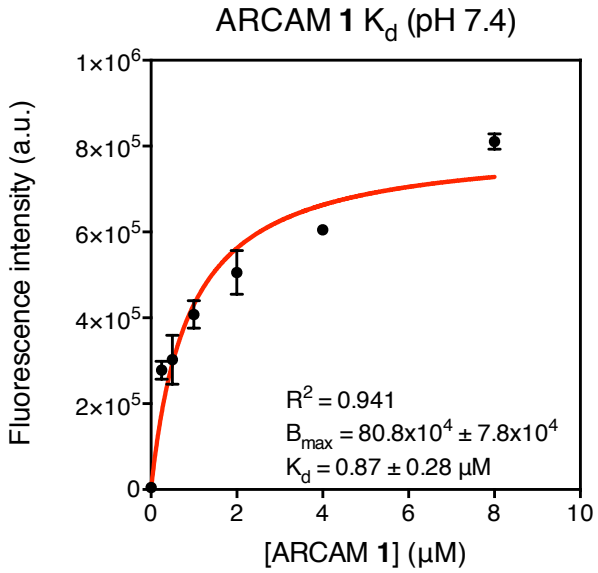

Figure 4.7 A plot of fluorescence intensity versus concentration of ARCAM-1 in the presence of aggregated Aβ(1-42) peptide at pH 7.4. The K_d was determined by fitting data to a one-site specific binding algorithm: $Y = B_{max} \cdot X/(K_d + X)$, where X is the concentration of the probe, Y is the specific binding fluorescence intensity, and B_{max} corresponds to the apparent maximal observable fluorescence upon binding of probes to aggregated Aβ(1-42) peptide.

Finally, I assessed the hydrolytic stability of ARCAM-1 in pH 7.4 1xPBS at 25°C in order to determine both an estimate of the shelf-life of the compound once formulated, as well as general stability in aqueous environments. In comparison to the half-life ($t_{1/2}$) of 24 hours for compound **1** (ANCA11), the ARCAM-1 molecule exhibited an extended $t_{1/2}$ = 148 hours.

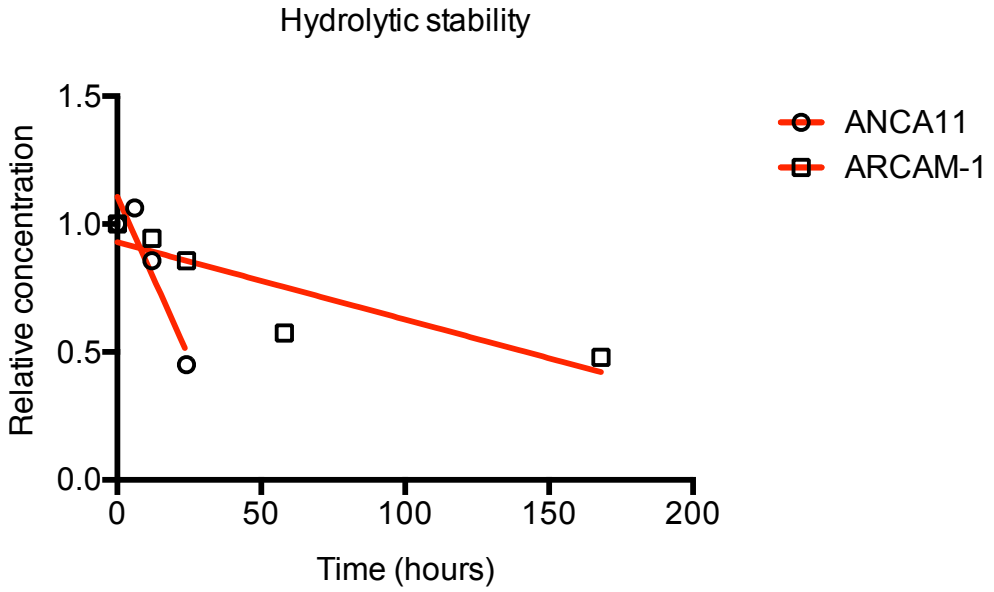

Figure 4.8 Hydrolytic stability studies of ARCAM-1 in pH 7.4 1xPBS monitored by LC/MS.

4.2.3 Determining ARCAM-1 dosage for *in vivo* retinal imaging

I first performed preliminary dosing experiments in wild-type C57BL/6 (Black 6, B6) mice in order to determine both the most tolerable as well as the optimal concentration of ARCAM-1 needed to reach the retina and fluoresce at a high enough intensity that could be detected with a fluorescence fundus retinal camera. Due to the low solubility of ARCAM-1 in aqueous media, we opted to use a formulation excipient of 20% dimethyl sulfoxide and 80% propylene glycol that was previously

used to solubilize similar environmentally sensitive fluorophores for intraperitoneal (IP) injection.[140]

Dosage experiments were performed at 10 mg/mL, which I found to be the maximum soluble concentration in the excipient. I performed the initial imaging experiments with a wild-type 6-month old C57BL/6 mouse. The pupils were first dilated and then the mouse anesthetized. Brightfield and fluorescence images of the left eye (ocular sinister, OS) were acquired using a fluorescence fundus camera both before and after intraperitoneal (IP) injection of the ARCAM-1 formulation (Figure 4.9) in approximately 1-2 minute intervals. While no visual changes were observed in the brightfield images, long-pass fluorescence images showed green fluorescent labeling of the underlying retinal tissue as well as along the vasculature. In contrast to fluorescein angiography used in the clinical setting for monitoring blood flow, these results suggested that ARCAM-1 leeched out of the vasculature into the surrounding tissue, which would allow us to detect tissue depositions of amyloids.

In order to assess the delivery of the compound into the retina, I quantified the fluorescence intensities of the retina images acquired and correlated the fold increase of fluorescence over pre-injection intensities to the imaging acquisition times (Figure 4.10). In WT mice, a 1.5 fold enhancement of fluorescence was seen 1.5-2 minutes after IP injection of ARCAM-1. This fluorescence persisted over 10 minutes, stabilizing at about a 1.2-fold enhancement over background. This last result was particularly important for the remaining experiments because it indicated that there was relatively low background fluorescence upon administration of ARCAM-1, which

would not impede or saturate the possible fluorescence from any amyloid aggregates in the tissue.

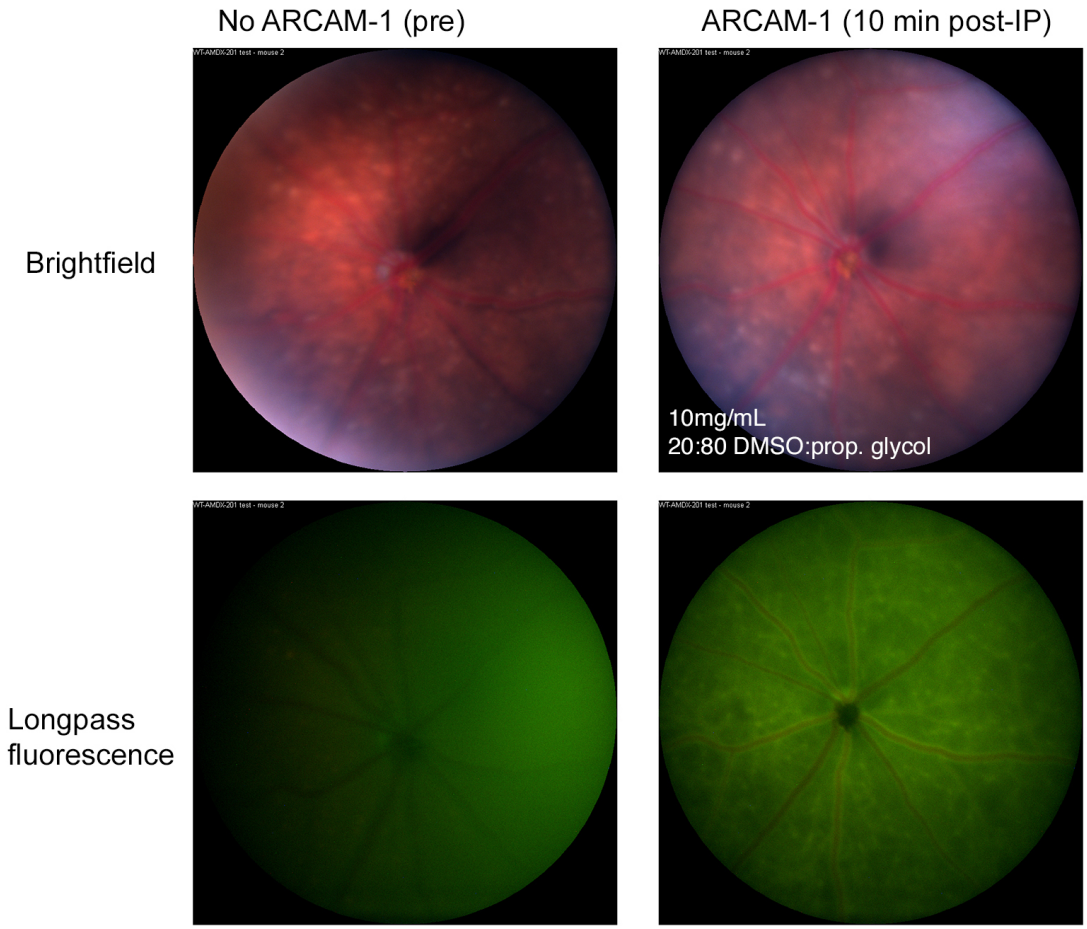

Figure 4.9 Retinal imaging of a the left eye (OS) of a wild-type C57BL/6 mouse injected with 10 mg/mL ARCAM-1 shows persistent fluorescence over 10 minutes. The green fluorescence seen in the absence of ARCAM-1 was attributed to autofluorescence.

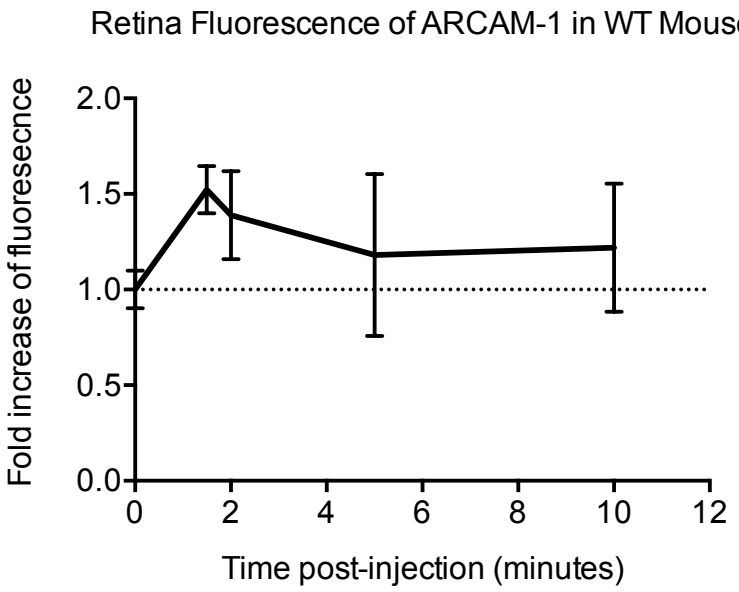

Figure 4.10 Retina fluorescence of left eye (OS) was monitored after IP injection of ARCAM-1.

In order to assess the resonance time of fluorescence in retinal tissue, I performed a second set of imaging experiments where ARCAM-1 was administered first, followed by a 15 or 25 minute wait period before anesthesia was given and the retinas imaged. This set of experiments allowed me to determine the maximum time that fluorescence would be seen in the retina tissue (Figure 4.11). The use of anesthesia was staggered late after ARCAM-1 delivery in order to keep the mice stable for imaging up to 45 minutes (the anesthesia typically wore off after about 20 minutes). As seen in the bottom panels of Figure 4.11, the retina began to become cloudy and translucent at 30-45 minutes, which we attributed to the formation of xylazine- and ketamine-induced reversible cataracts.[141,142] Quantification of the fold enhancement of fluorescence over background was consistent with the first experiment, where I observed an approximately 1.2-fold increase in fluorescence that persisted over 30 minutes after ARCAM-1 injection. However, upon formation of the

anesthesia-induced cataracts, the fluorescence appeared to drop to below pre-injection intensities (Figure 4.12).

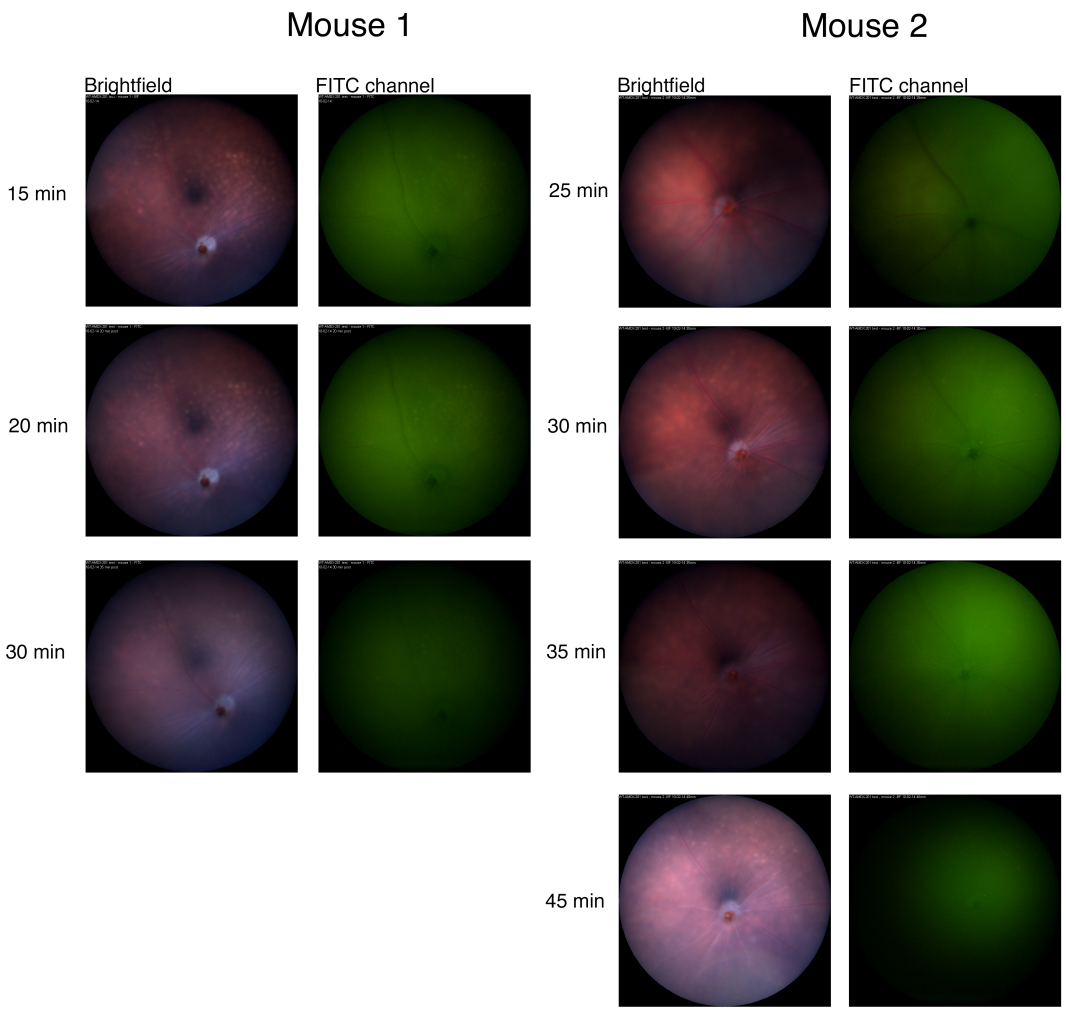

Figure 4.11 Brightfield and fluorescence retinal imaging of left eye (OS) over 30-45 minutes showed the formation of anesthesia-induced reversible cataracts over long-term imaging.

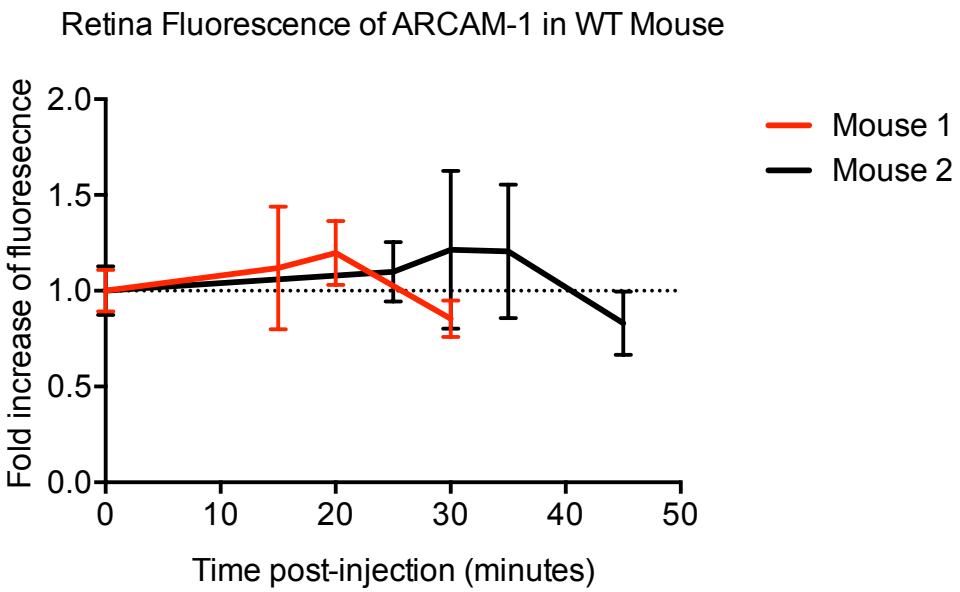

Figure 4.12 Quantification of the long-term fold fluorescence intensity enhancement of WT retina after IP injection of ARCAM-1.

Taken together, these control experiments on WT mice indicated that a 10 mg/mL dose of ARCAM-1 could be delivered to the retina within 5 minutes by IP injection. Experimental imaging was shown to be limited by the appearance of anesthesia-induced cataracts, albeit the appearance of cataracts was long-after the compound arrived into the retina tissue.[142] Finally, the fluorescence profile of the retina images also suggests that the compound did not localize in the vasculature, and instead readily migrated into surrounding tissue.

4.2.4 Retinal imaging of Alzheimer's Disease mice

The results from ARCAM-1 administration into WT mice for retinal imaging were supportive of our design features for the molecule. The lipophilic nature of the compound allowed it to leech into surrounding retina tissue, where we anticipated the

appearance of plaques. Fluorescence was also persistent over autofluorescence for at least half an hour, which provided a good timeframe to perform imaging experiments.

Initial experiments conducted on two 5 month-old APP/PS1 and 5xFAD transgenic AD mice models showed no plaque labeling.[143–146] As with the WT mice, experiments involved pre-imaging the left and right eyes followed by the IP injection of ARCAM-1 and subsequent imaging over 15-20 minutes (Figure 4.13).

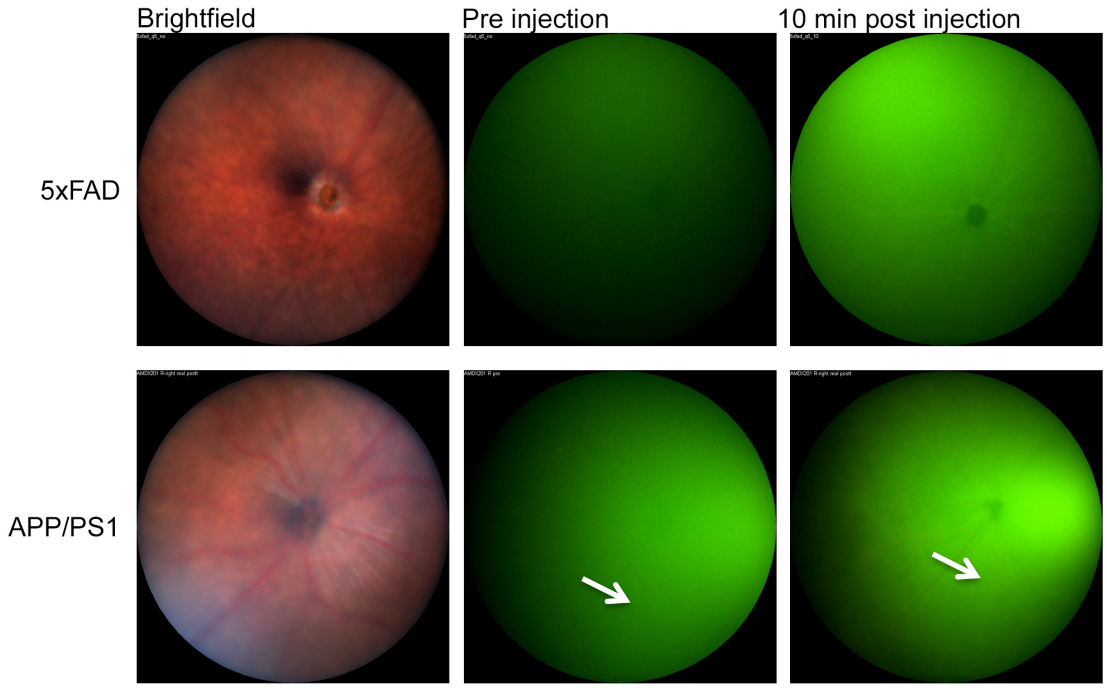

Figure 4.13 Retinal imaging of the left eyes (OS) of 5 month-old 5xFAD and APP/PSI mice models. 5xFAD models showed no signs of fluorescent objects, whereas the APP/PSI model had a small autofluorescent object (white arrow).

The 5xFAD retinal fluorescent images were similar to WT, and showed no fluorescent labeling of objects, while the APP/PSI mice retina had one faint autofluorescent object. Mice were then euthanized and *ex vivo* histology with exogenous ARCAM-1 staining was performed on the brains of these mice, which

showed 5xFAD brains containing plaques with typical morphology found in this Tg mouse strain. APP/PS1 did not show any plaques in the brain at this age. Additionally, cross-sectional analyses of the right eyes (OD) of our 5xFAD mice showed fluorescently labeled objects in the outer plexiform layer, consistent with previously published results for plaque deposition in the APP/PS1 mice studied by Koronyo-Hamaoui (Figure 4.14).[48] I was not able to detect any objects in the retinal cross sections of APP/PS1 mice at 5 months; however since a cross-sectional analysis is limited by tissue thickness, it is also likely that I did not stain any regions that contained possible fluorescent objects that would be visible by a top-down topographical view accessible through flat-mount tissue samples.

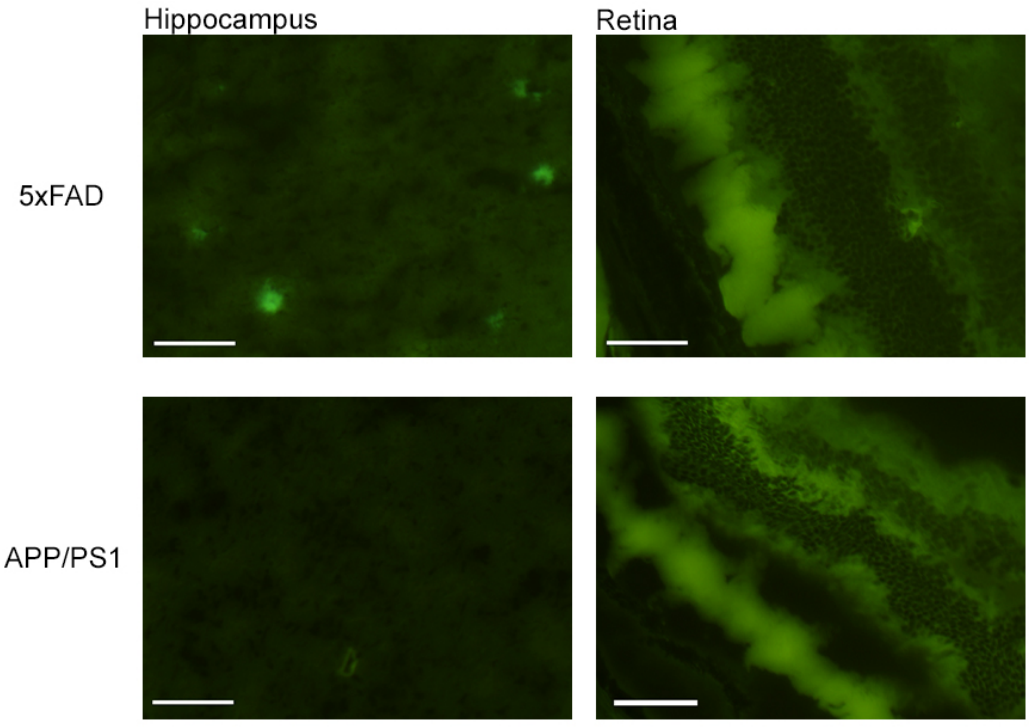

Figure 4.14 *Ex vivo* histology of the hippocampus and cross-sectional right (OD) retina tissue stained with ARCAM-1 showed typical plaque deposition in the hippocampus of 5xFAD, but not APP/PS1 mice. Retinal cross sections from 5xFAD mice also showed fluorescent objects in the OPL, which were not present in the APP/PS1 mice. Scale = 50 microns.

Taken together, these initial results were inconclusive in regards to the appearance of amyloid aggregates in the eye. The one 5xFAD mice we analyzed showed positive fluorescence signatures in *ex vivo* tissue samples, but no signals in *in vivo* live retinal imaging; the one APP/PS1 mice in contrast showed possible fluorescent objects in the retina (Figure 4.13 bottom row), but no detectable aggregates in *ex vivo* samples. In light of these results, I opted to continue *in vivo* imaging with APP/PS1 mice over several months in order to track the appearance of the fluorescent objects. Indeed additional APP/PS1 mice of several ages were ultimately imaged over ~12 months (Table 4.1, Table 4.15). These mice ranged from 9 months to 12 months of age, and exhibited distinct fluorescent puncta in their eyes. However, as with the initial 5-month old APP/PS1 mouse (Figure 4.13), these fluorescent objects were both autofluorescent without injection of ARCAM-1, and were visible under brightfield as white objects. Images were processed to increase contrast and then analyzed in ImagePro to obtain morphology dimensions. As Table 4.1 shows, the objects ranged from 20-40 microns in diameter, and were roughly spherical in morphology (circularity parameter, out of a maximum circularity of 1.0). The number of vesicles present was highly variable, and visual inspection of the images showed that most of these puncta localized around the optic nerve.

Table 4.1 Selection of APP/PS1 mice imaged and analyzed for morphology parameters.

Age (days)	No. Objects	Radius (μm)	Circularity	Area (μm^2)
239	24	18.7 ± 5.1	0.64 ± 0.21	1309 ± 701
273	5	27.4 ± 5.8	0.74 ± 0.14	1385 ± 633
276	11	11.4 ± 7.4	0.44 ± 0.17	314 ± 406
385	10	21.2 ± 2.2	0.84 ± 0.05	776 ± 161

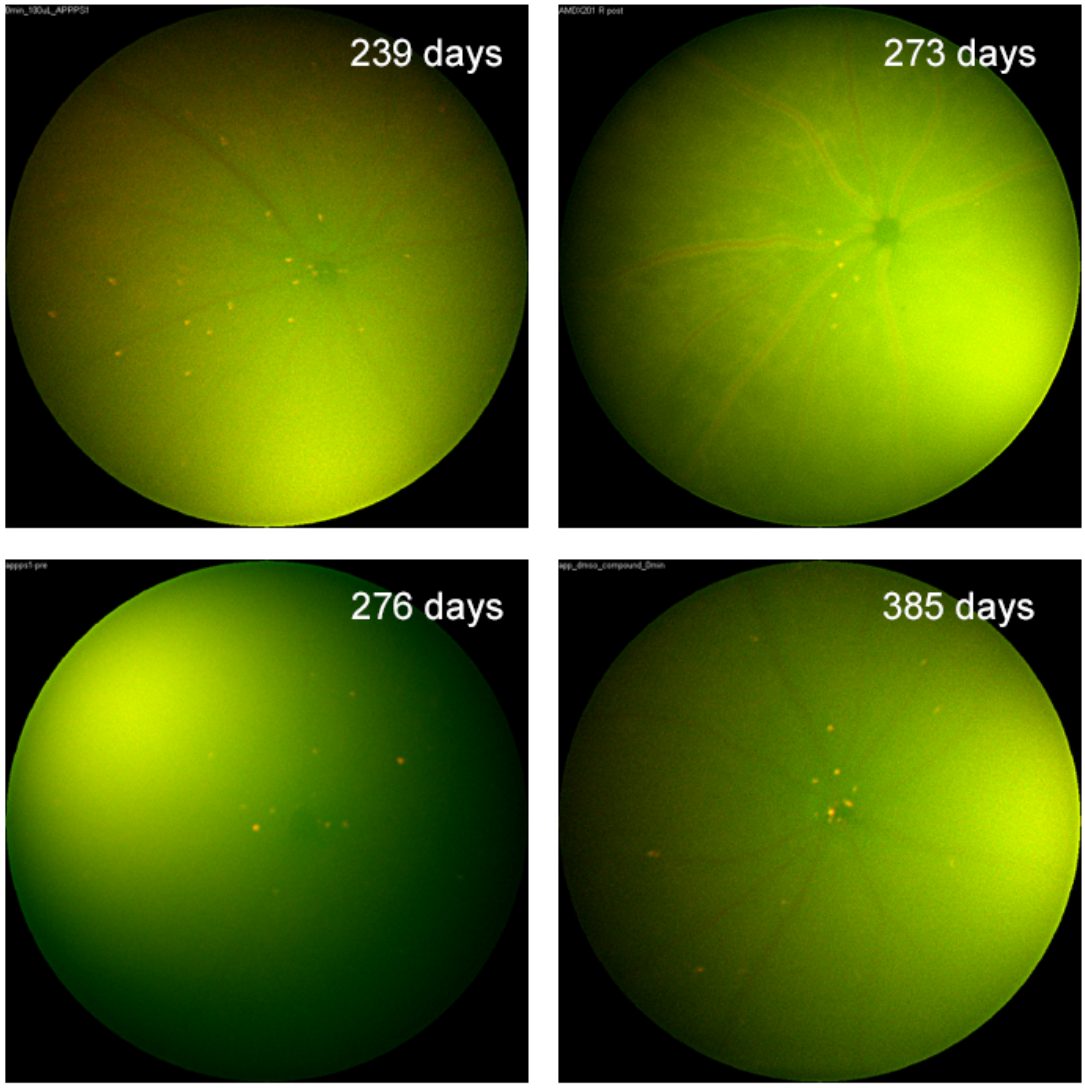

Figure 4.15 Contrast-adjusted fluorescence images of the OS of 4 different APP/PS1 mice ranging from ages 9-12 months show distinct fluorescent puncta.

Additionally, plots of these morphology parameters as a function of the ages of the mouse showed no age-dependent trends for the size or number of objects (Figure 4.16).

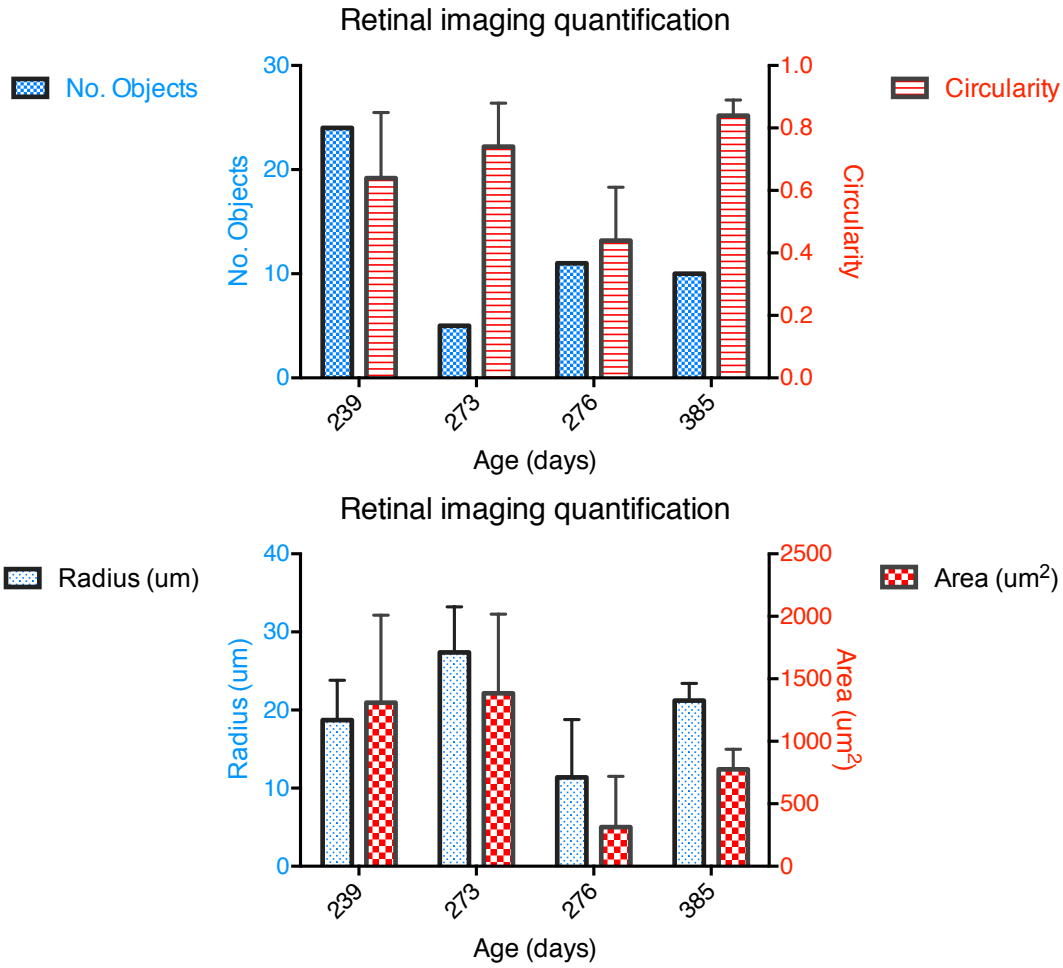

Figure 4.16 Plots of the morphology parameters as a function of age showed no age-dependence.

Finally, *ex vivo* flat-mount histology of the left eye (OS) of the 276-day old mouse in Figure 4.15 was performed without additional staining using antibodies or ARCAM-1 (Figure 4.17). Real-color images were obtained, which showed small fluorescent puncta that were yellow autofluorescent measuring approximately 20-30 microns in diameter. The same tissues were then imaged under using confocal microscopy to reduce background noise, where I observed objects (hereon called

deposits) with similar morphologies reported by Koronyo-Hamaoui. Consistent with the *in vivo* retinal images, these deposits were also autofluorescent under confocal and true-color microscopy. Spectral fluorescence emission scans performed on the aggregates showed an $\lambda_{emission}$ maxima at 510 nm ± 4 nm (Figure 4.18).

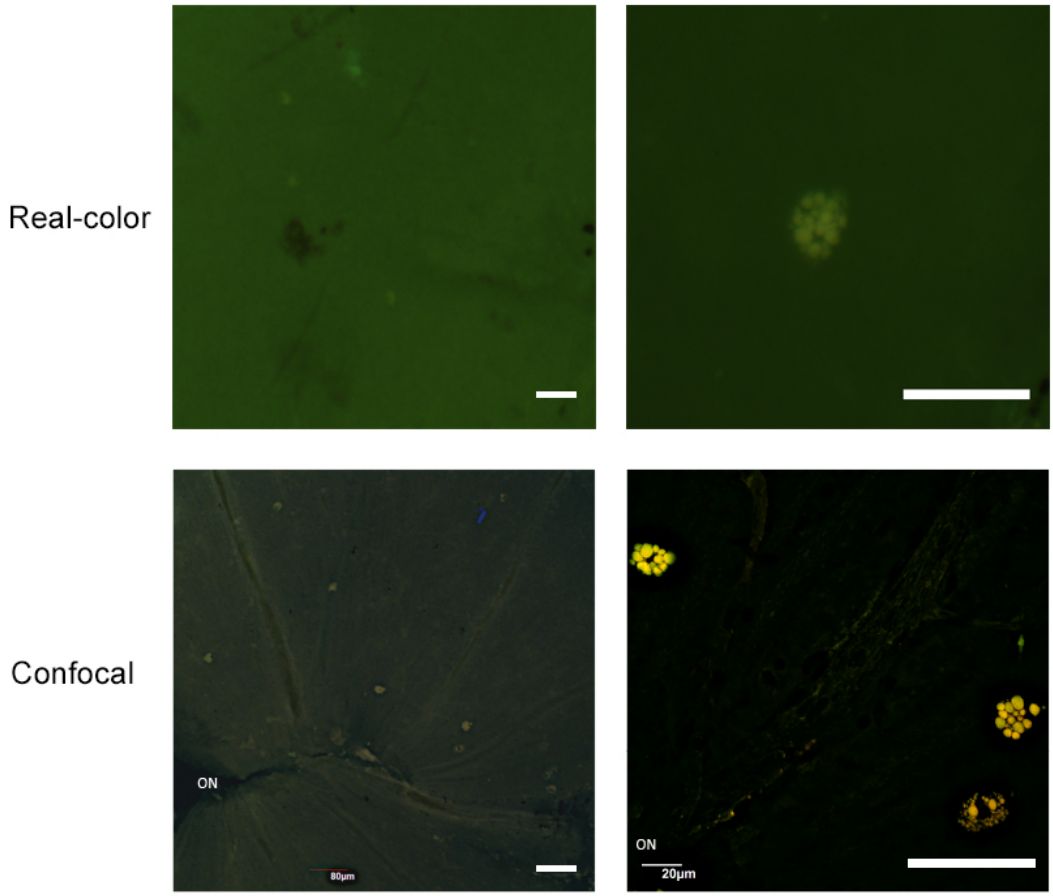

Figure 4.17 *Ex vivo* histology was performed on the OS retina of a ~280-day old mouse. Right images are magnifications of regions in the left images. The fluorescent objects showed autofluorescence with a globular morphology. Scale bars for left images = 80 microns, scale bar for left images = 50 microns.

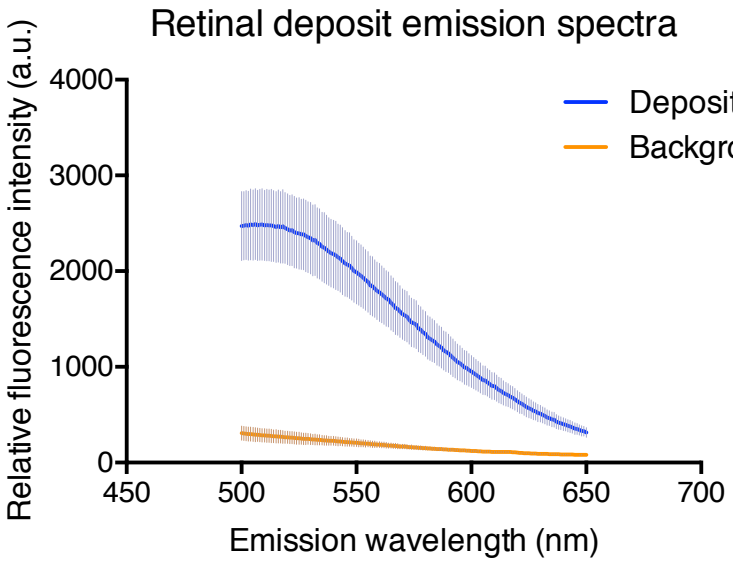

Figure 4.18 Spectral scan of the native fluoresce of the plaques in the OS retina images of APP/PS1 AD mice.

These results suggested that although the fluorescent deposits were autofluorescent, they maintained a high fluorescence in the emission range typically seen for ARCAM-1 and ANCA fluorophores bound to amyloid plaques (~520-530 nm). It is known that senescence results in the production of insoluble aggregates of lysosomal byproducts and lipids known as lipofuscin, or "age-pigments".[147–149] These assemblies typically are highly autofluorescent and appear readily in the retina, where it has been suggested as an intermediate in the development of age-related macular degeneration (AMD).[150] In order to check whether these deposits contained lipofuscin, I performed *ex vivo* histology with a Sudan-Black B (SBB) lipid stain and ARCAM-1 on cross-sectional retina tissue samples from the OD of the 238 day-old mouse. Additionally, immunofluorescence staining was also done in parallel with a mouse anti-human Aβ monoclonal antibody (Figure 4.19). The black objects under brightfield imaging are indicative of the presence of lipids or fatty acids in both the

outer nuclear layer (ONL), near the photoreceptor layer, and outer plexiform layers. The presence of lipid-based aggregates in the nuclear layer was a surprising discovery, however it was consistent with previously published data.[67] In contrast to the plaque locations seen in the 5xFAD retinal cross-section stains, ARCAM-1 staining showed the presence of fluorescent objects in the photoreceptor layer, at the cusp of the ONL. Immunofluorescence staining showed similar detection of amyloid-type plaques in the photoreceptor layer.

Together, these results indicated that while indeed composed of lipid materials, these deposits also contained β-amyloid aggregates. Lipofuscin is known to be autofluorescent, and is present in aging healthy WT animals as well. In order to assess the Aβ composition in these lipid-containing deposits, I performed Western Blot analyses of retinal homogenates against a mouse anti-human Aβ antibody (Figure 4.20). Briefly, after initial imaging, the flat-mounted OS tissues from each animal was collected and homogenized to obtain a tissue sample.

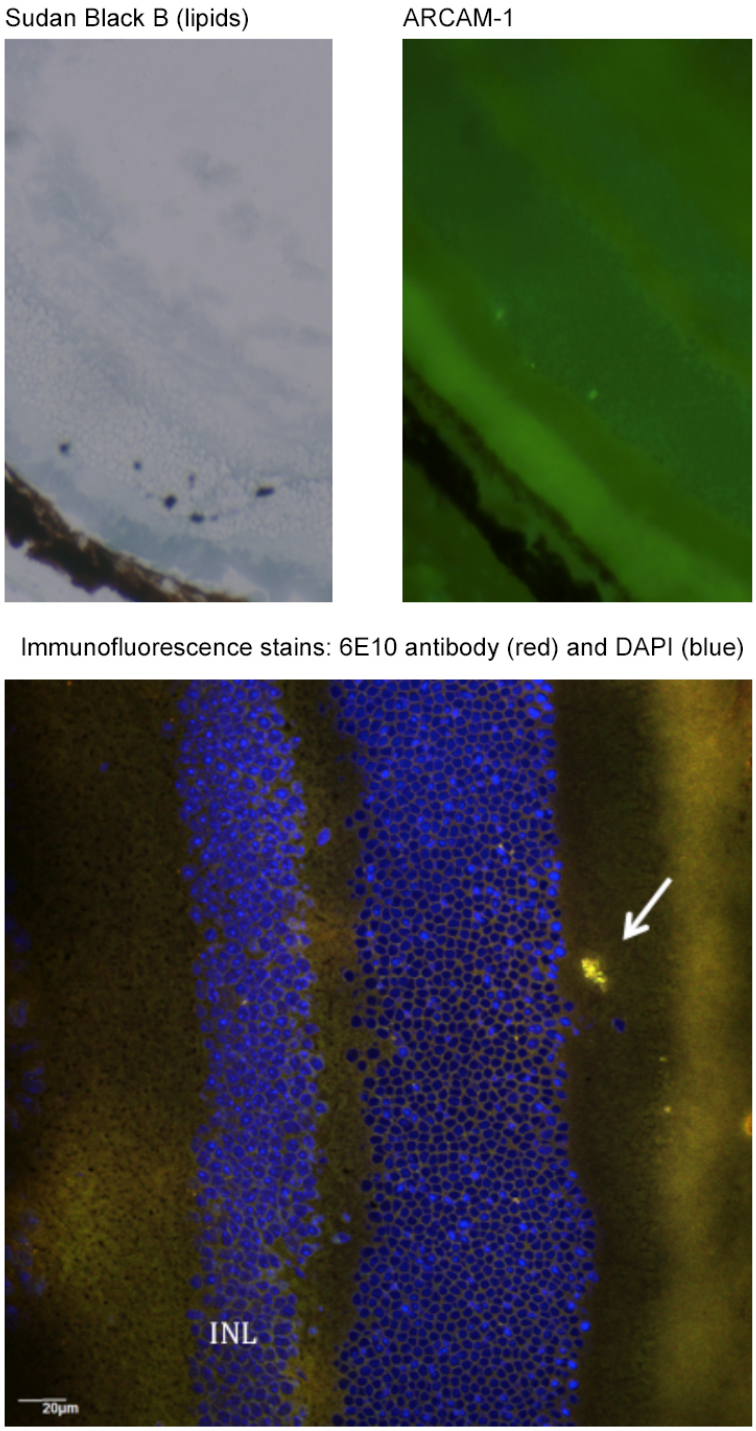

Figure 4.19 *Ex vivo* histology of the OD cross sections from 9 month-old APP/PS1 AD mice. Bottom panel shows immunofluorescence staining of a cross-section using the 6E10 antibody against Aβ (red), DAPI nuclear stain (blue), and inherent green fluorescence from ARCAM-1. The yellow deposit indicated by the white arrow is an objection that fluoresced both red and green, indicating co-staining with the antibody and ARCAM-1, or possibly autofluorescence.

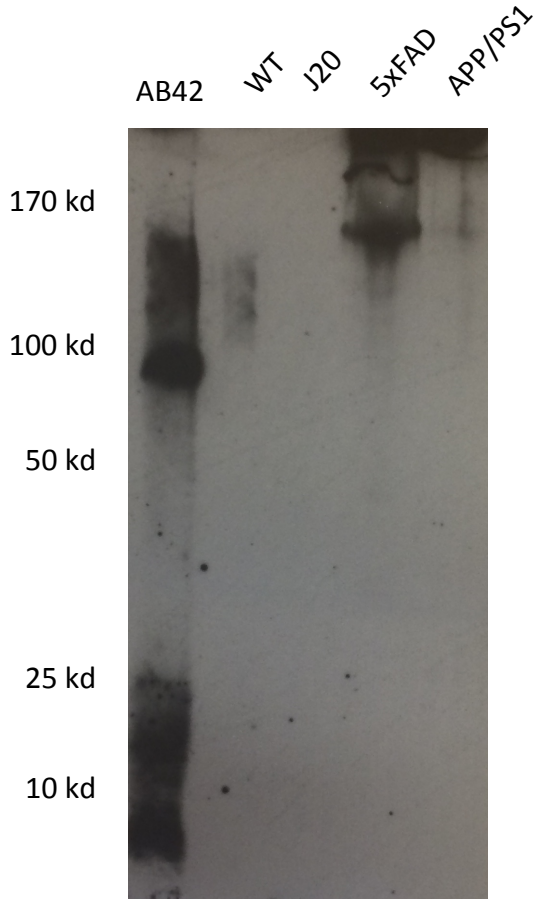

Figure 4.20 SDS-denaturing PAGE Western blot showed no β-amyloid aggregates in WT, 5xFAD, and APP/PS1 mice. Homogenates of retinal tissue from Transgenic J20 AD mice were also analyzed. 5xFAD and APP/PS1 mice showed large molecular weight bands at 165 and 200 kDa.

Western blot analyses showed no β-amyloid aggregates in retina homogenates at the oligomeric or even fibrillar stages (~100 kDa). However, I did observe bands at high molecular weight, near 165 and 200 kDa. These bands were more than double the weight of APP (~87 kDa), which may suggest the detection of highly aggregated amyloid species resistant to denaturing conditions. Due to the sparse nature of the plaque deposition patterns in the retina, homogenization may have also reduced the concentration of amyloid in the samples, leading to possible false-negatives.

Furthermore, recent work has shown that APP processing occurs readily in the RPE but not the retinal layers, and that Western blot detection methods have not been the most viable form of biochemical analyses. As a result, ongoing work has been aimed towards developing better biochemical methods to verify the presence of amyloid in these retinal samples. Nonetheless, the fluorescence images were indicative of the presence of plaques similar to the reports in literature.

4.2.5 Retinal imaging of prion mice

I next analyzed the retinas of approximately 500 day-old Tga20 prion mice inoculated with three strains of prion homogenates. A preliminary imaging experiment was carried out on a Tga20 B6 mouse inoculated with mouse chronic wasting disease (mCWD) into the brain (Figure 4.21). As with WT and AD mice, I performed an IP injection of 10 mg/mL ARCAM-1 in 20%DMSO and 80% propylene glycol. Interestingly prion mice retinas showed reflective, amorphous objects around the optic nerve under brightfield illumination prior to compound injection. These objects were dark in the fluorescence channels prior to administration of ARCAM-1, but were immediately illuminated within one minute after IP injection of the formulation that persisted for more than 10 minutes.

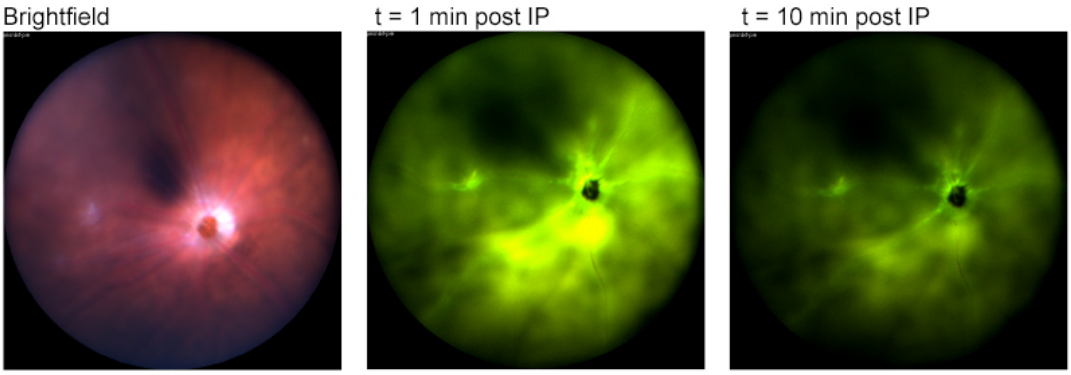

Figure 4.21 Brightfield and long-pass fluorescence images of the OS of a 500 day old prion mouse inoculated with mCWD. Fluorescence images were taken immediately after injection (t = 1 min) and 10 minutes later.

The eyes of this mouse were then enucleated and the OS retina flat-mounted to view the topographical distribution of the plaque deposits; tissues did not undergo any additional staining. Additionally, the RPE and choroid were also extracted and flat-mounted (Figure 4.22). Under epifluorescent illumination, the amorphous fluorescent objects were seen to have diffuse morphology, with deposits seen originating from the optic nerve, lining the vasculature, and lying in the retina tissues. Surprising, I found that the RPE/choroid showed one large aggregate distal to the optic nerve; the morphology was similar to the typical mCWD-type deposits seen in the corpus callosum of the brain, as seen in Chapter 2 and 3. In addition to their distinct morphologies and localization in the tissue, the retinal fluorescent objects were seen to have a fluorescence emission in the green channel when stained with ARCAM-1 delivered by IP injection, whereas the RPE/choroid object was more yellow in the emission color, likewise similar to the brain aggregates seen in Figure 4.4.

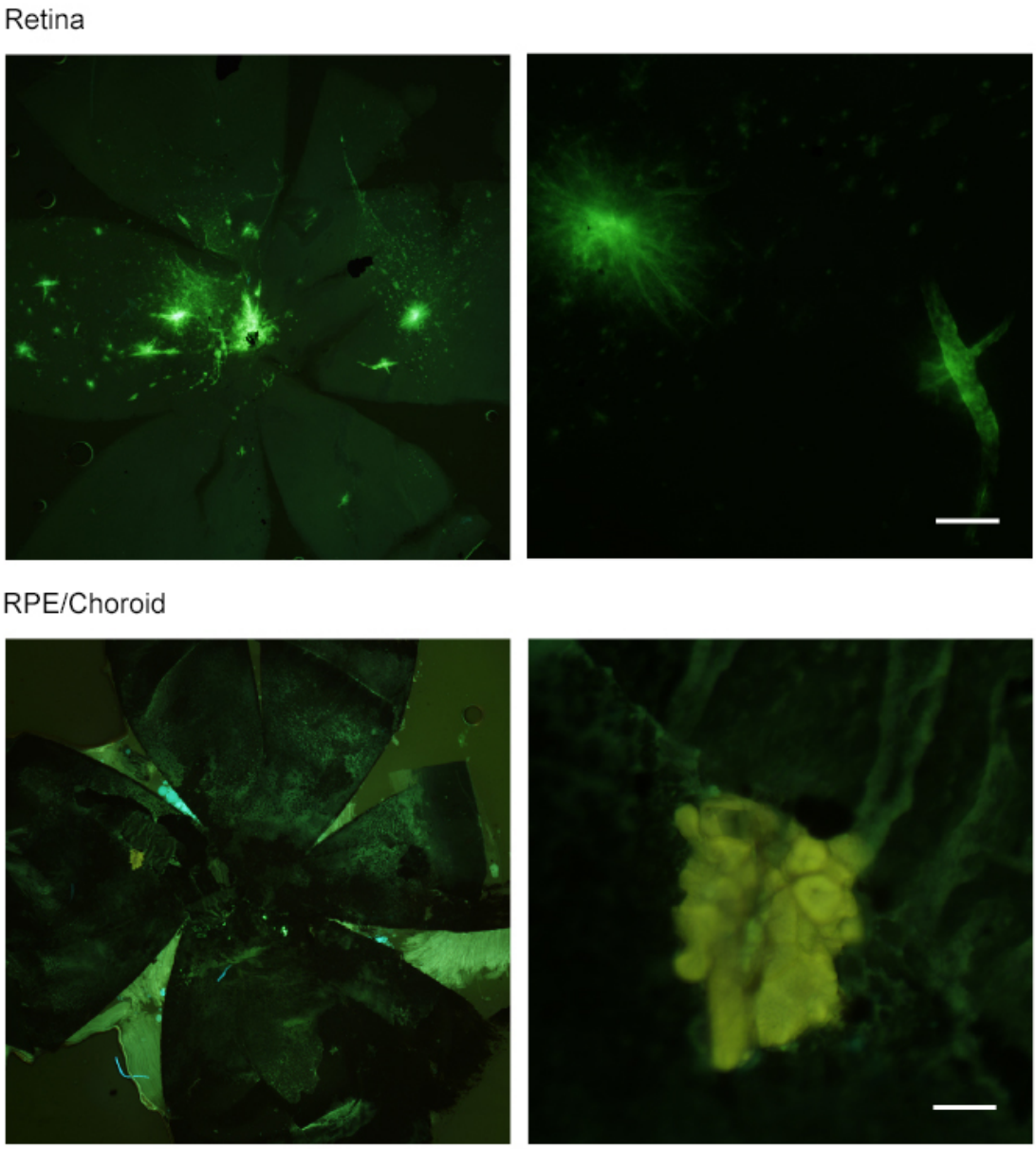

Figure 4.22 Real-color fluorescent images of OS flat-mounts of the retina and RPE/choroid from a 500 day-old prion mouse with mCWD. Left-side: full view of the flat-mounts, right-side: magnified views of the fluorescently labeled objects. Tissues were imaged immediately after dissection, with no additional histological stains. Scale bars = 50 microns.

The emission properties of the labeled aggregates in both the retina and RPE/choroid were measured by confocal microscopy (Figure 4.23). While the retina deposits emitted at 510 ± 4 nm, the RPE/choroid deposits showed a 525 ± 5 nm

fluorescence emission profile. While the identity of these aggregates has not been elucidated, both types were detectable by ARCAM-1. Because of the discriminatory ability of the ARCAM-1 fluorophore, these spectral results also suggested that the aggregates in the different regions of the eye could possibly be a result of unique conformation patterns that resulted in different aggregation states.

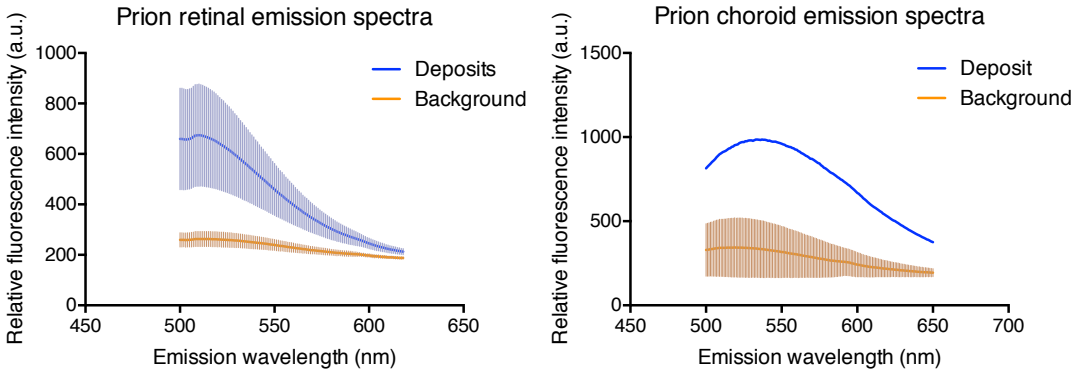

Figure 4.23 Confocal spectral scans of deposits in the retina and RPE/choroid of the OS from a 500 day-old prion mouse with mCWD showed different emission profiles.

In addition to mCWD, I also monitored the retinas of transgenic glycosylphosphotidylinositol-anchorless (GPI-anchorless) mice inoculated with the scrapie ME7 and 22L strains of prions. As previously discussed, the GPI is a C-terminus post-translational modification to the native PrP^{C} protein.[99,151] Ablation of this anchor has been shown to increase fibrillzation and aggregation of prion proteins, but with a concomitant decrease in infectivity and neuroinvasion.[98] These strains differ in their conformation, infectivity, and transmissibility of pathology between infected animals. In general, mCWD prions are slow-developing, with incubation times around 460 days before prion disease develops; ME7 and 22L have been shown to have incubation times around 80 days with high neuroinvasion.[81]

Similar to mCWD strains, ME7 GPI-anchorless mice showed large amorphous objects in their retina, localized around the optic nerve, that showed an enhancement of fluorescence emission over autofluorescent background upon IP administration of 10 mg/mL ARCAM-1 (Figure 4.24) Two GPI-anchorless ME7 littermates injected with ARCAM-1 showed similar fluorescent retinal plaque labeling as found in the mCWD strain. As before, amorphous depositions with high reflectance (white objects) were seen in the brightfield images of the retina in anesthetized ME7 mice (age ~300 days post inoculation). Long-pass fluorescence imaging of the retina prior to injection only showed autofluorescence, with fluorescent plaques appearing within 2 minutes post-injection. Also similar was the deposition pattern where it appeared that prion aggregation spread out from the optic nerve. These results would be consistent with the hypothesis of anterograde transmission of prion infectivity from the brain into the eye, along the optic nerve.[152,153]

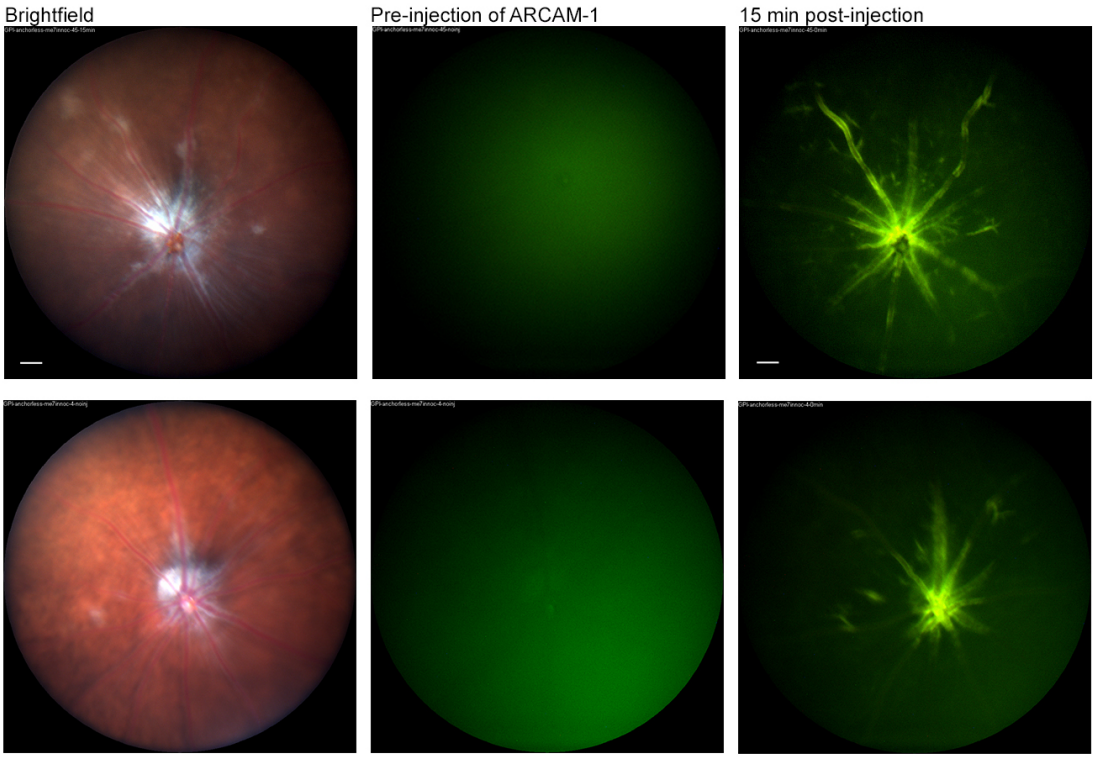

Figure 4.24 Brightfield and fluorescence retina images of the OS of two GPI-anchorless prion mice inoculated with ME7 prions and labeled with ARCAM-1 by IP injection. Scale bars = 100 microns.

The fluorescent objects were seen to follow the vasculature and radiate outward from the optic nerve, similar to the pattern seen in mCWD. The fluorescence from the plaques itself was found to persist for the duration of the experiment and were seen in *ex vivo* flat-mount histology samples (Figure 4.25).

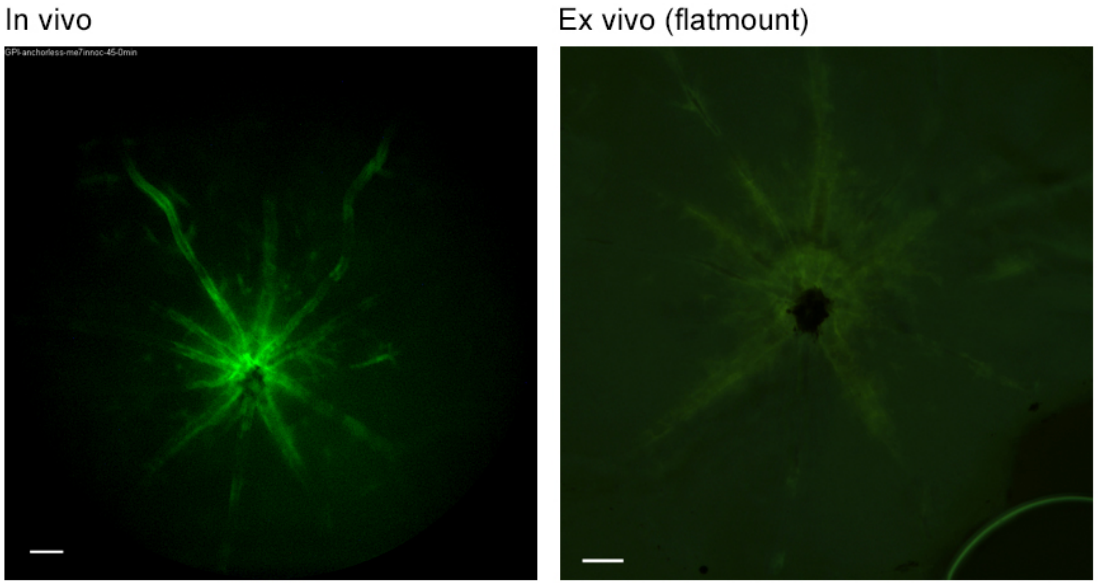

Figure 4.25 FITC band-pass filter and *ex vivo* flat-mount of the OS of a GPI- ME7 mouse showed persistent fluorescence. Scale bars = 100 microns

Interestingly, preliminary *in vivo* fluorescence retina imaging of GPI-anchorless 22L strain mice injected with ARCAM-1 did not show any labeled objects that were viewable via live fluorescence retinal imaging. Taken together, these live images in prion mice suggest the possible presence of large aggregates in the retina, although the strain, and hence the conformation state, may dictate the appearance of aggregation or deposition in the eye.

In collaboration with Dr. Patricia Aguilar, Western Blot analyses of the eyes and brains from the ME7 prion mice were performed using the sodium phosphotungstic acid (NaPTA) enrichment and purification assay (Figure 4.26).[98,154] While enrichment of the retina samples did not amplify protein signals from the prion proteins, the brains of both GPI- mice models showed high protease-resistant protein aggregates. Like the AD mice, the lack of detection in the retina biochemistry

suggested that the concentration of prion aggregates might be below the detection threshold of Western blot.

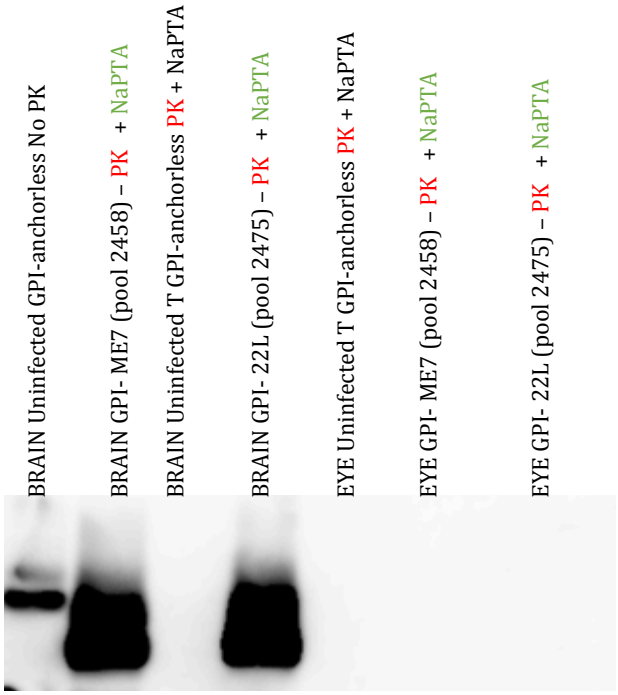

Figure 4.26 NaPTA enrichment assay followed by PK-digest and Western blot analysis on ME7 and 22L prion mice showed the presence of PrP^{Sc} in the brain, but not in the retina.

4.3 Conclusions

Using wild-type, AD, and prion mice, I was able to develop a preliminary method for the use of an environmentally sensitive fluorophore, ARCAM-1, to detect possible amyloid aggregation in the retina. Initial analyses from WT mice indicated that the compound did not stay in the vasculature upon IP injection, and rather localized into the retinal tissue. The fold enhancement of fluorescence of the background tissue was approximately 1.2 times that of autofluorescence from the

fundus camera laser. This low enhancement of nonspecific binding was ideal for the imaging experiments.

The transgenic mice imaged in these experiments were generated in order to model both the deposition patterns of amyloid in the brain, as well as the behavior and symptoms of neurodegenerative diseases.[98,143,145] While the transgenes are targeted to neuronal expression in the brain, it is unclear if the retina is also affected. Nonetheless, in AD mice models, the retinas exhibited mostly uniform puncta ranging from 20-40 microns in diameter that were autofluorescent, but capable of being stained with ARCAM-1 and antibodies for Aβ. In contrast, prion mice showed amorphous plaques, analogous to the brain, in the retina. Because the prion brain homogenates were inoculated into the brain, the deposition pattern of amyloid in the retina of prion mice suggested that the prion deposits likely traveled from the brain through the optic nerve.[152,153] *Ex vivo* histology of the AD mice hinted that the retinal plaques were possibly a mixture of lipofuscin infused with amyloid aggregates, although biochemical analysis of β-amyloid content in the retinas using Western blots was inconclusive. Similarly, the biochemical analysis of prion in the retinas also was inconclusive; the lack of detectable amyloidogenic proteins from both analyses could be due to concentrations of the respective proteins that were below the detection threshold for Western blots.

Finally, post-imaging processing and quantification of the protein aggregates showed, along with visual inspection of the deposits in each disease type, that retinal imaging presents a very clear method for the detection and differentiation of amyloid diseases. While these diseases are naturally very different in terms of behavioral and

psychological phenotypes (clinical symptoms), future research into correlating these types of deposits in the retina to these clinical symptoms would be beneficial in the development of this method into an early diagnostic. Along these lines, we have begun the investigation of amyloidosis in human eyes.

4.4 Materials and Methods

General synthesis techniques

Unless indicated, all commercially available reagents and anhydrous solvents were purchased at the highest commercial quality and were used as received without further purification. All non-aqueous reactions were carried out under argon atmosphere using dry glassware that had been flame-dried under a stream of argon unless otherwise noted. Anhydrous tetrahydrofuran (THF) and dichloromethane (CH_2Cl_2) were obtained by passing commercially available pre-dried, oxygen-free formulations through activated alumina columns. Flash column chromatography was performed on silica gel (Merck Kieselgel 60, 230-400 mesh) using Hexanes-EtOAc or EtOAc-MeOH or toluene-acetone or diethyl ether mixtures of increasing polarity. The progress of all the reactions was monitored by thin-layer chromatography (TLC) using glass plates precoated with silica gel-60 F254 to a thickness of 0.5 mm (Merck), and compounds were visualized by irradiation with UV light and/or by treatment with a solution of CAM stain or potassium permanganate ($KMnO_4$) in water stain followed by heating. ^{13}C NMR and ^{1}H NMR spectra were recorded on either 400 MHz or 500 MHz Varian instrument or 500 MHz JEOL instrument. $CDCl_3$ was treated with

anhydrous K_2CO_3, chemical shifts (δ) are quoted in parts per million (ppm) referenced to the appropriate residual solvent peak reference ($CDCl_3$), with the abbreviations s, br s, d, t, q, m, td, dt and qd denoting singlet, broad singlet, doublet, triplet, quartet, multiplet, quartet of doublets, triplet of doublets, doublet of triplets and quartet of doublets respectively. J = coupling constants given in Hertz (Hz). High-resolution Mass spectra (HRMS) were recorded on a trisector WG AutoSpecQ spectrometer.

Synthesis and ARCAM-1

2-(2-(2-methoxyethoxy)ethoxy)ethyl 4-methyl-benzene-sulfonate (A)

(Methoxyethoxy)ethoxy ethanol (20.0 g, 0.122 mol) was added to a solution of dry pyridine (49.0 mL) and CH_2Cl_2 (152 mL). The solution was cooled to 0 °C and p-toluenesulfonyl chloride (27.9 g, 0.146 mol) was added in one portion with stirring. The reaction was allowed to come to room temperature and stir for 24 hours. The reaction was then concentrated in vacuo and the solution was filtered to remove solids. The filtrate was purified by flash silica column chromatography (0-3% MeOH/EtOAc) to give **A** (20.5 g, 53%) as a clear pale yellow oil. (**A**): R_f = 0.85 (9% MeOH/EtOAc) ^{1}H NMR (500 MHz, $CDCl_3$) δ 7.79 (d, J = 8.0 Hz, 2H), 7.33 (d, J = 8.0 Hz, 2H), 4.15 (m, 2H), 3.52-3.69 (m, 10H), 3.37 (s, 3H), 2.44 (s, 3H); ^{13}C (125 MHz, $CDCl_3$) δ 144.9, 133.0, 129.9, 128.1, 72.0, 72.0, 71.5, 70.9, 7038, 70.7, 70.7, 70.7, 69.4, 68.8, 59.2, 42.9, 21.8; HRMS calcd for $C_{14}H_{22}O_6SNa$ $[M+Na]^+$ 341.1029, found 341.1030 by ESI.

1-azido-2-(2-(2-methoxyethoxy)ethoxy)ethane (B)

To a solution of **A** (1.0 g, 3.14 mmol) in DMF (125 mL) in a flask equipped with a condenser was added sodium azide (0.51 g, 7.85 mmol) and the reaction was heated to 67 °C for 15 hours. The reaction was then cooled to room temperature, diluted with water (125 mL), and stirred for 30 minutes. The reaction mixture was poured into ice (150 mL) and extracted with diethyl ether (3 x 50 mL). The combined organic extracts were washed with water (2 x 30 mL) and dried with anhydrous $MgSO_4$. The solvent was then removed in vacuo and the residue was purified via silica gel flash chromatography (10-70% EtOAc/hexanes) to give **B** (355 mg, 60%) as a clear colorless oil. (**B**): $R_f = 0.6$ (50 % EtOAc/hexanes)

^1H NMR (500 MHz, $CDCl_3$) δ 3.65 (m 8H), 3.55-3.56 (m, 2H), 3.39-3.40 (m, 2H), 3.38 (s, 3H); ^{13}C (125 MHz, $CDCl_3$) δ 72.0, 70.8, 70.8, 70.2, 59.2, 50.8; HRMS calcd for $C_7H_{15}N_3O_3Na$ $[M+Na]^+$ 212.1006, found 212.1006 by ESI.

2-cyano-N-(2-(2-(2-methoxyethoxy)ethoxy)ethyl)acetamide (C)

B (3.0 g, 15.7 mmol) was dissolved in diethyl ether (628 mL) and cooled to 0 °C. Triphenylphosphine (5.0 g, 18.8 mmol) was added in one portion and the mixture was allowed to stir at 0 °C for 1 hour and then at room temperature for 6 hours. Water (200 mL) was then added and the reaction was allowed to stir for 12 hours. Toluene (150 mL) was then added and the reaction was allowed to stir for an additional 12 hours. The water layer was then isolated and washed with toluene (1 x 200 mL) and then removed in vacuum to give the corresponding amine as a clear yellow oil which, without further purification, was subjected to the next reaction. A solution of the amine (1.79 g, 10.97 mmol), prepared as described above, and hydroxybenzotriazole

(HOBt) (1.48 g, 10.97 mmol) in CH_2Cl_2 (10 mL) was added drop-wise via syringe to a cold (0 °C) solution of cyanoacetic acid (0.621 g, 7.3 mmol) in CH_2Cl_2 (15 mL) under argon. The reaction mixture was then allowed to stir for 10 minutes at 0 °C. 1-Ethyl-3-(3-dimethylaminopropyl)-carbodiimide (EDC) (2.1g, 10.97 mmol) was then added in one portion and the reaction was allowed to stir overnight at 0 °C. The reaction was then concentrated in vacuo and purified via silica gel flash chromatography (0-2% MeOH/CH2Cl2) to give **C** (1.4 g, 83%) as a clear yellow oil. (**C**): R_f = 0.36 (10 % MeOH/EtOAc)

^{1}H NMR (500 MHz, $CDCl_3$) δ 7.04 (bs, 1H), 3.63-3.65 (m, 6H), 3.55-3.59 (m, 4H), 3.45-3.48 (m, 2H), 3.39 (s, 2H), 3.37 (s, 3H); 13C (125 MHz, CDCl3) δ 161.5, 114.8, 71.9, 70.6, 70.4, 70.2, 69.3, 59.0, 40.1, 25.9; HRMS calcd for $C_{10}H_{18}N_2O_4Na$ $[M+Na]^+$ 253.1159, found 253.1161 by ESI.

(E)-2-cyano-N-(2-(2-(2-methoxyethoxy)ethoxy)-ethyl)-3-(6-(piperidin-1-yl)naphthalen-2-yl)acrylamide (ARCAM-1)

To a solution of previously reported (Chapter 2) 6-(piperidin-1-yl)naphthalene-2-carbaldehyde (0.15 g, 0.627 mmol) and **C** (0.115 g, 0.501 mmol) in THF (2.5 mL) was added piperidine (0.01254 mmol) and the reaction was heated to 50 °C for 16 hours. The reaction was then concentrated in vacuo, adsorbed on to silica, and purified via silica gel flash chromatography (0-20% acetone/toluene) to give **ARCAM-1** (138 mg, 61%) as an orange solid. (**ARCAM-1**): R_f = 0.25 (5 % acetone/toluene);

^{1}H NMR (500 MHz, $CDCl_3$) δ 8.33 (s, 1H), 8.11 (s, 1H), 8.00-8.02 (dd, J = 8.5 Hz, 1.5 Hz, 1H), 7.69-7.71 (d, J = 9.5 Hz, 1H), 7.60-7.62 (d, J = 8.5 Hz, 1H), 7.24-7.26 (m, 1H), 7.01 (bs, 1H), 6.84 (m, 1H), 3.64-3.66 (m, 6H), 3.62-3.63 (m, 4H), 3.54-3.55 (m,

2H), 3.35 (s, 3H), 3.12-3.34 (m, 4H), 1.69 (m, 4H), 1.61-1.62 (m, 2H); ^{13}C (125 MHz, $CDCl_3$) δ 161.2, 152.9, 151.6, 137.2, 133.8, 130.3, 127.2, 126.6, 126.1, 125.7, 119.4, 117.8, 108.6, 100.5, 71.9, 70.6, 70.6, 70.5, 69.4, 59.0, 49.5, 40.2, 25.5, 24.3; HRMS calcd for $C_{26}H_{32}N_2O_5Na$ $[M+Na]^+$ 474.2363, found 474.2363 by ESI.

Preparation of Aβ(1-42) fibrils

Aggregated Aβ peptide was prepared by dissolving Aβ42 in 1xPBS pH 7.4 to a final concentration of 100 μM. This solution was magnetically stirred at 1200 rpm for 3 days at room temperature. Aggregation state was verified by Thioflavin-T activity.

Fluorescence studies with aggregated amyloid fibrils

15 μL of the aggregated amyloid solution was added to 285 μL of the probe (5% DMSO in nanopure water) to attain a final concentration of 5 μM Aβ42 and 4 μM of the probe. The solution was transferred to a 300 μL cuvette and the fluorescence was measured at 22.5 °C. Excitation wavelength depended on the probe; ARCAM-1 was excited at 440 nm.

Determination of K_d binding constants to Aβ42

As previously reported, in order to estimate the binding constant (K_d) for the probe-Aβ complexes from the fluorescence studies, we made the following assumptions:

1. All probes are completely in solution and free of any significant competing binding process such as self-aggregation.
2. The concentration of unbound probes can be approximated as close to the total concentration of the probes.

3. The binding sites in the aggregated Aβ peptides are not completely occupied at the concentration of Aβ binding probes used for the fluorescence studies (i.e., the experiments are carried out under non-saturated binding conditions).

Pre-aggregated Aβ(1-42) (5 μM final concentration) was mixed with various concentrations of ARCAM-1 in 5% DMSO in nanopure water and their K_d's were determined by fitting data to a one-site specific binding algorithm: $Y = B_{max}*X/(K_d+X)$, where X is the concentration of the probe, Y is specific binding fluorescence intensity, and B_{max} corresponds to the apparent maximal observable fluorescence upon binding of probes to aggregated Aβ42 peptide.

Hydrolytic stability studies of ARCAM-1 in PBS solution

A solution of ARCAM-1 was prepared at 100 μM in pH 7.4 1X PBS with 5% DMSO (by volume) and incubated quiescently at room temperature. Aliquots from this solution were removed at selected time points and flash frozen at -78°C. Aliquots were then warmed to room temperature and probe stability monitored by LC-UV-MS equipped with a CapCell MGIII C18 column with a 3μm particle size. The absorption was measured at 254 nm, 280 nm, and 480 nm using a solvent gradient of 2.5% to 100% MeCN in deionized H_2O with 0.1% formic acid at a flow rate of 0.3 mL/min. Relative probe stability was determined by integrating the peak area of the probe at different time intervals relative to the peak area at time zero.

The half-life of ARCAM 1 for hydrolysis was determined by linear regression of the relative concentration of **1**, $[\mathbf{1}]/[\mathbf{1}]_0$, as a function of time, t. The half-life was obtained at $[\mathbf{1}]/[\mathbf{1}]_0 = 0.5$

Measurements of pH dependence of ARCAM 1 fluorescence

ARCAM 1 was prepared to a final concentration of 4 μM in 5% DMSO in 1X PBS at various pH values both as free probe in solution and in the presence of 5 μM aggregated Aβ(1-42) (tmax). Sample preparations were incubated at room temperature for 10 minutes prior to measurement. Emission spectra were collected with 450 nm excitation wavelength on a PTI QuantaMaster 40 spectrofluorometer using FelixGX software.

Formulation of ARCAM-1 for *in vivo* application

For *in vivo* studies, AMDX201/ARCAM-1 was prepared as a 10 mg/mL solution in 2:8 dimethyl sulfoxide: propylene glycol. This formulation was made fresh per set of experiments and used within three hours of formulating.

The ARCAM-1 formulation was injected into the Tg AD and prion mice at a final administered dose of 10 mg/mL via a 100 uL intraperitoneal (IP) injection. The retina were then imaged over a 15 minute time-course, with images taken every minute for the duration of the experiment.

Detection of *in vivo* retinal deposits with ARCAM-1

Mouse retinal scans were performed using a Phoenix Systems Micron IV ophthalmoscope equipped with a long-pass and FITC band-pass filter. Mice pupils were first dilated with one drop of a 1% tropicamide solution (Akron) and one drop of a 2.5% phenylephrine hydrochloride solution (Paragon). Mice were then anesthetized with an intraperitoneal (IP) injection of ketamine and xylazine at 10% of the body weight.

For retinal imaging, mice were kept on a heated pad and their eyes kept moist with a 2.5% hydroxylpropyl methylcellulose (hypromellose) ointment (GONAK) (Akron, Lake Forest, Il).

***In vivo* aggregate qualification and quantification**

200 by 200 pixel images from the fundus camera were uploaded to FIJI for intensity processing. Briefly, the images were reduced to an 8-bit grayscale and then analyzed for their bulk fluorescence intensity over the entire circular image. The region of interest (ROI) corresponding to the optic nerve intensity was used as an internal reference for normalization.

Post-mortem histology and tissue analysis

Mice were euthanized by CO_2 followed by cervical dislocation, and their eyes enucleated. The left (OS) eye was placed in 4% paraformaldehyde at room temperature for 2.5 hours and the right (OD) eye was embedded in optimal cutting temperature compound (OCT) at -80C.

The OS eye was dissected and the retina was then placed in methanol (MeOH) for 20 minutes and then transferred to 1xPBS for 30 minutes, and then treated with the appropriate reagents for histological analysis.

Initial retina tissues were mounted using DAKO fluorescent mounting medium without any additional processing after initial MeOH and 1xPBS treatment. After imaging, the coverslips were removed and the tissue retrieved for either *ex vivo* ARCAM-1 staining or with immunofluorescence.

Quantification and characterization of retinal deposits

While visual analyses of the fluorescence retinal images from the Phoenix fundus camera could distinguish AD from prion pathologies based on morphology, we aimed to quantify and characterize the retina deposits. Parameters for detection and quantification of fluorescent objects in the retinal images were set in ImagePro. I performed two sets of measurements that used either a region-based detection where high-intensity pixels in the fluorescence gray-scale images were detected as a grouped set along a set radius, or using a point-based detection method where only adjacently localized high-intensity pixels were counted (Figures 4.27).

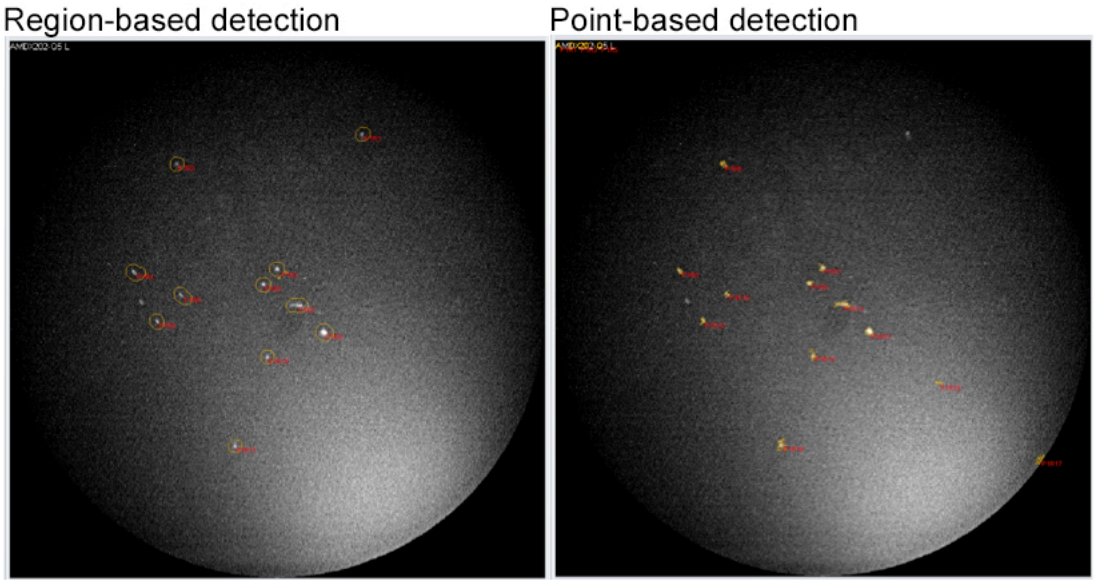

Figure 4.27 Two detection methods for quantifying and measuring plaque morphology.

While the first region-based method was able to achieve a higher selectivity for fluorescent objects with low-false positives, the measured morphology parameters were heavily overestimated. Ultimately I decided to use the point-based detection

method, which did have a higher rate of identifying false-positives, but gave more accurate measurements for the plaque morphology.

Brain tissue samples

Male and female transgenic mice overexpressing wild type mouse PrP (Tga20) were inoculated with the mouse-adapted prion strain mCWD and bovine adapted prion strains ME7 and 22L, and were euthanized upon developing terminal signs of prion disease. Transgenic mice (19959) harboring the Aβ plaques express the mutant human amyloid precursor protein APP_{SweInd}, which bears both the Swedish (K670N/M671L) and the Indiana (V717F) mutations, under the control of the Syrian hamster prion protein promoter. Mice were euthanized between 9 - 13 months of age for AD, and after 15-16 months for prions, and their brains extracted into optical cutting temperature (OCT) fixation media. Frozen brain sections were cut from these frozen blocks.

Staining frozen brain samples

Frozen tissue sections were dried for 1 hr, hydrated with 100%, 95%, and 70% ethanol for 5 min each, and then rinsed with deionized water. Sections were then buffered with phosphate-buffered saline (1X PBS) for 30 min. ARCAM-1 was diluted 1:50 in 1X PBS (from stock solutions of 3mM) to a final concentration of 60 μM, added to brain sections, incubated for 30 min at room temperature, washed three times with 1X PBS, and coverslipped using DAKO fluorescent mounting media.

Fluorescence microscopy

Brain tissue samples were excited with a 488 nm laser on an Olympus FluoView FV1000 spectral deconvolution confocal microscope with 5% power under 10x magnification. The emission spectra of ARCAM-1 bound to PrP^{Sc}, and background were collected in 1 nm increments from 450-650 nm. A minimum of 10 measurements was collected for each compound bound to plaque and non-plaque regions as a background control. The wavelength corresponding to the maximum relative fluorescence intensity was taken as the emission λ_{max}.

Brightfield color imaging

Brain tissue sections were imaged under an Olympus MVX10 Macroview equipped with a MWB2 (Japan) long-pass filter and a 2x MVX (PF) Plan Apochromat lens with a 0.5 numerical aperture. Each sample was illuminated with epifluorescence and imaged with an exposure time of 0.2-0.8 sec, depending on sample.

4.5 Additional Figures

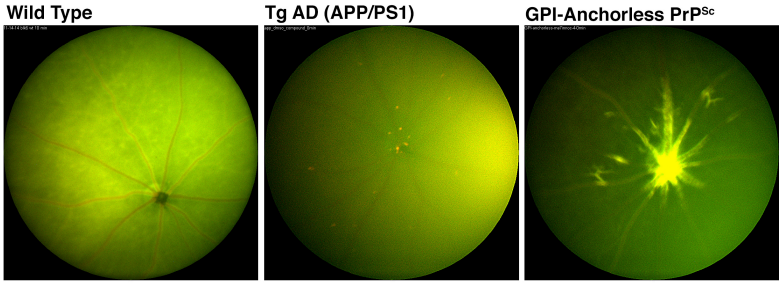

	Wild Type	APP/PS1	GPI-anchorless Prion[a]
No. Objects	None detected	15.5 ± 3.9	41.5 ± 29.0
Size (μm^2)	N/A	147.1 ± 64.0	841.9 ± 1392.7
Radius (μm)	N/A	7.85 ± 0.42	15.1 ± 10.5
Major axis (μm)	N/A	23.7 ± 2.8	51.2 ± 35.9
Minor axis (μm)	N/A	15.2 ± 1.5	26.0 ± 19.0
Circularity	N/A	0.33 ± 0.07	0.39 ± 0.14

Figure 4.28 ImagePro analyses of retinal fluorescence images from WT, AD, and prion mice.

Acknowledgements

Chapter 4 is a partial reprint of the material as it appears in "Real-time Monitoring of Alzheimer's-related amyloid via Probe Enhancement-Fluorescence Correlation Spectroscopy". Guan, Yinghua; Cao, Kevin J.; Cantlon, Adam; Elbel, Kristyna; Theodorakis, Emmanuel A.; Walsh, Dominic, Yang, Jerry, Shah, Jagesh V. (2015) *ACS Chemical Neuroscience*, 6 (9), 1503-1508. I am co-author on this publication.

Chapter 4 is also based on material currently being prepared for submission for publication "A Fluorescent Method to Monitor Amyloidosis in the Retina". Cao, Kevin J.; Aguilar-Calvo, Patricia; Liu, Jun; Sigurdson, Christina J.; Yang, Jerry. *In preparation.* I am the primary author on this publication.

Chapter 5

Use of environmentally sensitive fluorophores for the detection of oligomeric and fibrillar amyloid species in solution

5.1 Introduction

The use of environmentally sensitive fluorophores as amyloid-binding compounds has predominately been focused on the detection of amyloid plaques in neuronal tissue. While these plaques are a defining feature of Alzheimer's Disease (AD) pathology and other neurodegenerative diseases, recent evidence has shown that the causative agents for the clinical symptoms in these diseases are the soluble aggregate species.[155,156] Due to their transient appearance during amyloid formation and aggregation, the study of these soluble species has been largely dependent on indirect fluorescence measurements and computational modeling.[156]

In the case of AD, how the intrinsically disordered Aβ monomer converts to the fibrillar aggregates found in amyloid plaques and the relationship between Aβ aggregation and disease remains poorly understood. However, it is widely believed that intermediates in Aβ aggregation, referred to as oligomers, are the initiators of a complex molecular cascade that, over a course of decades, leads to dementia (Figure 5.1).[87] To date the real time study of Aβ aggregation in solution has been limited by methods that best detect abundant assemblies of protofibrils and mature fibrils.[157]

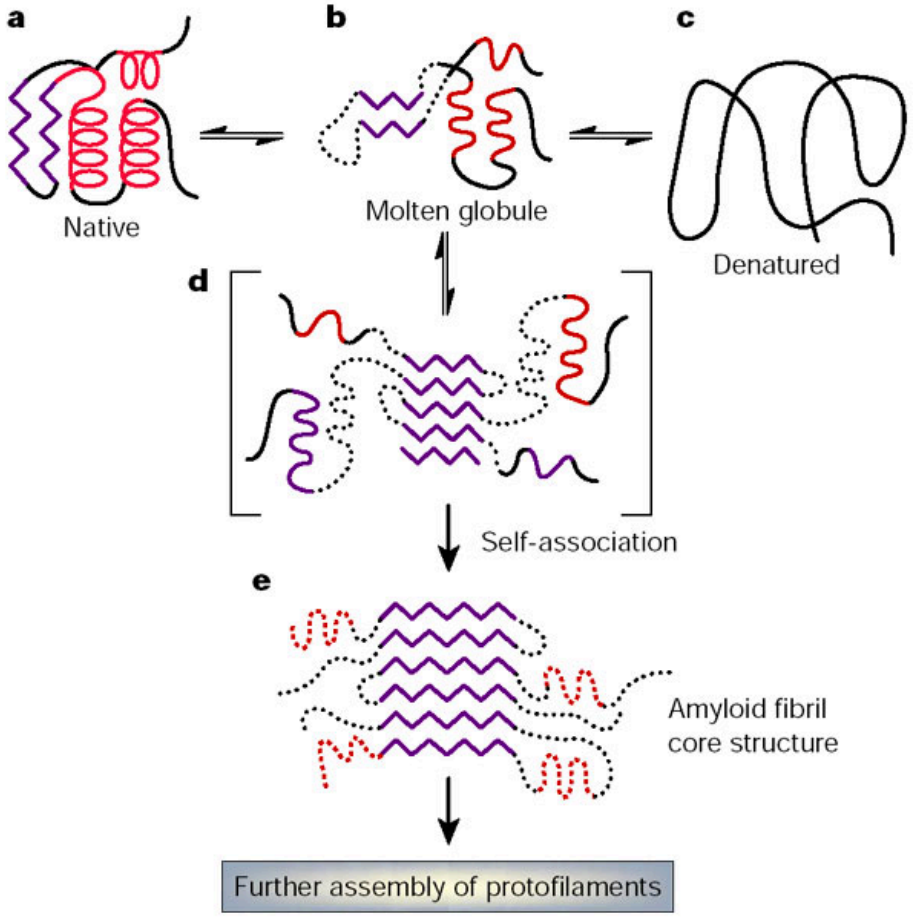

Figure 5.1 The amyloid cascade hypothesis rationales that the equilibrium between natively folded and misfolded protein conformations can shift towards the latter, resulting in self-association and amyloid aggregation. Adapted with permission from Nature Publishing Group, Nature. *Folding proteins in fatal ways*, 426, 900-904. Figure 1, copyright 2003.

In systemic biofluids, amyloidosis occurs with the absence of plaques, with evidence supporting the formation of oligomeric and fibrillar species instead. Recent work by Buhimschi and coworkers in 2014 reported evidence for the presence of amyloid aggregates in the urine of pregnant women symptomatic for pre-eclampsia (PE).[76,158] Using traditional CR absorption and ThT emission spectroscopy, they showed the ability of these small molecules to detect amyloid aggregates in urine samples. Due to the complex composition of urine, and in particular urine from pre-eclampsia patients, development of methods to accurately detect the presence of amyloidosis could potentially help with early diagnosis of the syndrome.

Here, I describe two efforts in the detection of amyloids in non-tissue environments. First, using ARCAM-1 described in Chapter 4, I we collaborated with Jagesh Shah and coworkers at Harvard Medical School to develop a Probe Enhancement-Fluorescence Correlation Spectroscopy (PE-FCS) technique to detect Aβ aggregates at earlier time points along the aggregation pathway in comparison to standard bulk fluorescence measurements. Second, in collaboration with Jamie Do in the Yang lab and Mana Parast and Louise Laurent in the Department of Pathology and Reproductive Medicine at UCSD, I performed bulk ARCAM-1 binding experiments in urine from pregnant women in order to determine if our fluorophores could also detect systemic amyloid in complex biofluids.

5.2 Results & Discussion: PE-FCS development

Real time detection of aggregates traditionally relies upon the use of fluorophores, such as ThT, that are applied in bulk fluorescence measurement assays. When ThT is introduced to a solution of amyloidogenic proteins or peptides, its emission intensity increases in a dose-dependent manner with increasing population of aggregates. A major limitation of amyloid aggregation assays that use ThT, however, is that the bulk fluorescence intensity increases above background only once protofibril and fibril structures have become abundant in solution, precluding the capability to detect small, transient intermediates.[57,159] Moreover, ThT has a significant background fluorescence as an unbound dye, decreasing the signal to noise ratio for sensitive measurements of small assemblies.

Fluorescence correlation spectroscopy (FCS) is a time-resolved spectroscopic technique that can measure the concentration and size of fluorescently labeled particles.[160] This method has wide applications in the study of aggregation phenomenon such as protein oligomerization or formation of large aggregates such as prions.[161–164] FCS has also been used to study Aβ aggregation using fluorescently labeled peptides.[165–168] However, the effect of the fluorescent label covalently attached to the peptide on assembly dynamics in these prior studies remains unclear. Moreover, the requirement of incorporation of exogenously added fluorescent Aβ peptides complicates translation to detect amyloid species in human biofluids such as cerebrospinal fluid. In order to circumvent these limitations, we explored whether ARCAM-1 could be used to detect intermediate species along the Aβ aggregation pathway, since this compound undergoes strong fluorescence emission when bound to

aggregates of amyloidogenic proteins and has a low unbound fluorescence. Fluorescence enhancement in the bound state can dramatically increase the signal to noise and permit fluorescent intensity fluctuations (required for FCS measurements) that are derived primarily from amyloid-bound probe rather than unbound probe in solution.

I previously described the ANCA family of fluorescent probes that bind Aβ assemblies in solution and in tissue.[104,113] These probes exhibit a large enhancement in fluorescence properties upon binding to aggregates compared to the weaker fluorescence of the free compounds in solution. For the experiments in this study, we used the more biocompatible ARCAM-1 fluorophore, described in Chapter 4.

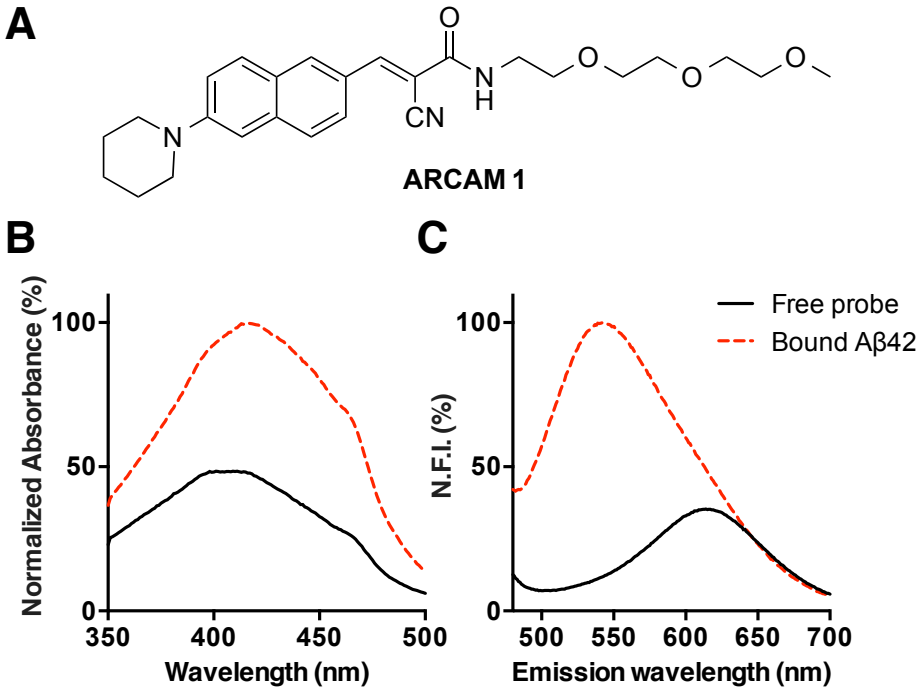

Figure 5.2 Structure and spectroscopic properties of fluorescent ARCAM-1. A) Structures of fluorescent, aggregate-binding compound ARCAM 1. Excitation (B) and emission (C) properties of 1 in the presence or absence of aggregated Aβ(1-42).

This probe displayed an ~8-fold increase (at a λ_{em}(bound) of ~540 nm) in fluorescence emission upon binding to aggregated Aβ in solution versus probe without Aβ. The affinity of ARCAM-1 for aggregated Aβ (K_d = 870 ± 280 nM at pH 7.4) was comparable to the binding of similar fluorescent probes.[113] An important advantage of ARCAM-1 for aggregation studies is its stability in aqueous solutions and its broad insensitivity of fluorescence wavelength as a function of pH (Figure 5.3).

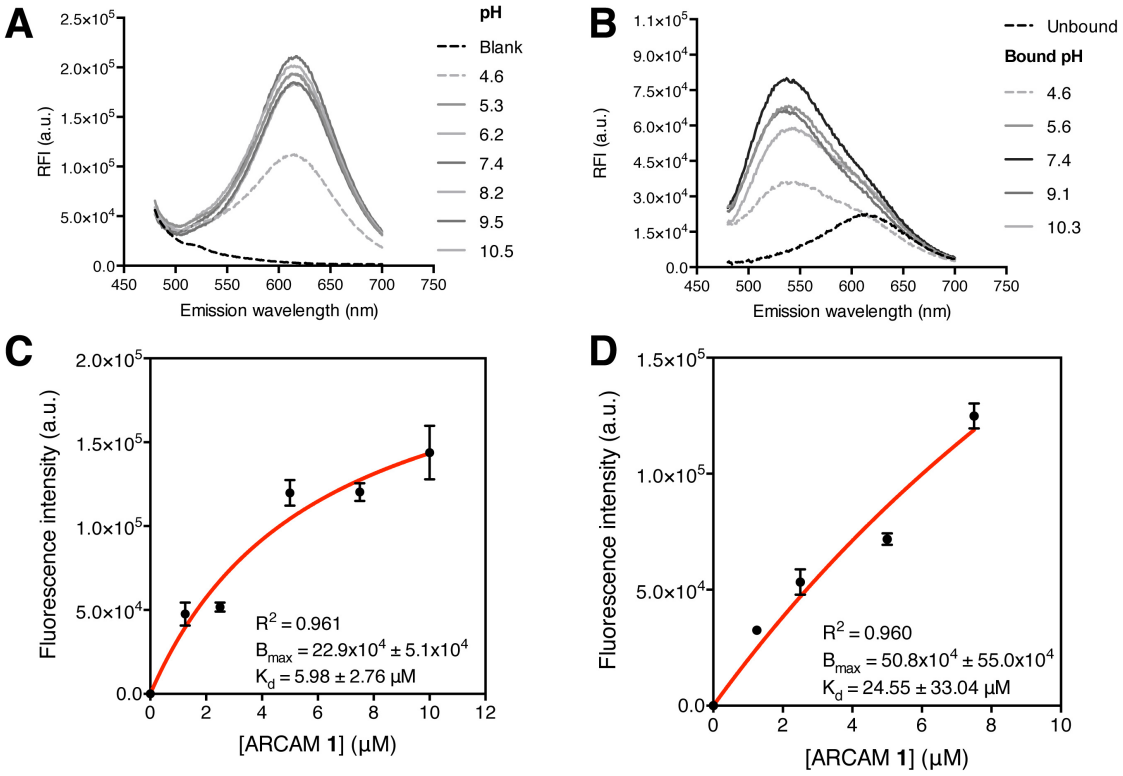

Figure 5.3 pH dependence of ARCAM 1 fluorescence free in solution (A) and bound to Aβ(1-42) aggregates (B). K_d dependence on pH shown for pH 5.6 and 9.1 Measurements were performed in independent triplicates and averaged; error bars indicate standard deviation, where visible. RFI = relative fluorescence intensity.

Importantly, this meant that there was negligible change in the effective concentration of ARCAM-1 over the aggregation time-courses. In addition, Shah and

coworkers showed that ARCAM-1 showed similar multi-photon excitation to that of ThT (Figure 5.4), but was much brighter than ThT.

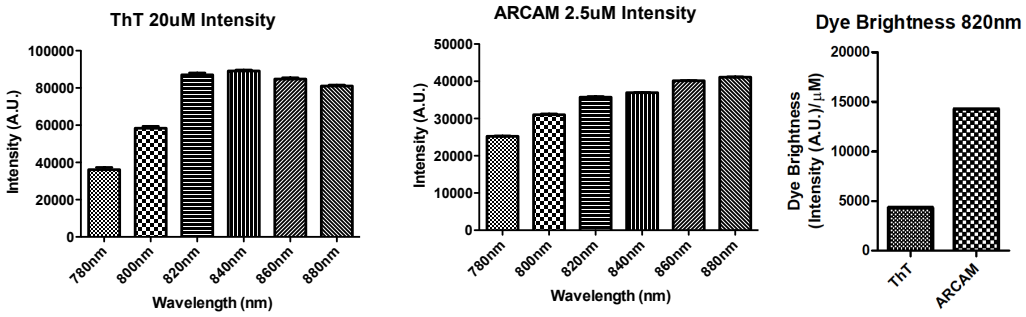

Figure 5.4 Unbound dye 2-photon emission and fluorescence brightness.

To determine whether ARCAM-1 could be used to monitor Aβ (1-42) aggregation kinetics, they prepared a 10 mM solution of peptide monomers completely free of aggregates added ARCAM-1 and monitored total fluorescence at intervals until a stable maximal fluorescence was achieved.[159,169] In parallel, an identical time course was monitored by ThT. Experiments were conducted at room temperature and were shaken in between sample readings. ARCAM-1 and ThT time courses looked identical when the probe was present in solution throughout the aggregation process (Figure 5.5).

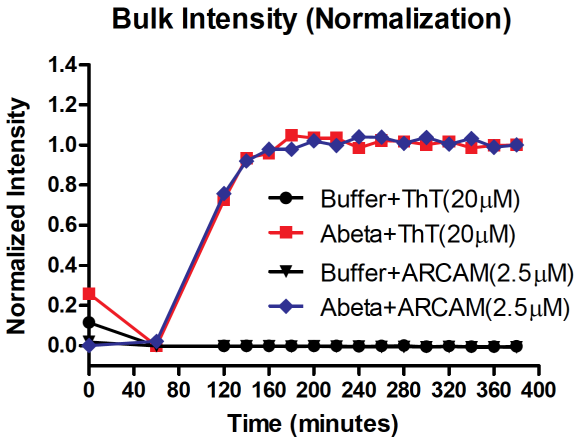

Figure 5.5 Aβ(1-42) aggregation kinetics are not perturbed by the addition of ARCAM-1 or ThT.

Probe-Enhancement FCS relies on the increase in fluorescence that occurs as a result of the probe binding to its target. To compare fluorescent probes for detecting Aβ aggregates, they measured FCS curves for solutions containing diluted, pre-aggregated Aβ and the probes. They added either ThT or ARCAM-1 to pre-aggregated Aβ samples. Separately, we added TAMRA-labeled Aβ(1-42) peptides or ARCAM-1 to another set of matched samples. FCS measurements of the probe-Aβ solutions were taken after 30 minutes of incubation at room temperature to permit probe binding (for ThT and ARCAM-1) or monomer incorporation (for TAMRA-Aβ). Autocorrelation spectra of ThT-Aβ solutions showed the presence of primarily large aggregates, whereas ARCAM-Aβ solutions of the match sample showed a range of small and large aggregates (Figure 5.6A). Conversely, TAMRA-Aβ solutions showed small aggregates whereas measurements of the matched ARCAM-Aβ solution showed a range of small and large aggregates (Figure 5.6B). Together these point to ARCAM-1 detecting a larger dynamic range of aggregate sizes compared to ThT or

TAMRA-labeled peptide, making it a useful choice for further studies by PE-FCS methods.

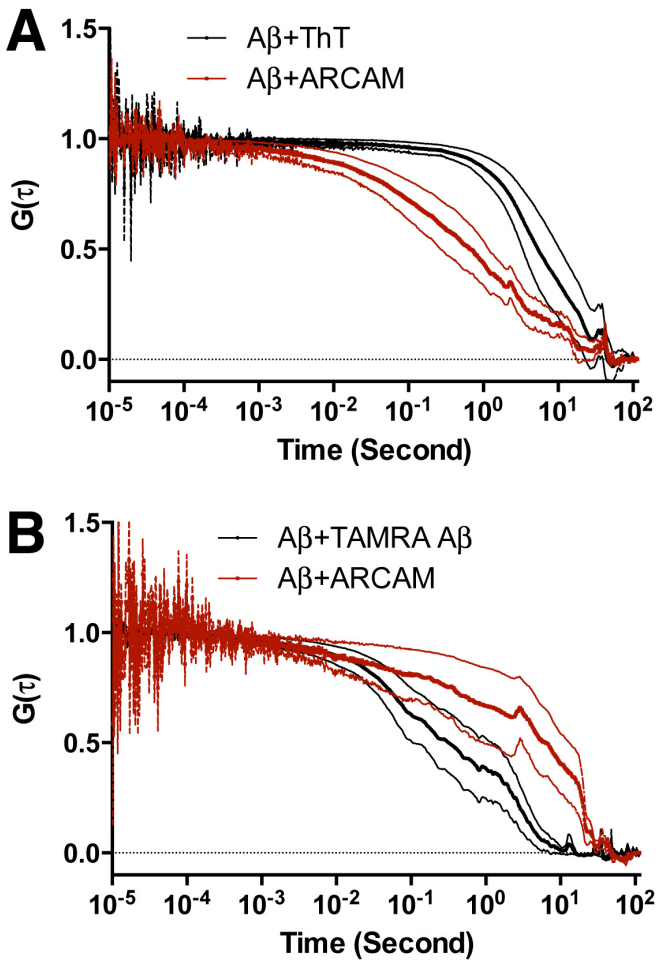

Figure 5.6 Comparison of aggregate size measured using ThT, ARCAM 1 and fluorescently labeled Aβ peptide. Dyes (ThT or ARCAM 1) or TAMRA-labeled Aβ(1-42) peptides were added to pre-aggregated Aβ samples. FCS measurements revealed larger species in the ThT labeled sample (A, $p < 0.05$ for 0.1, 1s delay time). ARCAM-1 revealed larger species in the pre-aggregated samples when compared to TAMRA-Aβ (1-42) peptides (B, $p<0.05$ for 10s delay time).

Bulk fluorescent measurement of an Aβ(1-42) aggregation time course (Figure 5.7A), in the presence of ARCAM-1 were also carried out in parallel with FCS

measurements. Aliquots were collected at 20-minute intervals and the samples were analyzed by multi-photon FCS.[170] The presence of bright fluorescent bursts in the intensity traces are indicative of aggregated amyloid species that were bound by ARCAM-1 diffusing through the multi-photon excitation volume (Figure 5.7B). Burst analysis of these intensity traces counts the statistically significant events (intensity values in top 0.01%) in a fixed time window to determine if ARCAM 1-bound material is present in significant quantities.

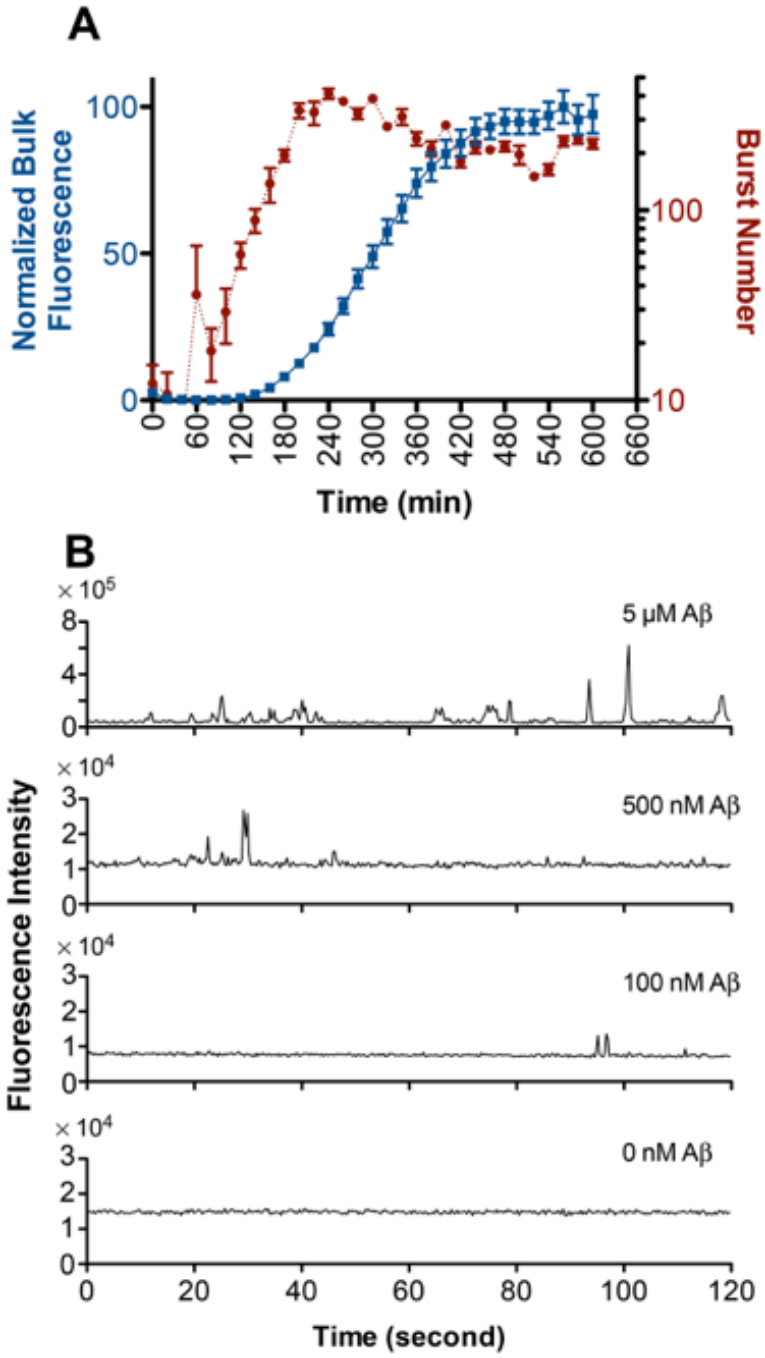

Figure 5.7 Monitoring the kinetics of aggregation of Aβ (1-42) peptides by bulk fluorescence and FCS burst analysis. A) Increase in total fluorescence (blue squares) or fluorescent burst number (red squares) in solutions containing Aβ and fluorescent ARCAM-**1**. B) Detection of aggregates interacting with ARCAM-**1** by monitoring the intensity and number of fluorescent bursts within a 120 second acquisition time window as a function of the concentration of total peptide.

This analysis revealed the presence of ARCAM-1-bound aggregated species at significantly earlier time points compared to aggregates that could be observed using bulk fluorescence measurements (Figure 5.7A, red circles compared to blue squares). Moreover, analysis of solutions of pre-formed aggregates revealed that the probe could detect aggregated species at total peptide concentrations as low as ~100 nM (Figure 5.7B). Notably, solutions containing fluorescent ARCAM-1 alone (Figure 5.7B, bottom trace) or Aβ peptide alone showed no fluorescence bursts by PE-FCS measurement.

In order to gain additional insight into the properties of the aggregates detected by PE-FCS, they also estimated the size of the species at the onset of increased burst activity (i.e., during the first 120 min of the aggregation of Aβ monomers, Figure 5.7A). To determine the size of the diffusing species, intensity time traces were subjected to autocorrelation analysis.[170,171] The result is a correlation function G(τ) that is proportional to the number of burst events while a molecule is resident in the excitation volume for the delay time, τ (Figure 5.8). The residence time is directly related to the translational diffusion constant and, therefore, its size. For mixed species solutions, individual species sizes can be distinguished when they exhibit sufficiently different diffusion constants (~5-fold difference in size). However, for more complex mixtures, FCS can only provide an average diffusion constant that is biased towards the more fluorescent species.

In addition, the G(0) point is inversely proportional to the number of particles in the solution. For ARCAM-1-Aβ (1-42) solutions, there were two diffusing species: unbound ARCAM-1 and bound to Aβ . The FCS curve at time = 0 min was analyzed

by a one component model, producing a diffusion coefficient (D1 = 148 ± 25 $\mu m^2/s$) consistent with the free diffusion of ARCAM-1.[41] They also fit a two-component fitting model, to distinguish free dye from bound, was used for the analysis of the aggregation time series. Three representative FCS curves with fitting are shown in Figure 5.8 for different time points.

Time autocorrelation analysis of intensity fluctuations revealed diffusing assemblies with a mean diffusion constant of 3.42 $\mu m^2/s$ (range: 2.99-3.85 $\mu m^2/s$) at 120 min. This mean diffusion constant corresponds to a hydrodynamic radius between 64-82 nm in size for a spherical particle and 300-420 nm for an 8 nm diameter rod. This hydrodynamic radius and proposed rod length are consistent with protofibrils, an early assembly intermediate in Aβ aggregation. [159]

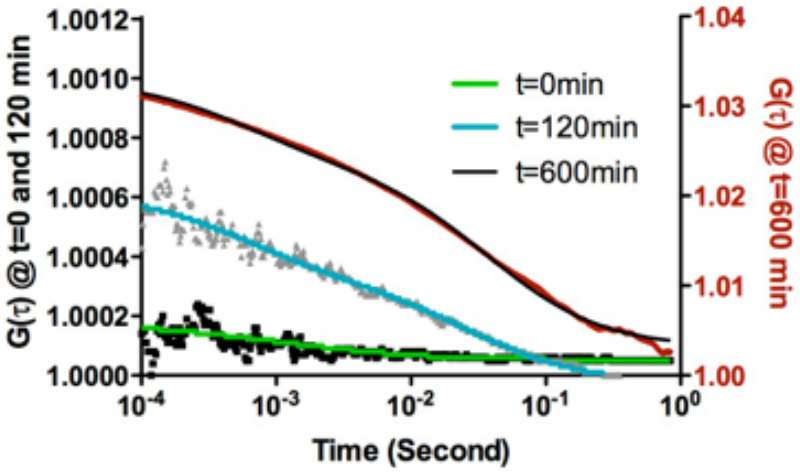

Figure 5.8 Representative raw FCS auto-correlation curves with fitting curves at three time points (t=0,120 and 600 minutes) are plotted together for comparison. Time points of t=0 min and t=120 min share the same left y-axis and the t=600 min time point uses the right y-axis with a different scale. The amplitude of autocorrelation curve G(0) increases along the reaction time point 0, 120 and 600 min, indicating a decrease in particle number for the dominant fluorescent species. The autocorrelation functions show increasing contribution from long delay times indicating the increasing size of the particles.

5.2.1 Conclusions

In collaboration with the Shah group, we have demonstrated that the combination of a novel amyloid-binding fluorophore and FCS enabled the sensitive direct detection of amyloid assemblies at time points at earlier stages than conventional bulk fluorescence measurements. Here, we detected, in real-time, amyloid aggregates that were only a few hundred nanometers in length, which is consistent in size with protofibrillar forms of Aβ intermediates.[87,159] Moreover, ARCAM-1 performed well in the detection of a large dynamic range of aggregate sizes in FCS measurements when compared to ThT or TAMRA-Aβ peptides. This PE-FCS method can detect low concentrations of early amyloid assembly intermediates that were consistent in size with a previous FCS study that used covalently labeled Aβ peptides. A major advantage of the method reported in this work is that using an exogenously added fluorescence reporter (as opposed to fluorescently labeled peptides) may make it possible to analyze patient samples containing a large mixture of native aggregated species. The combination of a fluorescent reporter and PE-FCS-based detection of aggregated Aβ represents a potentially important step towards establishing a reliable method for studying aggregate intermediates that may be present in human cerebrospinal fluid. [172]

5.3 Results & Discussion: Development of fluorescent assays to detect amyloidosis in pre-eclampsia

Pre-eclampsia (PE) is a fetus-linked gestational disorder affecting approximately 5% of pregnancies, with an estimated ~63,000 deaths due to complications associated with the syndrome.[76,173,174] The clinical symptoms for the disease have been established as the presentation of pregnancy-induced hypertension and proteinuria after 20 weeks of gestation. Left untreated, the disease can progress into eclamspia, which is defined by seizures, stroke, and severe bleeding. Although the only current treatment is delivery, early detection of the condition can help discern between PE and other underlying disease, which, in turn, can help with patient management.

Recent work by Buhimschi and coworkers showed the presence of amyloid precursor protein (APP) processing enzymes in the placenta and congophilic species in urine.[76] These results ultimately suggested a possible fetus-linked protein-misfolding and aggregation source for the development of PE. In order to detect protein aggregation in the urine, they used CR and ThT spectroscopic activity (changes in absorption and fluorescence emission, respectively), with the latter showing a near 10-fold enhancement of fluorescence upon binding from the urine of a patient with severe PE, indicating the presence of amyloid.[76]

Given these results, we hypothesized that environmentally sensitive fluorophores in general would be able to detect these amyloid species. Initial work in collaboration with Jamie Do (a previous MS student in the Yang lab) had shown that

the ARCAM-1 fluorophore had an increase in fluorescence emission when incubated with urine from patients suffering from PE. In order to expand on the results from this pilot study of four pre-eclampsic patients and four healthy controls, we began an extensive blinded study in collaboration with the UCSD Hillcrest Medical Center on approximately 60 pregnant women from the greater San Diego area. Patient urine samples were collected over the course of the second and third trimesters of pregnancy (11-39 weeks for these patient samples). Fluorescence binding assays revealed that urine typically had a sharp autofluorescent band with a λ_{max} at 510 ± 9 nm that varied in intensity (Figure 5.9, blue dashed lines). Upon binding of ARCAM-1, we saw an red-shift of the fluorescence emission λ_{max} in patient samples that ranged from 520 - 550 nm, over background autofluorescence (Figure 5.9, green solid lines).

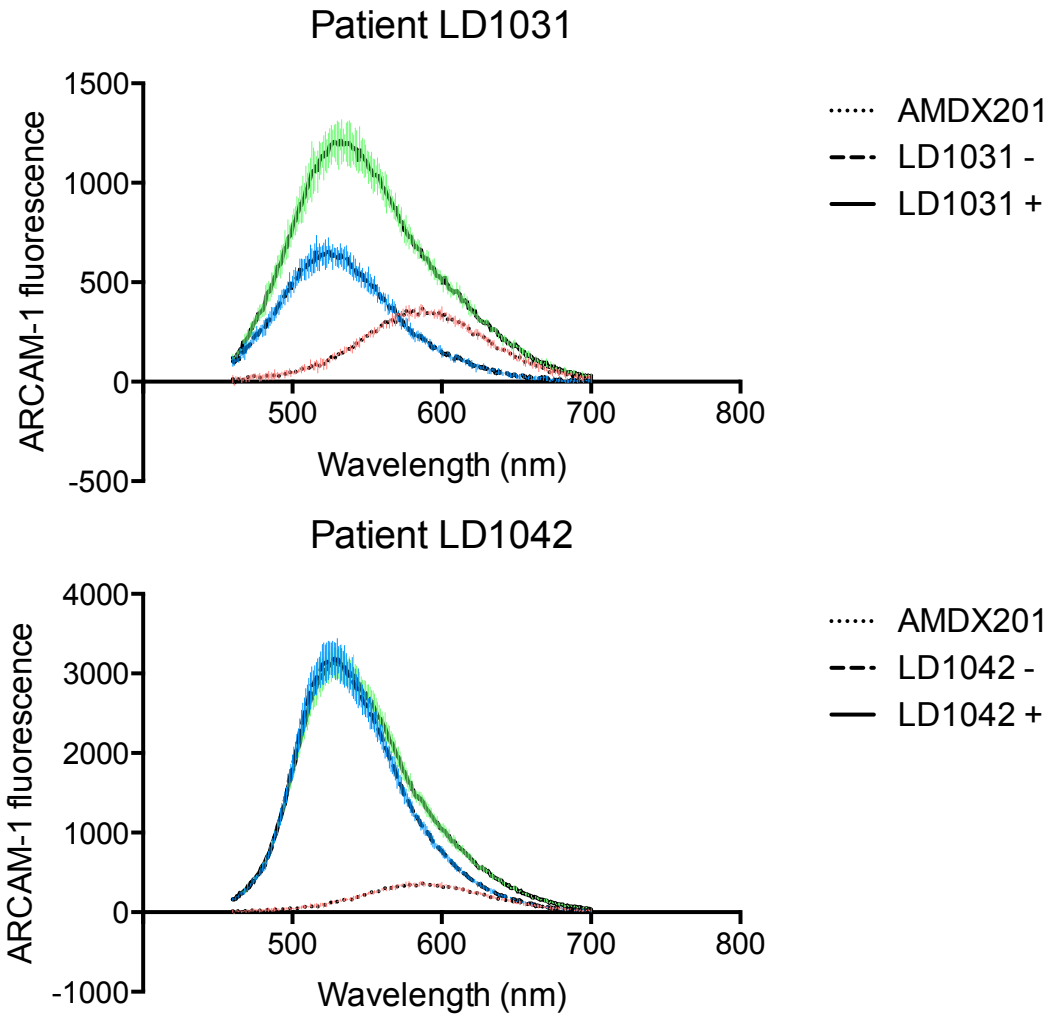

Figure 5.9 Representative fluorescence binding spectra of ARCAM-1 to urine samples from pregnant women. Blue lines indicate native autofluorescence of the urine, green lines indicate fluorescence of ARCAM-1 in the urine samples, and red lines are the free ARCAM-1 fluorescence in the absence of urine.

Upon the adjudication of the patients for whether or not they were pre-eclampsic or if they had other gestational disorders such as hypertension or diabetes, we unblinded our data and plotted the fold increase of fluorescence enhancement for several selected cohorts. We compared the fold increase of ARCAM-1 in urine from healthy patients (45 total) to the urine of those diagnosed with some form of pre-

eclampsia (17 total) and those with no pre-eclampsia, but with hypertension (14 total). Additionally, we separately analyzed the fluorescence intensity of ARCAM-1 in urine from a subset of patients with severe pre-eclampsia (sPET, 7 total patients) from the total pre-eclampsia population.

These four cohorts were then compared against each other using the fold increase of fluorescence emission of ARCAM-1 over background as the metric. Due to the sensitivity of ARCAM-1 to the environment, we chose to perform our fluorescence emission fold-increase and detection analyses using two methods. First we looked at the fold increase of fluorescence at 530 nm, which we previously saw to be the λ_{max} emission for β-amyloid aggregates in neuronal tissue (Figure 5.10). Using the 530 nm $\lambda_{emission}$, we saw that all forms of pre-eclampsia showed significantly higher fold increases of fluorescence emission than those of healthy controls, with a median of 3.4-fold increase for the pre-eclampsic cohort compared to 2.25-fold increase of ARCAM-1 fluorescence for the healthy patient samples ($P<0.01$). Interestingly, comparisons of the healthy cohort against non-pre-eclampsic hypertension (non-PET HTN) patient samples had a decrease in fold-enhancement from a median of 2.25-fold increase for the healthy cohort to 0.03-fold increase for the non-PET HTN ($P<0.05$).

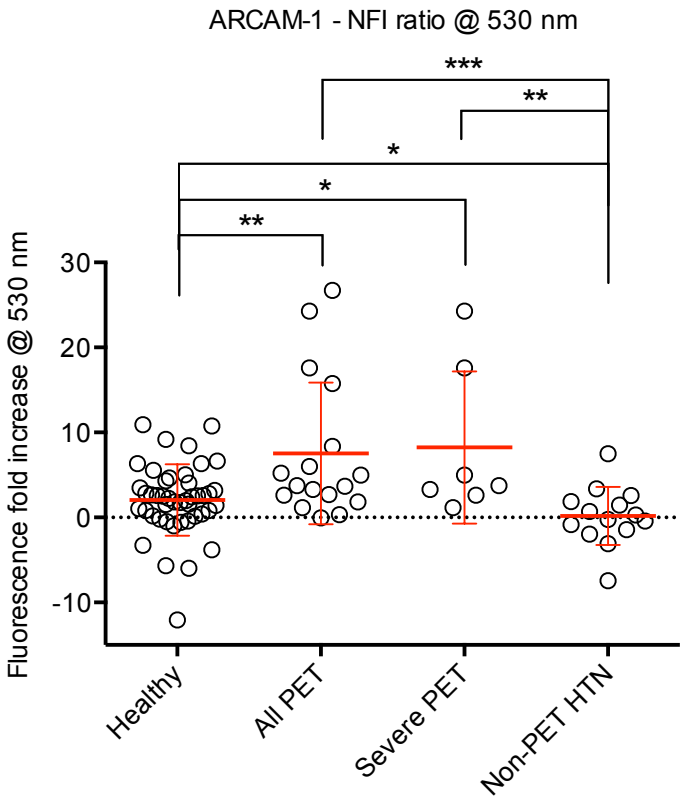

Figure 5.10 ARCAM-1 fold increase of fluorescence emission using λ_{530} upon binding urine samples from healthy patients, preeclampsic patients (PET), and non-preeclampsic patients suffering from hypertension (non-PET HTN). Red bars indicate the mean fold increase with standard deviation.

Because proteinuria may result in the aggregation of different species and conformations of proteins, we next looked at the λ_{max} of the overall emission spectra (Figure 5.11). Here we saw a more pronounced difference in fold increase of fluorescence emission of ARCAM-1 between the four cohorts. As with comparing the observed fold increase of fluorescence of ARCAM-1 at λ_{530}, using the maximum wavelength also showcased the capability of ARCAM-1 to distinguish between healthy and symptomatic cohorts. We compared healthy versus all pre-eclampsic samples and found that the median fold increase of fluorescence upon binding rose

from 1.73-fold increase for the healthy controls to 2.64-fold increase for all forms of pre-eclampsia ($P<0.01$). We also again noted the decrease of the fold increase when comparing healthy to non-PET HTN samples ($P<0.001$). Taken together, these results showed the ability of ARCAM-1 to distinguish pre-eclampsic samples from healthy samples based on the fold increase of fluorescence emission of ARCAM-1 at 530 nm as well as using the maximum fluorescence emission wavelength.

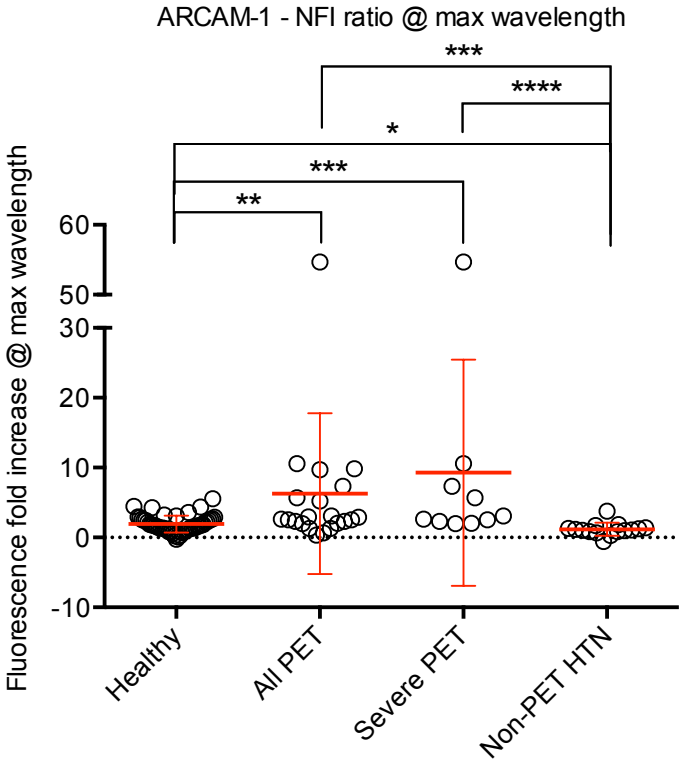

Figure 5.11 ARCAM-1 fold increase of fluorescence emission using λ_{max} upon binding urine samples from healthy patients, preeclampsic patients (PET), and non-preeclampsic patients suffering from hypertension (non-PET HTN). Red bars indicate the mean fold increase with standard deviation.

We next looked at ThT fluorescence emission fold increase at 485 nm as a control experiment. Here we observed that ThT selectively detected pre-eclampsic

patient samples over both healthy and non-pre-eclampsic samples (Figure 5.12). ThT bound to PET samples showed a larger fold increase of fluorescence at 485 nm (1.85-fold increase) than healthy patients (1.27-fold increase) ($P<0.01$). In contrast to ARCAM-1, ThT was not able to distinguish between healthy (1.27-fold increase) and non-PET HTN (1.52-fold increase) samples.

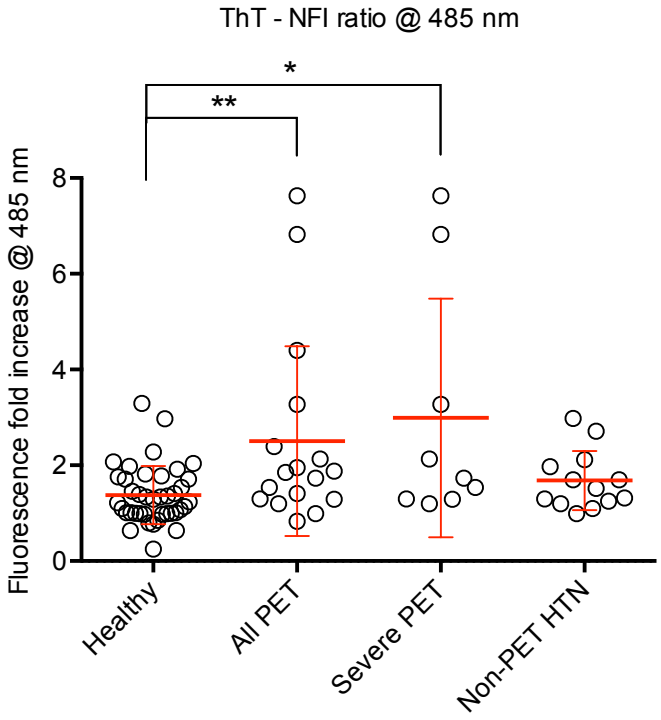

Figure 5.12 ThT fold increase of fluorescence emission using λ_{485} upon binding urine samples from healthy patients, preeclampsic patients (PET), and non-preeclampsic patients suffering from hypertension (non-PET HTN). Red bars indicate the mean fold increase with standard deviation.

Because these grouped analyses showed the potential of ARCAM-1 to detect amyloid aggregates in urine samples from patients, we wanted to further utilize this ability in tracking the fold-increase of fluorescence as a function of gestational age (Figure 5.13). These age-dependent plots showed that while linear regression lines

suggested a potential gestational age-dependent increase of fluorescence fold increase as a function of gestational age for ARCAM-1 λ_{max} and ThT λ_{485} measurements, the poor linear regression correlation indicates that the spot collection method used to obtain patient samples may not be representative of the exact amyloid concentration in urine at that gestational age. Rather, spot collections would be viable for rapid tests to check for the presence of amyloid aggregates.[175]

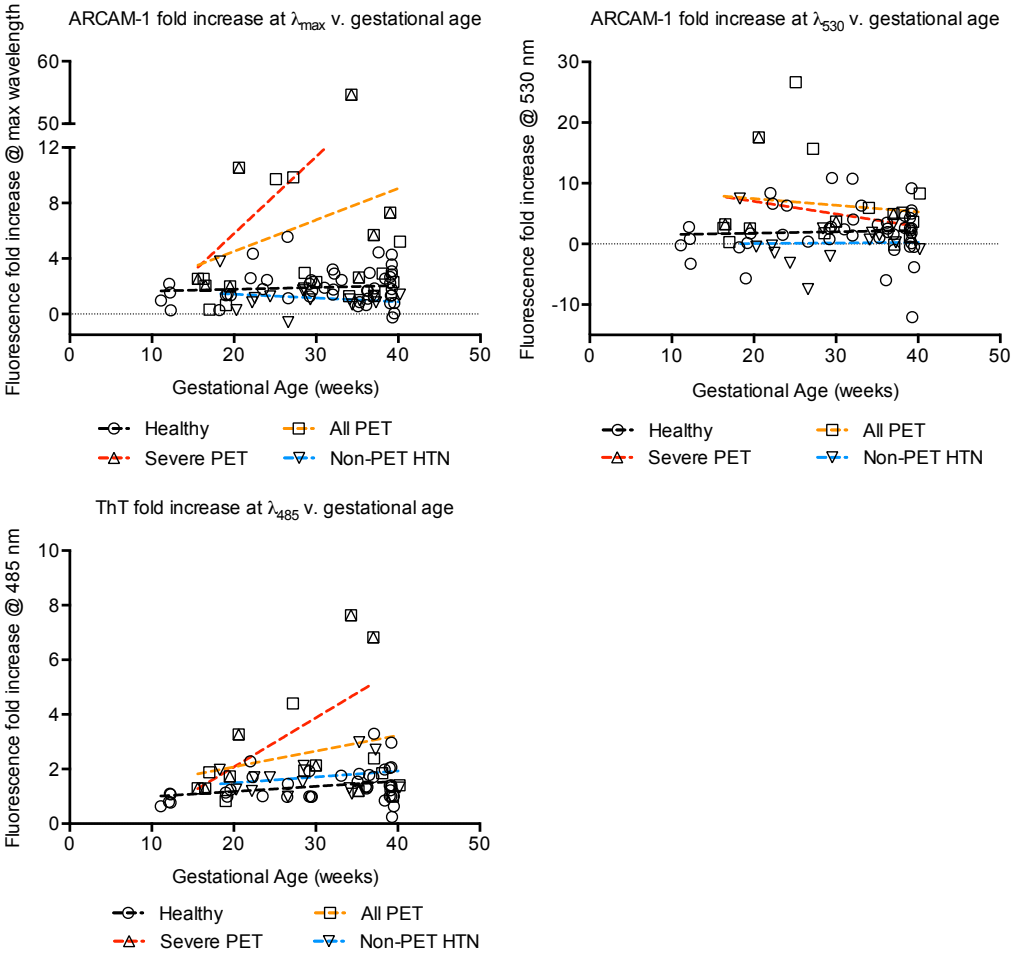

	ARCAM-1 max		ARCAM-1 530		ThT 485	
	Slope	Regression	Slope	Regression	Slope	Regression
Healthy	0.01 ± 0.02	0.01	0.02 ± 0.07	0.002	0.02 ± 0.01	0.09
All PET	0.23 ± 0.30	0.03	-0.11 ± 0.22	0.018	0.06 ± 0.06	0.07
Severe PET	0.55 ± 0.65	0.09	-0.21 ± 0.30	0.109	0.18 ± 0.09	0.39
non PET HTN	-0.03 ± 0.04	0.04	0.01 ± 0.14	0.0004	0.02 ± 0.03	0.06

Figure 5.13 Plots of the fluorescence fold increase of ARCAM-1 and ThT bound to urine samples from pregnant women as a function of the gestational age. Bottom table shows the linear regression fits.

Finally, we generated receiver operating characteristic (ROC) curves for the three methods—that is, the λ_{max}.of ARCAM-1 bound to urine samples, λ_{530}.of ARCAM-1 bound to urine, and λ_{485} for ThT bound to urine —to determine the specificity and sensitivity of ARCAM-1 and ThT towards the detection of amyloid

aggregates in urine. Briefly, ROC curves present the probability of obtaining true-positive diagnoses (i.e. sensitivity) against the probability of obtaining false-positive diagnoses (i.e., specificity). Hypothetically, as the probability of false positives decreases, an accurate diagnostic test would be expected to have an increase in the probability of true-positives. Thus, the closer the curve reaches a 45-degree angle, or linear diagonal line in the ROC curves, the less accurate the test.[176,177]

We plotted the fold increase of fluorescence enhancement for each cohort against each other in order to determine the optimal detection thresholds (Figure 5.14, 5.15, and 5.16). For ARCAM-1 λ_{530} and λ_{max} ROC curves, we saw the high accuracy of this method to distinguish pre-eclampsia samples from non-PET hypertension samples. In contrast, ThT ROC curves for the comparison of these two cohorts showed a near linear curve, indicating poor accuracy for distinguishing these two disease states.

Comparisons of the healthy versus all pre-eclampsia cohorts showed relatively good sensitivity and selectivity for ARCAM-1 λ_{530} and λ_{max} ROC curves, but at values lower than those found for non-PET HTN versus all pre-eclampsia. In general, ThT ROC curves showed an inability to distinguish any two cohorts of patients from each other. Lastly, in comparisons of ARCAM-1 λ_{530} versus λ_{max} ROC curves, the latter method shows the highest accuracies when comparing two cohorts.

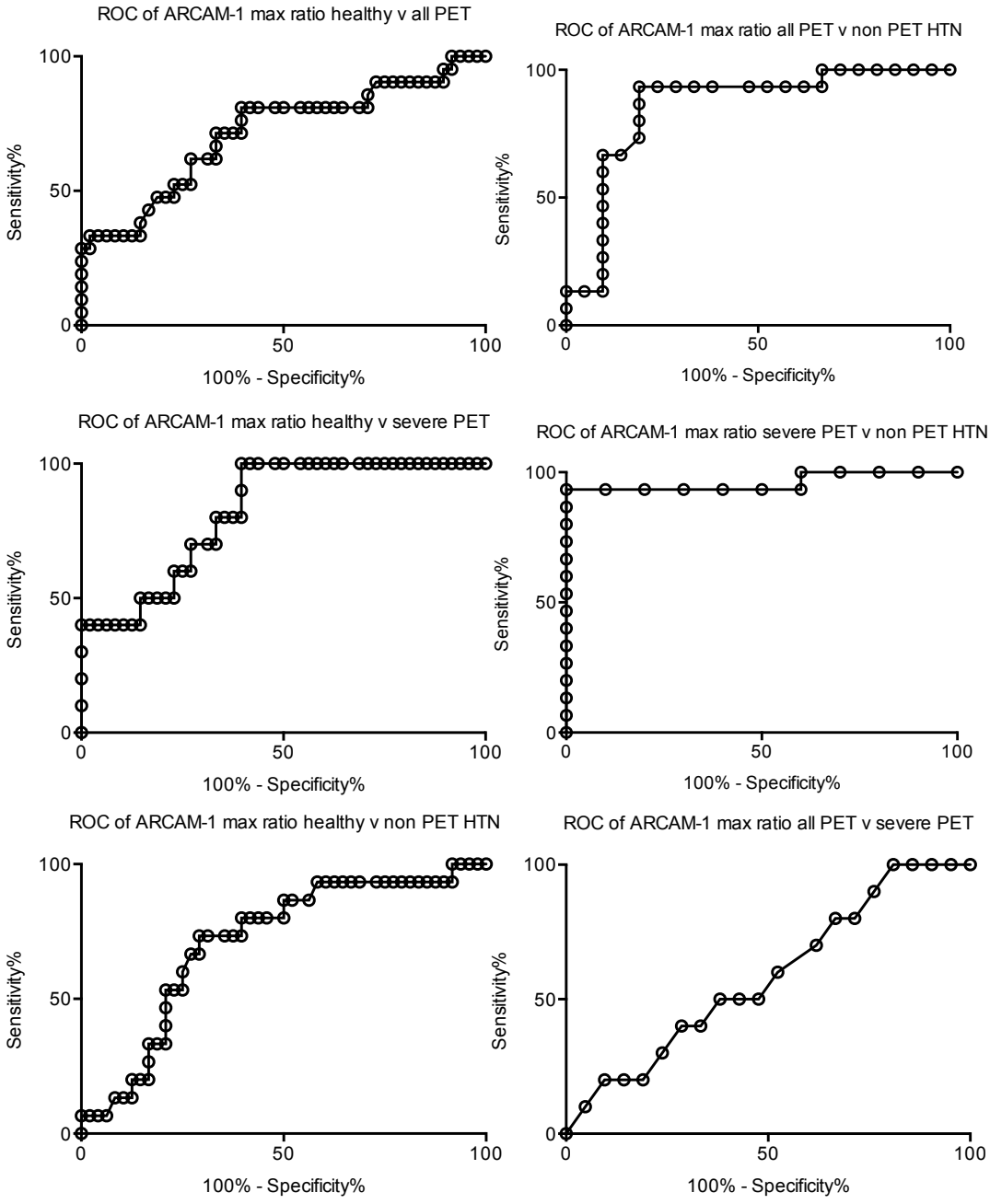

Figure 5.14 ROC curve analyses of ARCAM-1 λ_{530} for the healthy, all PET, severe PET, and non-PET HTN cohorts of pregnancy patients.

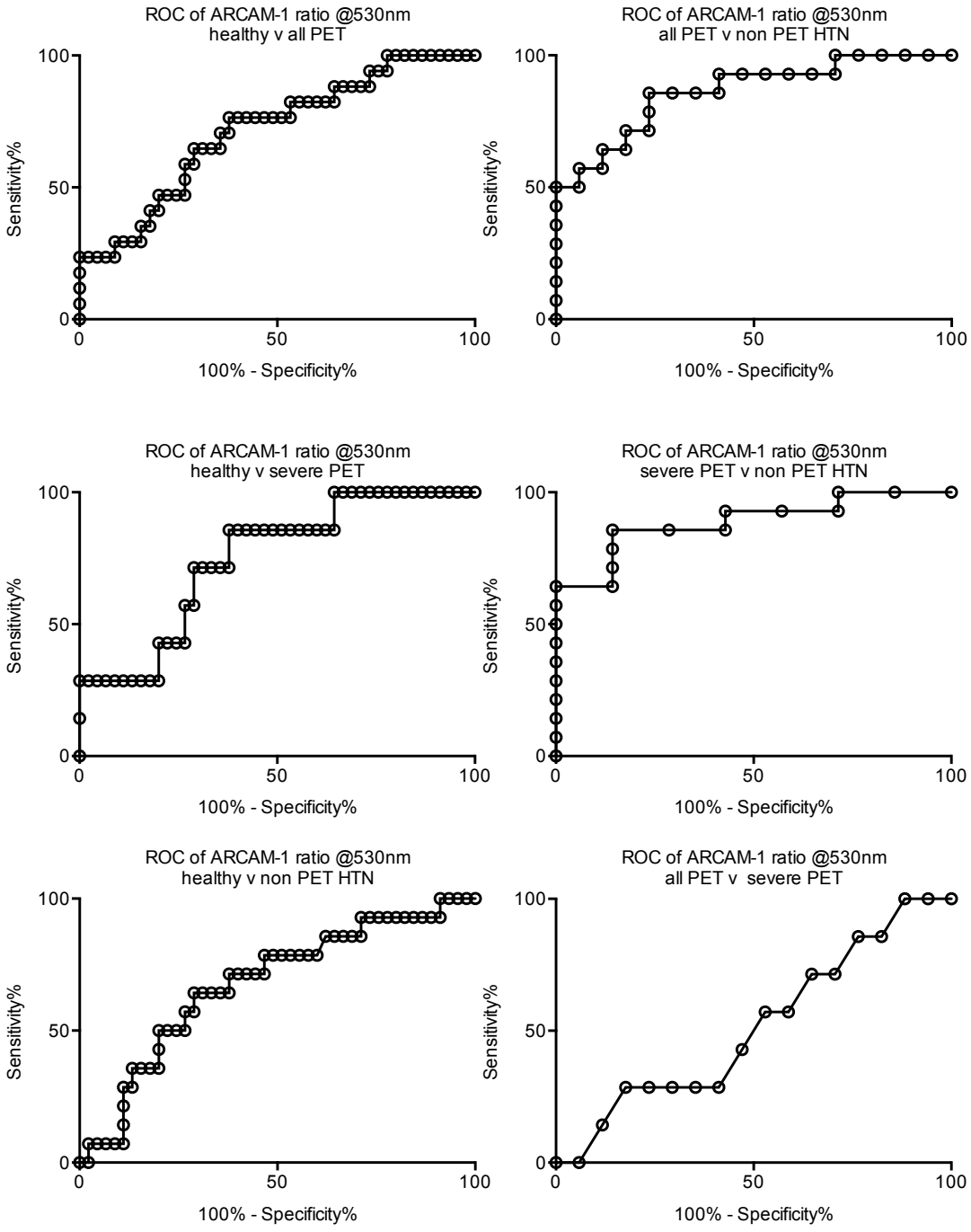

Figure 5.15 ROC curve analyses of ARCAM-1 λ_{530} for the healthy, all PET, severe PET, and non-PET HTN cohorts of pregnancy patients.

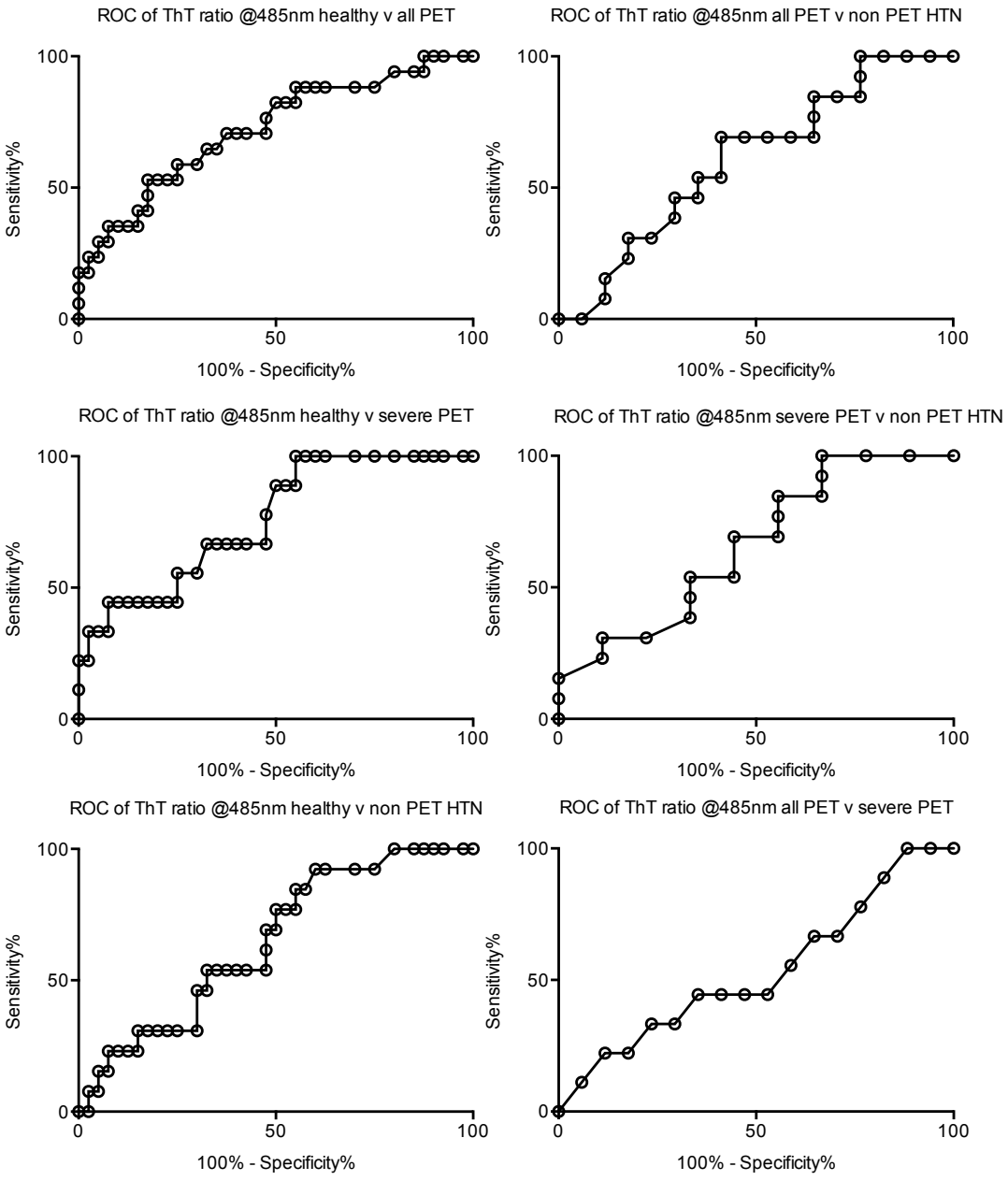

Figure 5.16 ROC curve analyses of ThT λ_{485} for the healthy, all PET, severe PET, and non-PET HTN cohorts of pregnancy patients.

5.3.1 Conclusions

These preliminary studies on the approximately 60 pregnancy patients showed that ARCAM-1 has potential utility as a diagnostic tool in the detection of amyloidosis in pre-eclampsic patients. By using the fold increase of ARCAM-1 fluorescence over background as our metric for measuring patient urine samples, we demonstrated that pre-eclampsia could be identified from healthy patients, and could be distinguished from non-pre-eclampsic hypertension conditions.

In particular, we compared the use of λ_{530} and λ_{max} for ARCAM-1 to the λ_{485} of ThT in order to establish the best method. We found that the maximum emission of ARCAM-1 had a range that depended on the patient urine sample being measured. While unclear what the exact protein composition was being detected in urine in these experiments that resulted in the particular emission maxima, these result indicate that ARCAM-1 λ_{max} would be a good candidate for further development of methods to identify pre-eclampsia from other non-pre-eclampsia conditions.

5.4 Materials and Methods

5.4.1 PE-FCS experiments

Aβ(1-42) monomer Preparation

Aβ(1-42) was synthesized, purified, and characterized by Dr. James I. Elliott at Yale University (New Haven CT). The peptide mass and purity (98%) were determined by electrospray/ion trap mass spectrometry and purified by reverse phase HPLC, respectively.

Production of aggregate-free solutions of Aβ (1-42) monomers involved 2 steps. First, Aβ(1-42) was dissolved at 1 mg/mL in disaggregation buffer (50 mM Tris-HCl, pH 8.5 containing 7M guanidium hydrochloride (GuHCl) and 200 μM EDTA) and incubated overnight at room temperature. Then monomer was isolated from the resulting solution by size exclusion chromatography (SEC) using a Superdex 75 10/300 GL column eluted at 0.5 mL/min in 20 mM Ammonium Bicarbonate pH 8.2. The concentration of the monomer peak fraction was determined using ε_{257} = 1361 M^{-1} cm^{-1}.

FCS measurement of pre-aggregated Aβ with ThT, ARCAM 1 and TAMRA- Aβ

ThT (20μM) and ARCAM-1 (2.5μM) were added into pre-aggregated Aβ (5μM) for comparison or TAMRA-Aβ (2.5μM, AnaSpec, Fremont, CA) and ARCAM-1 (2.5μM) were added into pre-aggregated Aβ for comparison in FCS measurement.

Monitoring the aggregation of Aβ(1-42) using ARCAM-1 and bulk fluorescence measurements. Solutions of SEC-isolated Aβ(1-42) monomer were

diluted to 10 μM with 20 mM ammonium bicarbonate pH 8.2 and ARCAM 1 was added to a final concentration of 2.5 μM. Aliquots (120 μL) of the peptide solutions were then dispensed into the wells of an ice-cold 96-well black microtiter plate (Nunc, Roskilde, Denmark) and read immediately. Plates were then sealed with an adhesive plastic cover (WVR, Radnor, PA) and incubated at room temperature with shaking at 500 rpm in a VorTemp 56 shaker/incubator with an orbit of 3 mm (Labnet International, Windsor, UK). The fluorescence of ARCAM-1 was measured every 20 minutes using a SpectraMax M2 microplate reader (Molecular Devices, Sunnyvale, CA) with excitation and emission of 410 nm and 570 nm, respectively. Data are presented as normalized bulk fluorescence plotted vs. time.

Determination of binding constant

As previously reported, in order to estimate the binding constant (K_d) for the probe-Aβ complexes from the fluorescence studies, we made the following assumptions:

1. All probes are completely in solution and free of any significant competing binding process such as self-aggregation.
2. The concentration of unbound probes can be approximated as close to the total concentration of the probes.
3. The binding sites in the aggregated Aβ peptides are not completely occupied at the concentration of Aβ binding probes used for the fluorescence studies (i.e., the experiments are carried out under non-saturated binding conditions).

Aggregated Aβ(1-42) (t_{max}) at a final concentration of 10 μM (based on the molecular weight of monomer) was mixed with increasing concentration of ARCAM-1 in 5% DMSO in 1X PBS at pH 7.4, 5.6, or 9.1. The K_d's were determined by fitting data to a one-site specific binding algorithm: $Y = B_{max}*X/(K_d+X)$, where X is the concentration of the probe, Y is specific binding fluorescence intensity, and B_{max} corresponds to the apparent maximal observable fluorescence upon binding of probes to aggregated Aβ42 peptide.

Measurements of pH dependence of ARCAM 1 fluorescence

ARCAM-1 was prepared to a final concentration of 4 μM in 5% DMSO in 1X PBS at various pH values both as free probe in solution and in the presence of 5 μM aggregated Aβ(1-42) (tmax). Sample preparations were incubated at room temperature for 10 minutes prior to measurement. Emission spectra were collected with 450 nm excitation wavelength on a PTI QuantaMaster 40 spectrofluorometer using FelixGX software.

Two photon excitation comparison of ThT and ARCAM-1

The intensities of fluorescence from 20μM ThT in HEPES or 2.5μM ARCAM-1 in HEPES were compared using FCS setup. The two-photon excitation wavelengths were set at 780nm, 800nm, 820nm, 840nm, 860nm and 880nm for comparison.

Comparing the aggregation kinetics of Aβ(1-42) with ARCAM-1 and ThT using bulk fluorescence measurements

Solutions of SEC-isolated Aβ(1-42) monomer were diluted to 10 μM with 20 mM ammonium bicarbonate pH 8.2 and ARCAM-1 was added to a final concentration of 2.5 μM. Aliquots (120 μL) of the peptide solutions were then dispensed into the

wells of an ice-cold 96-well black microtiter plate (Nunc, Roskilde, Denmark) and read immediately. Plates were then sealed with an adhesive plastic cover (WVR, Radnor, PA) and incubated at room temperature with shaking at 500 rpm in a VorTemp 56 shaker/incubator with an orbit of 3 mm (Labnet International, Windsor, UK). The fluorescence of ARCAM-1 was measured at 20 minute intervals using a SpectraMax M2 microplate reader (Molecular Devices, Sunnyvale, CA) with excitation and emission of 410 nm and 570 nm, respectively. Data are presented as normalized bulk fluorescence plotted vs. time.

Preparation of aggregated Aβ(1-42) to determine limit of detection by FCS

Aggregation of Aβ(1-42) was monitored using a continuous ThT assay and material which exhibited maximal fluorescence (t_{max}) was used as our aggregate standard. Briefly, solutions of Aβ(1-42) monomer were isolated as described above, but in 10.9 mM HEPES pH 7.8, diluted to 10 μM in the same buffer. A portion was held on ice and ThT added to the remainder to achieve a final concentration of 20 μM. Aliquots (120 μL) of the peptide solutions were then dispensed into the wells of an ice-cold 96-well black microtiter plate (Nunc, Roskilde, Denmark) and read immediately. Plates were sealed with an adhesive plastic cover (WVR, Radnor, PA) and incubated at room temperature with shaking at 700 rpm in a VorTemp 56 shaker/incubator with an orbit of 3 mm (Labnet International, Windsor, UK). ThT fluorescence was measured at 20-minute intervals using a SpectraMax M2 microplate reader (Molecular Devices, Sunnyvale, CA) with excitation and emission of 435 nm and 485 nm, respectively. Aggregation was allowed to proceed until the maximal fluorescence reached a plateau, then a portion of the same SEC-isolated monomer

sample that had been held on ice was used for a repeat experiment exactly as described above, but adding an equal volume of MQ water in place of ThT.

Monitoring the aggregation of Aβ(1-42) using ARCAM-1 and FCS

Aggregation of Aβ(1-42) by FCS was monitored using a modified version of method used for bulk fluorescence measurements. Briefly, Aβ(1-42) monomers were diluted to 10 μM with 20 mM ammonium bicarbonate pH 8.2 and incubated in the presence of fluorescence probe at a final concentration of 2.5 μM. Aliquots (120 μL) of the peptide solutions were then dispensed into the wells of an ice-cold 96-well black microtiter plate (Nunc, Roskilde, Denmark) and read immediately. Plates were then sealed with an adhesive plastic cover (WVR, Radnor, PA) and incubated at room temperature with shaking at 500 rpm in a VorTemp 56 shaker/incubator with an orbit of 3 mm (Labnet International, Windsor, UK). Aliquots were removed every 20 minutes and these aliquots were loaded onto microscope slides (treated with 0.1% BSA solution to reduce the non-specific adsorption) and used for FCS.

FCS setup

Two-photon FCS was performed on a customized setup based on an inverted Nikon TE2000 microscope. A collimated 820 nm IR laser (Mai Tai, Ti:Sapphire laser with 80MHz and 100 fs pulse width, Spectra-Physics, CA, USA) was aligned through an inverted Nikon microscope (TE-2000 U) into the back aperture of a Nikon 40X Plan Apochromat oil immersion objective (N.A.=1.0). The back aperture of the objective was slightly overfilled, creating a diffraction-limited focal spot. The laser power was set to 10mW (at entrance to microscope) to reduce photobleaching of the fluorescent probe. The emission fluorescence (collected via epifluorescence) was

passed through an emission filter (HQ525/50m-2p for ARCAM1, HQ485/70m-2p for ThT, HQ605/90m-2p for TAMRA-Aβ, Chroma Tech) and focused onto a photomultiplier tube (H7421, Hamamatsu, Japan) configured for single photon counting. Each autocorrelation curve measured was collected for 120 seconds using Flex02-01D/C correlator (correlator.com) and transferred to a personal computer through a high speed USB port. The raw intensity traces with 1ms resolution were also record corresponding to each autocorrelation curve.

FCS burst analysis

The raw intensity trace has 1 μs time resolution. By binning the time windows we can generate new time traces with 1 ms time resolution, which was analyzed by the burst analysis method.

To find a fluorescent burst, we analysis in the following four steps. First, the histogram of new intensity trace was plotted and the maximum peak (mode of the intensity trace) was used to designate the background signal. The standard deviation (or width) of this histogram was also determined. Second, any signals from the trace with intensities greater than four times the width of the histogram above the background baseline (mode) were selected as burst candidates. Third, due to the diffusion properties, there may be bursts in rapid succession without any intervening time. We therefore merge these bursts as single burst event. Finally, based on the previous three steps, we generated a final burst trace that was used to calculate the burst number.

FCS correlation curve analysis

All FCS curves were analyzed by custom-written Matlab code (Mathworks Inc, Waltham, MA) using a nonlinear least-squares fitting algorithm. The fitting formula of auto-correlation analysis for single-component diffusion was adapted from Krichevsky and Bonnet.

$$G(\tau)=\frac{1}{N}(1+\frac{\tau}{\tau_D})^{-1}(1+\frac{\tau}{\omega^2\tau_D})^{-1/2}$$

where N is the average particle number of species in the sampling volume, τD is the residence time of species within the sampling volume, τD =ω2xy/8D, D is the diffusion coefficient of the species, and ω = ωz/ωxy is the aspect ratio of the sampling volume. ωz is the axial size of the excitation volume and ωxy is its radius. Brightness (Q) was calculated by dividing the average fluorescence intensity by average particle number (N).

For two-component analysis, we use the following formula for fitting:

$$G(\tau)=\frac{Q_1^2N_1}{(Q_1N_1+Q_2N_2)^2}(1+\frac{\tau}{\tau_{D1}})^{-1}(1+\frac{\tau}{\omega^2\tau_{D1}})^{-1/2}+\frac{Q_2^2N_2}{(Q_1N_1+Q_2N_2)^2}(1+\frac{\tau}{\tau_{D2}})^{-1}(1+\frac{\tau}{\omega^2\tau_{D2}})^{-1/2}$$

where N1 and N2 are the average particle number of small species and large species in the sampling volume, individually. Q1 and Q2 are the particle brightness for small species and large species. τD1 and τD2 are the residence time of small species and large species, individually. From single component FCS curve analysis at time=0 minute, small species brightness Q1 and residence time τD1 can be obtained. These values were fixed in two-component analysis for small species. The average particle

number N1 for small species and N2 for large species, the brightness Q2 and residence time τD2 for large species can be obtained through the above two-component analysis.

For the FCS curve fitting analysis at time 0 minutes, we used single-component diffusion formula and obtained the initial diffusion coefficient D1=148±25 $\mu m^2/s$ for small species. The D1 value was fixed for the following time points with two-component analysis.

Diffusion coefficient calculation for rod shaped species

According to Stokes' diffusion the diffusion coefficient (D) and radius (r) of sphere-shape species have the following relationship:

$$D = \frac{kT}{6\pi\eta r}$$

k is Boltzmann constant (k=1.38 x 10^{-23} $m^2kgs^{-2}K^{-1}$), T is temperature (T=298K in our study) and η is viscosity of the solution (=8.9 x 10^{-4} $m^{-1}kgs^{-1}$). A rod-shaped species has a Stokes relationship that takes into account the long axis (a) and short axis (b) radii through the following relationship:

$$D = \frac{kT}{6\pi\eta r}\ln(\frac{2a}{b})$$

Our FCS fitting results gave the D=3.42 ± 0.43 $\mu m^2/s$, this corresponds to a 64 - 82 nm radius for spherical species and 306 - 420 nm for rod shape species (~8 nm diameter).

5.4.2 Pre-eclampsia

Study participants

This study was conducted in accordance to the approval of UCSD IRB. Informed consent was obtained from all of the patients before they partook in the study. Urine specimens from all participants were graciously obtained in collaboration with the research groups of Dr. Mana Parast (UCSD Department of Pathology) and Dr. Louise Laurent (UCSD Department of Reproductive Medicine).

62 patients were recruited into the blind prospective study from March 2015 – June 2015. The urine of patients who experienced premature rupture of membranes were excluded from the study. Spot collections of urine specimens were collected from patients presented at the labor and delivery department and the fetal center and genetics department at the UCSD Medical Center in Hillcrest. The gestational age of women in this prospective study ranged from 11 – 39 weeks. These samples were centrifuged at 2000 xg and the supernatants were retained for analyses. All specimens were aliquoted prior to analysis to prevent repetitive episodes of freezing and thawing. Specimens were stored at – 80°C before analysis. Samples were retrieved every 2 weeks and characterized within 48 hours. The outcomes of these patients were obtained following delivery.

Determination of urinary protein concentration

Bradford protein quantification assays were performed in accordance to the Bio-Rad instruction's manual. Briefly, a working solution of the Bradford dye concentrate was prepared by diluting 1 part of the Bio-rad dye concentrate with 4 parts of MQ water. 200 μL of this working solution 10 μL of standard BSA solution or 10

μL of undiluted urine. Optical densities were measured at 595 nm on a microplate reader. Analyses were performed in triplicate.

Thioflavin-T binding assays

ThT fluorescence studies were conducted in accordance to a protocol described by Buhimschi et al. Briefly, 70 μL of 114 μM ThT solution in 1xPBS was added to 30 μL of urine supernatant. The final concentration of ThT in the sample was 80 μM. Samples were measured within 5 minutes of adding ThT. Measurements were obtained in triplicate using a fluorescence plate reader with excitation and emission wavelengths set at 444 nm and 485 nm, respectively.

ARCAM-1 binding assays

5 μL of 60 μM ARCAM-1 in dimethyl sulfoxide (DMSO) were added to 30 μL of supernatant urine or 1xPBS in 65 μL of 1xPBS to a final concentration of 3 μM. Samples were incubated at room temperature for 10 minutes prior to fluorescence analyses. Measurements were made in triplicate using a fluorescence plate reader with excitation and emission wavelengths set at 450 nm and 525 nm, respectively.

Statistical analyses

Statistical analyses for the fold increase of fluorescence upon binding using a Mann-Whitney U test for non-normal population distributions. ROC curves were generated between two patient cohorts for each method using GraphPad.

5.5 Additional Figures

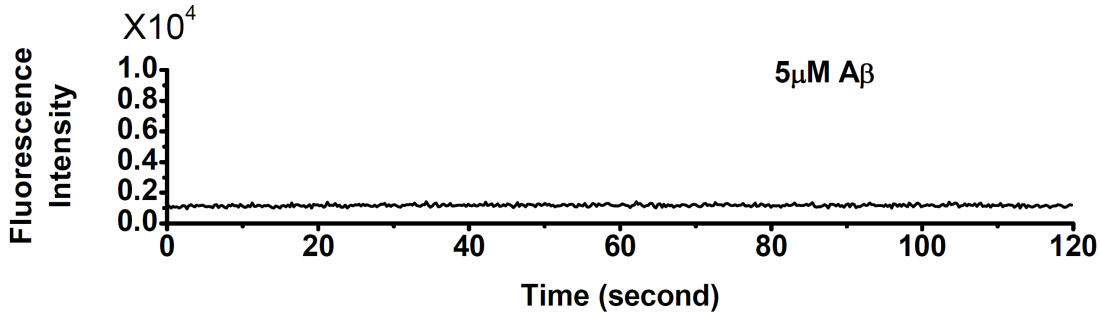

Figure 5.17 The intensity trace of Ab peptide (5 mM) alone by FCS measurement.

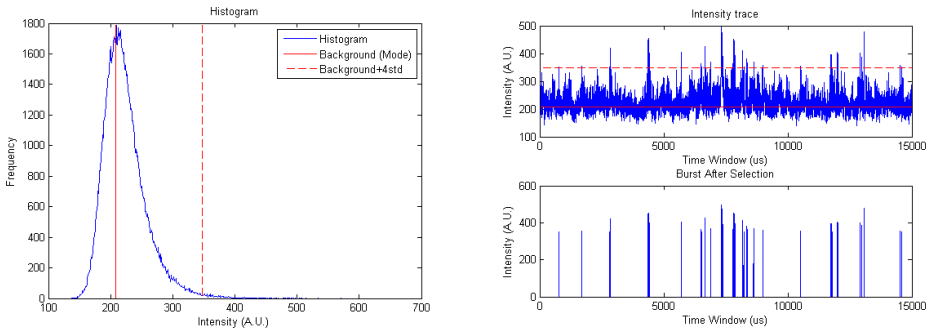

Figure 5.18 Burst selection method. (Left) the histogram of intensity trace with 1 ms resolution at 240 min of Aβ reaction. The solid red line indicates the modal value of the histogram. This value is treated as the average of intensity background due to the majority of intensity events. The dashed red line is the position at four times of the standard deviation of this intensity trace distribution above the average background. (Right above) solid and dash red lines are the same as left figure, showing the relative positions of cutoff. (Right below) Selected bursts clearly shown with all other intensities set as zero.

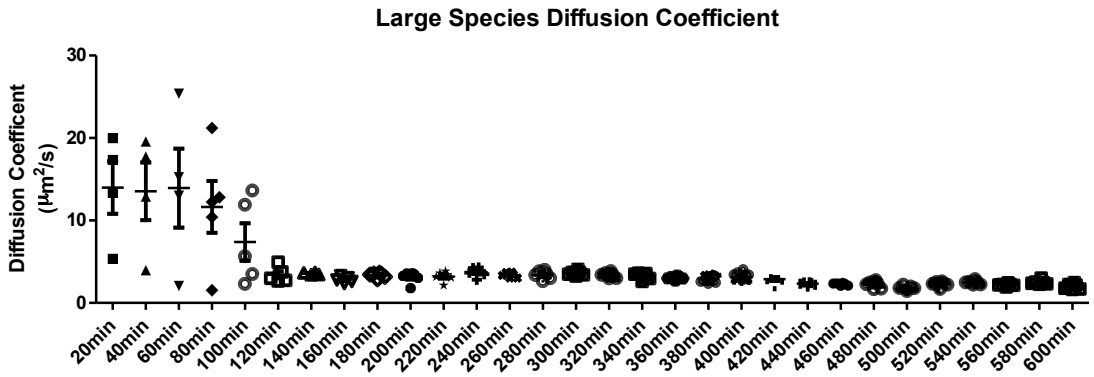

Figure 5.19 The diffusion coefficients of large species by two-component analysis at different time points.

Acknowledgements

Chapter 5 is a partial reprint of the material as it appears in "Real-time Monitoring of Alzheimer's-related amyloid via Probe Enhancement-Fluorescence Correlation Spectroscopy". Guan, Yinghua; Cao, Kevin J.; Cantlon, Adam; Elbel, Kristyna; Theodorakis, Emmanuel A.; Walsh, Dominic, Yang, Jerry, Shah, Jagesh V. (2015) *ACS Chemical Neuroscience*, 6 (9), 1503-1508. I am co-author on this publication.

Chapter 5 is also based on material currently being prepared for submission for publication "Amyloid-binding Fluorescence Diagnostic Assay for Pre-eclampsia". Do, Jamie P.; Cao, Kevin J.; Laurent, Louise; Parast, Mana; Yang, Jerry. *In preparation.* I am co-author on this publication.

References

(1) Dunker, A. K.; Silman, I.; Uversky, V. N.; Sussman, J. L. *Current Opinion in Structural Biology*. 2008, pp 756–764.

(2) Hartl, F. U.; Bracher, A.; Hayer-Hartl, M. *Nature* **2011**, *475* (7356), 324–332.

(3) Hardy, J. A.; Higgins, G. A. *Science* **1992**, *256* (5054), 184–185.

(4) Hardy, J.; Selkoe, D. J. *Science (80-.).* **2002**, *297* (July), 353–357.

(5) Tanzi, R. E.; Bertram, L. *Cell*. 2005, pp 545–555.

(6) Jaroniec, C. P.; MacPhee, C. E.; Bajaj, V. S.; McMahon, M. T.; Dobson, C. M.; Griffin, R. G. *Proc. Natl. Acad. Sci.* **2004**, *101* (3), 711–716.

(7) Barrow, C. J.; Yasuda, A.; Kenny, P. T.; Zagorski, M. G. *J. Mol. Biol.* **1992**, *225* (4), 1075–1093.

(8) Fabian, H.; Szendrei, G. I.; Mantsch, H. H.; Otvos Jr., L. *Biochem.Biophys.Res.Commun.* **1993**, *191* (0006-291X), 232–239.

(9) Sipe, J. D.; Cohen, A. S. *J. Struct. Biol.* **2000**, *130* (2-3), 88–98.

(10) Groenning, M. *J. Chem. Biol.* **2010**, *3* (1), 1–18.

(11) Schnabel, J. *Nature* **2011**, *475* (7355), S12–S14.

(12) Münch, J.; Rücker, E.; Ständker, L.; Adermann, K.; Goffinet, C.; Schindler, M.; Wildum, S.; Chinnadurai, R.; Rajan, D.; Specht, A.; Giménez-Gallego, G.; Sánchez, P. C.; Fowler, D. M.; Koulov, A.; Kelly, J. W.; Mothes, W.; Grivel, J.-C.; Margolis, L.; Keppler, O. T.; Forssmann, W.-G.; Kirchhoff, F. *Cell* **2007**, *131* (6), 1059–1071.

(13) Masliah, E.; Rockenstein, E.; Inglis, C.; Adame, A.; Bett, C.; Lucero, M.; Sigurdson, C. J. *Prion* **2012**, *6* (2), 184–190.

(14) Klunk, W. E.; Engler, H.; Nordberg, A.; Wang, Y.; Blomqvist, G.; Holt, D. P.; Bergstr??m, M.; Savitcheva, I.; Huang, G. F.; Estrada, S.; Aus??n, B.; Debnath, M. L.; Barletta, J.; Price, J. C.; Sandell, J.; Lopresti, B. J.; Wall, A.; Koivisto, P.; Antoni, G.; Mathis, C. A.; L??ngstr??m, B. *Ann. Neurol.* **2004**, *55* (3), 306–319.

(15) Klunk, W. E.; Koeppe, R. A.; Price, J. C.; Benzinger, T. L.; Devous Sr., M. D.; Jagust, W. J.; Johnson, K. A.; Mathis, C. A.; Minhas, D.; Pontecorvo, M. J.; Rowe, C. C.; Skovronsky, D. M.; Mintun, M. A. *Alzheimer's Dement.* **2015**, *11*

(1), 1–15.e4.

(16) Zhang, S.; Han, D.; Tan, X.; Feng, J.; Guo, Y.; Ding, Y. *Int. J. Clin. Pract.* **2012**, *66* (2), 185–198.

(17) Smid, L. M.; Vovko, T. D.; Popovic, M.; Petric, A.; Kepe, V.; Barrio, J. R.; Vidmar, G.; Bresjanac, M. *Brain Pathol.* **2006**, *16* (2), 124–130.

(18) Puchtler, H.; Sweat, F.; Levine, M. *J. Histochem. Cytochem.* **1962**, *10* (3), 355–364.

(19) Schütz, A. K.; Soragni, A.; Hornemann, S.; Aguzzi, A.; Ernst, M.; Böckmann, A.; Meier, B. H. *Angew. Chemie - Int. Ed.* **2011**, *50* (26), 5956–5960.

(20) Wu, C.; Scott, J.; Shea, J.-E. *Biophys. J.* **2012**, *103* (3), 550–557.

(21) Landau, M.; Sawaya, M. R.; Faull, K. F.; Laganowsky, A.; Jiang, L.; Sievers, S. a.; Liu, J.; Barrio, J. R.; Eisenberg, D. *PLoS Biol.* **2011**, *9* (6), 25–27.

(22) Biancalana, M.; Makabe, K.; Koide, A.; Koide, S. *J. Mol. Biol.* **2009**, *385* (4), 1052–1063.

(23) Stsiapura, V. I.; Maskevich, A. a.; Kuzmitsky, V. a.; Turoverov, K. K.; Kuznetsova, I. M. *J. Phys. Chem. A* **2007**, *111* (22), 4829–4835.

(24) Khurana, R.; Coleman, C.; Ionescu-Zanetti, C.; Carter, S. a.; Krishna, V.; Grover, R. K.; Roy, R.; Singh, S. *J. Struct. Biol.* **2005**, *151* (3), 229–238.

(25) Yagi, H.; Kusaka, E.; Hongo, K.; Mizobata, T.; Kawata, Y. *J. Biol. Chem.* **2005**, *280* (46), 38609–38616.

(26) Groenning, M.; Norrman, M.; Flink, J. M.; van de Weert, M.; Bukrinsky, J. T.; Schluckebier, G.; Frokjaer, S. *J. Struct. Biol.* **2007**, *159* (3), 483–497.

(27) Shi, S.; Mitteregger-Kretzschmar, G.; Giese, A.; Kretzschmar, H. a. *Acta Neuropathol. Commun.* **2013**, *1* (1), 44.

(28) Maruyama, M.; Shimada, H.; Suhara, T.; Shinotoh, H.; Ji, B.; Maeda, J.; Zhang, M. R.; Trojanowski, J. Q.; Lee, V. M.; Ono, M.; Masamoto, K.; Takano, H.; Sahara, N.; Iwata, N.; Okamura, N.; Furumoto, S.; Kudo, Y.; Chang, Q.; Saido, T. C.; Takashima, A.; Lewis, J.; Jang, M. K.; Aoki, I.; Ito, H.; Higuchi, M. *Neuron* **2013**, *79* (6), 1094–1108.

(29) Gustafson, L. *Arch. Gerontol. Geriatr.* **1987**, *6* (3), 209–223.

(30) Hong, G.; Diao, S.; Chang, J.; Antaris, A. L.; Chen, C.; Zhang, B.; Zhao, S.; Atochin, D. N.; Huang, P. L.; Andreasson, K. I.; Kuo, C. J.; Dai, H. *Nat.*

Photonics **2014**, *8* (9), 723–730.

(31) Cui, M.; Ono, M.; Watanabe, H.; Kimura, H.; Liu, B.; Saji, H. *J. Am. Chem. Soc.* **2014**, *136* (9), 3388–3394.

(32) Ono, M.; Watanabe, H.; Kimura, H.; Saji, H. *ACS Chem. Neurosci.* **2012**, *3* (4), 319–324.

(33) Sozmen, F.; Kolemen, S.; Kumada, H.-O.; Ono, M.; Saji, H.; Akkaya, E. U. *RSC Adv.* **2014**, *4* (92), 51032–51037.

(34) Tong, H.; Lou, K.; Wang, W. *Acta Pharm. Sin. B* **2015**, *5* (1), 25–33.

(35) Sutharsan, J.; Dakanali, M.; Capule, C. C.; Haidekker, M. a.; Yang, J.; Theodorakis, E. a. *ChemMedChem* **2010**, *5*, 56–60.

(36) Nilsson, K. P. R. *FEBS Lett.* **2009**, *583* (16), 2593–2599.

(37) Nilsson, K. P. R.; Hammarstrom, P.; Ahlgren, F.; Herland, A.; Schnell, E. A.; Lindgren, M.; Westermark, G. T.; Inganas, O. *Chembiochem* **2006**, *7* (7), 1096–1104.

(38) Brandenburg, E.; von Berlepsch, H.; Koksch, B. *Mol. Biosyst.* **2012**, *8* (2), 557–564.

(39) Dzwolak, W.; Pecul, M. *FEBS Lett.* **2005**, *579* (29), 6601–6603.

(40) Raymond, S. B.; Skoch, J.; Hills, I. D.; Nesterov, E. E.; Swager, T. M.; Bacskai, B. J. *Eur. J. Nucl. Med. Mol. Imaging* **2008**, *35* (SUPPL. 1).

(41) Usmani, S. M.; Zirafi, O.; Müller, J. A.; Sandi-Monroy, N. L.; Yadav, J. K.; Meier, C.; Weil, T.; Roan, N. R.; Greene, W. C.; Walther, P.; Nilsson, K. P. R.; Hammarström, P.; Wetzel, R.; Pilcher, C. D.; Gagsteiger, F.; Fändrich, M.; Kirchhoff, F.; Münch, J. *Nat. Commun.* **2014**, *5*, 3508.

(42) Ryu, E. K.; Choe, Y. S.; Lee, K. H.; Choi, Y.; Kim, B. T. *J. Med. Chem.* **2006**, *49* (20), 6111–6119.

(43) Yang, F.; Lim, G. P.; Begum, A. N.; Ubeda, O. J.; Simmons, M. R.; Ambegaokar, S. S.; Chen, P.; Kayed, R.; Glabe, C. G.; Frautschy, S. a.; Cole, G. M. *J. Biol. Chem.* **2005**, *280* (7), 5892–5901.

(44) Garcia-Alloza, M.; Borrelli, L. a.; Rozkalne, A.; Hyman, B. T.; Bacskai, B. J. *J. Neurochem.* **2007**, *102* (4), 1095–1104.

(45) Ferreira, N.; Santos, S. a O.; Domingues, M. R. M.; Saraiva, M. J.; Almeida, M. R. *Biochim. Biophys. Acta - Mol. Basis Dis.* **2013**, *1832* (1), 39–45.

(46) Rao, P. P. N.; Mohamed, T.; Teckwani, K.; Tin, G. *Chem. Biol. Drug Des.* **2015**, n/a – n/a.

(47) McCrate, O. A.; Zhou, X.; Cegelski, L. *Chem. Commun. (Camb).* **2013**, *49* (39), 4193–4195.

(48) Koronyo-Hamaoui, M.; Koronyo, Y.; Ljubimov, A. V.; Miller, C. a.; Ko, M. K.; Black, K. L.; Schwartz, M.; Farkas, D. L. *Neuroimage* **2011**, *54* (SUPPL. 1), S204–S217.

(49) Chongzhao, R.; Xiaoyin, X.; Raymond, S. B.; Ferrara, B. J.; Neal, K.; Bacskai, B. J.; Medarova, Z.; Moore, A. *J. Am. Chem. Soc.* **2009**, *131* (42), 15257–15261.

(50) Ran, C.; Moore, A. *Mol. Imaging Biol.* **2012**, *14* (3), 293–300.

(51) Zhang, X.; Tian, Y.; Zhang, C.; Tian, X.; Ross, A. W.; Moir, R. D.; Sun, H.; Tanzi, R. E.; Moore, A.; Ran, C. *Proc. Natl. Acad. Sci. U. S. A.* **2015**, 1505420112 – .

(52) Reinke, A. a.; Gestwicki, J. E. *Chem. Biol. Drug Des.* **2011**, *77* (6), 399–411.

(53) Streets, A. M.; Sourigues, Y.; Kopito, R. R.; Melki, R.; Quake, S. R. *PLoS One* **2013**, *8* (1), 1–10.

(54) Nielsen, L.; Khurana, R.; Coats, A.; Frokjaer, S.; Brange, J.; Vyas, S.; Uversky, V. N.; Fink, A. L. *Biochemistry* **2001**, *40* (20), 6036–6046.

(55) Atarashi, R.; Sano, K.; Satoh, K.; Nishida, N. *Prion* **2011**, *5* (3), 150–153.

(56) Atarashi, R.; Satoh, K.; Sano, K.; Fuse, T.; Yamaguchi, N.; Ishibashi, D.; Matsubara, T.; Nakagaki, T.; Yamanaka, H.; Shirabe, S.; Yamada, M.; Mizusawa, H.; Kitamoto, T.; Klug, G.; McGlade, A.; Collins, S. J.; Nishida, N. *Nat. Med.* **2011**, *17* (2), 175–178.

(57) Ban, T.; Hoshino, M.; Takahashi, S.; Hamada, D.; Hasegawa, K.; Naiki, H.; Goto, Y. *J. Mol. Biol.* **2004**, *344* (3), 757–767.

(58) Ries, J.; Udayar, V.; Soragni, A.; Hornemann, S.; Nilsson, K. P. R.; Riek, R.; Hock, C.; Ewers, H.; Aguzzi, A. a.; Rajendran, L. *ACS Chem. Neurosci.* **2013**, *4* (7), 1057–1061.

(59) Horrocks, M. H.; Lee, S. F.; Gandhi, S.; Magdalinou, N. K.; Chen, S. W.; Devine, M. J.; Tosatto, L.; Kjaergaard, M.; Beckwith, J. S.; Zetterberg, H.; Iljina, M.; Cremades, N.; Dobson, C. M.; Wood, N. W.; Klenerman, D. *ACS Chem. Neurosci.* **2016**, acschemneuro.5b00324.

(60) Barrio, J. R.; Small, G. W.; Wong, K.-P.; Huang, S.-C.; Liu, J.; Merrill, D. a.; Giza, C. C.; Fitzsimmons, R. P.; Omalu, B.; Bailes, J.; Kepe, V. *Proc. Natl. Acad. Sci.* **2015**, 201409952.

(61) Klunk, W. E.; Wang, Y.; Huang, G. F.; Debnath, M. L.; Holt, D. P.; Mathis, C. a. *Life Sci.* **2001**, *69* (13), 1471–1484.

(62) Neal, K. L.; Shakerdge, N. B.; Hou, S. S.; Klunk, W. E.; Mathis, C. a; Nesterov, E. E.; Swager, T. M.; McLean, P. J.; Bacskai, B. J. *Mol. Imaging Biol.* **2013**, *15* (5), 585–595.

(63) Zhang, X.; Tian, Y.; Li, Z.; Tian, X.; Liu, H.; Sun, H.; Moore, A.; Ran, C. *J. Am. Chem. Soc.* **2013**, *135*, 16397–16409.

(64) Crosignani, V.; Dvornikov, A.; Aguilar, J. S.; Stringari, C.; Edwards, R.; Mantulin, W. W.; Gratton, E. *J. Biomed. Opt.* **2012**, *17* (11), 116023.

(65) Hoshi, Y. *Psychophysiology* **2003**, *40* (4), 511–520.

(66) Ntziachristos, V.; Tung, C.-H.; Bremer, C.; Weissleder, R. *Nat. Med.* **2002**, *8* (7), 757–760.

(67) Perez, S. E.; Lumayag, S.; Kovacs, B.; Mufson, E. J.; Xu, S. *Invest. Ophthalmol. Vis. Sci.* **2009**, *50* (2), 793–800.

(68) Goldstein, L. E.; Muffat, J. a.; Cherny, R. a.; Moir, R. D.; Ericsson, M. H.; Huang, X.; Mavros, C.; Coccia, J. a.; Faget, K. Y.; Fitch, K. a.; Masters, C. L.; Tanzi, R. E.; Chylack, L. T.; Bush, A. I. *Lancet* **2003**, *361*, 1258–1265.

(69) Rafii, M. S.; Wishnek, H.; Brewer, J. B.; Donohue, M. C.; Ness, S.; Mobley, W. C.; Aisen, P. S.; Rissman, R. A. *Front. Behav. Neurosci.* **2015**, *9* (March 2013), 1–11.

(70) Kerbage, C.; Sadowsky, C. H.; Jennings, D.; Cagle, G. D.; Hartung, P. D. *Front. Neurol.* **2013**, *4 MAY* (May), 1–9.

(71) La Morgia C, Ross-Cisneros FN, Koronyo Y, Hannibal J, Gallassi R, Cantalupo G, Sambati L, Pan BX, Tozer KR, Barboni P, Provini F, Avanzini P, Carbonelli M, Pelosi A, Chui H, Liguori R, Baruzzi A, Koronyo-Hamaoui M, Sadun AA, C. V. *Ann Neurol.* **2015**, *Epub ahead*, 1–20.

(72) Kam, J. H.; Lenassi, E.; Jeffery, G. *PLoS One* **2010**, *5* (10).

(73) Head, M. W.; Northcott, V.; Rennison, K.; Ritchie, D.; McCardle, L.; Bunn, T. J. R.; McLennan, N. F.; Ironside, J. W.; Tullo, A. B.; Bonshek, R. E. *Invest. Ophthalmol. Vis. Sci.* **2003**, *44* (1), 342–346.

(74) van Dijk, H. W.; Verbraak, F. D.; Kok, P. H. B.; Stehouwer, M.; Garvin, M. K.; Sonka, M.; Hans Devries, J.; Schlingemann, R. O.; Abràmoff, M. D. *Investig. Ophthalmol. Vis. Sci.* **2012**, *53* (6), 2715–2719.

(75) Kawaji, T.; Ando, Y.; Nakamura, M.; Yamashita, T.; Wakita, M.; Ando, E.; Hirata, A.; Tanihara, H. *Ophthalmology* **2005**, *112* (12), 2212–2218.

(76) Buhimschi, I. a.; Nayeri, U. a.; Zhao, G.; Shook, L. L.; Pensalfini, a.; Funai, E. F.; Bernstein, I. M.; Glabe, C. G.; Buhimschi, C. S. *Sci. Transl. Med.* **2014**, *6* (245), 245ra92–ra245ra92.

(77) Bermejo-Pareja, F.; Antequera, D.; Vargas, T.; Molina, J. a; Carro, E. *BMC Neurol.* **2010**, *10*, 108.

(78) Shi, M.; Sui, Y.-T.; Peskind, E. R.; Li, G.; Hwang, H.; Devic, I.; Ginghina, C.; Edgar, J. S.; Pan, C.; Goodlett, D. R.; Furay, A. R.; Gonzalez-Cuyar, L. F.; Zhang, J. *J. Alzheimers. Dis.* **2011**, *27* (2), 299–305.

(79) Moda, F.; Gambetti, P.; Notari, S.; Concha-Marambio, L.; Catania, M.; Park, K.-W.; Maderna, E.; Suardi, S.; Haïk, S.; Brandel, J.-P.; Ironside, J.; Knight, R.; Tagliavini, F.; Soto, C. *N. Engl. J. Med.* **2014**, *371* (6), 530–539.

(80) Lee, S. J.; Desplats, P.; Sigurdson, C.; Tsigelny, I.; Masliah, E. *Nat Rev Neurol* **2010**, *6* (12), 702–706.

(81) Bett, C.; Joshi-Barr, S.; Lucero, M.; Trejo, M.; Liberski, P.; Kelly, J. W.; Masliah, E.; Sigurdson, C. J. *PLoS Pathog.* **2012**, *8* (2).

(82) Jack, C. R.; Wiste, H. J.; Weigand, S. D.; Knopman, D. S.; Lowe, V.; Vemuri, P.; Mielke, M. M.; Jones, D. T.; Senjem, M. L.; Gunter, J. L.; Gregg, B. E.; Pankratz, V. S.; Petersen, R. C. *Neurology* **2013**, *81* (20), 1732–1740.

(83) Clark, C. M.; Pontecorvo, M. J.; Beach, T. G.; Bedell, B. J.; Coleman, R. E.; Doraiswamy, P. M.; Fleisher, A. S.; Reiman, E. M.; Sabbagh, M. N.; Sadowsky, C. H.; Schneider, J. A.; Arora, A.; Carpenter, A. P.; Flitter, M. L.; Joshi, A. D.; Krautkramer, M. J.; Lu, M.; Mintun, M. A.; Skovronsky, D. M. *Lancet Neurol.* **2012**, *11* (8), 669–678.

(84) Nesterov, E. E.; Skoch, J.; Hyman, B. T.; Klunk, W. E.; Bacskai, B. J.; Swager, T. M. *Angew. Chemie - Int. Ed.* **2005**, *44* (34), 5452–5456.

(85) Zhao, X.; Yang, J. *ACS Chem. Neurosci.* **2010**, *1* (10), 655–660.

(86) Cras, P.; Kawai, M.; Lowery, D.; Gonzalez-DeWhitt, P.; Greenberg, B.; Perry, G. *Proc. Natl. Acad. Sci. U. S. A.* **1991**, *88* (17), 7552–7556.

(87) Hardy, J.; Selkoe, D. J. *Science* **2002**, *297* (5580), 353–356.

(88) Petkova, A. T.; Leapman, R. D.; Guo, Z.; Yau, W.-M.; Mattson, M. P.; Tycko, R. *Science* **2005**, *307* (5707), 262–265.

(89) Lindgren, M.; Sörgjerd, K.; Hammarström, P. *Biophys. J.* **2005**, *88* (6), 4200–4212.

(90) LaFerla, F. M.; Green, K. N.; Oddo, S. *Nat. Rev. Neurosci.* **2007**, *8* (7), 499–509.

(91) Alzheimer's Association. *Alzheimers. Dement.* **2015**, *11* (3), 332–384.

(92) Prusiner, S. B. *Science (80-.).* **2012**, *336* (June), 1511–1513.

(93) Prusiner, S. B. *Science* **1982**, *216* (4542), 136–144.

(94) Eghiaian, F.; Grosclaude, J.; Lesceu, S.; Debey, P.; Doublet, B.; Tréguer, E.; Rezaei, H.; Knossow, M. *Proc. Natl. Acad. Sci. U. S. A.* **2004**, *101* (28), 10254–10259.

(95) Guerreiro, R.; Brás, J.; Wojtas, A.; Rademakers, R.; Hardy, J.; Graff-Radford, N. *Neurobiol. Aging* **2014**, *35* (11), 2656.e13–e16.

(96) Imran, M.; Mahmood, S. *Virol. J.* **2011**, *8* (1), 559.

(97) Mayor, S.; Riezman, H. *Nat. Rev. Mol. Cell Biol.* **2004**, *5* (February), 110–120.

(98) Bett, C.; Kurt, T. D.; Lucero, M.; Trejo, M.; Rozemuller, A. J.; Kong, Q.; Nilsson, K. P. R.; Masliah, E.; Oldstone, M. B.; Sigurdson, C. J. *PLoS Pathog.* **2013**, *9* (4).

(99) Priola, S. A.; McNally, K. L. *Prion* **2009**, *3* (3), 134–138.

(100) Weissmann, C. *Nat. Rev. Microbiol.* **2004**, *2* (11), 861–871.

(101) Aguzzi, A.; Heikenwalder, M.; Polymenidou, M. *Nat. Rev. Mol. Cell Biol.* **2007**, *8* (7), 552–561.

(102) Bruce, M. E.; Will, R. G.; Ironside, J. W.; McConnell, I.; Drummond, D.; Suttie, a; McCardle, L.; Chree, a; Hope, J.; Birkett, C.; Cousens, S.; Fraser, H.; Bostock, C. J. *Nature* **1997**, *389* (6650), 498–501.

(103) Hueston, W. D. *Preventive Veterinary Medicine*. 2013, pp 179–184.

(104) Chang, W. M.; Dakanali, M.; Capule, C. C.; Sigurdson, C. J.; Yang, J.; Theodorakis, E. a. *ACS Chem. Neurosci.* **2011**, *2* (5), 249–255.

(105) Sigurdson, C. J.; Nilsson, K. P. R.; Hornemann, S.; Manco, G.; Polymenidou,

M.; Schwarz, P.; Leclerc, M.; Hammarström, P.; Wüthrich, K.; Aguzzi, A. *Nat. Methods* **2007**, *4* (12), 1023–1030.

(106) Haidekker, M. A.; Theodorakis, E. A. *Org. Biomol. Chem.* **2007**, *5* (11), 1669–1678.

(107) Sigurdson, C. J.; Aguzzi, A. *Biochim. Biophys. Acta - Mol. Basis Dis.* **2007**, *1772* (6), 610–618.

(108) Ludlage, E.; Murphy, C. L.; Davern, S. M.; Solomon, A.; Weiss, D. T.; Glenn-Smith, D.; Dworkin, S.; Mansfield, K. G. *Vet. Pathol.* **2005**, *42* (2), 117–124.

(109) Kimura, Y.; Ikegami, a. *J. Membr. Biol.* **1985**, *85* (3), 225–231.

(110) Benzeid, H.; Mothes, E.; Essassi, E. M.; Faller, P.; Pratviel, G. *Comptes Rendus Chim.* **2012**, *15* (1), 79–85.

(111) Lippert, E. *Zeitschrift Fur Naturforsch. Part a-Astrophysik Phys. Und Phys. Chemie* **1955**, *10* (7), 541–545.

(112) Mataga, N.; Kaifu, Y.; Koizumi, M. *Bull. Chem. Soc. Jpn.* **1955**, *28* (9), 690–691.

(113) Cao, K.; Farahi, M.; Dakanali, M.; Chang, W. M.; Sigurdson, C. J.; Theodorakis, E. a.; Yang, J. *J. Am. Chem. Soc.* **2012**, *134*, 17338–17341.

(114) Haidekker, M. a; Theodorakis, E. a. *J. Biol. Eng.* **2010**, *4*, 11.

(115) Groenning, M. *J. Chem. Biol.* **2010**, *3* (1), 1–18.

(116) Wu, C.; Wang, Z.; Lei, H.; Zhang, W.; Duan, Y. *J. Am. Chem. Soc.* **2007**, *129* (5), 1225–1232.

(117) Bird, C. W. *Tetrahedron* **1985**, *41* (7), 1409–1414.

(118) Nyulászi, L.; Várnai, P.; Veszprémi, T. *J. Mol. Struct. THEOCHEM* **1995**, *358* (C), 55–61.

(119) Reichardt, C. *Chem. Rev.* **1994**, *94*, 2319–2358.

(120) Bagchi, B.; Oxtoby, D. W.; Fleming, G. R. *Chem. Phys.* **1984**, *86* (3), 257–267.

(121) Lakowicz, J. R. *Principles of fluorescence spectroscopy*; 2006.

(122) Curtis, J. C.; Sullivan, P. B.; Meyer, T. J. *Inorg. Chem.* **1983**, *22* (7), 224–236.

(123) Liptay, W. *Angew. Chemie Int. Ed. English* **1969**, *8* (3), 177–188.

(124) Barnhart, M. M.; Chapman, M. R. *Annu. Rev. Microbiol.* **2006**, *60*, 131–147.

(125) Westermark, P.; Andersson, A.; Westermark, G. T. *Physiol. Rev.* **2011**, *91* (294), 795–826.

(126) Revesz, T.; Holton, J. L.; Lashley, T.; Plant, G.; Rostagno, A.; Ghiso, J.; Frangione, B. *Brain Pathol.* **2002**, *12* (3), 343–357.

(127) Hafner-Bratkovič, I.; Gašperšič, J.; Šmid, L. M.; Bresjanac, M.; Jerala, R. *J. Neurochem.* **2008**, *104* (6), 1553–1564.

(128) Galea, M.; Woodward, M. *Aust. J. Physiother.* **2005**, *51* (3), 198.

(129) Pozueta, A.; Rodríguez-Rodríguez, E.; Vazquez-Higuera, J. L.; Mateo, I.; Sánchez-Juan, P.; González-Perez, S.; Berciano, J.; Combarros, O. *BMC Neurol.* **2011**, *11* (1), 78.

(130) Ali, R. R.; Sowden, J. C. *Nature* **2011**, *472* (7341), 42–43.

(131) Cepko, C. *Nat. Rev. Neurosci.* **2014**, *15* (9), 615–627.

(132) Ho, C. Y.; Troncoso, J. C.; Knox, D.; Stark, W.; Eberhart, C. G. *Brain Pathol.* **2014**, *24* (1), 25–32.

(133) Ratnayaka, J. A.; Serpell, L. C.; Lotery, A. J. *Eye (Lond).* **2015**, *29* (8), 1013–1026.

(134) Ohno-Matsui, K. *Prog. Retin. Eye Res.* **2011**, *30* (4), 217–238.

(135) Anderson, D. H.; Talaga, K. C.; Rivest, A. J.; Barron, E.; Hageman, G. S.; Johnson, L. V. *Exp. Eye Res.* **2004**, *78* (2), 243–256.

(136) Head, M. W.; Peden, a H.; Yull, H. M.; Ritchie, D. L.; Bonshek, R. E.; Tullo, a B.; Ironside, J. W. *Br. J. Ophthalmol.* **2005**, *89* (9), 1131–1133.

(137) Head, M. W.; Ritchie, D.; Smith, N.; McLoughlin, V.; Nailon, W.; Samad, S.; Masson, S.; Bishop, M.; McCardle, L.; Ironside, J. W. *Am J Pathol* **2004**, *164* (1), 143–153.

(138) Kercher, L.; Favara, C.; Striebel, J. F.; LaCasse, R.; Chesebro, B. *J. Virol.* **2007**, *81* (19), 10340–10351.

(139) Kerbage, C.; Sadowsky, C. H.; Tariot, P. N.; Agronin, M.; Alva, G.; Turner, F. D.; Nilan, D.; Cameron, A.; Cagle, G. D.; Hartung, P. D. *Am. J. Alzheimers. Dis. Other Demen.* **2014**.

(140) Fu, H.; Cui, M.; Tu, P.; Pan, Z.; Liu, B. *Chem. Commun. (Camb).* **2014**, *50*

(80), 11875–11878.

(141) Calderone, L.; Grimes, P.; Shalev, M. *Exp. Eye Res.* **1986**, *42* (4), 331–337.

(142) Saha, J. K.; Xia, J.; Grondin, J. M.; Engle, S. K.; Jakubowski, J. a. *Exp. Biol. Med. (Maywood).* **2005**, *230* (10), 777–784.

(143) Eimer, W. A.; Vassar, R. *Mol. Neurodegener.* **2013**, *8*, 2.

(144) Kimura, R.; Ohno, M. *Neurobiol. Dis.* **2009**, *33* (2), 229–235.

(145) Lok, K.; Zhao, H.; Shen, H.; Wang, Z.; Gao, X.; Zhao, W.; Yin, M. *Neurosci. Lett.* **2013**, *557* (PB), 84–89.

(146) Trinchese, F.; Liu, S.; Battaglia, F.; Walter, S.; Mathews, P. M.; Arancio, O. *Ann. Neurol.* **2004**, *55* (6), 801–814.

(147) Bancher, C.; Grundke-Iqbal, I.; Iqbal, K.; Kim, K. S.; Wisniewski, H. M. *Neurobiol. Aging* **1989**, *10* (2), 125–132.

(148) Katz, M. L.; Eldred, G. E.; Robison, W. G. *Mech. Ageing Dev.* **1987**, *39* (1), 81–90.

(149) Katz, M. L.; Robison, W. G. In *Archives of Gerontology and Geriatrics*; 2002; Vol. 34, pp 169–184.

(150) Dorey, C. K.; Wu, G.; Ebenstein, D.; Garsd, A.; Weiter, J. J. *Investig. Ophthalmol. Vis. Sci.* **1989**, *30* (8), 1691–1699.

(151) Paulick, M. G.; Bertozzi, C. R. *Biochemistry*. 2008, pp 6991–7000.

(152) Borchelt, D. R.; Koliatsos, V. E.; Guarnieri, M.; Pardo, C. A.; Sisodia, S. S.; Price, D. L. *J. Biol. Chem.* **1994**, *269* (20), 14711–14714.

(153) Hachiya, N. S.; Watanabe, K.; Yamada, M.; Sakasegawa, Y.; Kaneko, K. *Biochem. Biophys. Res. Commun.* **2004**, *315* (4), 802–807.

(154) Collins, S. J.; Lewis, V.; Brazier, M. W.; Hill, A. F.; Lawson, V. A.; Klug, G. M.; Masters, C. L. *Neurobiol. Dis.* **2005**, *20* (2), 336–346.

(155) Fändrich, M. *Journal of Molecular Biology*. 2012, pp 427–440.

(156) Benilova, I.; Karran, E.; De Strooper, B. *Nat. Neurosci.* **2012**, *15* (3), 349–357.

(157) Walsh, D. M.; Teplow, D. B. *Prog. Mol. Biol. Transl. Sci.* **2012**, *107*, 101–124.

(158) Jonas, S. M.; Deserno, T. M.; Buhimschi, C. S.; Makin, J.; Choma, M. A.; Buhimschi, I. A. *J. Am. Med. Inform. Assoc.* **2015**.

(159) Walsh, D. M.; Hartley, D. M.; Kusumoto, Y.; Fezoui, Y.; Condron, M. M.; Lomakin, A.; Benedek, G. B.; Selkoe, D. J.; Teplow, D. B.; Biol, D. B. J. *Biochemistry* **1999**, *274* (36), 25945–25952.

(160) Botvinick, E. L.; Shah, J. V. *Methods in Cell Biology*. 2007, pp 81–109.

(161) Gaglia, G.; Guan, Y.; Shah, J. V; Lahav, G. *Proc. Natl. Acad. Sci. U. S. A.* **2013**, *110* (38), 15497–15501.

(162) Rajagopalan, S.; Huang, F.; Fersht, A. R. *Nucleic Acids Res.* **2011**, *39* (6), 2294–2303.

(163) Bieschke, J.; Giese, A.; Schulz-Schaeffer, W.; Zerr, I.; Poser, S.; Eigen, M.; Kretzschmar, H. *Proc. Natl. Acad. Sci. U. S. A.* **2000**, *97* (10), 5468–5473.

(164) Kayatekin, C.; Matlack, K. E. S.; Hesse, W. R.; Guan, Y.; Chakrabortee, S.; Russ, J.; Wanker, E. E.; Shah, J. V; Lindquist, S. *Proc. Natl. Acad. Sci.* **2014**, *111 VN* - (33), 12085–12090.

(165) Paredes, J. M.; Casares, S.; Ruedas-Rama, M. J.; Fernandez, E.; Castello, F.; Varela, L.; Orte, A. *Int. J. Mol. Sci.* **2012**, *13* (8), 9400–9418.

(166) Tjernberg, L. O.; Pramanik, A.; Bjorling, S.; Thyberg, P.; Thyberg, J.; Nordstedt, C.; Berndt, K. D.; Terenius, L.; Rigler, R. *Chem. Biol.* **1999**, *6* (1), 53–62.

(167) Mittag, J. J.; Milani, S.; Walsh, D. M.; Rädler, J. O.; McManus, J. J. *Biochem. Biophys. Res. Commun.* **2014**, *448* (2), 195–199.

(168) Pitschke, M.; Prior, R.; Haupt, M.; Riesner, D. *Nat. Med.* **1998**, *4* (7), 832–834.

(169) O'Malley, T. T.; Oktaviani, N. A.; Zhang, D.; Lomakin, A.; O'Nuallain, B.; Linse, S.; Benedek, G. B.; Rowan, M. J.; Mulder, F. a a; Walsh, D. M. *Biochem. J.* **2014**, *461* (3), 413–426.

(170) Schwille, P.; Haupts, U.; Maiti, S.; Webb, W. W. *Biophys. J.* **1999**, *77* (4), 2251–2265.

(171) Ries, J.; Schwille, P. *BioEssays* **2012**, *34* (5), 361–368.

(172) Hellstrand, E.; Boland, B.; Walsh, D. M.; Linse, S. *ACS Chem. Neurosci.* **2010**, *1* (1), 13–18.

(173) Bauer, S. T.; Cleary, K. L. *Seminars in Perinatology*. 2009, pp 158–165.

(174) Noris, M.; Perico, N.; Remuzzi, G. *Nat. Clin. Pract. Nephrol.* **2005**, *1* (2), 98–114.

(175) Cade, T. J.; Gilbert, S. A.; Polyakov, A.; Hotchin, A. *Aust. New Zeal. J. Obstet. Gynaecol.* **2012**, *52* (2), 179–182.

(176) Park, S. H.; Goo, J. M.; Jo, C.-H. *Korean J. Radiol.* **2004**, *5* (March), 11–18.

(177) Hanley, J. A.; McNeil, B. J. *Radiology* **1982**, *143* (1), 29–36.